Flow Boiling of a Dilute Emulsion on a Microporous Surface

A DISSERTATION
SUBMITTED TO THE FACULTY OF THE GRADUATE SCHOOL
OF THE UNIVERSITY OF MINNESOTA
BY

Brandon Shadakofsky

IN PARTIAL FULFILLMENT OF THE REQUIREMENTS
FOR THE DEGREE OF
DOCTOR OF PHILOSOPHY

Francis A. Kulacki, Adviser

JANUARY 2019

Acknowledgement

First, I would like to extend my gratitude to my wife, Cati, for her encouragement, comfort, and patience through this doctoral process. It has been a joy being married these four years and it is to your honor and credit that I was able to persevere in this work. This gratitude extends as well to our family members that have always loved me and supported me in my work. Without your influence on me as a young boy until now in early adulthood, I would not have been able to complete this work. As well, although I imagine it may have been somewhat tedious learning about heat transfer, phase change and "cooking"- as my research has been called- you always listened intently and were willing to learn and encourage me to grow deeper in my own understanding. I am immensely grateful for the presence of you all in my life.

I would also like to express my appreciation to the many lab mates and friends I have come to know and grow close to during my time here. Your questions and comments on my research deepened my understanding greatly and- especially to my friends in the department- my knowledge of engineering in general has increased dramatically through your instruction in your own areas of specialty. It has been such a pleasure coming to know all of you and taking a brief reprieve from the daily rigor of graduate school through frequent time spent together.

Next, I thank my advisor, Dr. Frank Kulacki, for his instruction, advice and guidance through graduate school in general and this research process in particular. Though our discussions about research pushed me to delve more deeply in understanding the thermal sciences- and I would have floundered if you had not continually pushed me to understand more- I immensely enjoyed the discussions that often moved from research to topics as far ranging as history and politics to religion and family life. Graduate school ought to be a time of growth in many areas, and these conversations have been an impetus for my own growth, thinking and understanding on an innumerable number of topics.

Finally, and most importantly, I would like to express my deepest gratitude to my God and my savior, Jesus Christ. Had You not called us, Cati and I would not have undertaken this adventure to receive our graduate degrees at this historic institution and without Your comfort, strength, and correction, I could not have started nor completed this work. Though I have done it imperfectly in many ways, it has been an enormous pleasure to perform this work for You and I have thoroughly enjoyed growing in my understanding of and relationship with You. Your rod and staff have guided and comforted me through all these years and I hope and pray that this work will bring glory to Your great name.

Dedication

This dissertation is dedicated to two people whom I love. First, to my older brother, Matt. You may not know this- because I do not do a good job of articulating it- but you have had more influence on my life than you can ever know. As a young boy, all I wanted to be was my older brother and this has driven my life in many ways that I still do not fully comprehend. Second, to my wonderful wife, Cati. Going through graduate school would have been a lonely and much more difficult experience without your presence by my side. I love you dearly and thank God that He brought you into my life to help me in this and so many other aspects of life.

Abstract

In this investigation, an experimental apparatus was designed and constructed for studying flow boiling of water and dilute emulsions. Experiments were conducted in microgaps of 200, 500 and 1000 μm hydraulic diameter and mass fluxes of 150, 350 and 550 kg/m^{2}s. The emulsions comprised droplets of FC-72 suspended in water at FC-72 volume fractions of 0.1, 0.5, 1 and 2%. Experiments were conducted for a smooth surface and three microporous surfaces of varying thickness (708, 633, 412 μm) and porosity (0.354, 0.410, 0.413).

For water on the smooth surfaces, the single-phase heat transfer coefficient increases with increasing mass flux and decreasing gap size. After the onset of nucleate boiling and prior to transition to the critical heat flux, the heat transfer curves collapse to one curve. CHF increases with increasing gap size and mass flux. The effects of the liquid subcooling, applied heat flux, mass flux, and gap size on the two-phase heat transfer coefficient are correlated using the Nusselt, Jakob, Reynolds and Boiling numbers, with 98% of the experimental data within ±30% of the predicted Nusselt number.

For boiling of emulsions on the smooth surface, increasing the volume fraction up to 0.1 or 0.5% enhances cooling in some cases, but increasing ε further to 1 or 2% provides no additional benefit and decreases heat transfer in some experiments. The emulsion improves heat transfer compared to water for larger gap sizes and lower mass fluxes. In almost all experiments, the heat transfer coefficient for the emulsion increases with increasing wall temperature. Based on these observations, it was posited that two heat transfer mechanisms exist. Conduction in a thin film of FC-72 impairs heat transfer due to the low conductivity of FC-72. Mixing due to boiling of FC-72 increases heat transfer.

From these two mechanisms, correlations are developed for the emulsion heat transfer coefficient and the ratio of the emulsion and water heat transfer coefficients. These correlations include a new non-dimensional number, GC_pd/k_d, to account for conduction in the thin film and sensible heat advected from the wall. A very good fit is seen for h, with 95.7% of the experimental data falling within ±10% of the correlation. For the heat transfer coefficient ratio, 58.7% of the experimental data falls within ±30% of the predicted value, though the correlation captures the trend of the data well.

For boiling of water on the porous surfaces, better heat transfer is measured, especially at higher mass flux and gap sizes. The best heat transfer for the porous surfaces is consistently displayed on Porous Surface 1. The measured pressure drop for the porous surfaces is generally higher than that for water on the smooth surface and the highest pressure drops were measured for Porous Surface 2.

For boiling of emulsions on the porous surfaces, Surface 1 shows a mixture of enhanced and degraded heat transfer. For Surface 2, the emulsions enhance heat transfer for the majority of the data set, and this is especially pronounced for smaller gaps. The emulsions also decrease the measured pressure drop on Porous Surface 2 for the cases where heat transfer is increased. Porous Surface 3 shows similar behavior for the emulsions and water for most of the data set. The better emulsion heat transfer behavior for Surface 2 is likely due the open pore network seen from both the side and top of Surface 2. This allows FC-72 droplets to flow down in the porous structure and nucleate bubbles. The resulting vapor can also release more easily in this open structure.

Finally, maps are given to show where the emulsions enhance or degrade heat transfer on each surface. Recommendations are given for further study in boiling of emulsions.

Table of Contents

Abstract iii
List of Tables vi
List of Figures vii
Nomenclature xvi
1. Introduction 1
2. Literature Review 4
    2.1 Microgap flow boiling 8
    2.2 Boiling on microporous surfaces 18
    2.3 Boiling of emulsions 26
3. Apparatus and Procedure 62
4. Results 77
    4.1 Water on the smooth surface 82
    4.2 Emulsions on the smooth surface 94
    4.3 Water on the porous surfaces 107
    4.4 Emulsions on the porous surfaces 116
5. Physical Mechanisms and Correlation 130
6. Conclusion 141
References 157
Appendices 168
    A. FC-72 Tables of Properties 168
    B. Experimental Apparatus Drawings 170
    C. Single-Component, Single-Phase Analytical Solution 178
    D. One-Dimensional Conduction Resistance Model 185
    E. Measured Mass Flux for Each Experiment 188
    F. Tabulated Experimental Results 190
    G. Other Forms of Emulsion Correlations 232

List of Tables

Table 3.1	Quantities for parameters.	64
Table 3.2	Porous surface characteristics.	70
Table 3.3	Uncertainty estimates.	76
Table 4.1	Eigenvalues and constants evaluated from the power series solutions.	78
Table 6.1	Comparison of emulsion investigations	152
Table A1	Properties for FC-72 at 1 atm and 25 °C.	168
Table A2	FC-72 properties as a function of temperature.	169
Table B1	List of test section parts and drawing numbers.	170
Table C1	Eigenvalues and constants evaluated from the power series solutions.	183
Table E1	Mass flux for each experiment performed on the smooth surface. The inlet temperature for all emulsion runs is 30 °C.	188
Table E2	Mass flux for each experiment performed on Porous Surface 1. The inlet temperature for all runs is 30 °C.	188
Table E3	Mass flux for each experiment performed on Porous Surface 2. The inlet temperature for all runs is 30 °C.	189
Table E4	Mass flux for each experiment performed on Porous Surface 3. The inlet temperature for all runs is 30 °C.	189

List of Figures

Fig. 2.1	(a) Pool boiling curve for water at atmospheric pressure. (b) The flow conditions for each respective point on the pool boiling curve. Reprinted from [2].	5
Fig. 2.2	Flow regimes for flow boiling in a horizontal tube. Reprinted from [2].	7
Fig. 2.3	Flow regimes present for flow boiling of FC-77 in microchannels and microgaps of 400 μm height and varying width. Reprinted from [23].	10
Fig. 2.4	Heat transfer coefficient associated with various flow regimes for flow boiling of deionized water in gaps with 300 μm and 1000 μm height. Reprinted from [29].	12
Fig. 2.5	Local wall temperature and heat flux measurement as a slug passes a microchannel wall. Reprinted from [11].	15
Fig. 2.6	Heat transfer coefficient comparison for boiling in microchannels and microgaps. Reprinted from [27].	17
Fig. 2.7	Axial and lateral temperature measurements in microgaps and microchannels. Reprinted from [27].	17
Fig. 2.8	Representative elementary volume for a porous medium. Reprinted from [67].	20
Fig. 2.9	Comparison of pool boiling curves for smooth copper and porous graphite surfaces. Reprinted from [81].	23
Fig. 2.10	Superheat at ONB and CHF as a function of surface thickness (denoted as particle diameter) for diamond flake microporous surfaces. Adapted from [71].	25
Fig. 2.11	Pool boiling curve for FC-72 in water emulsions [92]. Equations (1) and (2) noted are Eqns. (2.3) and (2.4) here, respectively.	30
Fig. 2.12	Pool boiling curve for pentane in water emulsions [92]. Equations (1) and (2) noted are Eqns. (2.3) and (2.4) here, respectively.	32
Fig. 2.13	Heat transfer coefficient, α, as a function of wall temperature. Data sets 1 and 2 are for water/PES-5 emulsions with d = 1.5 μm and 35 μm, respectively. $\Delta T = Tw - Tsat$ [95].	34

Fig. 2.14	Heat transfer coefficient as a function of water volume fraction, εd, in water-in-PES5 emulsions [100]. Data sets 1-5 correspond to wall temperatures of 100, 190, 205, 220 and 235 °C, respectively. Data sets 6 - 8 correspond to emulsions stabilized with 1% (by weight) tri-sodium phosphate at wall temperatures of 100, 190 and 220 °C, respectively.	36
Fig. 2.15	Heat transfer coefficient for pool boiling of a pentane/water emulsion on an electrically heated wire of 10.1 μm diameter. $\varepsilon = 0.2\%$, $T_\infty = 23.5$ °C [102]. Equation (1) noted is Eqn. (2.3) here. Letters denoting locations on the heat transfer coefficient curve correspond to bubble images in Fig. 2.16.	39
Fig. 2.16	Bubbles in boiling pentane-in-water emulsions on a heated wire [102]. $\varepsilon = 0.2\%$, $T_\infty = 23.5$ °C. Heat flux increases from (a) - (d) as labeled in Fig. 2.15. Optical resolution is 4.5 μm/pixel at a frame rate of 30 s-1.	39
Fig. 2.17	Heat transfer coefficient, α, for (1) water, $T_\infty = 20.1$ °C, and (2) pentane-in-water emulsions, $\varepsilon = 4\%$, $T_\infty = 22.1$ °C [103]. Letters denoting locations ae and de correspond to images in Fig. 2.18.	40
Fig. 2.18	Bubbles in boiling pentane-in-water emulsions on a heated wire. $\varepsilon = 4\%$, $T_\infty = 22.1$ °C [103]. The experimental condition for each image is noted in Fig. 2.17. Time evolution of bubbles on the wire are shown from left to right. Arrows show the movement of two bubbles at de in Fig. 2.17.	40
Fig. 2.19	Heat transfer coefficient for heated wire in an FC72-in-water emulsion; 0.1% FC72 by volume, and $T_\infty = 35$ °C [102]. Letters denote images in Fig. 2.20. Equations (1) and (2) noted are Eqns. (2.3) and (2.4) here, respectively, and are calculated using the properties of water.	41
Fig. 2.20	Images of heated wire during boiling in FC72-in-water emulsion, 0.1% FC72 by volume: (a) onset of boiling; (b) attached bubbles at higher heat flux; (c) rapid bubble detachment; and (d) boiling at high heat flux, average bubble rise velocity is 0.0087 m/s [102]. The experimental condition for each image is noted in Fig. 2.19.	41
Fig. 2.21	Convective heat transfer coefficients, α, in peripherally heated pipe flow [104]. Qflow = 2.5 × 10-6 m3/s. 1: VO-IC oil; 2: coarse grained water-in-VO1C oil emulsion; 3: fine grained water-in-VO1C oil emulsion. $\varepsilon = 1\%$.	44

Fig. 2.22	Heat transfer coefficients, α (kW/m2K), versus temperature difference between heated surface and bulk fluid (deg K) [105]. 1: PES4 fluid; 2: water; 3-7: emulsions by weight percent of PES4, 3.0, 6.0, 12.0, 20.0, 33.0, respectively.	44
Fig. 2.23	Augmentation of average heat transfer coefficient for the FC72-in-water emulsions relative to water, h0. Tsat = 56 ^{oC} for FC72 at 1 atm [107]. H = 0.25 mm. Qflow = 0.006 L/min.	46
Fig. 2.24	Boiling of disperse emulsion considered by Bulanov [98]. Reprinted from [90].	55
Fig. 3.1	Experimental flow loop.	62
Fig. 3.2	Emulsion preparation loop.	63
Fig. 3.3	Measured distribution of emulsion droplet diameters.	64
Fig. 3.4	Test section.	65
Fig. 3.5	Temperature profile used in the oven brazing cycle.	66
Fig. 3.6	SEM images for porous surface 1. (a) - (c) are images from the top with magnification of ×150, ×350 and ×550, respectively. (d) - (f) are images from the side with magnification of ×70, ×150 and ×300, respectively.	67
Fig. 3.7	SEM images for porous surface 2. (a) - (c) are images from the top with magnification of ×150, ×350 and ×550, respectively. (d) - (f) are images from the side with magnification of ×70, ×150 and ×300, respectively.	68
Fig. 3.8	SEM images for porous surface 3. (a) - (c) are images from the top with magnification of ×150, ×350 and ×550, respectively. (d) - (f) are images from the side with magnification of ×70, ×150 and ×300, respectively.	69
Fig. 3.9	Conversion of the Surface 3 top view SEM image into black and white. The red circles denote areas where the solid is determined to be void by the computer algorithm. (a) Original SEM image, (b) Converted black and white image.	71
Fig. 3.10	Porosity measurement for Porous Surface 1. (a) - (c) are the original SEM image, converted black and white image and porosity distribution, respectively, for the side image at ×70 magnification. (d) - (f) are the original SEM image, converted black and white image and porosity distribution, respectively, for the top image at ×150 magnification.	72

Fig. 3.11	Porosity measurement for Porous Surface 2. (a) - (c) are the original SEM image, converted black and white image and porosity distribution, respectively, for the side image at ×70 magnification. (d) - (f) are the original SEM image, converted black and white image and porosity distribution, respectively, for the top image at ×150 magnification.	73
Fig. 3.12	Porosity measurement for Porous Surface 3. (a) - (c) are the original SEM image, converted black and white image and porosity distribution, respectively, for the side image at ×70 magnification. (d) - (f) are the original SEM image, converted black and white image and porosity distribution, respectively, for the top image at ×150 magnification.	74
Fig. 4.1	Comparison between the mean wall temperature from the analytical temperature expression (line), Eqn. (4.1), and single-phase experimental results (circles). Dh = 1000 μm, G = 262 kg/m2s, Ti = 51 °C. (a) Without accounting for heat losses. (b) Accounting for heat losses in experimental results.	79
Fig. 4.2	Comparison of the boiling curves for three experimental runs on the smooth surface. (a) Water, Ti = 51 °C, Dh = 1000 μm, (b) 1% emulsion, Ti = 30 °C, Dh = 500 μm.	80
Fig. 4.3	Demonstration of surface conditioning for (a) Porous Surface 1, (b) Porous Surface 2, and (c) Porous Surface 3. Water, Ti = 30 °C, Dh = 500 μm.	81
Fig. 4.4	Comparison of the boiling curves for three experimental runs on Porous Surface 1. 1% emulsion, Ti = 30 °C, Dh = 500 μm.	81
Fig. 4.5	Boiling curves for water on the smooth surface, Ti = 30 °C. ΔT = Tw - Tsat.	82
Fig. 4.6	Heat transfer coefficient for water on the smooth surface, Ti = 30 °C.	83
Fig. 4.7	Pressure drop for water on the smooth surface, Ti = 30 °C.	83
Fig. 4.8	Boiling curves for water on a smooth surface, Ti = 30 °C. (a) - (c) are for Dh = 200, 500 and 1000 μm, respectively.	85
Fig. 4.9	Boiling curves for water on a smooth surface, Ti = 30 °C. (a) - (c) are for G = 150, 350 and 550 kg/m2s, respectively.	86
Fig. 4.10	Heat transfer coefficient for water on a smooth surface, Ti = 30 °C. (a) - (c) are for Dh = 200, 500 and 1000 μm,	87

respectively.

Fig. 4.11 Heat transfer coefficient for water on a smooth surface, Ti = 30 °C. (a) - (c) are for G = 150, 350 and 550 kg/m2s, respectively. 88

Fig. 4.12 Pressure drop for water on a smooth surface, Ti = 30 °C. (a) - (c) are for Dh = 200, 500 and 1000 μm, respectively. 89

Fig. 4.13 Pressure drop for water on a smooth surface, Ti = 30 °C. (a) - (c) are for G = 150, 350 and 550 kg/m2s, respectively. 90

Fig. 4.14 Nusselt number as a function of the Reynolds and Boiling numbers for two-phase heat transfer on the smooth surface. Ti = 30 °C. 92

Fig. 4.15 Nusselt number as a function of the Reynolds and Boiling numbers at various inlet temperatures. 92

Fig. 4.16 Comparison between the measured Nusselt number and the Nusselt number predicted by Eqn. (4.8). The solid line represents equivalence between the measured and predicted Nusselt numbers. 93

Fig. 4.17 Typical heat transfer coefficient curves for emulsions compared to those for water. Ti = 30 °C, Dh = 1000 μm, G = 350 kg/m2s. ΔT = Tw - Tsat. 94

Fig. 4.18 Boiling curves for emulsions on the smooth surface, Ti = 30 °C, G = 350 kg/m2s. (a) - (c) are for Dh = 200, 500 and 1000 μm, respectively. ΔT = Tw - Tsat. 96

Fig. 4.19 Heat transfer coefficient for emulsions on the smooth surface, Ti = 30 °C, G = 350 kg/m2s. (a) - (c) are for Dh = 200, 500 and 1000 μm, respectively. 97

Fig. 4.20 Pressure drop for emulsions on the smooth surface, Ti = 30 °C, G = 350 kg/m2s. (a) - (c) are for Dh = 200, 500 and 1000 μm, respectively. 98

Fig. 4.21 Boiling curves for water and 1% emulsions on the smooth surface, Ti = 30 °C. (a) - (c) are for Dh = 200, 500 and 1000 μm, respectively. 99

Fig. 4.22 Heat transfer coefficient for water and 1% emulsions on the smooth surface, Ti = 30 °C. (a) - (c) are for Dh = 200, 500 and 1000 μm, respectively. 100

Fig. 4.23	Boiling curves for water and 1% emulsions on the smooth surface, Ti = 30 °C. (a) - (c) are for G = 150, 350 and 550 kg/m2s, respectively.	102
Fig. 4.24	Heat transfer coefficient for water and 1% emulsions on the smooth surface, Ti = 30 °C. (a) - (c) are for G = 150, 350 and 550 kg/m2s, respectively.	103
Fig. 4.25	Pressure drop for water and 1% emulsions on the smooth surface, Ti = 30 °C. (a) - (c) are for Dh = 200, 500 and 1000 μm, respectively.	104
Fig. 4.26	Pressure drop for water and 1% emulsions on the smooth surface, Ti = 30 °C. (a) - (c) are for G = 150, 350 and 550 kg/m2s, respectively.	105
Fig. 4.27	Comparison of Dh = 500 μm, G=150 kg/m2s emulsion boiling data with that of Janssen and Kulacki [107] (Dh = 500 μm, G = 133 kg/m2s) and Morshed et al. [108] (Dh = 672 μm, G = 129 kg/m2s).	106
Fig. 4.28	(a) Boiling curve and (b) heat transfer coefficient for water on Porous Surface 1, Ti = 30 °C. $\Delta T = Tw - Tsat$.	107
Fig. 4.29	(a) Boiling curve and (b) heat transfer coefficient for water on Porous Surface 2, Ti = 30 °C.	108
Fig. 4.30	(a) Boiling curve and (b) heat transfer coefficient for water on Porous Surface 3, Ti = 30 °C.	108
Fig. 4.31	Pressure drop on (a) Porous Surface 1, (b) Porous Surface 2, and (c) Porous Surface 3. Ti = 30 °C.	109
Fig. 4.32	Boiling curves for water on smooth and porous surfaces, Dh = 500 μm, Ti = 30 °C. (a) - (c) are for G = 150, 350, and 550 kg/m2s, respectively.	110
Fig. 4.33	Heat transfer coefficient for water on smooth and porous surfaces, Dh = 500 μm, Ti = 30 °C. (a) - (c) are for G = 150, 350, and 550 kg/m2s, respectively.	111
Fig. 4.34	Boiling curves for water on smooth and porous surfaces, G = 350 kg/m2s, Ti = 30 °C. (a) - (c) are for Dh = 200, 500, and 1000 μm, respectively.	112
Fig. 4.35	Heat transfer coefficient for water on smooth and porous surfaces, G = 350 kg/m2s, Ti = 30 °C. (a) - (c) are for Dh =	113

200, 500, and 1000 μm, respectively.

Fig. 4.36 Pressure drop for water on smooth and porous surfaces, Dh = 500 μm, Ti = 30 °C. (a) - (c) are for G = 150, 350, and 550 kg/m2s, respectively. 114

Fig. 4.37 Pressure drop for water on smooth and porous surfaces, G = 350 kg/m2s, Ti = 30 °C. (a) - (c) are for Dh = 200, 500, and 1000 μm, respectively. 115

Fig. 4.38 (a) - (c) Boiling curves and (d) - (f) heat transfer coefficient for emulsions on Porous Surface 1 with Dh = 200, 500, and 1000 μm. Ti = 30 °C, G = 350 kg/m2s. 117

Fig. 4.39 Pressure drop for emulsions on Porous Surface 1, Ti = 30 °C, G = 350 kg/m2s. (a) - (c) are for Dh = 200, 500 and 1000 μm, respectively. 118

Fig. 4.40 (a) - (c) Boiling curves and (d) - (f) heat transfer coefficient for emulsions on Porous Surface 2 with Dh = 200, 500, and 1000 μm. Ti = 30 °C, G = 350 kg/m2s. 119

Fig. 4.41 Pressure drop for emulsions on Porous Surface 2, Ti = 30 °C, G = 350 kg/m2s. (a) - (c) are for Dh = 200, 500 and 1000 μm, respectively. 120

Fig. 4.42 (a) - (c) Boiling curves and (d) - (f) heat transfer coefficient for emulsions on Porous Surface 3 with Dh = 200, 500, and 1000 μm. Ti = 30 °C, G = 350 kg/m2s. 123

Fig. 4.43 Pressure drop for emulsions on Porous Surface 3, Ti = 30 °C, G = 350 kg/m2s. (a) - (c) are for Dh = 200, 500 and 1000 μm, respectively. 124

Fig. 4.44 (a) - (c) Boiling curves and (d) - (f) heat transfer coefficient for water and 1% emulsions on smooth and microporous surfaces with G = 150, 350, and 550 kg/m2s, respectively. Ti = 30 °C, Dh = 500 μm. 126

Fig. 4.45 (a) - (c) Boiling curves and (d) - (f) heat transfer coefficient for water and 1% emulsions on smooth and microporous surfaces with Dh = 200, 500, and 1000 μm, respectively. Ti = 30 °C, G = 350 kg/m2s. 127

Fig. 4.46 Pressure drop for water and 1% emulsions on the smooth and microporous surfaces, Dh = 500μm, Ti = 30 °C. (a) - (c) are for G = 150, 350 and 550 kg/m2s, respectively. 128

Fig. 4.47	Pressure drop for water and 1% emulsions on the smooth and microporous surfaces, G = 350 kg/m2s, Ti = 30 °C. (a) - (c) are for Dh = 200, 500 and 1000 μm, respectively.	129
Fig. 5.1	Droplet deposition and release geometry.	135
Fig. 5.2	Comparison between the measured emulsion heat transfer coefficient and that predicted by Eqn. (5.11). The solid line represents equivalence between the measured and predicted values.	139
Fig. 5.3	Comparison between the measured ratio of the emulsion and water heat transfer coefficients and the ratio predicted by Eqn. (5.12). The solid line represents equivalence between the measured and predicted values.	140
Fig. 6.1	(a) Comparison of Dh = 500 μm, G=150 kg/m2s emulsion boiling data with that of Janssen and Kulacki [107] in a 500 μm gap and Morshed et al. [108] in a 672 μm gap. (b) Heat transfer coefficient measured in [107] compared to that predicted by Eqn. (5.11). The solid line represents equivalence between measured and predicted values.	143
Fig. 6.2	Ratio of the emulsion heat transfer coefficient to that for water at the same wall temperature on the smooth surface. (a) - (c) are for Dh = 200, 500 and 1000 μm.	147
Fig. 6.3	Ratio of the emulsion heat transfer coefficient to that for water at the same wall temperature on Porous Surface 1. (a) - (c) are for Dh = 200, 500 and 1000 μm.	148
Fig. 6.4	Ratio of the emulsion heat transfer coefficient to that for water at the same wall temperature on Porous Surface 2. (a) - (c) are for Dh = 200, 500 and 1000 μm.	149
Fig. 6.5	Ratio of the emulsion heat transfer coefficient to that for water at the same wall temperature on Porous Surface 3. (a) - (c) are for Dh = 200, 500 and 1000 μm.	150
Fig. 6.6	Map of existing emulsion boiling experiments. The corresponding publications are listed in Table 6.1. $Dh \rightarrow \infty$ represents pool boiling results.	151
Fig. C1	Channel Geometry.	178
Fig. C2	Velocity profiles for D_h = 1000 μm, G = 500 kg/m^{2}s.	180

Fig. D1	Conduction resistance network in the microgap	185
Fig. G1	(a) Comparison between the measured emulsion heat transfer coefficient and that predicted by Eqn. (G2). (b) Comparison between the measured ratio of the emulsion and water heat transfer coefficients and the ratio predicted by Eqn. (G3). The solid line represents equivalence between the measured and predicted values.	233
Fig. G2	(a) Comparison between the measured emulsion heat transfer coefficient and that predicted by Eqn. (G4). (b) Comparison between the measured ratio of the emulsion and water heat transfer coefficients and the ratio predicted by Eqn. (G5). The solid line represents equivalence between the measured and predicted values.	234
Fig. G3	(a) Comparison between the measured emulsion heat transfer coefficient and that predicted by Eqn. (G6). (b) Comparison between the measured ratio of the emulsion and water heat transfer coefficients and the ratio predicted by Eqn. (G7). The solid line represents equivalence between the measured and predicted values.	235
Fig. G4	(a) Comparison between the measured emulsion heat transfer coefficient and that predicted by Eqn. (G8). (b) Comparison between the measured ratio of the emulsion and water heat transfer coefficients and the ratio predicted by Eqn. (G9). The solid line represents equivalence between the measured and predicted values.	236
Fig. G5	(a) Comparison between the measured emulsion heat transfer coefficient and that predicted by Eqn. (G10). (b) Comparison between the measured ratio of the emulsion and water heat transfer coefficients and the ratio predicted by Eqn. (G11). The solid line represents equivalence between the measured and predicted values.	237

Nomenclature

A	Area, m^2
Ar	Archimedes number, $(\rho_{eff} - \rho_b) g \rho_d D^3 / \mu_{eff}^2$
a	Series constant
B	Work due to body forces, W/kg
Bl	Boiling number, $q"/Gh_{fg}$
$\vec{b}$	Body force vector, N/kg
C	Constant
C_p	Constant pressure specific heat, J/kgK
C_v	Constant volume specific heat, J/kgK
D	Bubble diameter, m
D_h	Hydraulic diameter, m
d	Droplet diameter, m
E	Work due to interaction with other phases, W/m^3
e	Internal energy, J/kg
F	Source flow strength, m^3/s
$\vec{F}$	Force, N
f	Friction factor
G	Mass flux, kg/m^2s
$\vec{g}$	Gravity vector, m/s^2
H	Height of the microgap, m
h	Heat transfer coefficient, W/m^2K
h_{fg}	Latent heat of evaporation, J/kg
I	Applied current, A
J	Nucleation rate, $/m^3s$
Ja	Jakob number based on subcooling, $C_p(T_{sat} - T_i)/h_{fg}$
K	Porous layer permeability
k	Thermal conductivity, W/mK
L	Boundary layer thickness, m
l	Pipe length, m
$\vec{M}$	Force due to interaction with other phases, N/m^3
m	Mass, kg
$\dot{m}$	Mass flow rate, kg/s
N	Total number of droplets in a boundary layer
Nu	Nusselt number, hD_h/k_f
n_b	Number of boiling droplets in a boundary layer
n_d	Number of droplets that deposit on a hot surface
P	Pressure, Pa
Pr	Prandtl number, ν/α or $\mu_{eff} C_{p_d}/k_c$
p	Probability that a droplet boils
Q	Energy, J
Q_{flow}	Volumetric flowrate, m^3/s
q	Heat, W
R	Radius, m
Ra	Rayleigh number, $Pr\, g\beta\rho^2 d_{wire}^3 (T - T_\infty)/\mu^2$
Re	Reynolds number, $\rho D_h u_m/\mu$
r	In the radial direction
S	Strain rate, /s
St	Stefan number, $C_{p_d}(T - T_{sat})/i_{fg}$
T	Temperature, K
$\boldsymbol{T}$	Traction tensor, N/m^2
t	Film thickness, m
$\vec{U}$	Velocity vector, m/s
u	x-direction velocity, m/s
$\bar{u}$	Mean velocity, m/s
u'	Velocity fluctuation, m/s
V	Volume, m^3
$V_{applied}$	Applied Voltage, V
V_d	Volume of droplet, m^3
v	y-direction velocity, m/s
W	Width of the microgap, m
w	z-direction velocity, m/s

x	Streamwise direction
x^*	Non-dimensional x
Y	Eigenfunction
y	Normal direction
y^*	Non-dimensional y
z	Spanwise direction

Greek Symbols

α	Thermal diffusivity, m^2/s, $k/\rho C_p$
α_k	Volume fraction for the k^{th} phase
β	Thermal expansion coefficient, /K
Γ	Mass production rate, kg/m^3s
ΔT	T_w - T_{sat}, K
ΔW_{cr}	Work of formation of a critical size bubble, J
δ	Uncertainty
ε	Disperse phase volume fraction
ε_{diss}	Turbulent energy dissipation, J
η	Kolmogorov length scale, m
η_{coll}	Collision efficiency
θ	Non-dimensional temperature
λ	Eigenvalue
μ	Dynamic viscosity, Ns/m^2
ν	Kinematic viscosity, m^2/s, μ/ρ
ρ	Density, kg/m^3
σ	Surface tension, N/m^2
τ	Boundary layer residence time
ϕ	Porous layer porosity
φ	Number of collisions between droplets and bubbles in a chain reaction

Subscripts

0	Reference state
∞	The surroundings
b	Disperse component, vapor
c	Continuous component
$coll$	From collisions
$cond$	From condensation
cr	Of critical size
D_h	Based on the hydraulic diameter
d	Disperse component, liquid
e	Exposed to continuous component flow
eff	Effective value for the emulsion
f	Liquid
$film$	In the oil film
g	Vapor
i	Inlet
k	For the k^{th} phase
kj	For the k^{th} phase relative to the j^{th} phase
m	Mean
min	Minimum
mix	Due to mixing
o	Covered by an oil film
$pore$	At the pore scale
s	Surface
sat	Saturated condition
T	Turbulent
$total$	Total for porous surface
$void$	Porous surface void space
w	Wall
$wire$	Pertaining to the wire

Superscripts

$'$	Denotes dummy variable
$''$	Flux, m^{-2}

Other

$\nabla = \hat{\imath}\frac{\partial}{\partial x} + \hat{\jmath}\frac{\partial}{\partial y} + \hat{k}\frac{\partial}{\partial z}$	Cartesian gradient operator
$\bar{A}$	Average of A

1. Introduction

Though the first studies into boiling as a mode of coiling date to the 1700s, the amount of research conducted in this area increased dramatically with the rise of nuclear energy and rocket research in the 1940s and '50s [1, 2]. From that time, the subject has proven to be a fruitful area of study but there are still many aspects and mechanisms that are not well understood. To underscore this point, in 1963 J.W. Westwater published a paper titled, "Things We Don't Know About Boiling Heat Transfer," raising questions pertaining to boiling that were unanswered at the time [3]. This theme also was discussed by Lienhard in 1988, commemorating the 25th anniversary of the paper by Westwater [4].

While many of the questions raised by these two researchers have been answered, still others remain. Specifically, the boiling community continues seeking to answer the question about what heat transfer mechanisms are present during bubble nucleation, growth and departure from a heated surface. Much of the difficulty in answering this question is attributable to boiling being an unsteady process that is in thermodynamic nonequilibrium, and that there is strong coupling between the fluid motion and the heat transfer. In addition to these factors about boiling in general, difficulty arises from experiments demonstrating conflicting results, possibly due to experiments that were not well controlled/designed or suffered from large experimental uncertainty or varying boundary conditions [5].

The state of affairs was such that some researchers questioned whether understanding the physical mechanisms is a feasible task, headlined by Vijay Dhir arguing for the use of Computational Fluid Dynamics for prediction rather than mechanism-based correlations

in his Max Jakob Memorial Award paper titled, " Mechanistic Prediction of Nucleate Boiling Heat Transfer- Achievable or a Hopeless Task?" [6]. Yet, recent studies were conducted into the physical mechanisms of heat transfer in pool boiling [7], flow boiling in a microchannel [8 - 12], and bubble nucleation in flow boiling [13], to name a few.

Though the question about physical mechanisms in pool boiling or flow boiling at the conventional scale (applications with hydraulic diameter ~ 3 mm or larger) remains unresolved and is important to address, the primary focus of flow boiling research has shifted from the large scale to the small scale in recent decades. The vast majority of this research was conducted for microchannels (channels with $W/H < 10$), with research into flow boiling in microgaps (channels with $W/H > 10$) only coming more recently. Some applications for flow boiling in microchannels have been suggested, ranging from miniature refrigeration systems to cooling of PEM fuel cells [14].

The application that may prove to be the most important in the future is cooling of high-performance electronics. As the power density of modern computer chips continues to increase, it has become necessary to explore cooling means other than forced gaseous convection. Both single-phase liquid and two-phase cooling strategies are being explored, with studies focused on boiling in microchannels and microgaps showing that the heat transfer coefficient increases with decreasing channel/gap size.

Other means of increasing boiling heat transfer have been studied and shown to be effective, including the use of microporous surfaces or an emulsion (a mixture of two immiscible fluids) in pool and/or flow boiling. To date, neither of these have been applied at the small scale. In the case of boiling emulsions, relatively few studies exist and almost the entirety of them were conducted in pool boiling. Each of these areas may

be a viable method of improving cooling in electronic applications. More study is needed, though, before any of these can be applied in design.

In this context, the thermal engineer as an *applied* scientist has two roles: 1) to seek to better understand the mechanisms of boiling heat transfer, and 2) apply our understanding to the design of systems that take advantage of any enhancement in heat transfer while minimizing any drawbacks that arise due to the boiling process. Both of these roles depend on the existence of a large and robust experimental data set. To these ends, the primary goals of this study are,

- to build a large experimental database for flow boiling of emulsions in microgaps with smooth and microporous surfaces to study the emulsion-microporous surface interaction. Data sets for boiling of water on a smooth surface and on microporous surfaces will also be generated to add to the scant data that currently exist in these areas and to serve as a basis for comparing the performance of the emulsions.
- to draw conclusions from the experimental data about the physical mechanisms for flow boiling of emulsions.
- to determine correlations for boiling of water and emulsions in microgaps that can be used for thermal design.
- to demonstrate areas worthy of further study within these topics.

2. Literature Review

This study deals with boiling in microgaps, boiling on microporous surfaces, and boiling of dilute emulsions. Each of these areas have been researched individually, and attention is given to reviewing the studies for each below. However, before addressing each individual topic, it is prudent to discuss the basics of boiling in general.

To begin, consider the pool boiling curve shown in Fig 2.1a. On this curve, several letters are marked corresponding to transition to a new fluid state, and these states are noted in Fig 2.1b. From location A to B, and potentially further along the dotted line shown, single-phase natural convection is the heat transfer mode present. At location B, bubbles start to nucleate and grow on the surface, indicating the presence of two-phase heat transfer. Location B is commonly called the "onset of nucleate boiling" (ONB).

Note that on the graph, point B is located at a wall temperature higher than the corresponding saturation temperature of the fluid (100 °C here). In both pool and flow boiling, it is often necessary for the surface temperature to be higher than the saturation temperature of the fluid before nucleation will begin. Thus, the system exists in a metastable state until the wall temperature is high enough to nucleate bubbles larger than a critical size. The difference between the wall temperature at ONB and the saturation temperature is termed the "surface superheat." Generally, the fluid near the wall demonstrates a larger superheat in pool boiling than in flow boiling. It is possible for point B to be further along the dotted line shown, depending on the surface geometry, pressure, fluid temperature, and the fluid used.

Once ONB is reached, the system will rapidly move from point B to point B'. The heat transfer mechanisms present during boiling are much more efficient than natural

convection, resulting in a much higher heat transfer coefficient once ONB is reached. This will cause the surface temperature to decrease quickly if the heat flux is constant. The temperature difference between locations B and B' is the "temperature overshoot." It is desirable to limit this overshoot in design, and the overshoot is not present in all systems.

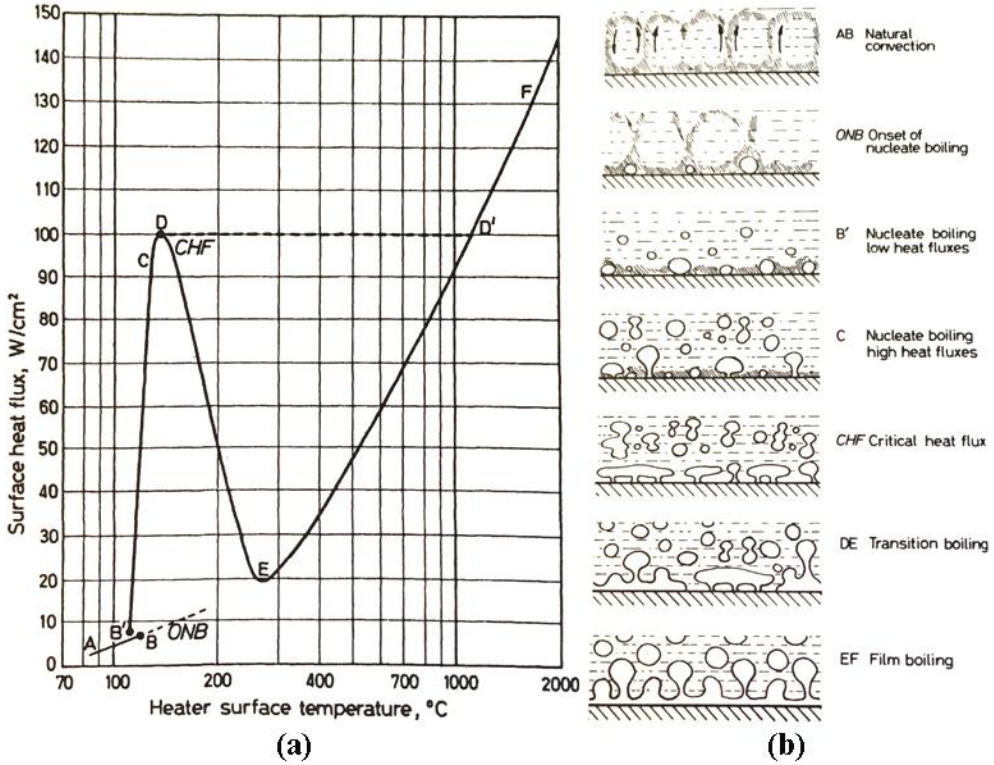

Fig. 2.1. (a) Pool boiling curve for water at atmospheric pressure. (b) The flow conditions for each respective point on the pool boiling curve. Reprinted from [2].

Between points B' and C, nucleate boiling is the dominant heat transfer mode. In this regime, small bubbles nucleate on the surface, grow and depart, and the heat transfer mechanisms associated with the bubble growth and departure are very efficient at transferring heat from the heated surface to the fluid. As the wall temperature or heat flux increases, the frequency of bubble growth and release increases, resulting in higher heat transfer coefficients with increasing wall temperature.

As the wall temperature or heat flux increases further to point C, neighboring bubbles start to interact and form larger vapor structures on the wall. These vapor structures slightly inhibit heat transfer, causing a change in the slope of the boiling curve. As the wall temperature increases even further to point D, these vapor structures cover large portions of the wall, limiting the ability of liquid to wet the wall. Because heat transfer is much less efficient in vapor than liquid, the wall temperature will increase dramatically from point D to D' without the heat flux increasing. Thus, the heat flux dissipated at point D is termed the "critical heat flux" (CHF). If CHF is reached in the system, this often results in failure of the part being cooled.

Generally, the area of the boiling curve between points D and E cannot be accessed, unless the wall temperature is being carefully controlled. In this region, the wall is covered over by a vapor film. Liquid will periodically break through the vapor to rewet portions of the wall. Point E is called the "Leidenfrost point," and marks the transition to stable film boiling, where the vapor film covers the entire wall and liquid never comes into contact with the wall. Thus, in film boiling, heat transfer is characterized primarily by conduction and convection within this vapor film. The film boiling region extends from point E to F and beyond.

This discussion elucidates the fact there is strong coupling between the two-phase flow behavior and heat transfer, with the flow behavior being dependent on the heat transfer and the heat transfer being dependent on the flow behavior. In general, this coupling is not present in single-phase heat transfer, where the flow behavior can be determined first and then used to determine the heat transfer. This represents one of the main difficulties in studying two-phase flow. Although the discussion above revolves

around pool boiling, coupling is also equally present in flow boiling. However, the fluid flow behavior is slightly different in flow boiling due to the presence of mean flow and shear. The typical flow regimes present in flow boiling are shown in Fig 2.2.

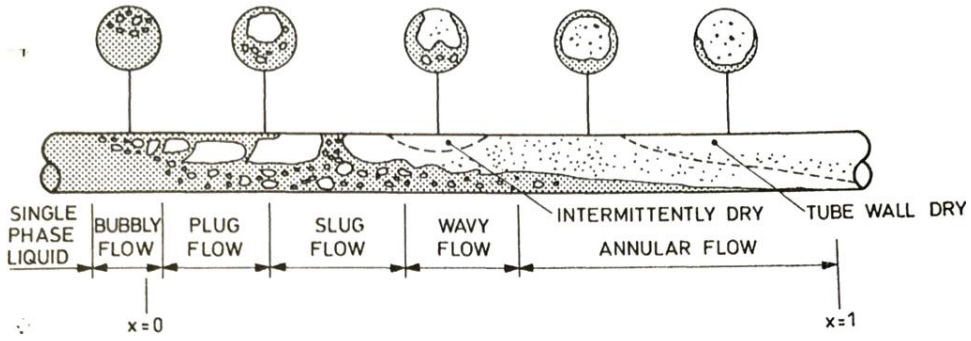

Fig. 2.2. Flow regimes for flow boiling in a horizontal tube. Reprinted from [2].

When nucleation begins in flow boiling, small bubbles are formed and release from the surface. These bubbles largely remain independent of each other and the flow is termed "bubbly flow." As the quality increases- either with increasing position downstream or an increase in wall temperature/heat flux- the flow transitions to "plug flow" or "slug flow," where the bubbles start to agglomerate and form larger slugs. At a fixed location, the wall will periodically see vapor slugs passing- with a thin liquid layer below them- with successive slugs separated by liquid "bridges."

As the quality increases further, the flow can transition to either "wavy flow" or "annular flow." In wavy flow, the vapor and liquid completely separate, with the vapor occupying the top of the pipe and the liquid occupying the bottom due to gravity. Ripples can often be seen on the interface between the vapor and liquid. This flow regime is also called "stratified flow" if these ripples are not present. Generally, stratified flow is seen at lower flow rates and wavy flow is seen at high flow rates. Because these regimes are dependent on gravity, they are not seen when flow is in the vertical direction.

In annular flow, a thin liquid film wets the entire wall surface and surrounds a core of vapor. Heat transfer coefficients are generally very high when annular flow is present due to heat transfer in this thin liquid film. However, as the wall temperature or heat flux increases, the film will thin further until portions of the wall start to be covered by vapor patches and the system will transition to critical heat flux.

Though this classification is used here, other classifications exist, with some researchers preferring to classify transitions to sub states between those given here. As well, not all systems will demonstrate all of these flow regimes. The specific regimes present depend largely on the temperature or heat flux, pressure, flow rate, wall geometry and pipe size.

2.1 Microgap flow boiling

The majority of the research on flow boiling at the small scale has focused on boiling in microchannels. This research has led to several good reviews worth considering (e.g. [5, 14 - 18]). Due to the high aspect ratio in a microgap, boiling in microgaps leads to slightly different flow and heat transfer behavior than boiling in a microchannel. Because boiling in a microgap is the focus of this investigation, attention will be given here to boiling in microgaps rather than in microchannels, except when comparing the two.

2.1.1 Flow regimes

The flow regimes present in microgaps were studied by Bar-Cohen et al. [19 - 22], Harirchian and Garimella [23, 24], and Alam et al. [25 - 29]. Bar-Cohen et al. [19 - 22] assume that the traditional Taitel and Dukler [30] flow regime map developed for flow boiling at the conventional scale is applicable for microgap flow. This map uses the superficial gas and liquid velocities to plot the transition between bubbly, intermittent

(generally slug or plug), stratified and annular flow. In [20], Bar-Cohen and Rahim use the Taitel and Dukler map to plot the flow regimes present for R113 flowing in gaps of D_h from 0.1-100 mm, G from 100-400 kg/m^{2}s and 0.01 to 0.9 thermodynamic quality. The maps show that for the 0.1 mm and 1 mm gaps, the majority of the data falls in the annular flow regime. At very low quality, intermittent flow is present, with the data shifting closer to annular flow with increasing G.

Bar-Cohen and Rahim [20] also plot the data from the experiments of Yang and Fujita [31] and Lee and Lee [32] for R113 flowing in 0.4 mm and 1 mm gaps, respectively, to gain insight into how the flow regimes affect heat transfer behavior. For the 1 mm gap with G from 52-208 kg/m^{2}s, the entirety of the data falls in the annular flow regime. For the 0.4 mm gap with G = 100 and 200 kg/m^{2}s, the majority of the data falls in the annular regime, though some low quality data points fall in the intermittent flow regime. The previous R113 maps show that annular flow is more prevalent for smaller gap sizes, so the presence of intermittent flow in the smaller gap of [31] and not in the larger gap of [32] may be due to differences in the system pressure. The 0.4 mm gap experiments were conducted at a pressure of 219 kPa and those of the 1 mm gap were conducted at 108 kPa.

The flow regimes present during boiling heat transfer were measured via high-speed videography by Harirchian and Garimella [23, 24] and Alam et al. [25 - 29]. Harirchian and Garimella [23, 24] studied boiling of FC-77 in microchannels and a microgap of D_h = 707 μm, with G from 225-1420 kg/m^{2}s. Between bubbly and annular flow, they observed several subregimes of intermittent flow. In addition to slug flow, they observed churn flow- a regime similar to slug flow but with smaller, irregular vapor structures and

much more chaotic mixing than slug flow- and wispy-annular flow- a regime similar to annular flow characterized by a thicker liquid film on the wall and large wave structures that allow the vapor to entrain larger droplets in the vapor core.

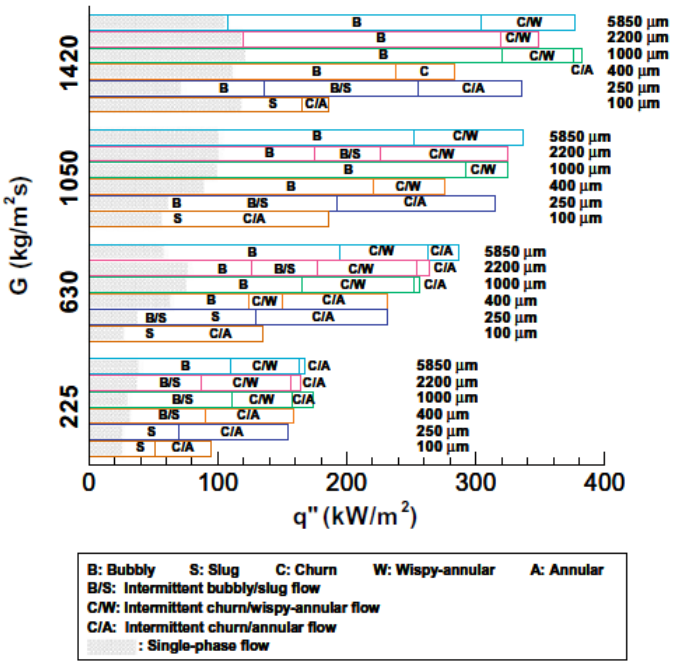

Fig. 2.3. Flow regimes present for flow boiling of FC-77 in microchannels and microgaps of 400 µm height and varying width. Reprinted from [23].

In the microgap of width 5850 µm, they found that multiple of these regimes can exist side-by-side due to the large aspect ratio. As shown in Fig 2.3, at lower heat fluxes, bubbly flow predominated. As the heat flux increased, bubbly flow was replaced by intermittent churn and wispy-annular flow, which was followed by churn-annular flow at still higher heat fluxes. As the mass flux increased, the bubbly flow regime was present over a much wider range of heat flux. Harirchian and Garimella further point to the dissimilarity between the flow regimes in the 100-250 µm channels and the 400-5850 µm wide channels to differentiate the microchannels and microgaps based on flow regimes.

Alam et al. [25 - 29] noted bubbly, slug and annular flow present in their microgaps of 12.7 mm width and 80-1000 µm height. For the same heat and mass fluxes, bubbly

flow tended to dominate in the larger gaps and the flow regime shifted to slug then annular flow with decreasing gap height [25, 26, 29]. They also noted that the flow condition was unsteady, with varying flow regimes present at the same experimental condition. At a given gap size, heat and mass flux, bubbly, slug and annular flow were all seen sequentially as bubbles nucleated, grew, coalesced, and flowed downstream [26, 27, 29].

It can be seen that the studies by Harirchian and Garimella [23, 24] and Alam et al. [25 - 29] show similar trends to those predicted by Bar-Cohen et al. [19 - 22] via the use of the Taitel and Dukler flow regime maps. Though the trends are similar, comparisons have not yet been made between the flow regime seen via the use of videography and that predicted by the Taitel and Dukler map for a given experimental condition. Therefore, the accuracy of the Taitel and Duler map at the small scale has not yet been proven.

2.1.2 Heat transfer

Similar to flow boiling at the conventional scale, heat transfer at the small scale is dependent on the flow regime. Bar-Cohen and Rahim [20] and Alam et al. [29] show that changes in the slope of the boiling curve or heat transfer coefficient curve correlate with changes in the flow regime (Fig. 2.4). It is seen that higher heat transfer coefficients are measured as the flow transitions from bubbly to slug and annular flow due to the effectiveness of evaporation in the thin liquid film around the wall.

Heat transfer is also affected by the gap size, mass flux, fluid used, subcooling- the difference between the saturation temperature and the inlet temperature- and the wall condition. Heat transfer for various gap sizes was investigated in [25, 26, 33 - 35]. In general, the boiling curve shifts to lower wall temperatures and the heat transfer

coefficient increases with decreasing gap size, especially at wall temperatures near ONB. This is probably due to the early transition to annular flow in smaller gaps. Although higher heat transfer is seen near ONB, the early transition to annular flow also results in an earlier transition to CHF. Thus, for higher wall temperature and heat flux, smaller gaps can have decreased heat transfer than larger gaps at the same heat flux, and CHF values are generally lower for smaller gaps [33].

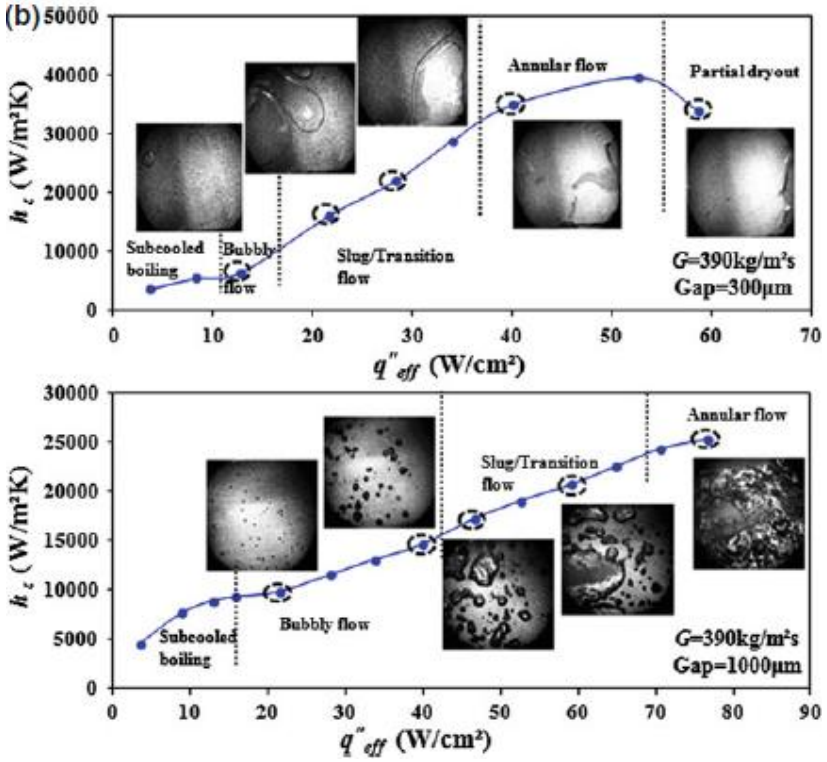

Fig. 2.4. Heat transfer coefficient associated with various flow regimes for flow boiling of deionized water in gaps with 300 μm and 1000 μm height. Reprinted from [29].

The effect of the mass flux was studied in [25, 35 - 39]. In the single-phase region, increasing G decreases the wall temperature and increases the heat transfer coefficient, as is typical at the conventional scale. However, the higher wall temperatures for lower G mean that boiling is initiated at lower heat fluxes, which can result in higher heat transfer coefficients at low heat flux for lower G [25]. Increasing G also delays the onset of CHF

due to the effectiveness of single-phase cooling at higher G as well as the prevalence of bubbly flow and the delayed transition to annular flow (Fig. 2.3).

Young et al. [38] show that the designs of the entry and exit manifolds have a significant impact on the heat transfer and fluid flow characteristics. Therefore, comparison of multiple fluids can only be achieved when the fluids are used in the same experimental setup. Water and FC-72 were studied jointly in [34] and water, Novec 7200 and Novec 7300 were studied in [35, 36]. In these studies, it was shown that the use of water resulted in higher heat transfer coefficients in both single- and two-phase flow due to water having a higher specific heat, latent heat of vaporization and thermal conductivity. However, the use of FC-72, Novec 7200 and Novec 7300 offer two distinct advantages over water. First, these are all dielectric fluids that can be brought into direct contact with functioning electronics for cooling. Second, the saturation temperature of these cooling fluids can be tuned by modifying the chemical composition of the fluid. The maximum operating temperature of most electronics is ~95 °C, so the lower saturation temperature of FC-72 (56 °C) and Novec 7200 (76 °C) at atmospheric pressure make them attractive fluids for cooling of high-performance electronics.

This difference in saturation temperature adds one additional difficulty in studying the exact impact of different fluid properties on heat transfer. The difference in saturation temperature means that various fluids experience varying levels of subcooling for the same inlet temperature, and subcooling has also been shown to have an impact on boiling heat transfer [33, 35 - 39]. For a given fluid, the heat transfer coefficient increases at a given heat flux for increasing inlet temperature (or decreasing subcooling) due to boiling initiating at lower heat flux. This is a benefit to heat transfer at lower heat

flux, but decreasing subcooling is a detriment to heat transfer at increasing heat flux and CHF decreases with decreasing subcooling due to the earlier transition to annular flow and dryout [33].

Finally, the wall condition and the design of the experimental apparatus significantly impact both the fluid flow and heat transfer behavior. Most of the microgap research is performed for a gap asymmetrically heated on one wall, with variations on the inlet and outlet flow geometries. However, symmetric and asymmetric heating was studied by Geisler and Bar-Cohen [33] on aluminum and silicon heaters. Symmetric heating for a single pair of heaters and for three pairs of heaters at uniform and non-uniform heat flux profiles was studied by Janssen et al. [35, 36]. The effect of surface roughness was studied by Alam et al. [28] and Geisler and Bar-Cohen [33]. Increasing surface roughness increases the number of nucleation sites available to nucleate bubbles, thereby decreasing the temperature at ONB and increasing heat transfer thereafter. Geisler and Bar-Cohen [33] report that the surface roughness has little effect on CHF as the gap size decreases.

2.1.3 Flow boiling mechanisms

The mechanisms associated with boiling in microgaps have not been studied to date. However, slug flow is one of the prevalent flow regimes in microgaps, and the heat transfer mechanisms present in slug flow in microchannels was studied by Moghaddam et al. [8 - 12] and modeled by Thome et al. [40 - 43].

In the studies by Moghaddam et al., a device was constructed to measure heat transfer and wall temperature as a slug passed over the wall. The bubble that formed the slug was nucleated upstream of the test section and passed through an adiabatic channel that

housed the heat flux and temperature sensors. The local wall temperature and heat flux measurements as a slug passed over the sensors are shown in Fig. 2.5.

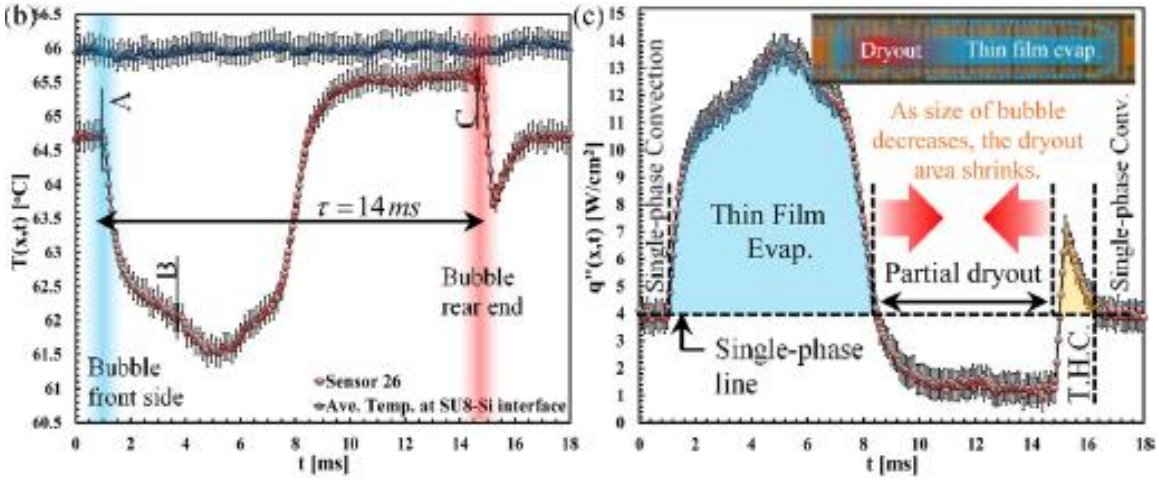

Fig. 2.5. Local wall temperature and heat flux measurement as a slug passes a microchannel wall. Reprinted from [11].

As the front of the slug passed over the sensor, the wall temperature decreased and the local heat transfer increased dramatically. The authors attribute this to evaporation in the thin film of liquid separating the slug and the channel wall. After part of the slug had passed, the wall temperature started to increase, demonstrating a decrease in local heat transfer. The authors assume that this is indicative of partial dryout of the liquid film and the decreased heat transfer associated with the wall being partially covered by vapor. After the rear of the slug passed the sensor, the wall temperature decreased again, though not as dramatically as when the front of the slug reached the sensor. This decrease in temperature was followed by a gradual increase in temperature until it reached an asymptotic value consistent with liquid convection in the microchannel.

The authors note that this increase and decrease of temperature are caused by the dry wall being gradually wetted with liquid after the slug passes. It is possible that transient heat conduction is the primary heat transfer mode here. This mechanism was modeled in

pool boiling by Mikic and Rohsenow [44] and their model was updated by Demiray and Kim [45]. Bigham and Moghaddam [10] demonstrate that their heat transfer results in the section labeled T.H.C. in Fig. 2.5 are predicted well by the model by Demiray and Kim [45]. Thus, they infer that the dominant heat transfer mechanism directly following the passing of the slug is transient heat conduction.

These physical mechanisms are very similar to those assumed by Thome et al. [40 - 42] in the development of their three-zone model for heat transfer in microchannels. Thome et al. also assume that as a slug passes, thin film evaporation is the dominant heat transfer mode and can lead to partial dryout of the wall in the rear of the slug. In front of and behind the slug, heat transfer is governed by single-phase liquid convection. The basic three-zone model was recently updated by Magnini and Thome to include various other parameters, including more detail for the slug geometry [43].

2.1.4 Comparison with microchannels

Both microchannels and microgaps are being considered for cooling of high-performance electronics. For this reason, both were studied on the same platform by Alam et al. [27, 29] and Harirchian and Garimella [46] to determine which provides more effective cooling. Alam et al. found that heat transfer coefficients in the microgap were higher than in the microchannel at the same experimental condition and that CHF was greater in the microgap (Fig. 2.6). It is important to note that the microgap hydraulic diameter (375 μm) is slightly greater than that of each microchannel (270 μm) but the total volume available for flow was equivalent in the microgaps and microchannels.

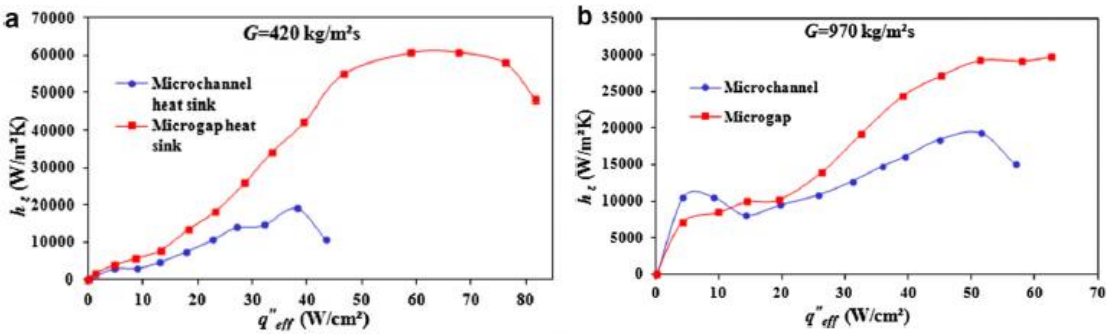

Fig. 2.6. Heat transfer coefficient comparison for boiling in microchannels and microgaps. Reprinted from [27].

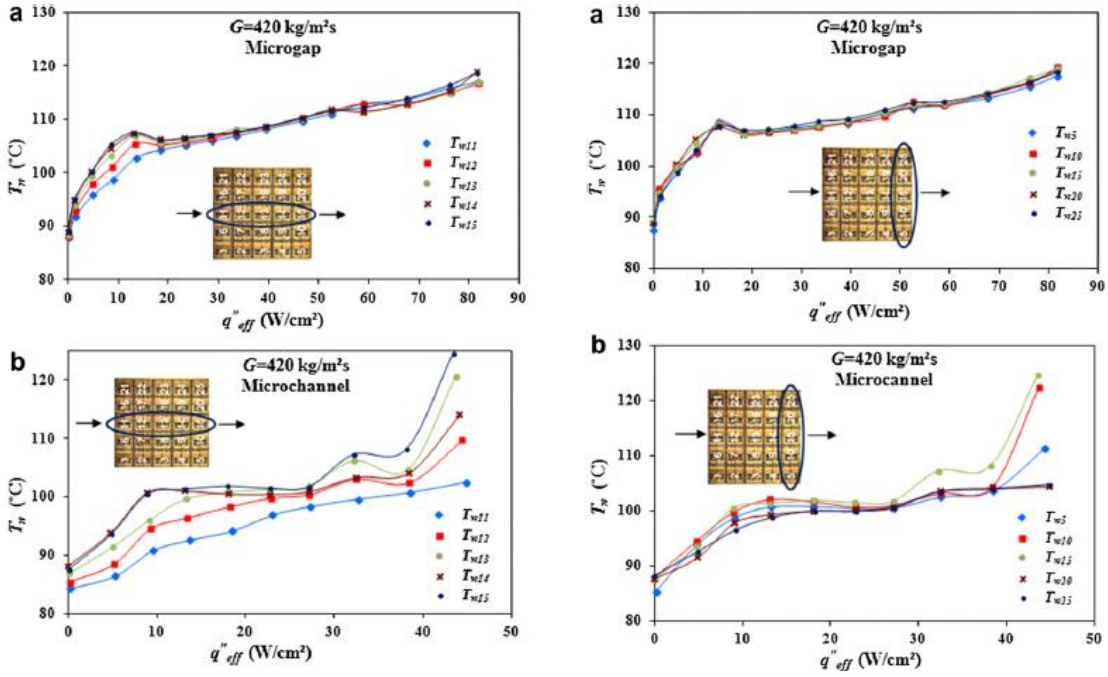

Fig. 2.7. Axial and lateral temperature measurements in microgaps and microchannels. Reprinted from [27].

In addition to providing higher heat transfer coefficients, the microgap produced more consistent temperature measurements in both the axial and lateral directions (Fig. 2.7). The temperature is more uniform in the microgap because the vapor is able to expand in both the lateral and axial directions as bubbles grow. In the microchannels, the bubbles are confined by the microchannel width and are only able to expand in the axial direction. As a bubble grows and constricts flow in a single channel, liquid will flow to surrounding

channels with lower resistance. This results in a nonuniform flow and temperature distribution in the microchannels.

The temperature measurements in Fig. 2.7 are average measurements. However, Alam et al. demonstrate that both the microchannels and microgap demonstrate cyclic variation in the wall temperature. The amplitude of this variation is significantly larger in the microchannels. Unsteady wall temperature measurements were also reported in microgaps by Sheehan and Bar-Cohen [47]. Alam et al. also demonstrate unsteady pressure drop measurements in both the microchannels and microgap. The average pressure drop and the amplitude of variation was lower in the microgap than in the microchannels.

Finally, microgaps can provide one additional benefit noted by Bar-Cohen and Wang [48]. With the microchannels, a thermal interface material must be used at the interface between the microchannel base and the electronic substrate being cooled. This interface represents the largest resistance to heat transfer in some electronics [48]. If a microgap is used for cooling, the cooling fluid can be brought into direct contact with the electronics, eliminating this large resistance to heat transfer.

2.2 Boiling on microporous surfaces

A large database of studies for boiling on structured and unstructured surfaces has been generated recently due to the effectiveness of these structures at increasing heat transfer and delaying the transition to CHF. Many of these studies are for structured surfaces used in microgaps and microchannels, e.g. [49 - 63]. Because the literature base is so large for boiling on structured and unstructured surfaces and this investigation is only for boiling on unstructured microporous surfaces, attention will only be given here

to this subset of the literature. However, the interested reader can consult [61, 64 - 66] for more complete lists of the relevant literature to date.

2.2.1 Description of porous media

A porous medium is a medium that consists of solid material interspersed with interstitial void spaces (pores) through which fluid can flow. A representative volume of a porous medium is shown in Fig. 2.8. In this figure, the grey volume represents the solid material and the white volume represents the pores where fluid flows. If a porous medium is deposited on a wall with bulk flow above, flow must be considered at not only the macroscopic level but also at the pore level. Generally, the flow and transport behavior in a porous medium is dependent on the fluid flowing and the solid wall material in the medium as well as the pore size, porosity and permeability.

The porosity, ϕ, for a porous medium is defined as the ratio of void space to total space in a representative volume in the medium. A common assumption in measuring porosity is that the solid and void areas are constant in one direction, so that the porosity can be approximated by the void and solid areas rather than volume,

$$\phi = \frac{V_{void}}{V_{total}} \approx \frac{A_{void}}{A_{total}} \tag{2.1}$$

The permeability, K, relates to the momentum loss due to flow at the pore scale, which has one component associated with viscous losses and one associated with inertia. Thus, the pressure drop at the pore scale is related to the permeability by [67]

$$\nabla P_{pore} = -\frac{\mu \vec{U}}{K} - \frac{\rho C}{K^{1/2}} \left|\vec{U}\right| \vec{U} \tag{2.2}$$

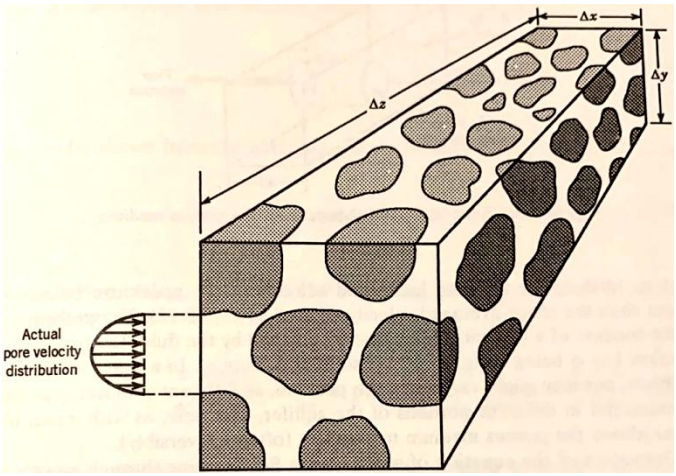

Fig. 2.8. Representative elementary volume for a porous medium. Reprinted from [67].

2.2.2 Methods of creating porous surfaces

Various techniques have been developed for creating microporous surfaces. One of the most popular techniques is that developed and patented by You et al. [68 - 75]. You et al. use this technique to deposit Alumina (Al_2O_3), silver or diamond flakes on substrates. First, the flakes are mixed with Omegabond 101 and an alcohol that evaporates at atmospheric pressure, often Methyl-Ethyl-Ketone. Next, the mixture is dripped onto the surface with a pipette or a paint brush, or sprayed on with an airbrush, depending on the substrate size. The mixture is allowed to sit at atmospheric pressure and the alcohol evaporates, leaving a mixture of flakes and Omegabond binder. The primary adhesion forces between the mixture and the substrate are Van der Waals forces.

The pore size and porosity of this porous surface can be varied by using various flake sizes. Usually, a range of pore sizes are seen for a given flake size, but the dominant pore size is on the order of the flake size. The coating thickness can be set by varying the amount of mixture applied to the substrate. Often, the thickness also increases with flake size. This technique was also utilized by Sarwar et al. [76] to deposit Al_2O_3 and TiO_2

surfaces for flow boiling in vertically-oriented 11 mm diameter tubes and Liu and Yang [77, 78] to deposit aluminum particles for pool boiling between parallel plates.

A second technique for depositing microporous surfaces was developed by El-Genk and Ali [79]. In this process, electrochemical deposition is used to deposit the surface and increase the bond strength between the surface and substrate. Two copper plates are connected to a voltage supply and oriented horizontally and parallel to each other in an electrolyte solution of sulfuric acid (H_2SO_4) and copper sulfate ($CuSO_4$). Voltage is applied to drive a chemical reaction, where the copper cathode will serve as the substrate on which the porous surface is deposited. In this reaction, the copper and hydrogen in the elctrolyte solution are stripped of electrons and travel toward the copper cathode, causing the copper to deposit on the surface and hydrogen atoms near the surface to combine with free electrons to form H_2 bubbles.

This reaction proceeds in two steps. First, a high voltage is applied so that 3 A/cm^2 flows between the copper cathode and anode. In this step, the majority of the copper atoms are deposited but the bond between the surface and substrate is relatively weak. The released hydrogen bubbles at the cathode form semi-regular circular pores. The thickness of the layer is set by the length of time this voltage is applied, with surfaces of 95-230 μm thickness resulting from 15-44 s of applied voltage. The porosity of the surface is insensitive to the time in this stage.

In the second stage, the current density is set to be very low and held for 10's of minutes. In this stage, the bonds between the surface and the substrate and between individual copper atoms strengthen, resulting in a very robust surface. The porosity decreases as additional copper atoms fill out the structure. At the end of the first stage,

the bonded copper atoms form more dendritic structures; after the second stage, the small-scale structures are more rounded. El-Genk and Ali note that this also increases the wettability of the surface. In previous work by Parker and El-Genk [80 - 82], their surfaces were created by simply bonding a graphite surface to a heated substrate.

2.2.3 Boiling heat transfer on microporous surfaces

In general, boiling on microporous surfaces offers three benefits over boiling on smooth surfaces. First, the superheat at ONB is much lower on the microporous surfaces, with a correspondingly low, or often nonexistent, overshoot of temperature before boiling begins. This is attributed to the nucleation site characteristics and the ability of the porous surface to trap air that can serve as bubble embryos. Second, CHF is much higher on porous surfaces, with CHF more than double that of a smooth surface at the same condition in some cases [71].

Two mechanisms are often discussed for increasing CHF on these surfaces. First, the porous surfaces increase the frequency of bubble release and decrease the bubble diameter. This has been supported with visual evidence in pool boiling [80]. Second, the pore network on the microporous surface can serve to wick fluid to the heated surface via surface tension and capillary pressure. This decreases the ability of vapor to wet the surface and cause a transition to CHF. The last benefit that microporous surfaces provide is a decrease in the wall temperature and a corresponding increase in the heat transfer coefficient.

The three benefits of microporous use are all shown in Fig. 2.9 at various levels of subcooling. This figure also shows that, as in pool boiling on smooth surfaces, the subcooling has a significant effect on the boiling curve. In the nucleate boiling region

just after ONB, increasing subcooling decreases the wall temperature and increases the slope of the boiling curve. As the heat flux increases, the impact of subcooling decreases and the slope of the boiling curve is seen to be the same for various levels of subcooling. At high heat flux, CHF is seen to be a linear function of subcooling. Subcooling in pool boiling on microporous surfaces was studied in [74, 75, 80 - 82] and these trends were consistent among the various studies.

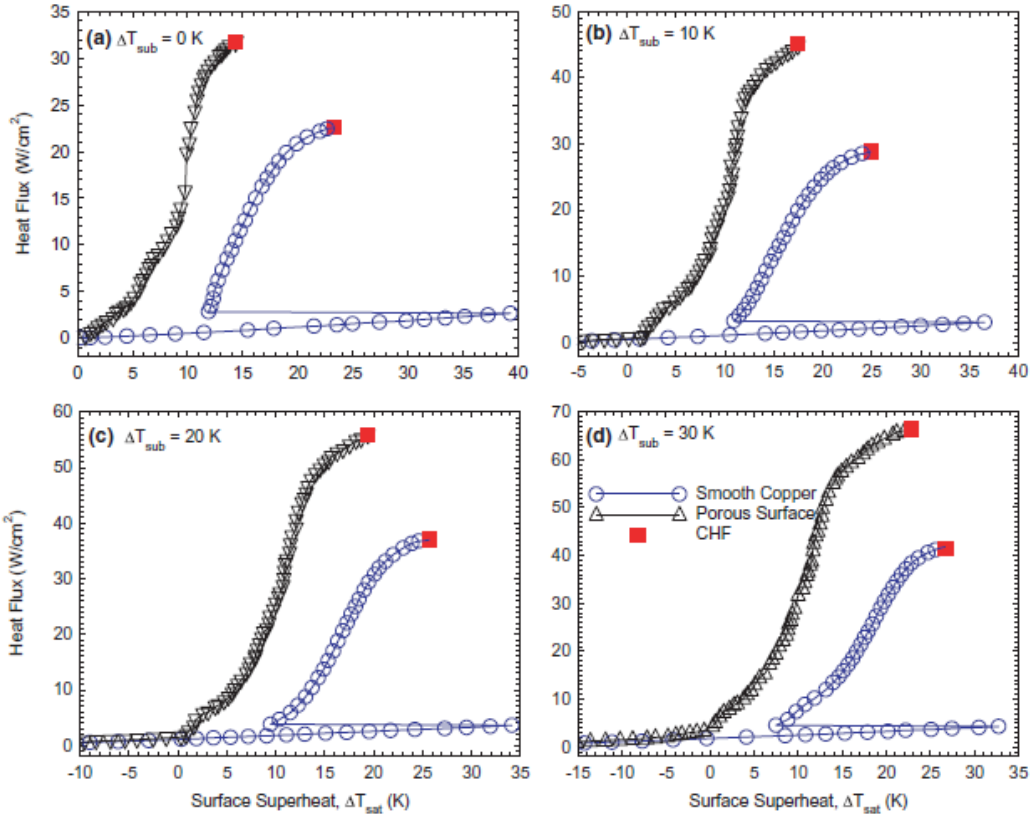

Fig. 2.9. Comparison of pool boiling curves for smooth copper and porous graphite surfaces. Reprinted from [81].

In addition to subcooling, it is known that the system pressure, heater size and heater orientation impact pool boiling heat transfer on smooth surfaces. On microporous surfaces, the system pressure was studied by You et al. [74, 75], and the trends for the microporous surfaces are similar to trends on smooth surfaces. Increasing the system

pressure generally decreases the superheat at ONB and increases CHF, with the impact on CHF being more dramatic on the microporous surfaces.

The heater size effect was studied by Rainey and You [73]. As in pool boiling on smooth surfaces, the critical heat flux decreased with increasing heater size until a "transition point" is reached, after which the critical heat flux was insensitive to heater size. Rainey and You show that the "transition point" is approximately equivalent to that determined by Bar-Cohen and McNeil [83] for pool boiling on smooth surfaces. The effect of the heater orientation was studied by Rainey and You [73] and El-Genk and Parker [82]. For pool boiling on smooth surfaces, increasing the surface angle generally shifts the boiling curve to slightly lower temperatures up to an angle of ~135°; thereafter, the heat transfer diminishes and the boiling curve shifts to significantly higher wall temperatures. On the microporous surfaces, Rainey and You report a relative insensitivity to change in heater angle throughout much of the boiling curve. El-Genk and Parker note that that the maximum heat transfer coefficient is insensitive to heater orientation, but that the heat transfer coefficient at higher wall temperatures decreases with increasing heater angle. This is consistent with decreasing CHF with increasing angle, as is shown for both smooth and microporous surfaces [73, 82].

Finally, we may suspect that the pore size, porosity, and thickness of the surface will impact heat transfer. The surface thickness was investigated by Chang and You [71] and El-Genk and Ali [79], though the process used for creating the porous surfaces resulted in variation in both porosity and pore size with increasing thickness so it is hard to determine from these studies what the important factor is. Chang and You found that increasing the porous surface thickness decreased the superheat at ONB and increased

CHF. Both of these effects reached an asymptote, after which increasing the thickness had no impact on superheat or CHF (Fig. 2.10).

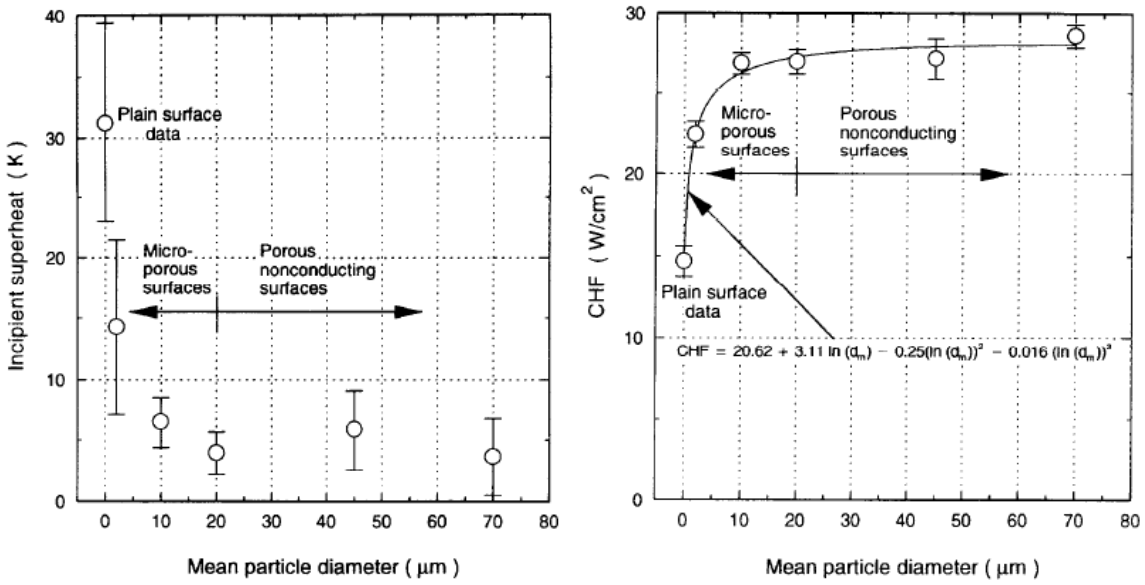

Fig. 2.10. Superheat at ONB and CHF as a function of surface thickness (denoted as particle diameter) for diamond flake microporous surfaces. Adapted from [71].

Chang and You [71] assume that a superheated liquid layer of thickness ~100 μm exists on the heated wall. They reason that if the surface is thinner than the superheated layer, the entire surface can be activated during nucleate boiling. If the surface is thicker than the superheated liquid layer, only the bottom portion of the surface will be activated. Thus, they term their surfaces either microporous or porous based on the surface thickness in relation to the superheated liquid layer thickness. Chang and You's CHF results are consistent with those of El-Genk and Ali [79], who also measured an increase in CHF with increasing surface thickness up to limiting value, followed by insensitivity of CHF to surface thickness.

The trends in superheat, heat transfer coefficients and CHF for pool boiling on microporous surfaces are also consistent with the limited data available for flow boiling on microporous surfaces [72, 76]. However, in studying flow boiling in a vertically

oriented tube of 10.9 mm inner diameter, Sarwar et al. [76] varied the particle size and surface thickness independently. They found that Al_2O_3 particles of 1 μm diameter showed little effect on the heat transfer behavior compared to the smooth tube. SEM images reveal that particles of this size effect created a second hard surface, with little interstitial area. Particles of 10 μm diameter resulted in an ~25% increase in CHF over the smooth tube case. They also measured that increasing the surface thickness in the range 20-50 μm for a fixed particle size of 10 μm increased CHF.

In flow boiling, the effect of the mass flux was investigated by Ammerman and You [72] in a single 2mm×2mm microchannel and Sarwar et al. [76] in the tube noted above. Both studies demonstrate that increasing the mass flux leads to an increase in CHF for boiling on both microporous and smooth surfaces. A linear increase for the microporous surfaces is noted by Sarwar et al. [76]. Chang and You [71] also measured pressure drop in their study. They note that the pressure drop is comparable between the microporous and smooth channels for lower mass flux and higher subcooling. At higher mass flux and lower subcooling, the pressure drop for the microporous surfaces is greater, as high as ~33% larger than that for the smooth channel at the highest mass flux and lowest value of subcooling.

2.3 Boiling of emulsions

Boiling heat transfer in mixtures has been studied for many decades, and most research has focused on boiling in mixtures of miscible liquids. Several reviews have arisen from this research [84 - 87]. However, in the last 30 years, research has focused on boiling in mixtures of immiscible liquids. Heat transfer coefficients are generally lower in miscible mixtures than in the same pure components, but higher heat transfer

coefficients can be obtained in boiling of immiscible mixtures, particularly emulsions. This suggests that systems involving high heat flux could benefit from boiling emulsions rather than single-component fluids.

The following sections elaborate current understanding of heat transfer in pool and flow boiling of dilute emulsions. Discussion is restricted to emulsions comprising two components, but more generally emulsions can contain more than two components. The effect of various system and fluid properties, e.g., droplet size, droplet concentration, use of stabilizing agents, etc., are described with respect to their effects on the underlying thermodynamics and energy transport. The currently proposed mechanisms governing pool boiling of emulsions are described, followed by various techniques used to model pool and flow boiling of dilute emulsions ($\varepsilon < 5\%$).

2.3.1 Early research

The earliest investigation of boiling of emulsions was conducted by Mori et al. [88] and involved pool boiling of oil-in-water and water-in-oil emulsions on a horizontal wire. The emulsions they studied were stabilized using surfactants. The four oils studied- KF96, KF54, n-Dodecane and n-Undecane- all have saturation temperatures much higher than that of water at atmospheric pressure. In their experiments, the temperature of the emulsion was held at 100 °C.

Mori et al. found that when water is the disperse component (water-in-oil), boiling of the emulsion always progresses at lower surface temperatures compared to that of the oil. They also found that the water-in-oil emulsions required surface superheats of ~ 40 - 100 °C to initiate boiling on the wire surface. Because they used a transparent test apparatus, initiation of boiling could be observed visually by noting bubbles on the wire surface.

Initiation of boiling is also accompanied by a shift in the slope of the boiling curve. When oil was the disperse component (oil-in-water), boiling initiated at much lower surface superheats, often of 15 - 30 °C. Presumably boiling was able to initiate at much lower temperatures owing to the high water fraction (with much lower saturation temperature) in the emulsion.

They find that their results depend on the type of surfactant. They utilized Tween 80 and sodium oleate to stabilize the oil-in-water emulsions and Span 80 to stabilize the water-in-oil emulsions. When experiments are conducted with sodium oleate, the surfactant reduces single-phase natural convection prior to boiling initiation, and this effect is more pronounced with increasing volume fraction of oil. However once boiling initiates, the presence of the sodium oleate shifts the boiling curve to lower surface temperatures compared to the water experiment. When Tween 80 is used, heat transfer coefficients are lower in both the natural convection and boiling regimes compared to those in water.

Another early investigation is that of Ostrovskiy [89], who investigated boiling of water-in-R113, water-in-benzene and water-in-butyl alcohol emulsions on a vertically oriented wire. Ostrovskiy did not utilize a surfactant, and the emulsion was continually stirred to maintain the suspension. The water-in-R113 experiments result in measured heat transfer coefficients almost equivalent to those measured in Ostrovskiy's measurements of boiling of R113 without the dispersed component. Similar results are found for water-in-butyl alcohol and at higher heat fluxes in water-in-benzene. One interesting observation that Ostrovskiy makes is that the dependence of the heat transfer coefficient on heat flux is very similar to that of turbulent free convection. Ostrovskiy

notes that the emulsions were preheated prior to running the experiments, but he does not indicate at what temperature experiments are performed. Keeping in mind the large surface superheats required to initiate boiling as measured by Mori et al. [88], it has been suggested that the results are similar to that for free convection because boiling was not initiated [90].

2.3.2 Effect of system properties

Research has shown that many system properties, such as the two fluids present in the emulsion, heater geometry, temperature, droplet size/distribution, concentration and use of surfactants affect heat transfer behavior. Consider first the fluid properties. If some of the property dependences of single-phase systems apply to two-phase systems, we should expect that the Nusselt number is dependent on either the Rayleigh number in pool boiling or the Reynolds and Prandtl numbers (Peclet number) in flow boiling. Additional non-dimensional parameters account for the effect of latent heat and surface tension, e.g., the Boiling or Jakob number and the Bond or Weber number [91]. The way the two fluids in the emulsion interact will also affect heat transfer. Consider, for example, FC72-in-water and pentane-in-water emulsions.

Roesle and Kulacki [92] measured the heat transfer coefficient for pool boiling of FC72-in-water and pentane-in-water emulsions on a small diameter horizontal wire. In [92], droplets of the dispersed components (pentane and FC72) produce a poly-disperse emulsion with a mean diameter of 8 μm. Their FC72-in-water results (Fig. 2.11) demonstrate some interesting trends. In the natural convection portion of the curve prior to the initiation of boiling, the heat transfer coefficients for $\varepsilon = 0.1\%$ are close to those predicted by the Morgan correlation for natural convection of water on a cylinder,

$$Nu = 1.02Ra^{0.148} \tag{2.3}$$

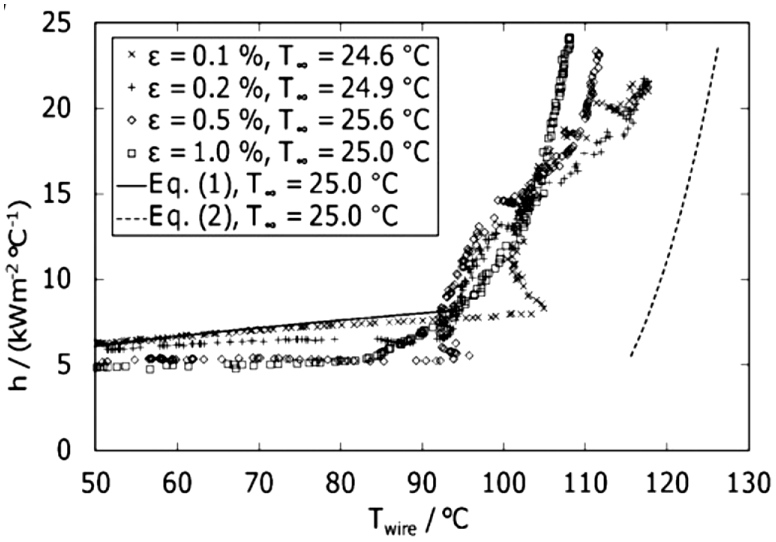

Fig. 2.11. Pool boiling curve for FC-72 in water emulsions [92]. Equations (1) and (2) noted are Eqns. (2.3) and (2.4) here, respectively.

As the volume fraction of FC72 is increased, the heat transfer coefficient decreases and Morgan's correlation no longer approximates the data set. For dilute emulsions, the mixture properties should be nearly equivalent to those of the continuous component, and therefore the decrease in the heat transfer coefficient is probably not caused by the effect of FC72 on bulk mixture properties. FC72 has a higher density than water so they conclude that it settles onto the wire, and its lower thermal conductivity results in the decreased heat transfer coefficient.

Once boiling initiates, the opposite trend is seen. Higher heat transfer coefficients are measured for increasing volume fractions of FC72. All emulsion data sets demonstrate higher two-phase heat transfer coefficients compared to those for water, as predicted by the Rohsenow correlation, Eqn. (2.4), for boiling on a horizontal cylinder where the heat transfer coefficient is defined $h = q/(T_{wire} - T_{\infty})$ [92],

$$\frac{C_p(T_{wire} - T_{sat})}{h_{fg}Pr} = 0.013\left(\frac{q}{\mu_f h_{fg}}\right)^{\frac{1}{3}}\left[\frac{\sigma}{g(\rho_f - \rho_g)}\right]^{\frac{1}{6}} \quad (2.4)$$

At the onset of boiling, the FC72 data for ε = 0.1% also demonstrate a slight overshoot in temperature. This overshoot decreases with increasing volume fraction and is nonexistent for ε = 1%. Roesle and Kulacki do not give an explanation for what may have caused this overshoot. However, the role of mass transfer may be able to explain this phenomenon [85]. When the FC72 droplet nears the heated wire, phase change occurs, and bubbles of FC72 vapor rise from the wire. If the wire temperature is low enough that the water cannot boil, boiling can then only progress when more FC72 droplets come into contact with the wire. For very dilute emulsions, this may lead to a time delay in the next stage of bubble nucleation with the observed overshoot of temperature until the heat flux is large enough to cause a larger fraction of the FC72 to boil. At larger volume fractions, there is more FC72 to rewet the wire when a vapor bubble leaves, leading to either a decreased or no temperature overshoot.

In the pentane-in-water emulsions, trends are similar but with some marked differences (Fig. 2.12). Although natural convection heat transfer coefficients in the pentane-in-water emulsions are lower than that for water, the decrease is significantly less compared to that in the FC72-in-water results. This may be due to the lower density of pentane compared to water, thereby making it less likely that it would coat the wire and decrease heat transfer coefficients due to its lower thermal conductivity. The pentane-in-water emulsions demonstrate higher heat transfer coefficients after the onset of boiling compared to those in water, and the pentane data collapse to a single curve at high wire temperatures. This is not seen in the data for FC72-in-water because the

applied heat flux is greater in the pentane studies. It is possible this occurs because the wire temperature is high enough to cause boiling of the continuous water phase.

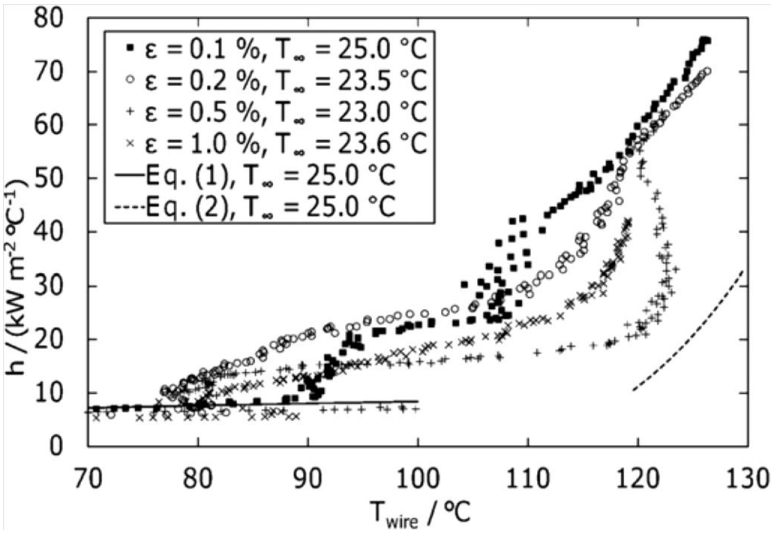

Fig. 2.12. Pool boiling curve for pentane in water emulsions [92]. Equations (1) and (2) noted are Eqns. (2.3) and (2.4) here, respectively.

The low volume fraction pentane-in-water emulsions do not exhibit a temperature overshoot, but the temperature overshoot is observed for ε= 0.5% and 1%. It is possible that mass transfer is also contributing to this effect. Because pentane has a lower density than water, as the wire temperature increases, the increased buoyancy force causes more pentane to rise above the surrounding water than would otherwise occur at lower temperatures. This effect would be exaggerated at higher volume fractions of pentane and could lead to a larger temperature overshoot. Although mass transfer plays a role in single-component, single-phase heat transfer, the results of this study demonstrate that thinking about the effect of mass transfer may be critical to understanding single- or two-phase heat transfer in dilute emulsions.

Very few emulsion studies have been conducted with varying bulk temperatures. One such investigation is that of Bulanov et al. [93]. Water-in-PMS300 emulsions with ε = 0.8 and 3.2% show that at a bulk temperature of 40 °C in single-phase convection, the

emulsion demonstrates nominally the same heat transfer coefficient as PMS300 alone. However, when the surface is ~20 °C above the saturation temperature of water, the emulsion starts to boil and the heat transfer coefficient is nearly twice that of the PMS300 up to wall temperatures of 230 °C.

When the bulk temperature is increased to 99 °C so that the dispersed water droplets are nearly at the saturation temperature, the heat transfer coefficient for PMS300 alone nearly doubles in the natural convection regime. The heat transfer coefficient in the emulsion is also higher compared to the natural convection values measured at T = 40 °C. However, the heat transfer coefficient decreases until wall temperatures are ~140 °C and increases thereafter. This effect is seen in both the ε = 0.8% and 3.2% emulsions, although the decrease in the heat transfer coefficient is less for ε = 0.8%. Even though heat transfer coefficients decrease at lower wall temperatures, they were measured to be higher in the 99 °C data set for all wall temperatures. In [94], the emulsion temperature is varied from 30 - 65 °C, but the results are not dependent on the emulsion temperature.

Gasanov and Bulanov report the effect of droplet size on the heat transfer coefficient in water-in-PES5 [95] and water-in-VM1S oil emulsions [96]. In both investigations, they classify the emulsions as either “coarse grained” (d ~ 20 - 30 μm) or “fine grained” (d ~ 1 - 2 μm). In natural convection, droplet size does not affect the heat transfer coefficient (Fig. 2.13). However, the boiling curve tends to shift to lower surface temperatures for the coarse-grained emulsions, and the temperature at the onset of nucleate boiling is higher in the fine-grained emulsions. This is to be expected owing to the effect of surface tension, which increases the pressure inside the droplet,

$$P - P_{\infty} = \frac{\sigma}{d} \tag{2.5}$$

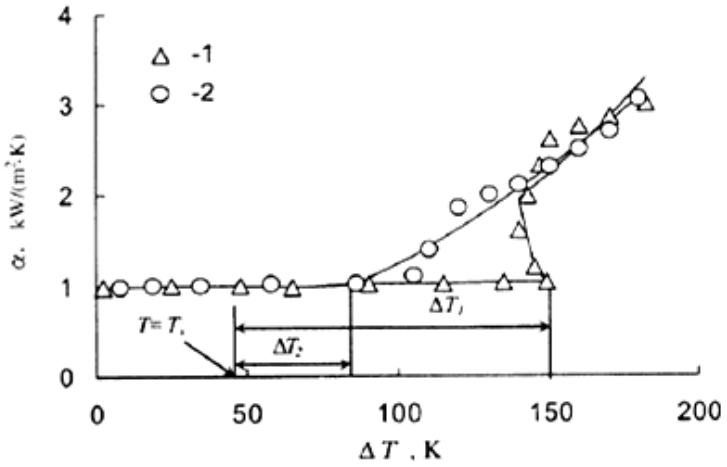

Fig. 2.13. Heat transfer coefficient, α, as a function of wall temperature. Data sets 1 and 2 are for water/PES-5 emulsions with d = 1.5 μm and 35 μm, respectively. $\Delta T = T_w - T_{sat}$ [95].

Because the pressure inside the droplet increases with decreasing diameter, the saturation temperature of the disperse component is higher for the fine grained emulsions. Boiling in the fine-grained emulsions in [95] initiate at a wall temperature ~70 °C higher than in the coarse-grained emulsions (Fig. 2.13). For water droplets of this size, the rise in the saturation temperature compared to atmospheric conditions would be ~5 - 10 °C, so it is clear that surface tension alone does not account for the large surface temperature required to initiate boiling in [95]. In [96], the difference in surface temperature required to initiate boiling is ~10 °C.

Figure 2.13 also shows two additional features in the water/PES5 emulsions of [95] that do not appear in the water/VM1S oil emulsions of [96]. The fine-grained emulsions demonstrate a small overshoot at the onset of boiling that gradually decreases as the heat flux increases. This feature has also been demonstrated in the pentane-in-water and FC72-in-water emulsions [92]. At high heat flux the coarse-grained and fine-grained emulsions collapse to a single curve. Once boiling is initiated in the water-in-VM1S oil

emulsions, the fine-grained and coarse-grained emulsion heat transfer curves are separated by a consistent temperature difference [96].

It can be expected that the droplet size distribution will also impact heat transfer. In developing an analytical model of boiling in emulsions, Bulanov [98] utilizes statistical mechanics to include the effect of the bubble nucleation rate. Because the nucleation rate is probabilistic, the droplet size distribution plays a role in determining the nucleation rate. The effect of droplet size distribution has not, however, been investigated experimentally. Most experimental studies and models assume that the emulsion is monodisperse [97, 98]. However, the results in [92] are for a droplet size distribution that is non-Gaussian [99], and the experimental results of Bulanov et al. are for emulsions that are almost bi-disperse [100].

Most emulsion experiments involve studying the impact of volume fraction of the dispersed component on heat transfer coefficients. Increasing the volume fraction generally shifts the boiling curve to the left such that higher heat transfer coefficients are seen at the same wall temperatures for higher volume fraction of the dispersed component (Fig. 2.11). However, as noted before, mass transfer may also play a role in both single-phase and two-phase heat transfer, causing a decrease in heat transfer coefficients depending on the fluids used and geometry of the heat transfer surface.

Bulanov et al. [100] systematically vary the volume fraction and measure heat transfer coefficients for a range of wall temperatures in water-in-PES5 emulsions (Fig. 2.14). For $\varepsilon \leq 1\%$, an increase in the heat transfer coefficient by a factor of two to four is measured. However, for $\varepsilon > 1\%$, no increase in the heat transfer coefficient is found for a wide range of wall temperatures.

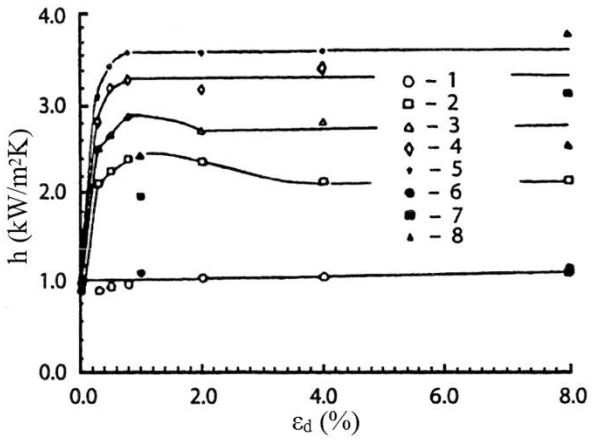

Fig. 2.14. Heat transfer coefficient as a function of water volume fraction, ε_d, in water-in-PES5 emulsions [100]. Data sets 1-5 correspond to wall temperatures of 100, 190, 205, 220 and 235 °C, respectively. Data sets 6 - 8 correspond to emulsions stabilized with 1% (by weight) tri-sodium phosphate at wall temperatures of 100, 190 and 220 °C, respectively.

As noted previously, a study of the use of surfactants was conducted in [88]. The use of activated carbon in emulsions of water-in-PES5 and n-pentane-in-glycerin, zeolites in a water-in-PES4 emulsion, and sodium hydrate and tri-sodium phosphate surfactants in a water-in-PES5 emulsion was subsequently investigated by Bulanov and Gasanov [95]. They find that when water-in-PES5 emulsions are stabilized with activated carbon, the use of the carbon shifts the boiling curve to lower wall temperatures by ~10 - 15 °C. The heat transfer results are also relatively insensitive to the amount of carbon added in the range 0.045 - 0.3% by weight. When n-pentane-in-glycerin emulsions are stabilized with 0.3% activated carbon, the presence of carbon delays the onset of boiling and shifts the boiling curve to higher wall temperatures by ~10 °C. Bulanov and Gasanov theorize that nucleation of bubbles occurs on small floccules in the emulsions that adsorb atmospheric gas [101]. Thus, they attribute these results to activated carbon forming the floccules in the water-in-oil emulsions and the formation of floccules being hindered in oil-in-oil emulsions.

When water-in-PES5 emulsions are stabilized with 0.6% and 2% NaX zeolites by weight, the use of the zeolites inhibits the onset of boiling, with the temperature at the onset of nucleate boiling increasing with increasing mass of zeolite added. They attribute this to adsorbed water by the zeolite rather than atmospheric gases, thus limiting the number of possible nucleation sites. At higher heat flux, the results for emulsions with and without zeolites collapse to the same curve.

When a water-in-PES5 emulsion is stabilized with either sodium hydrate or tri-sodium phosphate, Bulanov and Gasanov state that at low volume fraction of the dispersed component, the presence of the surfactant leads to an increase in the wall temperature required to initiate boiling. However, they also state that at high temperatures or large volume fraction of the disperse component, the addition of a surfactant results in larger heat transfer coefficients and an increase in the critical heat flux. Bulanov et al. also investigate the effect of tri-sodium phosphate on water-in-PES5 emulsions, and their results are shown in Fig. 2.14. In [100], they note that the presence of tri-sodium phosphate has no effect on the heat transfer coefficient. From these studies, it is not clear how the presence of either surfactants or other stabilizing agents affects the heat transfer coefficient.

2.3.3 Visualization of pool boiling

Visualization of pool boiling has been limited to photography to track bubble formation and transit around and from the heated surface. While qualitative in nature, these observations give some insight to physical mechanisms, bubble kinematics and bubble morphology along the boiling curve. There are however two significant challenges to using visualization techniques. First, small droplets in the emulsion scatter

incident light, making the mixture opaque and difficult to observe. Second, the index of refraction of many of the liquids studied, e.g., water, FC72, pentane and VO1C oil, are nearly identical, making it difficult to differentiate between the two liquid components. Though these difficulties exist, videography has been applied to study boiling of FC72-in-water [102], pentane-in-water [102, 103], pentane-in-glycerin [103] and water-in-VO1C oil emulsions [104]. In the following, several observations are elaborated.

In [102] it is demonstrated that for boiling of pentane-in-water emulsions, large bubbles attach to the wire at low heat flux, and as the heat flux increases, bubble size decreases (Figs. 2.15 and 2.16). The pentane droplets have diameters of $4 \leq d \leq 22$ μm with average $d \approx 8$ μm, and in the bulk of the emulsion are subcooled, $T_{sat} - T_{\infty} = 13$ °C. No spontaneous vaporization in the liquid phase away from the wire is observed. Vapor bubbles nucleate on the wire and grow prior to liftoff at various diameters on departure. It is speculated that the large bubbles seen are a result not of individual droplets boiling but of droplets of pentane attaching to the wire, agglomerating with other droplets, then boiling. Also evident in Fig. 2.16 are bubbles that form at the surface, collect with other bubbles to form a packet, then lift off of the surface without coalescing to form one large bubble. It is shown that at higher heat fluxes, bubbles can form at the surface and be propelled downward and away from the wire, rather than simply rising off of the wire. This is the source of the bubbles that are present below the wire in images (c) and (d).

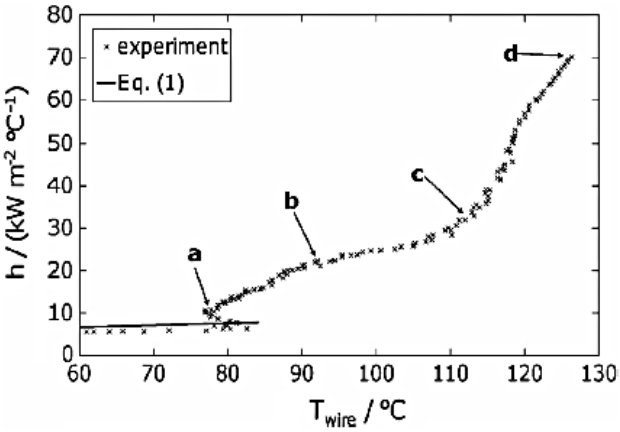

Fig. 2.15. Heat transfer coefficient for pool boiling of a pentane/water emulsion on an electrically heated wire of 10.1 μm diameter. ε = 0.2%, T_∞ = 23.5 °C [102]. Equation (1) noted is Eqn. (2.3) here. Letters denoting locations on the heat transfer coefficient curve correspond to bubble images in Fig. 2.16.

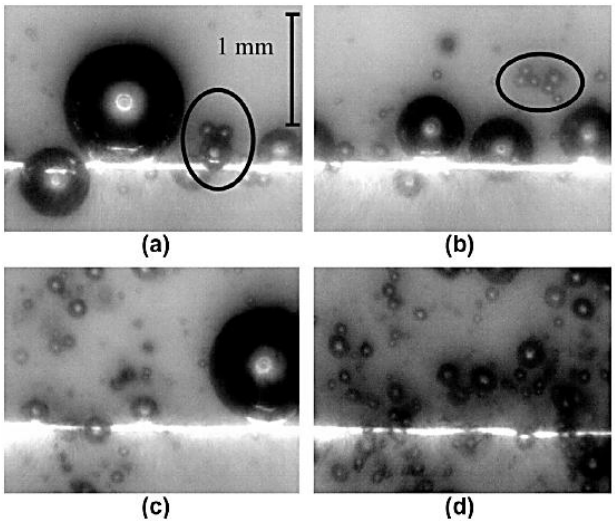

Fig. 2.16. Bubbles in boiling pentane-in-water emulsions on a heated wire [102]. ε = 0.2%, T_∞ = 23.5 °C. Heat flux increases from (a) - (d) as labeled in Fig. 2.15. Optical resolution is 4.5 μm/pixel at a frame rate of 30 s^{-1}.

The pentane-in-water results obtained in [103] are shown in Figs. 2.17 and 2.18 and demonstrate many of the same trends. At lower heat flux, large bubbles are seen attached to the wires while at higher heat fluxes, the bubbles attached tend to decrease in size and increase in number, and at high heat fluxes, some bubbles are shown to be driven downward and away along the wire. However, bubbles are observed to form on the wire and coalesce to form larger bubbles. This may provide an alternate mechanism for the

formation of large bubbles, though it was not demonstrated that most of the large bubbles form in this manner. Again, spontaneous vaporization in the liquid away from the wire is not observed.

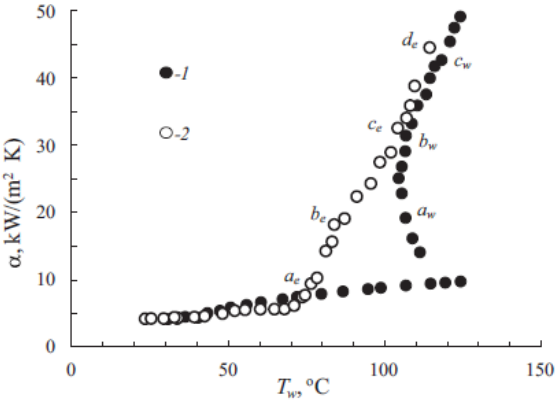

Fig. 2.17. Heat transfer coefficient, α, for (1) water, T_∞ = 20.1 °C, and (2) pentane-in-water emulsions, ε = 4%, T_∞ = 22.1 °C [103]. Letters denoting locations a_e and d_e correspond to images in Fig. 2.18.

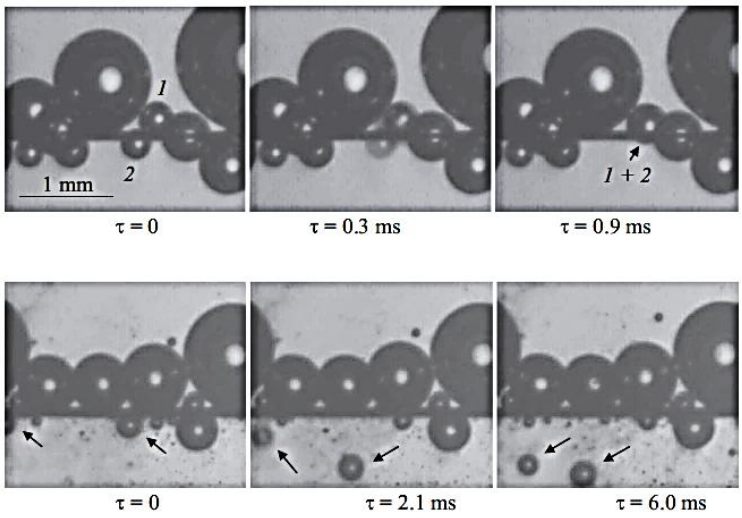

Fig. 2.18. Bubbles in boiling pentane-in-water emulsions on a heated wire. ε = 4%, T_∞ = 22.1 °C [103]. The experimental condition for each image is noted in Fig. 2.17. Time evolution of bubbles on the wire are shown from left to right. Arrows show the movement of two bubbles at d_e in Fig. 2.17.

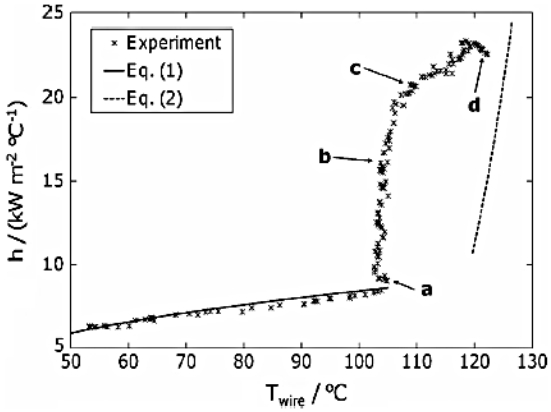

Fig. 2.19. Heat transfer coefficient for heated wire in an FC72-in-water emulsion; 0.1% FC72 by volume, and T_∞ = 35 °C [102]. Letters denote images in Fig. 2.20. Equations (1) and (2) noted are Eqns. (2.3) and (2.4) here, respectively, and are calculated using the properties of water.

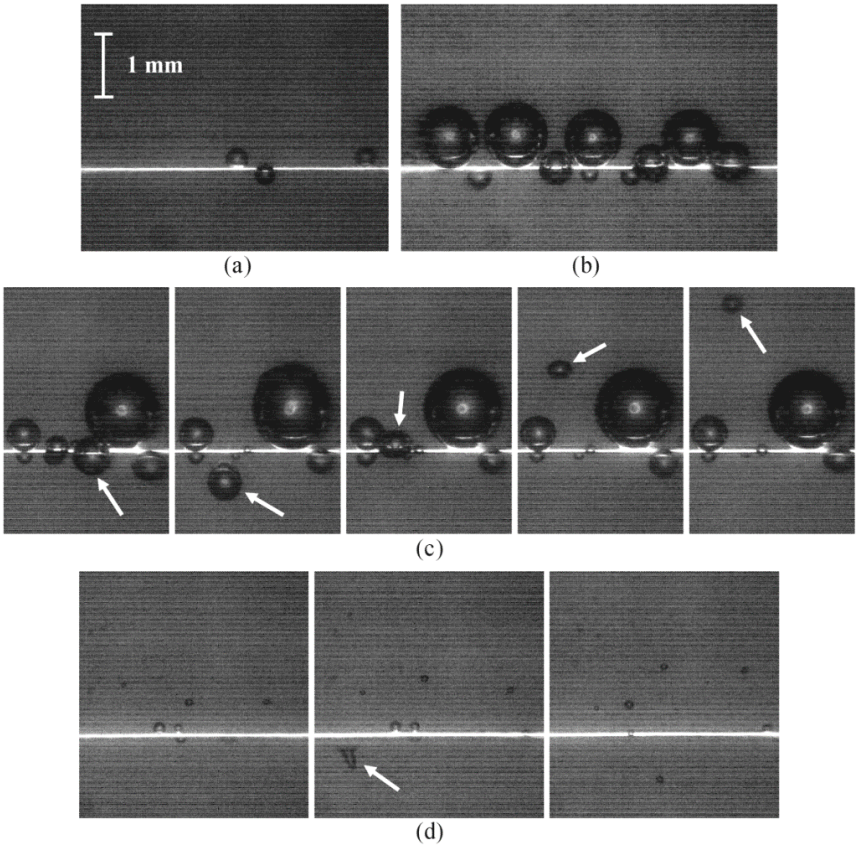

Fig. 2.20. Images of heated wire during boiling in FC72-in-water emulsion, 0.1% FC72 by volume: (a) onset of boiling; (b) attached bubbles at higher heat flux; (c) rapid bubble detachment; and (d) boiling at high heat flux, average bubble rise velocity is 0.0087 m/s [102]. The experimental condition for each image is noted in Fig. 2.19.

To this point, observations suggest that bubbles are formed at the heated surface, not in either the bulk of the emulsion or the thermal boundary layer on the heated surface. Owing to the near equivalence of the indices of refraction of the liquid droplets and water, only bubbles can be imaged, and droplet behavior cannot be observed. To observe droplet mechanics and heat transfer, other imaging techniques may be necessary.

Similar bubble behavior is observed for emulsions of FC72-in-water. Figures 2.19 and 2.20 show images of boiling on a 10 μm DIA wire at several points along the boiling curve. The bulk temperature of the fluid is 35 ^{o}C, and imaging is similar to that in Fig. 2.18. Bubbles first become visible on the wire at the same time that the heat transfer data shows the first sign of boiling (Fig. 2.20a). As heat flux increases, more bubbles form, grow larger (Fig. 2.20b), and detach from the wire with increasing frequency. An interesting behavior is that some bubbles depart the wire with significant velocity. Figure 2.20c shows a bubble, initially attached to the near side of the wire, departing from the wire and initially travelling downward before rising in front of the wire due to buoyancy. The bubble also shrinks visibly owing to condensation as it rises out of the frame.

At high heat flux bubbles that nucleate on the heated wire detach at a much smaller diameter than at lower heat flux (Fig. 2.20d). Due to the high temperature of the wire, it is not clear whether the bubbles that nucleate on the wire are FC72 or water. The detached bubbles visible in Fig. 2.20 have $50 < d < 100$ μm, and so could be the result of boiling of individual FC72 droplets with $10 < d < 20$ μm. As is seen in the second frame of Fig. 2.20d, some bubbles that nucleate on the wire surface are propelled downward, so the dispersed bubbles seen throughout the frame could be the result of this process instead. The elongation of the bubble in the second frame (middle image) is an artifact of

the rolling shutter in the image sensor. It is likely that processes are occurring that are either too small or too fast to capture, for the small number of bubbles observed in Fig. 2.20d could not be responsible for such a large change in the heat transfer coefficient.

2.3.4 Flow boiling

Investigations of flow boiling in dilute emulsions have been reported only recently. The findings of three investigations which find significant augmentation of heat transfer coefficients are summarized. As with pool boiling, the mechanism of bubble nucleation remains undetermined, and the role of droplet-surface interactions is unresolved.

Gasanov and Bulanov [104] investigate flow boiling of water-in-vacuum oil (VO1C oil) emulsions in a peripherally heated 16 mm DIA pipe with inlet bulk temperature ~25 °C and mass flux of 12 kg/m^{2}s. Water concentrations are $0.1\% \leq \varepsilon \leq 1.5\%$ by volume, and droplet size is denoted as either coarse (20 μm < d < 30 μm) or fine grained (1 μm < d < 2 μm). As seen in pool boiling, the fine grained emulsions boil at higher wire temperatures than the coarse grained emulsions. They find that the critical heat flux decreases with increasing water fraction and increasing droplet size at a given concentration. They attribute this to a vapor film forming more easily due to a higher volume of water in larger droplets or higher concentration. Heat transfer coefficients for both the coarse and fine grained emulsions exhibit significant increases once boiling commences (Fig. 2.21).

Bulanov et al. [105] boiled water-in-organosilicon fluid (PES4) emulsions at a mass flow of 0.006 kg/s in an 8.4 mm DIA pipe with an inlet temperature of 60 °C. The mass percent of PES4 was varied between 3 and 33% by weight. They find that heat transfer coefficients shift to lower wall temperatures with increasing volume fraction. They note

that increases in the heat transfer coefficient are seen up to 33% by mass (Fig. 2.22), whereas previous pool boiling studies demonstrate increases in heat transfer coefficient only up to ε ~ 1% (Fig. 2.14). The 12, 20 and 33% data sets all fall within experimental scatter of each other, so it is possible that improvement is only seen up to ε ~ 12%. This is a marked difference from the trends seen in pool boiling. Bulanov et al. also note that boiling begins at the saturation temperature of water, whereas the pool boiling results discussed previously and the flow boiling study [104] require a significant superheat to initiate boiling.

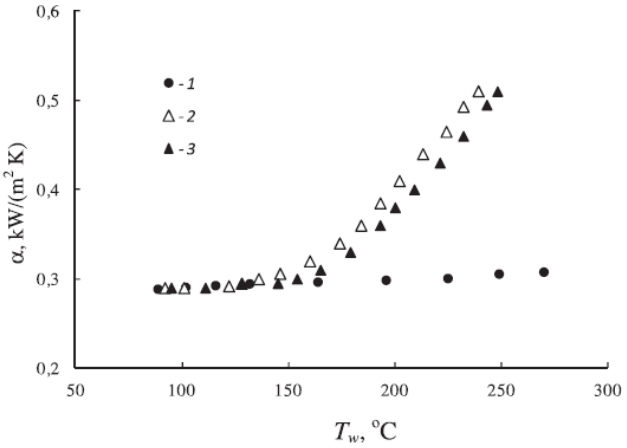

Fig. 2.21. Convective heat transfer coefficients, α, in peripherally heated pipe flow [104]. $Q_{flow} = 2.5 \times 10^{-6}$ m^3/s. 1: VO-IC oil; 2: coarse grained water-in-VO1C oil emulsion; 3: fine grained water-in-VO1C oil emulsion. ε = 1%.

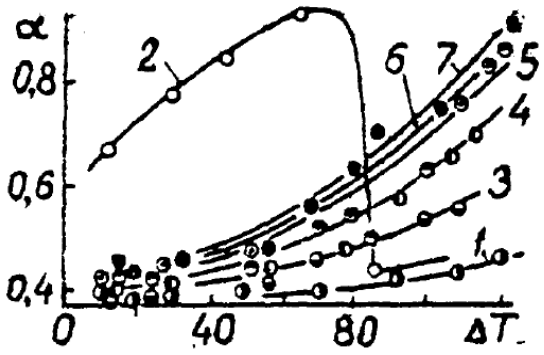

Fig. 2.22. Heat transfer coefficients, α (kW/m^2K), versus temperature difference between heated surface and bulk fluid (deg K) [105]. 1: PES4 fluid; 2: water; 3-7: emulsions by weight percent of PES4, 3.0, 6.0, 12.0, 20.0, 33.0, respectively.

Recent flow boiling experiments have been reported in microgap channels 30 mm wide with gaps of 0.1 mm [106] and 0.25 mm [107]. The design of the microgap in [106] was such that unsteady filling and emptying of the emulsion in the channel was demonstrated, making it difficult to draw conclusions on the heat transfer behavior. However in [107], FC72-in-water and pentane-in-water emulsions were prepared in advance and pumped through the microgap at 133 kg/m^{2}s (0.006 L/min) with a flow development length of 70 mm. Emulsions with ε = 0.1, 1 and 2% were investigated with a bulk inlet temperature of 25 ^{o}C. The dominant droplet size in the emulsion was 5 - 7 μm. The increasing volume fraction of FC72 initiates boiling at lower wall temperatures, with the onset of nucleate boiling occurring at wall temperatures of ~ 85 and 75 °C in the 1% and 2% emulsions respectively. At 20 - 30 °C wall superheat, these temperatures are also lower than those normally required to initiate pool boiling. The heat transfer coefficient is 70% higher in the 2% emulsion compared to that in water at temperatures below the saturation temperature of water. This enhancement is attributed to mixing caused by the turbulent motion of the boiling droplets. For the pentane-in-water emulsions, no enhancement in heat transfer is measured up to ε = 1%. Figure 2.23 shows the augmentation of heat transfer coefficient achieved for the FC72-in-water emulsions.

Morshed et al. report experiments on boiling of FC72-in-water emulsions in a single 5 mm × 0.360 mm microchannel and in five parallel 0.5 mm × 0.5 mm microchannels [108]. For both flow configurations, the channels were bottom-heated. Similar to pool boiling studies of FC72-in-water emulsions [92], the emulsions exhibited decreasing single-phase heat transfer coefficients with increasing volume fraction of FC72. This

effect is observed only for the single microchannel and is not evident in the parallel microchannels data.

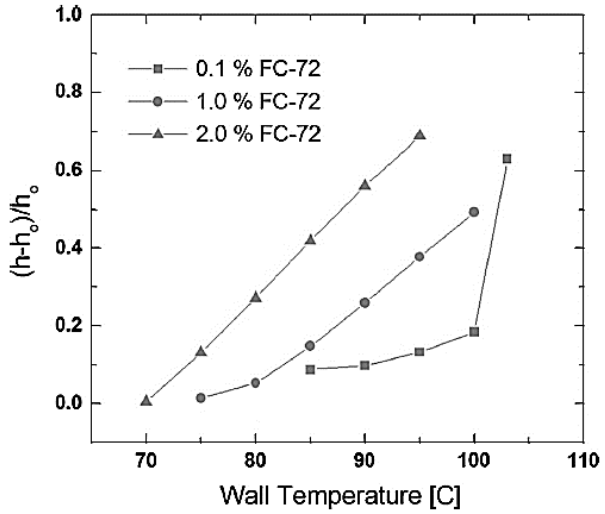

Fig. 2.23. Augmentation of average heat transfer coefficient for the FC72-in-water emulsions relative to water, h_0. T_{sat} = 56 ^oC for FC72 at 1 atm [107]. H = 0.25 mm. Q_{flow} = 0.006 L/min.

The researchers note that due to the design of the single channel, the emulsion comes into contact with one hot surface, whereas it contacts three hot surfaces in each parallel microchannel. They conclude that FC72 accumulates on the bottom of the channel, but this affects heat transfer more significantly in the single microchannel due to the emulsion only contacting one hot surface. In contrast to the flow boiling studies mentioned above, once boiling initiates, they do not measure any enhancement in the heat transfer coefficient. They also measured the axial temperature distribution via the use of five thermocouples and find that the temperature change in the axial direction is not as large as observed in boiling of water.

2.3.5 Mechanisms in pool boiling

Boiling can occur via either homogeneous, spontaneous nucleation in the bulk of a liquid or heterogeneous nucleation at a heated surface or other existing nucleation site.

For spontaneous nucleation of bubbles to occur, the emulsion temperature must be close to the kinetic limit of superheat, which is often hundreds of degrees Celsius above the saturation temperature [109]. Although a high level of superheat has been demonstrated experimentally, the temperatures measured to initiate boiling are much lower than the kinetic limit of superheat so it is unlikely that spontaneous nucleation is occurring in the emulsions. Rather, it is likely that droplets in emulsions are boiling either via contact with a heated surface or via interactions between a superheated droplet and a bubble, or both.

When a superheated droplet contacts a heated surface with available nucleation sites, we can expect that the droplet will boil and it may be reasonable to assume that the mechanisms present are the same as those that govern pool boiling of single component liquids. There are four generally agreed upon mechanisms: thin film evaporation, contact line heat transfer, transient conduction and micro convection [7]. After a bubble nucleates on the surface, a thin film of liquid exists between the edges of the curved bubble and the surface. Evaporation in this thin film and heat transfer at the contact line between the bubble surface and the heated surface contribute much of the heat transfer between the bubble and the surface. As the bubble becomes larger, more of the surface is exposed to vapor in the interior of the bubble, and transient conduction between the vapor phase and the surface becomes gradually more important. Transient conduction to the surrounding liquid is also generally considered to be important during this phase of growth. After the droplet has completely evaporated and the bubble lifts off of the surface, the space once filled by the bubble now gets replenished by the surrounding

liquid and this replenishment process results in micro-convection between the liquid and the surface.

Although these may be the dominant processes taking place between the bubble and the heated surface, it is likely that before the entire droplet evaporates, there is interaction between the growing bubble and the droplet. It may be that the outward movement of the bubble surface causes movement in the droplet, resulting in convection within the droplet. An alternative energy transfer mechanism may be evaporation at the heated surface and at the surface between the bubble and the surrounding liquid. The interaction between the droplet and a bubble growing on a surface has not apparently been investigated thus far.

After a droplet boils, interaction between the bubble and another superheated droplet can cause the droplet to subsequently boil. It is not clear how this interaction takes place, but several mechanisms have been proposed. Bulanov et al. [110] theorize that the droplet boils very rapidly, and the rapid outward movement of the bubble surface produces a shock wave. The droplets exist in a metastable state so that as the shock wave passes surrounding droplets, the pressure of the wave disturbs the superheated droplets and causes them to boil. The amplitude of this wave decreases with distance from the original bubble but is sufficient to start a chain reaction of boiling droplets. Bulanov et al. utilize the theory of point explosions to determine the amplitude of the resulting shock wave.

Roesle and Kulacki [90] contend that thermal diffusion is too slow to produce shock waves. They attribute this chain boiling process to physical contact between a bubble and a droplet. In a dispersed emulsion with droplets of diameter ~ $O(10^{-6}$ m), the

distance between individual droplets may be fairly small. If this distance is less than the diameter of the bubble, the bubble surface will contact every droplet within one bubble diameter of its center. The contact between the bubble and the droplet can disturb the metastable droplet and cause it to boil. If there are many droplets that are contacted by the bubble, a chain reaction of boiling droplets can be started through simple contact.

Regardless of which proposed mechanism causes boiling, the speed with which the droplets boil and interact with surrounding droplets is important in determining the rate of formation of new bubbles. As more bubbles form, either at a surface or in the bulk of the fluid at microscopic nucleation sites, the turbulence of the boiling process will enhance energy transport. Thus, increasing the speed of the chain activation process will increase heat transfer.

The chain activation process is limited by the rate at which individual droplets boil, and this process takes place via two distinct mechanisms that cause a bubble to expand: inertia-driven growth caused by the difference between the pressure inside the bubble and the surrounding fluid, and thermally driven growth caused by heat diffusion coupled with phase change and mass transfer at the vapor/liquid interface [111]. When a single droplet boils, the bubble formation process involves both of these stages, with the initial growth being inertial and the later stages of growth being thermally driven [112]. These two mechanisms would both contribute to the bubble growth rate, thus setting the speed of the chain activation process.

2.3.6 The Roesle-Kulacki pool boiling model

In [90, 97, 99], Roesle and Kulacki describe a model formulation based on the RANS equations. This technique splits every variable in the mass, momentum and energy

conservation equations into the mean value for that variable and fluctuations around the mean. For example, velocity in the x-direction would be represented,

$$u = \bar{u} + u' \tag{2.6}$$

where $\bar{u}$ is the mean velocity and u' is the fluctuation around the mean. The differential equations are averaged, generally using ensemble averaging. Because the average of the fluctuations for each variable is zero by definition, the differential equations are solved for the mean motions. However, this formulation results in terms that will include the average of two fluctuations multiplying each other, e.g., from $\vec{U}_k\vec{U}_k$ in the advection terms, and this average is not necessarily equal to zero. Constitutive equations are therefore required to model these terms. In the momentum equations, these terms are the Reynolds stress, and they are often modeled in a manner similar to viscous stress.

For their numerical model, Roesle and Kulacki consider three phases: the liquid continuous phase, the droplet (liquid disperse) phase and the bubble (vapor disperse) phase. They do not consider the situation where the temperature of the emulsion is high enough to boil the continuous phase. They further assume each phase is an incompressible, Newtonian fluid. Thus, the continuity equation is written,

$$\frac{\partial(\alpha_k)}{\partial t} + \nabla \cdot \left(\alpha_k \vec{U}_k\right) = \frac{\Gamma_k}{\rho_k} \tag{2.7}$$

For the continuous phase, there is no mass production, and $\Gamma_c = 0$. The mass production for the droplet and bubble phase must be equal and have opposite signs. Mass production is positive for the bubble phase when boiling is occurring, so $\Gamma_b = \dot{m}$, and $\Gamma_d = -\dot{m}$.

To determine the mass transfer rate, the various sources of mass production are: boiling by contact with heated surfaces, boiling by bubble-droplet collisions, boiling via

spontaneous nucleation and condensation in subcooled regions of flow. From experiments, it is unclear whether most droplets boil upon contact with or away from the heated surface. However, it is assumed numerically that the surface temperature is sufficiently greater than the saturation temperature of the dispersed component such that if any droplets do contact it, they boil immediately. This is effectively accomplished by setting the boundary condition so that the mass transfer of the droplet phase at the surface is equal to the mass transfer of the bubble phase away from the surface.

If a droplet either boils at the surface and then rises into the free stream or boils away from a surface, it can then interact with other superheated droplets that have not yet boiled, thereby causing nucleation in surrounding droplets. To determine the rate of nucleation and the mass production via this process, Roesle and Kulacki utilize statistical mechanics to determine the nucleation rate and collision efficiency as droplets and bubbles translate toward and slide around each other. This collision efficiency is used to find the mass production rate due to collisions between droplets and bubbles,

$$\dot{m}_{coll} = \alpha_b \alpha_d \rho_d \left|\vec{U}_d - \vec{U}_b\right| \eta_{coll} \bar{\varphi} \frac{3(R_d + R_b)^2}{4R_b^3} \tag{2.8}$$

where η_{coll} is the collision efficiency and $\bar{\varphi}$ is the average number of collisions between droplets and bubbles in a chain reaction of boiling droplets.

Next, they consider spontaneous nucleation of bubbles. They find that the temperature of most emulsions is well below the kinetic limit required for spontaneous nucleation to occur, and they neglect this as a means of mass production. Finally, they consider condensation of bubbles in portions of the emulsions that are subcooled below the saturation temperature of the dispersed component. They account for convection of a

sphere in a quiescent medium and the latent heat of the disperse component to find the mass transfer rate via condensation,

$$\dot{m}_{cond} = \min\left[-3\alpha_b \frac{k_c}{h_{fg} R_b^2}(T_{sat} - T), 0\right] \tag{2.9}$$

The total rate of mass transfer is the sum of these sources.

In the momentum equation, gravity is taken to be the only body force present and the Boussinesq approximation is applied to the body force term. With this approximation, the momentum equation takes the form,

$$\begin{aligned}\frac{\partial(\alpha_k \vec{U}_k)}{\partial t} + \nabla \cdot (\alpha_k \vec{U}_k \vec{U}_k) = \nabla \cdot \left[\frac{\alpha_k}{\rho_k}(\bar{\mu}_k + \mu_{k,T})\left(\nabla \vec{U}_k + \nabla^T \vec{U}_k - \frac{2}{3}\nabla \cdot \vec{U}_k I\right)\right] \\ -\frac{\alpha_k}{\rho_k}\nabla P + \alpha_k \vec{g}\left[1 - \beta_k(T - T_{k,0})\right] + \sum_{j=b,c,d,j\neq k} \frac{\vec{F}_{kj}}{\rho_k}\end{aligned} \tag{2.10}$$

For determining the forces between phases, it is assumed that for dilute emulsions, the droplets and bubbles do not exchange momentum. Therefore, only the forces between the droplets and the continuous phase, $\vec{F}_{dc}$, and the bubbles and the continuous phase, $\vec{F}_{bc}$, are needed. When considering the interphase forces, virtual mass, lift, rotational and Stokes drag forces are considered. However, it is assumed that the virtual mass, lift and rotational forces are negligible, and the interphase forces are modeled as Stokes drag,

$$\vec{F}_{dc} = -\vec{F}_{cd} = -\frac{18\alpha_d \mu_{eff}}{d_d^2}(\vec{U}_d - \vec{U}_c) \tag{2.11}$$

$$\vec{F}_{bc} = -\vec{F}_{cb} = -\frac{18\alpha_b \mu_{eff}}{d_b^2}(\vec{U}_b - \vec{U}_c) \tag{2.12}$$

It can be seen that the momentum equation also contains a term involving the turbulent viscosity, $\mu_{k,T}$. This term is a model for the Reynolds stress that arises due to

the RANS averaging procedure. As the RANS formulation arose to solve turbulent fluid dynamics, an analogy is drawn between the motions of boiling droplets and turbulent eddies to determine the turbulent viscosity. For the continuous phase,

$$\mu_{c,T} = 0.1\dot{m}\frac{\rho_c}{\rho_b}R_b^2 \tag{2.13}$$

Due to the large spacing between individual droplets or bubbles (dilute dispersions), shear stress cannot transmit through turbulent motion, and the turbulent viscosity in the droplet and bubble phases is set equal to zero.

For the energy equation, it is first assumed that the three phases are in thermodynamic equilibrium. With this assumption, the mixture temperature can be obtained without modeling interphase heat transfer. Rather than writing the equation in terms of internal energy, specific heat and Fourier's law of conduction are used to write the mixture energy equation in terms of temperature,

$$\frac{\partial T}{\partial t}\sum_k \alpha_k \rho_k C_{v,k} + \sum_k \alpha_k \rho_k C_{v,k}\,\vec{U}_k \cdot \nabla T = \nabla \cdot \left[\left(k_{eff} + k_T\right)\nabla T\right] - \dot{m}h_{fg} \tag{2.14}$$

The turbulent conductivity, k_T, arises due to the RANS formulation similarly to turbulent viscosity. As is often done in single-component fluids, the Reynolds analogy is utilized to determine this conductivity. Thus, the turbulent conductivity is set equal to the turbulent viscosity.

This model has the drawbacks of being difficult to implement, computationally expensive, and it does involve many simplifying assumptions. However, most importantly, Roesle and Kulacki show that the model matches their experimental results for pool boiling on a thin wire. Thus their model can elucidate the physical mechanisms taking place in boiling of dilute emulsions.

2.3.7 The Bulanov pool boiling model

Rather than solving the differential equations with the difficulties inherent therein, Bulanov [98] develops an analytical solution for pool boiling of a dilute emulsion. The quiescent medium he considered is similar to that shown in Fig. 2.24. In this analysis, the heated wire has a surface temperature greater than the saturation temperature of the disperse component, T_s, which is also greater than the temperature of the surrounding pool, T_∞. As the disperse component droplets enter the thermal boundary layer surrounding the wire, they start to boil, rise through the boundary layer and interact with droplets above the boundary layer that had not previously boiled.

Statistical thermodynamics is used first to determine the number of droplets within the thermal boundary layer that will boil. For a monodisperse emulsion, the probability that a single droplet of diameter d and volume V_d will boil is,

$$p = 1 - \exp\left(-JV_d\tau\right) \tag{2.15}$$

and that the number of droplets, n_b, within the boundary layer that boil is,

$$n_b = Np = N[1 - \exp(-JV_d\tau)] \tag{2.16}$$

In the expressions above, N is the total number of droplets within the thermal boundary layer, J is the bubble nucleation rate, and τ is the time of residence of bubbles in the boundary layer. The number of droplets within the boundary layer can be determined if the disperse component volume fraction, ε, and the volume of the thermal boundary layer are known. Bulanov assumes the boundary layer has a thickness L and surface area A_s. The nucleation rate, time of residence and boundary layer thickness are unknown a priori so Bulanov next attempts to determine the residence time and boundary layer thickness through a force balance and heat transfer modeling.

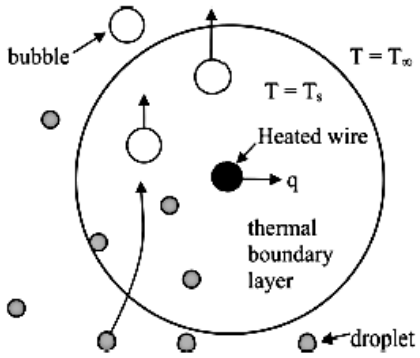

Fig. 2.24. Boiling of disperse emulsion considered by Bulanov [98]. Reprinted from [90].

Bulanov assumes that bubbles within the boundary layer experience two forces: Stokes drag and a buoyancy force due to the difference in density between the emulsion and vapor bubbles of the disperse phase. He further assumes that the bubbles are traveling at a constant speed as they rise through the boundary layer so the speed of the bubbles can be determined by equating these two forces. The average bubble speed is,

$$u = \frac{(\rho_{eff} - \rho_b) g D^2}{18 \mu_{eff}} \tag{2.17}$$

If the boundary layer thickness is defined as $L = u\tau$, Eqn. (2.17) can be used to determine the boundary layer thickness in terms of the residence time,

$$L = \frac{(\rho_{eff} - \rho_b) g d^2 \tau}{18 \mu_{eff} (\rho_b / \rho_d)^{2/3}} \tag{2.18}$$

In Eqn. (2.18), the bubble diameter, D, is replaced by the droplet diameter, d, via conservation of mass.

Next, it is assumed that the droplets enter the thermal boundary layer at their saturation temperature such that the energy required to boil N droplets is given by the latent heat of vaporization,

$$Q = \varepsilon A_s L \rho_d h_{fg} [1 - \exp(-J V_d \tau)] \tag{2.19}$$

The heat flux can then be determined by dividing by the surface area and the residence time. The fitting factor, C, accounts for approximations in the model formulation,

$$q" = C\frac{\varepsilon\rho_d(\rho_{eff}-\rho_b)gd^2h_{fg}}{\mu_{eff}(\rho_b/\rho_d)^{2/3}}[1-\exp(-JV_d\tau)] \tag{2.20}$$

With heat flux in terms of the heat transfer coefficient, Eqn. (2.20) can be rewritten in terms of the non-dimensional Nusselt, Archimedes, Prandtl and Stefan numbers,

$$Nu = C\frac{ArPr}{St}[1-\exp(-JV_d\tau)] \tag{2.21}$$

Bulanov notes that the above formulation is valid only for large values of superheat and very low droplet concentrations. However, the model formulation is modified to show how it can be used when these assumptions are not met. He also provides the probability distribution functions for various droplet diameter distributions so that the model can be used for emulsions that are not monodisperse. He concludes by showing the consistency between his model and experimental results. It is important to note, however, that this consistency is achieved by varying the nucleation rate and fitting parameters for each experiment, not by measuring the nucleation rate for a given experiment and then using it as an input for the model.

Although Bulanov shows that his model can match experimental results, it has been shown that several assumptions in the formulation of it are internally inconsistent [90]. Setting aside this inconsistency, there are two additional deficiencies. Because the model does not hold any ties to the differential equations and involves an *ad hoc* model for the forces and energy required to initiate boiling, it does not have the ability to inform either the physical mechanisms or the dynamics of the boiling process. Therefore, it cannot capture any of the myriad effects that have been demonstrated experimentally. Secondly,

the formulation does not include a way to determine directly the nucleation rate. The nucleation rate is generally a complex function of the thermodynamic conditions as well as surface properties and geometry of the system of interest, and predicting the nucleation rate a priori to input it into the model remains a significant challenge. Nevertheless, Bulanov's theory of the nucleation and chain boiling processes represents an important step forward.

2.3.8 The Rozenstvaig-Strashinskii flow boiling model

Rozentsvaig and Strashinskii [113] also developed a model to describe boiling of emulsions. However, unlike the previous models discussed, this model is for flow boiling of emulsions and only determines the temperature at which bubbles will start to nucleate. Rozenstvaig and Strashinskii consider turbulent flow of a monodisperse emulsion. They assume that portions of the droplet surface are deformed slightly, causing a local decrease of the capillary pressure there with respect to the rest of the droplet. This decrease in the capillary pressure decreases the superheat temperature required to cause nucleation. To develop their model, they consider two deformation mechanisms.

First, for droplets whose diameter is greater than the turbulent Kolmogorov length scale, η, Rozenstvaig and Strashinskii assume that the turbulent kinetic energy of vortices of size η is able to deform the droplet surface. Thus, it is required that the tubulent kinetic energy of a vortex of size η be greater than the work of formation of a bubble whose size is large enough to grow, D_{cr},

$$m_c(u')^2 \geq \sigma D_{cr}^2 \tag{2.22}$$

It is assumed that the minimum droplet size that can undergo nucleation via this mechanism is equivalent to the Kolmogorov length scale. Hence, Rozentsvaig and Strashinskii formulate the mass of the vortex in the continuous component, m_c, in terms of this minimum diameter,

$$\rho_c (u')^2 d_{min}^3 \geq \sigma D_{cr}^2 \tag{2.23}$$

Next, Rozenstvaig and Strashinskii relate the total turbulent kinetic energy to the energy dissipated by vortices of this size,

$$(u')^2 \approx (\varepsilon_{diss} d_{min})^{2/3} \tag{2.24}$$

To determine the turbulent kinetic energy dissipated, they consider turbulent flow in a pipe of diameter D_h and equate the dissipation and the wall shear stress,

$$\frac{\pi D_h^2 l \rho_c \varepsilon_{diss}}{4} = \tau_w \pi D_h l U \tag{2.25}$$

It is noted that the wall shear stress is related to the friction factor, which is given by the Blasius equation for turbulent flow in a round pipe,

$$f = \frac{0.3164}{Re^{0.25}} = 0.3164 \left(\frac{\mu_c}{U D_h \rho_c} \right)^{0.25} \tag{2.26}$$

With the use of Eqn. (2.26), Eqn. (2.25) can be rearranged to obtain an equation for the dissipation,

$$\varepsilon_{diss} = \frac{0.158 \mu_c^{0.25} U^{2.75}}{D_h^{1.25} \rho_c^{0.25}} \tag{2.27}$$

Having obtained an equation for the turbulent kinetic energy dissipated, Rozenstvaig and Strashinskii insert Eqn. (2.27) into Eqn. (2.23) and assume equality to determine the minimum diameter of droplets that would boil via this mechanism,

$$d_{min} = C \Delta W_{cr}^{0.27} \mu_c^{-0.05} \tag{2.28}$$

Note that ΔW_{cr} is used to generalize the work of formation term in Eqn. (2.23). They state that, for a metastable droplet, the work of formation is given by

$$\Delta W_{cr} = \frac{16\pi^3\sigma^3}{3(P_{sat} - P_f)^2(1 - \rho_g/\rho_f)^2} \tag{2.29}$$

Finally, they assume that the surface tension is linearly related to temperature, the viscosity is exponentially dependent on temperature, and the saturation pressure varies as

$$P_{sat} = C \exp\left(-\frac{C_1}{T + C_2}\right) \tag{2.30}$$

Thus, they obtain an expression for the minimum droplet size that will boil via the "resonance" mechanism as a function of the temperature of the emulsion,

$$d_{min} = C \frac{(C_4 - C_5 T)^{0.81}}{\left[\exp\left(-\frac{C_1}{T+C_2}\right) - P_f\right]^{0.54}} \exp\left(-\frac{0.05 C_0}{T}\right) \tag{2.31}$$

For droplets whose diameter is smaller than the Kolmogorov length scale, Rozenstvaig and Strashinskii note that at that scale, the dynamics are largely governed by the viscous shear stress associated with the turbulent fluctuations. Thus, they assume that the shear stress is able to deform the droplet surface and the energy associated with that shear stress must be larger than the work of formation of a critically-sized bubble radius,

$$\mu_c \frac{\partial u'}{\partial r} d_{min}^3 \geq \sigma d_{cr}^2 \tag{2.32}$$

For isotropic turbulence, the derivative of the turbulent fluctuations is related to the turbulent kinetic energy dissipated,

$$\frac{\partial u'}{\partial r} = \sqrt{\frac{2\varepsilon_{diss}\rho_c}{15\mu_c}} \tag{2.33}$$

Equation (2.32) can be rearranged to solve for d_{min}. With the use of Eqns. (2.27) and (2.33),

$$d_{min} = C\Delta W_{cr}^{0.33}\mu_c^{-0.21} \tag{2.34}$$

Finally, substituting the expression for the work of formation given by Eqn. (2.29) and utilizing the same assumptions regarding the surface tension, viscosity and saturation pressure, the minimum diameter that will boil via the "gradient" mechanism is

$$d_{min} = C\frac{A_1 - A_2T}{\left[\exp\left(-\frac{B_1}{T+B_2}\right) - P_f\right]^{0.66}}\exp\left(-\frac{0.21B_0}{T}\right) \tag{2.35}$$

After the model development, Rozenstvaig and Strashinskii compare the model results to experimental results from [114] for water in PES-5 emulsions with droplet diameters of 1.5 and 35 μm. It is shown that the resonance model provides good consistency with the temperature at the onset of nucleate boiling for droplets with d = 35 μm and the gradient regime model predicts well the temperature for droplets with d = 1.5 μm. Although the model shows good consistency with these experimental results, the model does have a few flaws.

First, the experimental results that are referenced are for pool boiling of emulsions. As such, there would be no turbulence present to nucleate bubbles via these turbulent flow mechanisms prior to the initiation of boiling. After the onset of nucleate boiling, Rozenstvaig and Strashinskii do state that for a laminar flow, the boiling process can cause local turbulence that would further nucleate bubbles via these mechanisms. However, these mechanisms rely on the use of the Kolmogorov length scale based on the large-scale flow behavior and the Reynolds number based on the pipe scales (see Eqns. (2.26) and (2.27)). If the turbulence is due solely to boiling of droplets, it is not clear that the turbulent kinetic energy and dissipation should scale with the pipe scales.

As well, because the model only focuses on the effect of the droplet diameter, these mechanisms do not explain how the volume fraction, subcooling, disperse phase properties, etc. affect the nucleation characteristics. However, the most significant flaw of the model is an inconsistency in the model formulation itself. In both the resonant and gradient regimes, the mechanisms rely on a determination of the turbulent kinetic energy dissipation. To determine the dissipation, Rozenstvaig and Strashinskii equate the dissipation and the wall shear stress. However, these are two completely distinct mechanisms for the diffusion of energy. The dissipation describes the amount of energy diffused at the molecular scale due to the transport of energy from large vortices to small vortices in the turbulent regions of the boundary layer (the turbulent core). The wall shear stress describes the amount of momentum and energy diffused in the near-wall region of the boundary layer (the viscous sublayer) due to viscosity and the presence of the wall. Equating these two mechanisms, therefore, represents a fundamental inconsistency in this model.

3. Apparatus and Procedure

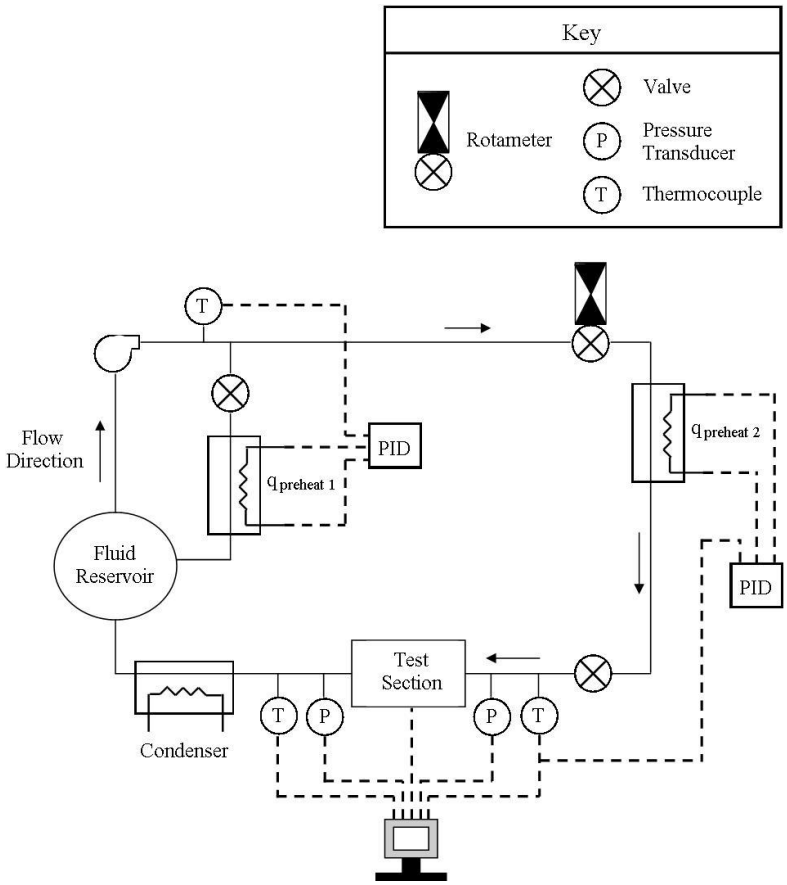

Fig. 3.1. Experimental flow loop.

The flow loop used in this investigation is shown in Fig. 3.1. It includes a recirculation loop with a heater to control the temperature of the fluid in the fluid reservoir. A second heater is included just before the entrance to the test section to account for any heat losses to the surroundings while the fluid flows from the reservoir to the test section. The inlet fluid temperature for a given experimental run is thus set using these two heaters, which are controlled with proportional integral derivative (PID) controllers.

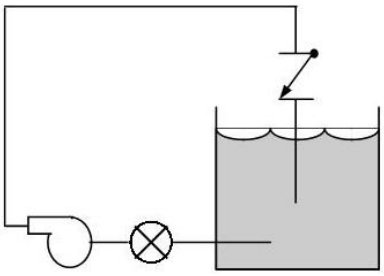

Fig. 3.2**.** Emulsion preparation loop.

The emulsions in this investigation consist of suspended droplets of FC-72[1] in water. Prior to each experimental run, the water is degassed by boiling for 30 min to remove any dissolved gases that may be present. Then, it is cooled to 30 °C and the FC-72 is added. The emulsion is prepared by pumping the FC-72/water mixture through the flow loop shown in Fig. 3.2. As the mixture flows through the check valve, the valve breaks the FC-72 up into small suspended droplets. The mixture flows through this preparation loop for five minutes before being transferred to the fluid reservoir shown in Fig. 3.1. Once the emulsion is created, the droplet diameter is independent of the length of time the emulsion is processed in the loop [97]. The distribution of measured droplet diameters is shown in Fig. 3.3. The distribution has a mean and standard deviation of 10.7 μm and 4.4 μm, respectively, and skewness of 1.5.

When the emulsion is transferred to the fluid reservoir, the reservoir temperature is set to 30 °C. After the fluid reservoir reaches the correct temperature for an experimental run, the valve for the recirculation loop is closed and the fluid flows through a rotameter.

[1]FC-72 is a thermally and chemically stable, dielectric Flourinert™ Electronic Liquid produced by 3M™ and intended to be used for leak detection and cooling of electronic equipment. At 1 atm and 25 °C, FC-72 has the properties $\rho = 1680$ kg/m^3, $\mu = 64\times10^{-5}$ Ns/m^2, $C_P = 1100$ J/kg°C, and $k = 0.057$ W/m°C. FC-72 also has a low saturation temperature (56 °C at 1 atm). A more thorough list of FC-72 properties and their variation with temperature is given in Appendix A.

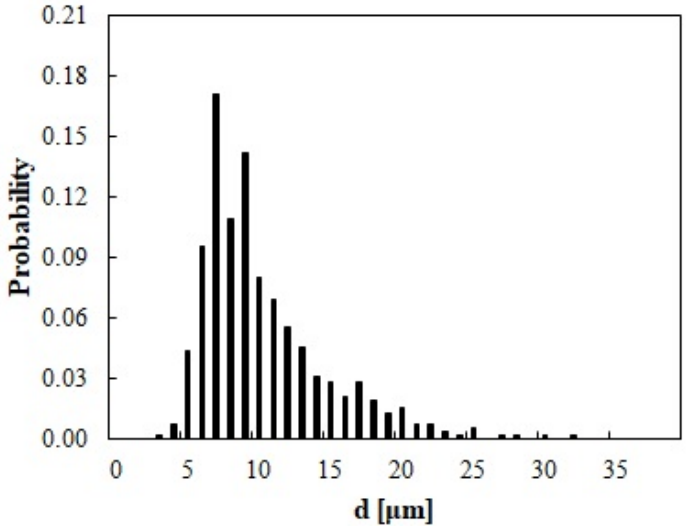

Fig. 3.3. Measured distribution of emulsion droplet diameters.

The rotameter is used to roughly set the flowrate and the actual flowrate for each experimental run is determined by collecting a volume of fluid and measuring the amount of time required for that volume of fluid to collect. After leaving the rotameter, the fluid flows through a valve to increase the pressure drop upstream of the test section and decrease the pressure fluctuations due to boiling.

The test section includes a long entry length upstream of the heated portion of the test section designed to achieve fully developed laminar flow prior to the flow entering the heated section. In this study, the mass flux is limited to less than 550 kg/m^{2}s and the largest gap hydraulic diameter is 1000 μm (Table 3.1). This combination of mass flux and hydraulic diameter are chosen to assure that laminar flow is present for all experimental trials.

Table 3.1. Quantities for parameters.

Parameter	Quantities Studied
D_H (μm)	200, 500, 1000
G (kg/m^2-s)	150, 350, 550
ε (%)	0, 0.1, 0.5, 1, 2
Surfaces	1 smooth, 3 porous

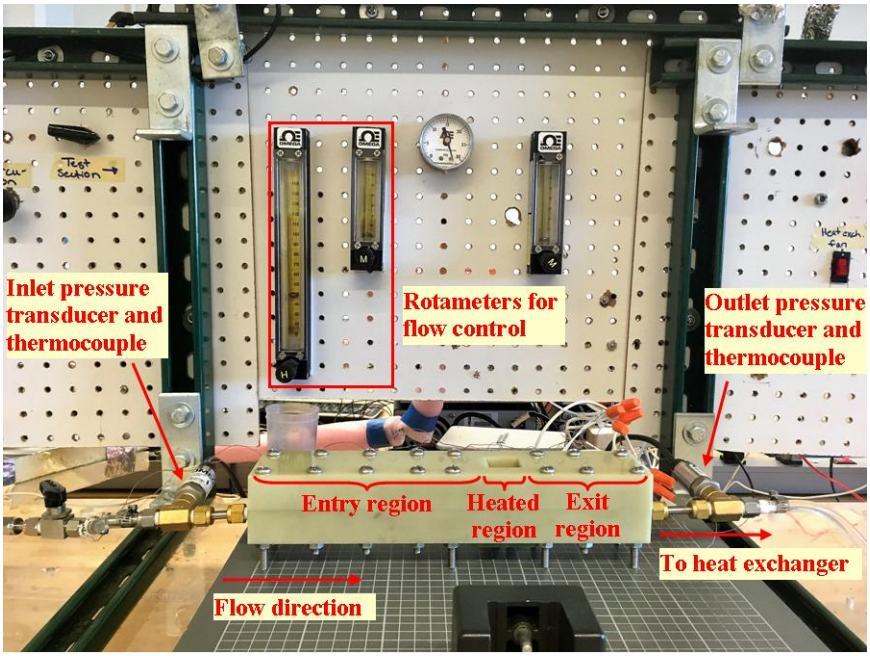

Fig. 3.4. Test section.

The test section also has a long exit region downstream of the heated portion. It has been shown experimentally that the design of the inlet and outlet manifolds affects the heat transfer performance in two-phase flow [38]. Thus, the length of the exit region is set to minimize the impact of the exit manifold design in this study. The test section is shown in Fig. 3.4.

A constant heat flux boundary condition is applied in the heated portion of the test section via the use of four Al-Ni heaters. The heaters are placed inside a Garolite™ G-10[2] box to limit the amount of heat lost to the surroundings. The four heaters are in contact with a copper substrate through a thermal grease and the top surface of the copper plate is exposed to the flowing fluid in the microgap. The copper plate has nine holes drilled to within 0.5 mm of the top surface and E-type thermocouples are placed in these holes to measure the surface temperature.

[2] Garolite™ G-10 has the properties $\rho = 1800$ kg/m^3, $k = 0.288$ W/mK and in-plane and out-of-plane coefficient of thermal expansion of 9.9×10^{-6} /°C and 11.9×10^{-6} /°C, respectively.

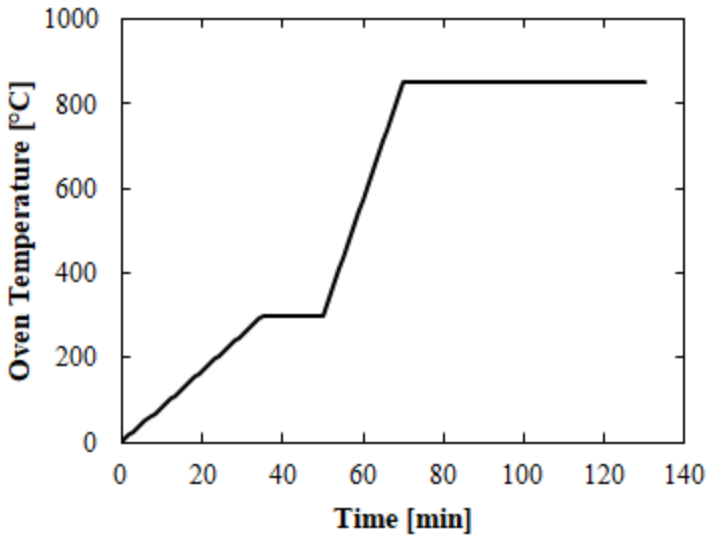

Fig. 3.5. Temperature profile used in the oven brazing cycle.

The copper substrate used in the smooth plate experiments was sanded up to 2000 grit sandpaper. For the microporous experiments, the porous surfaces are applied to the copper substrate via an oven brazing process. Detailed drawings of all test section components are included in Appendix B.

To create the microporous surfaces, a mixture of 3M L-20227 copper powder, polypropylene carbonate, propylene carbonate and methyl ethyl ketone (MEK) are sprayed onto the copper substrate. The copper powder, MEK, polypropylene carbonate and propylene carbonate are combined in proportions of 202.1:86.5:6.7:1 by weight, respectively. The MEK evaporates at atmospheric pressure and is used to decrease the viscosity of the mixture for spraying. The polypropylene carbonate and propylene carbonate strengthen the bond between the copper powder and the copper substrate and combine with oxygen during the oven brazing process to form H_2O and CO_2, leaving only the copper powder on the substrate.

Prior to the brazing process, the mixture is sprayed onto the substrate using an Iwata CM-B airbrush at a pressure of 40 psig. Next, the substrates are left at atmospheric

conditions overnight to allow the MEK to evaporate. The substrates are then brazed in a vacuum oven held at a pressure of 0.01 mTorr and reaching a maximum temperature of 850 °C. The temperature-time profile of the brazing process is shown in Fig. 3.5 and SEM images of each brazed surface are shown in Figs. 3.6 - 3.8.

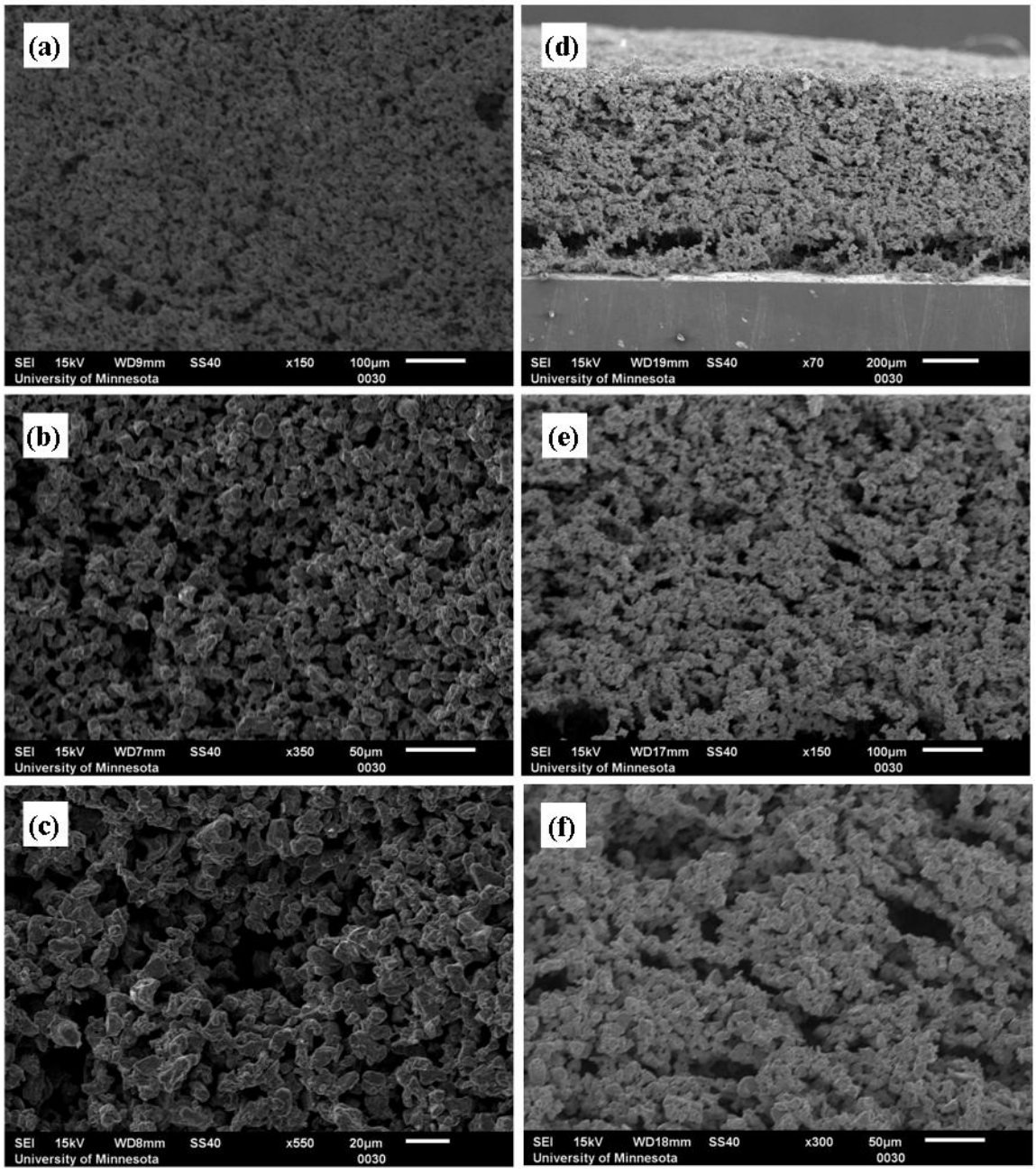

Fig. 3.6. SEM images for porous surface 1. (a) - (c) are images from the top with magnification of ×150, ×350 and ×550, respectively. (d) - (f) are images from the side with magnification of ×70, ×150 and ×300, respectively.

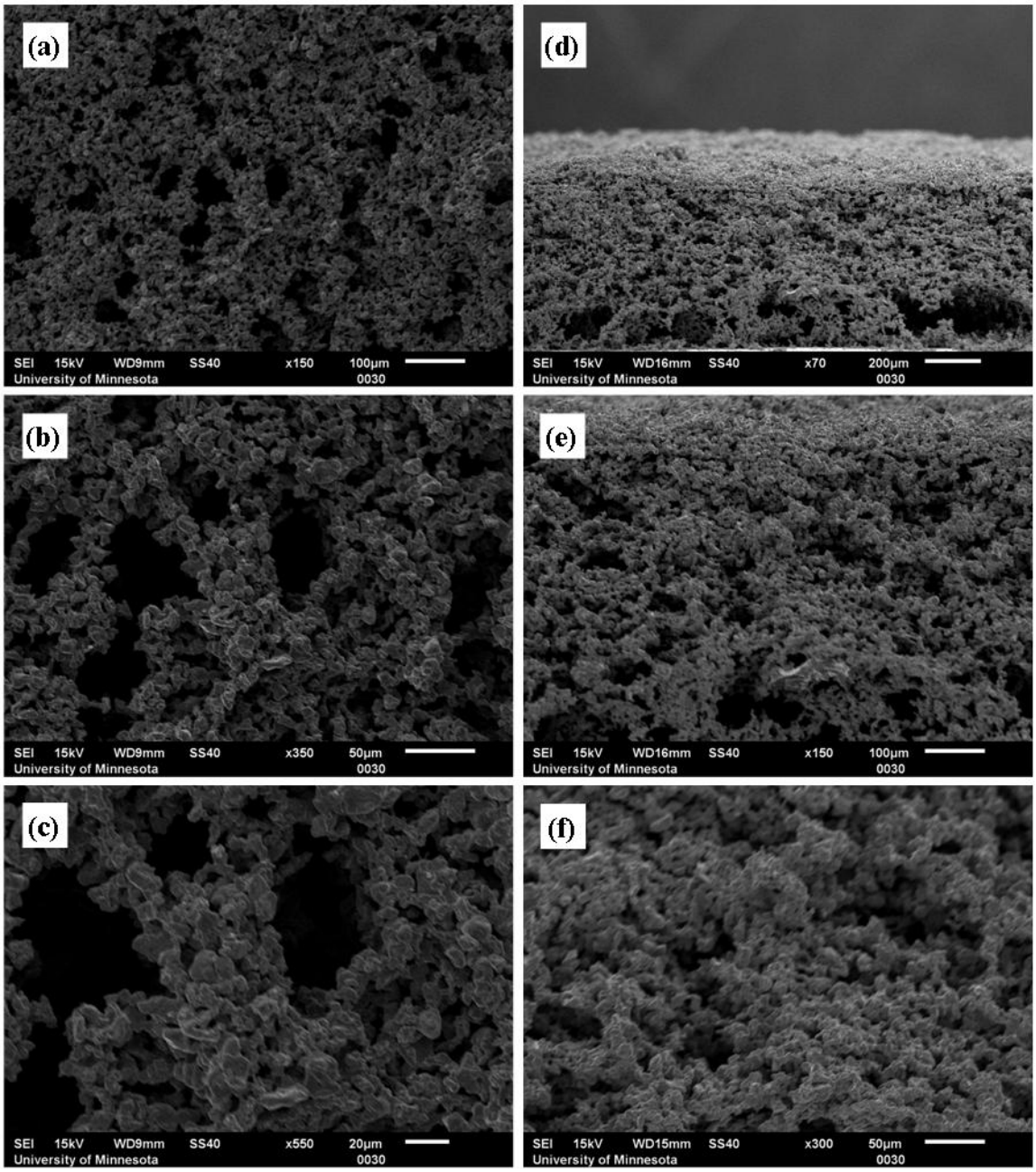

Fig. 3.7. SEM images for porous surface 2. (a) - (c) are images from the top with magnification of ×150, ×350 and ×550, respectively. (d) - (f) are images from the side with magnification of ×70, ×150 and ×300, respectively.

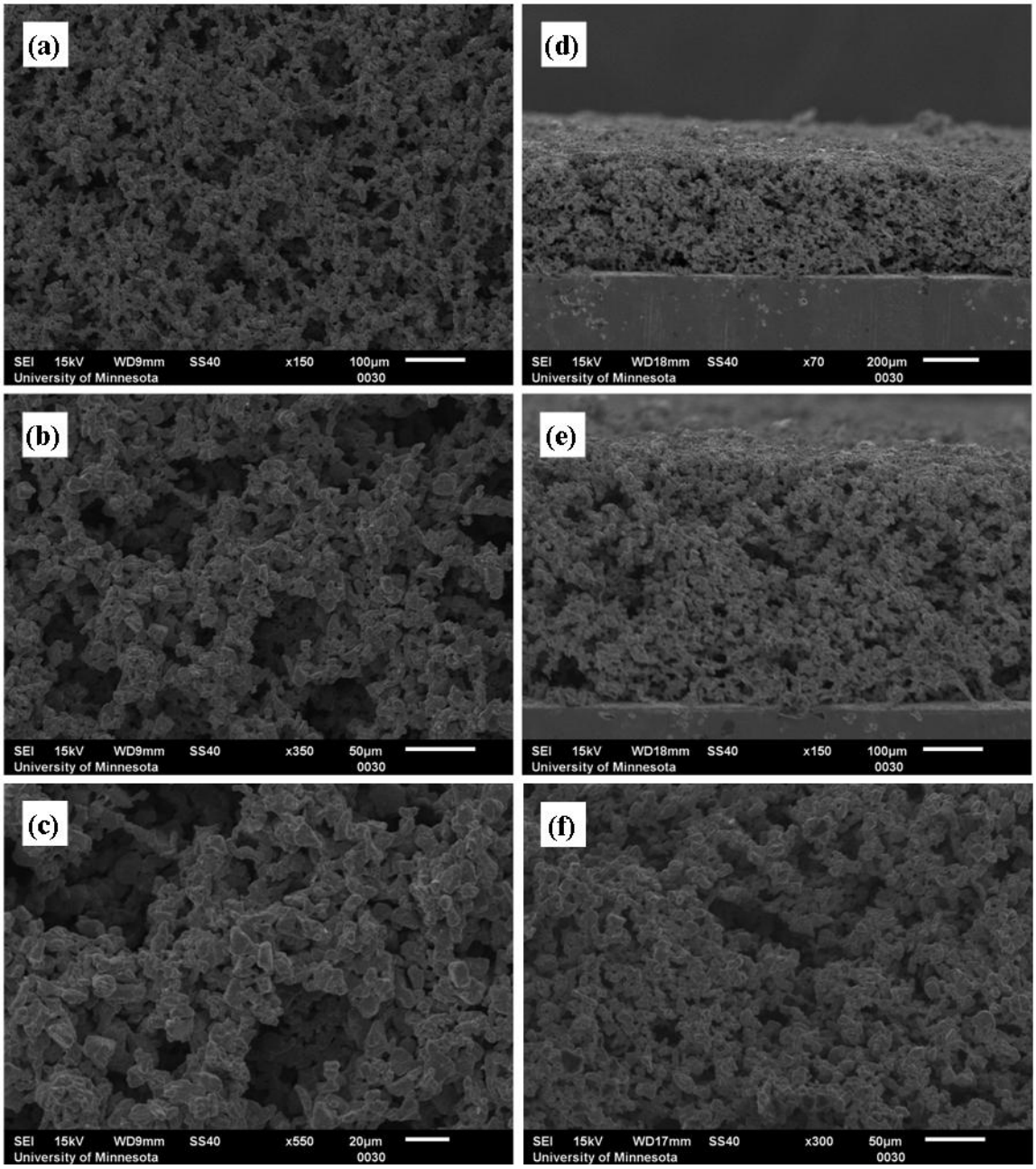

Fig. 3.8. SEM images for porous surface 3. (a) - (c) are images from the top with magnification of ×150, ×350 and ×550, respectively. (d) - (f) are images from the side with magnification of ×70, ×150 and ×300, respectively.

Table 3.2. Porous surface characteristics.

	Surface Area	Volume of Coating Mix	Mass of Copper Powder	Surface Porosity	Coating Depth
Surface 1	0.992×0.961 in^2	1.1 mL	1.308 g	0.354	708 μm
Surface 2	0.989×0.993 in^2	0.75 mL	0.844 g	0.410	633 μm
Surface 3	0.983×0.997 in^2	0.4 mL	0.611 g	0.413	412 μm

The amount of copper powder applied to each surface and various surface characteristics are included in Table 3.2. The porosity is measured by converting the SEM images to black and white images using MATLAB, where the black pixels represent voids and the white pixels represent solid material. Thus, the porosity is simply equal to the number of black pixels divided by the total number of pixels in a given image. This does require the assumption that the porosity is uniform normal to the image plane so the porosity can be calculated using void and solid area rather than volume. This technique was previously applied to measure the porosity of frost layers in frost growth and melting studies [115, 116].

In the conversion process, the software calculates a greyscale threshold to determine which grey pixels should be converted to black or white. At times, this threshold may result in solid areas from the SEM images being converted to black void pixels. Two examples of this are shown in Fig. 3.9 by the red circles demonstrating two areas where solid material can clearly be seen in the pore in the SEM image but whose greyscale value is determined to be void by the computer algorithm. In these examples, it can be argued that the areas in question should be counted as void because the solid material is behind the plane in view- and the porosity here is a planar measurement. However, if the user determines that a specific area has been counted as void and should be solid- or vice

versa- the user can vary the threshold value and compare the original and converted images until the conversion is suitable.

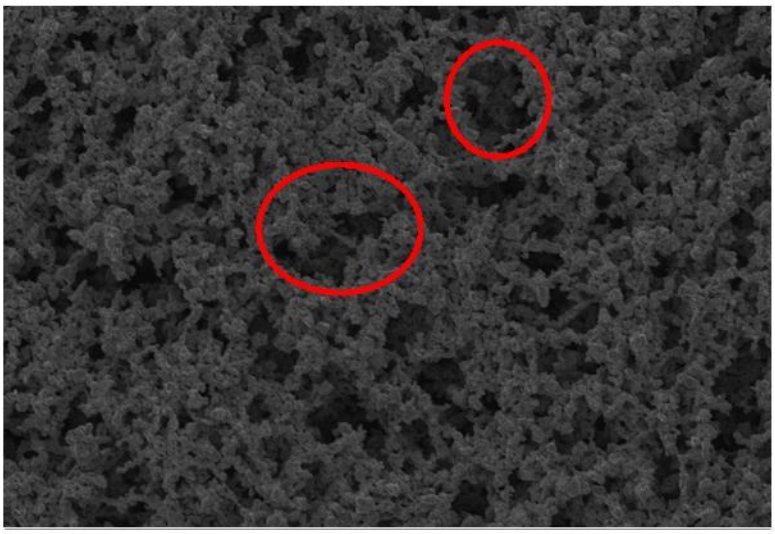

(a)

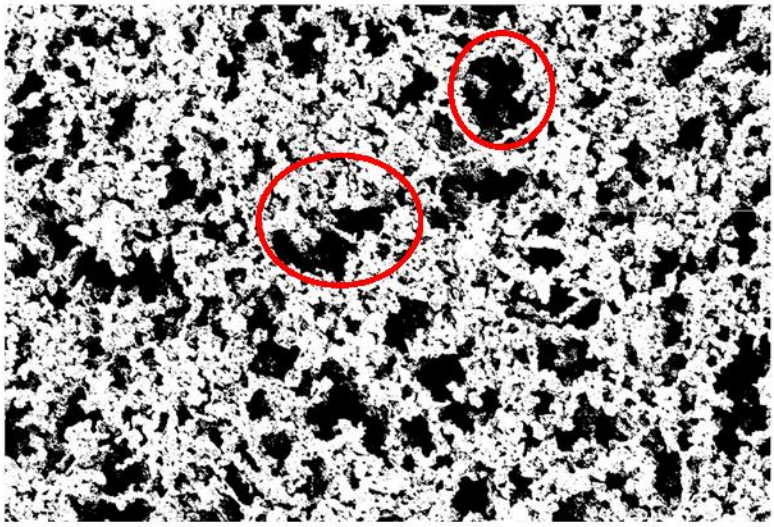

(b)

Fig. 3.9. Conversion of the Surface 3 top view SEM image into black and white. The red circles denote areas where the solid is determined to be void by the computer algorithm. (a) Original SEM image, (b) Converted black and white image.

To measure the porosity, the SEM images were split into 25 segments, converted to black and white, and the porosity for each segment was calculated. The converted images and porosity distribution for each image are shown in Figs. 3.10 - 3.12.

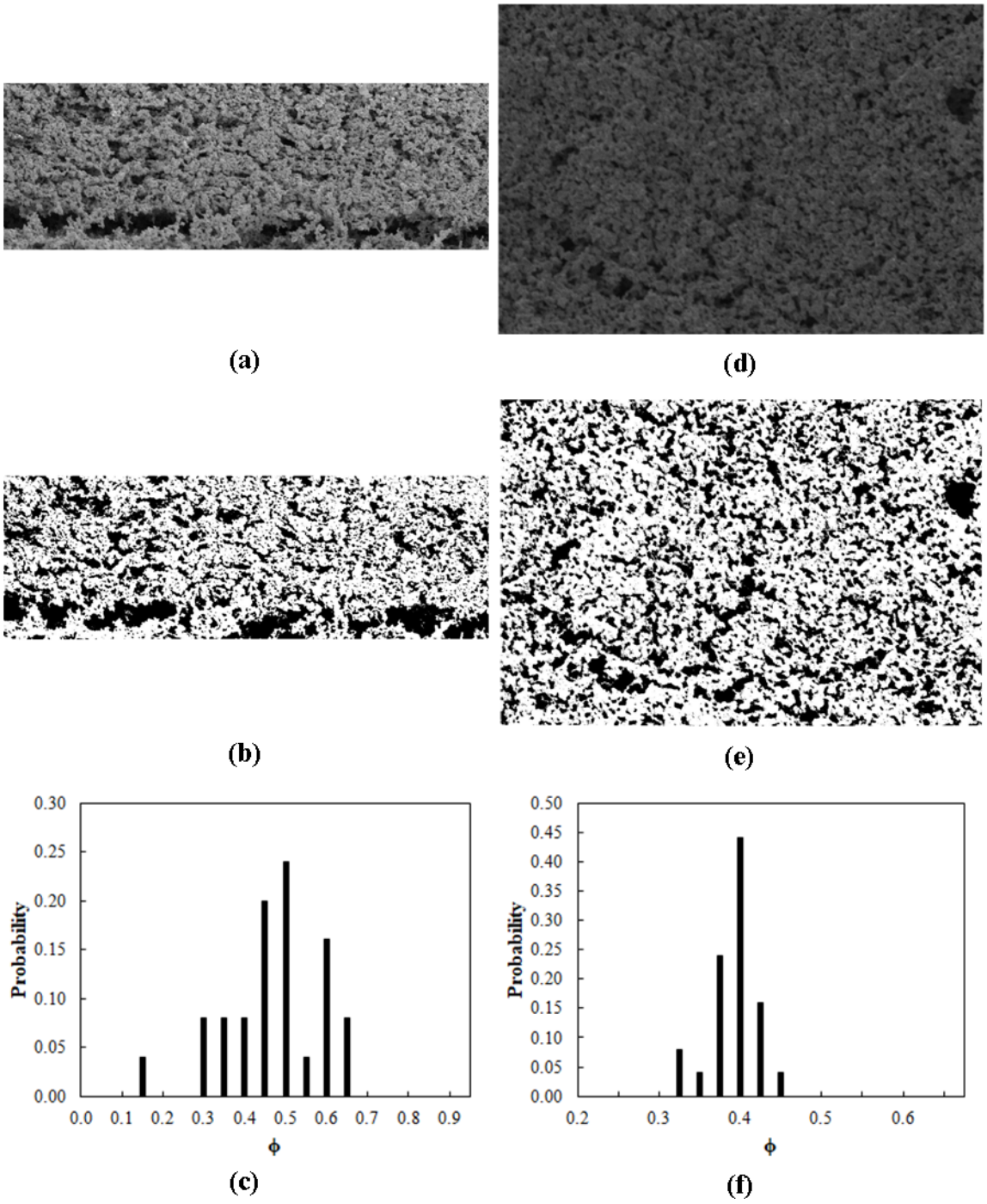

Fig. 3.10. Porosity measurement for Porous Surface 1. (a) - (c) are the original SEM image, converted black and white image and porosity distribution, respectively, for the side image at ×70 magnification. (d) - (f) are the original SEM image, converted black and white image and porosity distribution, respectively, for the top image at ×150 magnification.

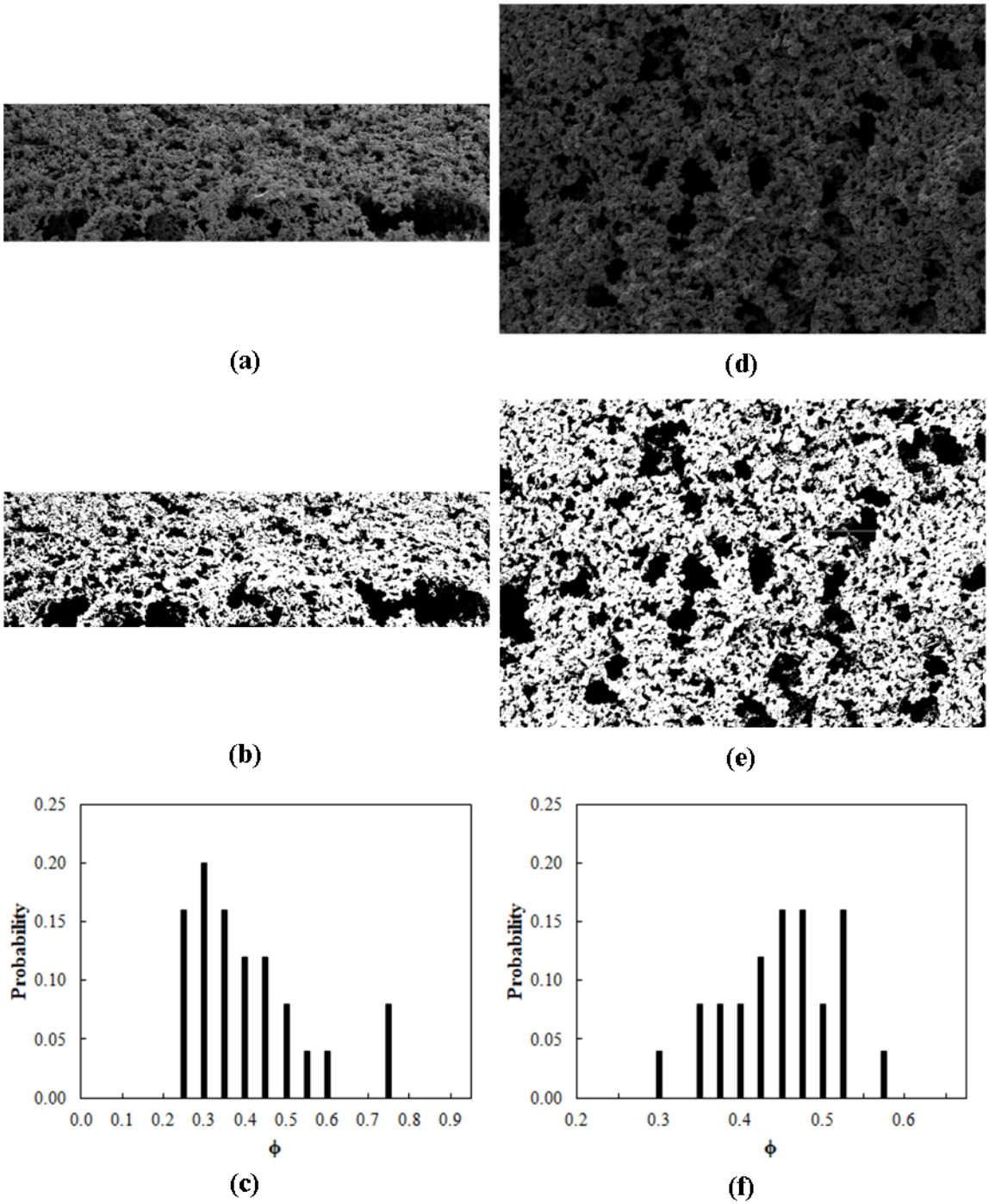

Fig. 3.11. Porosity measurement for Porous Surface 2. (a) - (c) are the original SEM image, converted black and white image and porosity distribution, respectively, for the side image at ×70 magnification. (d) - (f) are the original SEM image, converted black and white image and porosity distribution, respectively, for the top image at ×150 magnification.

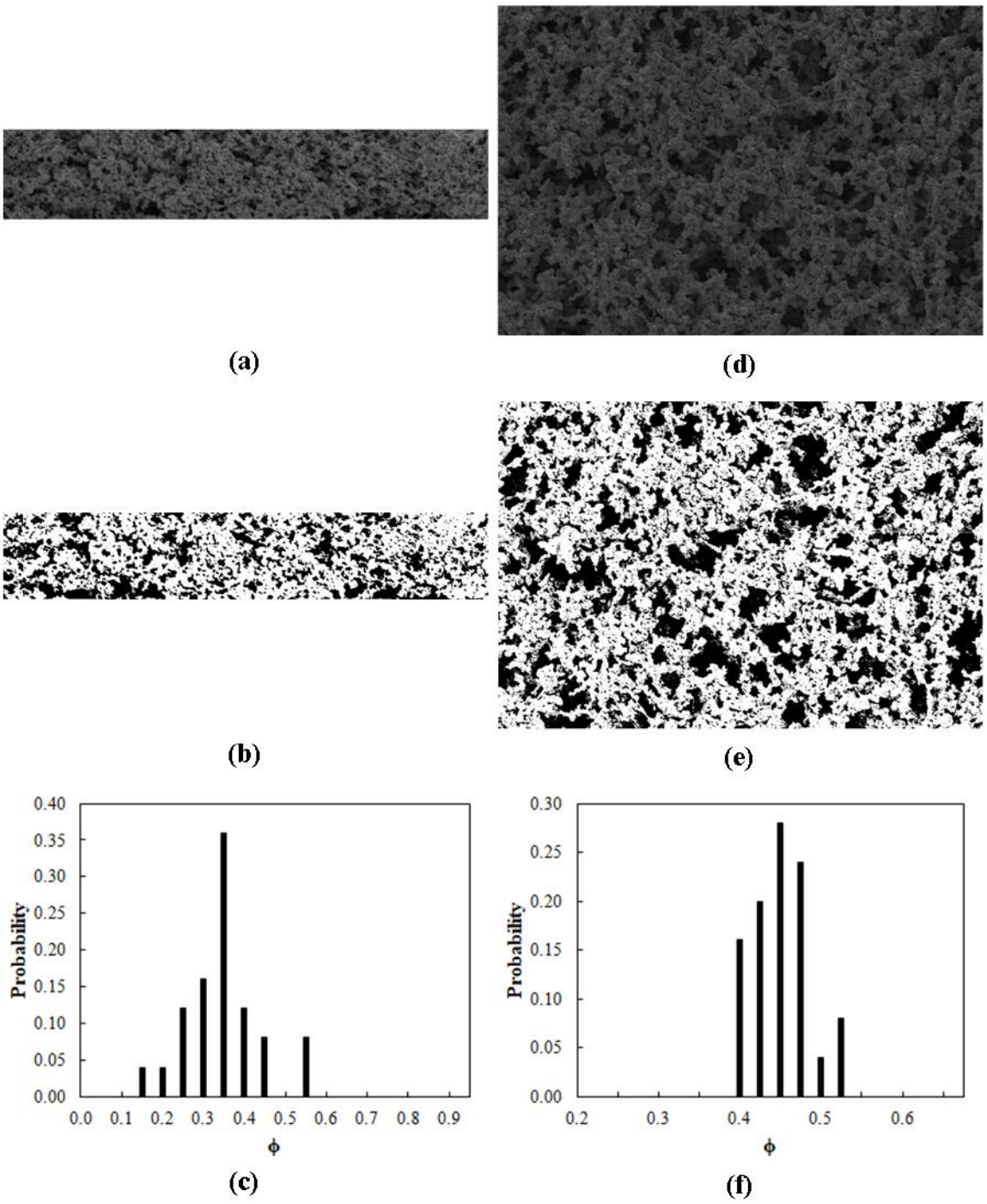

Fig. 3.12. Porosity measurement for Porous Surface 3. (a) - (c) are the original SEM image, converted black and white image and porosity distribution, respectively, for the side image at ×70 magnification. (d) - (f) are the original SEM image, converted black and white image and porosity distribution, respectively, for the top image at ×150 magnification.

It can be seen that the porosity distribution and average porosity for each surface are slightly different for the top and side views. The average porosity measured from the top view of each surface is that reported in Table 3.2.

The temperature and pressure of the flowing fluid are measured upstream and downstream of the test section. The temperature is measured using E-type thermocouples and the pressure is measured with PX-309 Omega pressure transducers. After the temperature and pressure measurements are taken downstream of the test section, the fluid flows through a heat exchanger to condense the vapor before returning to the inlet reservoir.

All temperature and pressure measurements are collected with a National Instruments (NI) USB-9171 data acquisition device (DAQ) and an NI USB-6000 DAQ, respectively, in conjunction with a LabVIEW program. Once the copper surface temperature reaches steady state, measurements are recorded for five seconds at a sampling frequency of 50 Hz. The program then calculates the mean temperature and pressure at each measurement location from the respective 250 individual measurements. The program also acquires heater power, surface area and heat loss as inputs by the user and calculates the net applied heat flux and heat transfer coefficient. The heat transfer coefficient is,

$$h = \frac{q''_{net}}{T_w - T_f} \tag{3.1}$$

where the wall temperature is taken to be the mean of the nine wall temperature measurements and the fluid temperature is the mean of the inlet and outlet fluid temperature. The uncertainty for measured and calculated items are given in Table 3.3.

For quantities that include multiple uncertainty sources, the total uncertainty is determined by the square root of the sum of the squares. For variables whose uncertainty

is calculated as a function of other variables, the partial derivatives are used. For example, the uncertainty in h is,

$$\delta h = \sqrt{\left(\frac{\partial h}{\partial q"_{net}}\delta q"_{net}\right)^2 + \left(\frac{\partial h}{\partial T_w}\delta T_w\right)^2 + \left(\frac{\partial h}{\partial T_f}\delta T_f\right)^2} \tag{3.2}$$

For uncertainties given as a range, the uncertainty decreases as the quantity increases. The heat flux is determined by multiplying the voltage and current output from the power supply and dividing by the surface area. The area for each surface is measured using a micrometer whose uncertainty is negligible compared to that of the voltage and current. Thus, the uncertainty in applied heat flux only contains these two sources.

Table 3.3. Uncertainty estimates.

Parameter	Uncertainty
$V_{applied}$	±1.5%
H	±13 μm
I	±1.5%
P	±1.0%
Q	±3-5%
T	±1.0 °C
G	±2-5%
h	±3-14%
q"	±2.1%
ε	±3-6% of measurement

4. Results

To increase confidence in the experimental results, it is necessary to quantify the uncertainty associated with each measured parameter (Table 3.3) and the heat losses to the surroundings and demonstrate that the experimental apparatus produces results that are expected and repeatable. Because the apparatus is designed to provide hydrodynamically fully developed laminar flow at the entrance to the heated region, an analytical expression for the liquid temperature in the heated region can be obtained. This expression can be compared to single-phase water experimental data to demonstrate that the apparatus is functioning as expected and to quantify heat losses.

For laminar, steady, incompressible, hydrodynamically fully developed flow of a Newtonian fluid being heated by one constant heat flux wall, the Navier-Stokes and energy equations can be solved to find that the fluid temperature is,

$$T(x,y) = T_i + \frac{2Hq_w^{"}}{k_f}\left[\frac{3}{32}\left(\frac{2y}{H}\right)^2 - \frac{1}{64}\left(\frac{2y}{H}\right)^4 - \frac{1}{8}\left(\frac{2y}{H}\right) - \frac{39}{2240} + \frac{x}{HRe_{D_h}Pr} + \sum_{n=1}^{\infty} C_n Y_n(y)\exp\left(-\frac{32}{6HRe_{D_h}Pr}\lambda_n^2 x\right)\right] \tag{4.1}$$

If the heat transfer coefficient is defined using Eqn. (3.1), the Nusselt number is,

$$Nu(x) = \left[\frac{26}{140} + \sum_{n=1}^{\infty} C_n Y_n\left(-\frac{H}{2}\right)\exp\left(-\frac{32}{6HRe_{D_h}Pr}\lambda_n^2 x\right)\right]^{-1} \tag{4.2}$$

$$\overline{Nu(x)} = \frac{1}{x}\int_0^x Nu(x')dx' \tag{4.3}$$

In Eqns. (4.1) - (4.3), each function Y_n is represented by a power series,

$$Y_n(y^*) = \sum_{m=0}^{\infty} a_m {y^*}^m \tag{4.4}$$

$$y^* = \frac{2y}{H} \tag{4.5}$$

whose coefficients a_m follow the recursive relation,

$$a_0 = 1 \quad a_2 = -a_0\frac{\lambda_n^2}{2} \quad a_3 = -a_1\frac{\lambda_n^2}{6} \quad a_m = \frac{\lambda_n^2}{m(m-1)}(a_{m-4} - a_{m-2}) \tag{4.6}$$

The constants C_n are given by,

$$C_n = \frac{\int_{-1}^{1} Y_n(y^*) * \left[-\frac{3}{32}y^{*2} + \frac{1}{64}y^{*4} + \frac{1}{8}y^* + \frac{39}{2240}\right] dy^*}{\int_{-1}^{1} Y_n^2(y^*) dy^*} \tag{4.7}$$

The first seven values of λ_n, a_1, C_n and the value of the eigenfunctions at the heated wall are shown in Table 4.1. The full solution procedure is given in Appendix C.

Table 4.1. Eigenvalues and constants evaluated from the power series solutions.

n	λ_n	a_1	C_n	$Y_n(-1)$
1	4.2872	2.3715	0.0687	-0.9052
2	8.3037	9.9307	-0.0301	0.4919
3	12.3106	11.2041	0.0304	-0.7426
4	16.3145	12.0152	-0.0299	0.9207
5	20.3171	12.5437	0.0291	-1.0578
6	24.3190	12.8984	-0.0281	1.1681
7	28.3232	13.1439	0.0272	-1.2529

The mean wall temperature obtained from Eqn. (4.1) is compared in Fig. 4.1a with liquid water experimental data. The analytical expression and the experimental results follow the same trend but there is an offset between the experimental data and the analytical equation. This offset represents the heat lost to the surroundings. If these losses are subtracted, the analytical temperature equation and the experimentally measured wall temperature are in accord (Fig. 4.1b).

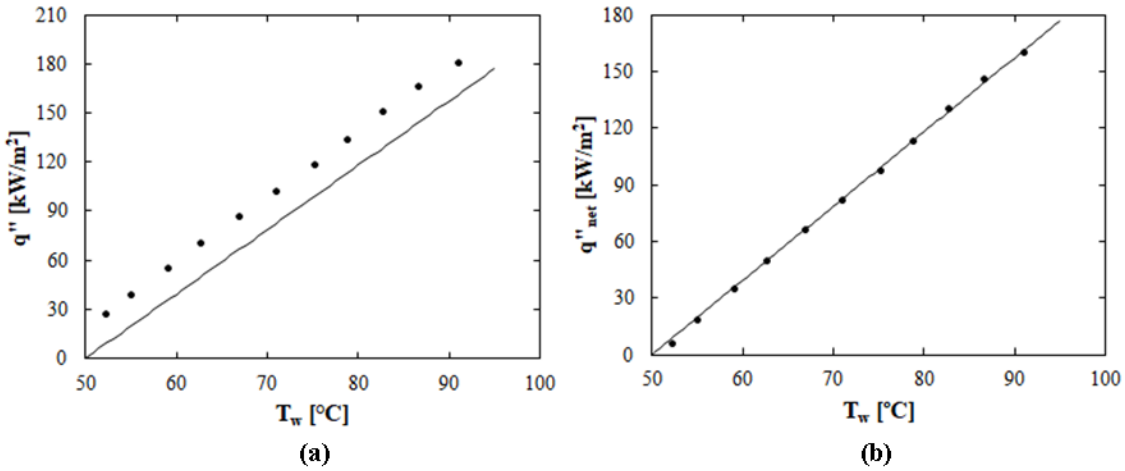

Fig. 4.1. Comparison between the mean wall temperature from the analytical temperature expression (line), Eqn. (4.1), and single-phase experimental results (circles). D_h = 1000 µm, G = 262 kg/m^{2}s, T_i = 51 °C. (a) Without accounting for heat losses. (b) Accounting for heat losses in experimental results.

As a check for the measured heat losses, the approximate heat lost is calculated via a one-dimensional conduction model. The model formulation is shown in Appendix D. Though the conduction in the test section walls may be two- or three-dimensional, the low thermal conductivity of Garolite and the long conduction paths in the transverse and axial directions result in the resistance to conduction heat losses being significantly lower in the wall-normal direction. Thus, a 1D conduction model provides a good approximation of the heat lost to the surroundings, and the approximation yields heat losses in good agreement with the measured losses. In this investigation, measured heat losses are accounted for in all experimental results.

To demonstrate repeatability, water and emulsion experiments were conducted at nominally the same mass flux. These experiments were run on separate days following the same experimental procedure. The resulting boiling curves (Fig. 4.2) demonstrate that the experimental apparatus produces repeatable results when boiling pure water and emulsions on the smooth surface.

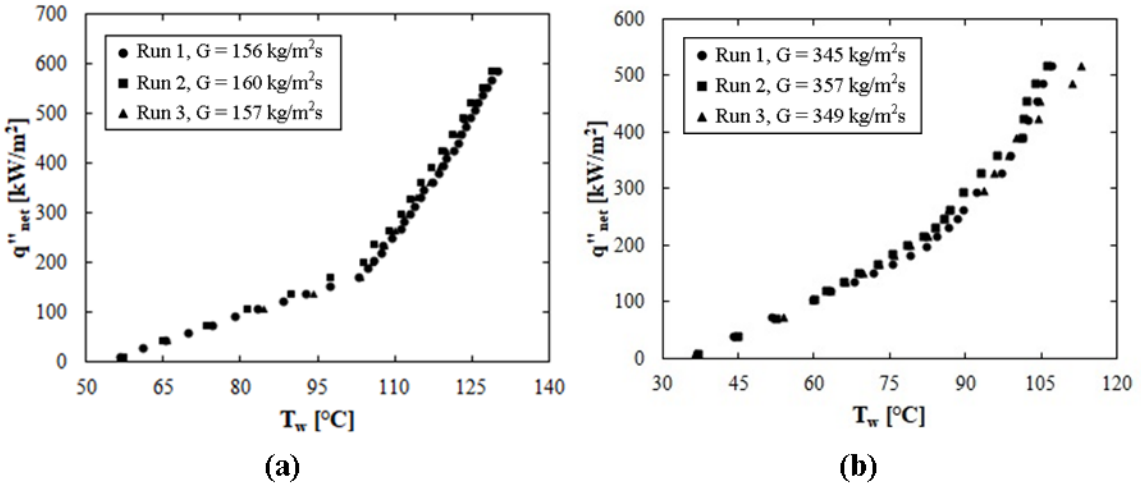

Fig. 4.2. Comparison of the boiling curves for three experimental runs on the smooth surface. (a) Water, T_i = 51 °C, D_h = 1000 μm, (b) 1% emulsion, T_i = 30 °C, D_h = 500 μm.

Prior to conducting experiments on the porous surfaces, the surfaces must be conditioned by running repeated experiments [79]. After the conditioning process, the surfaces produce more consistent results. Here, each surface is conditioned by running 1-2 experiments, after which each surface produces repeatable results when boiling water (Fig. 4.3). The porous surfaces also produce repeatable results when boiling emulsions (Fig. 4.4). The results shown in Fig. 4.4 are from experiments conducted both before and after the rest of the emulsion data set was generated. Thus, Fig. 4.4 demonstrates that the surfaces did not degrade over the course of experiments.

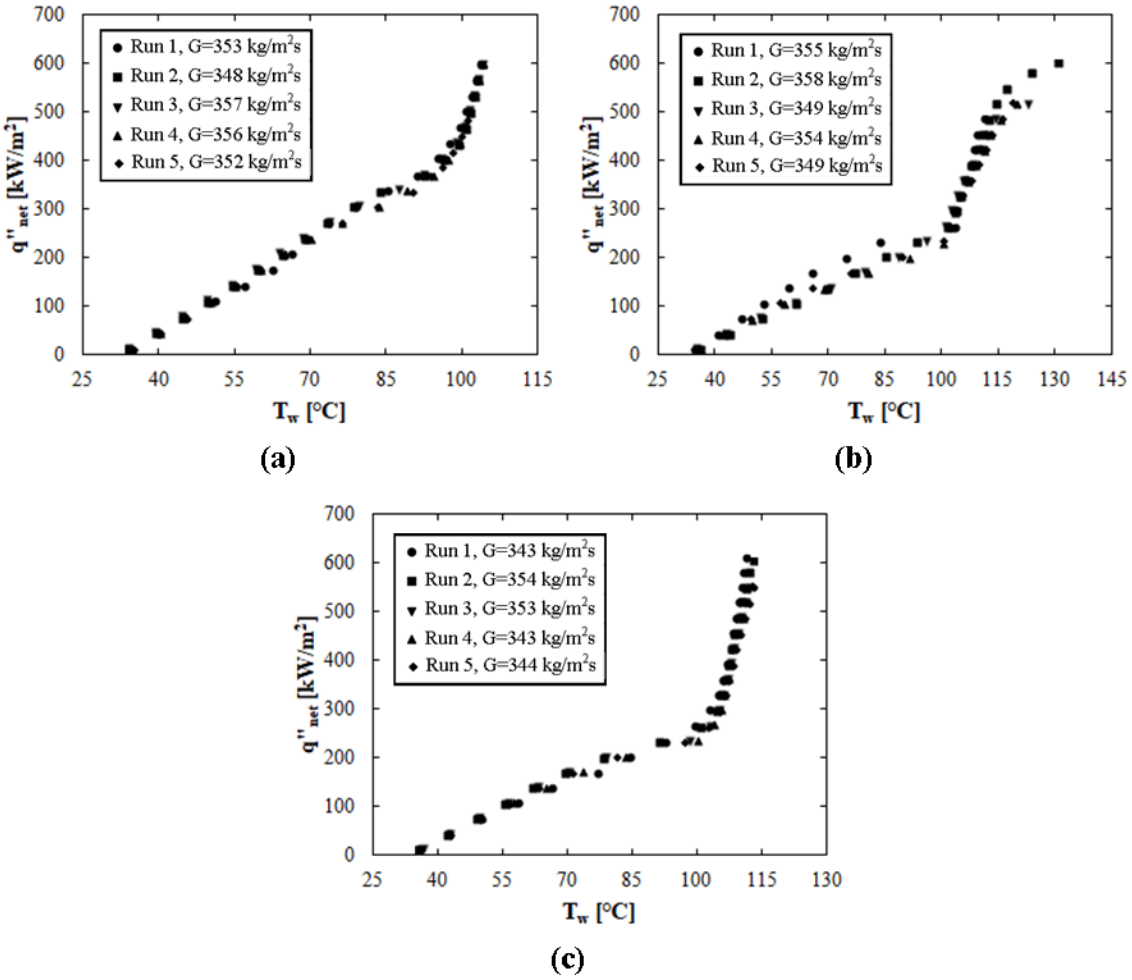

Fig. 4.3. Demonstration of surface conditioning for (a) Porous Surface 1, (b) Porous Surface 2, and (c) Porous Surface 3. Water, T_i = 30 °C, D_h = 500 μm.

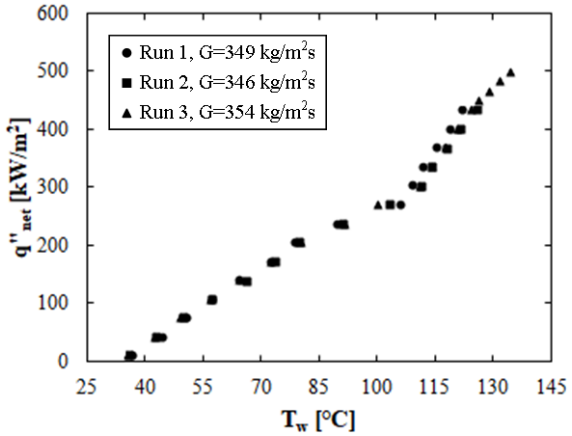

Fig. 4.4. Comparison of the boiling curves for three experimental runs on Porous Surface 1. 1% emulsion, T_i = 30 °C, D_h = 500 μm.

4.1 Water on the smooth surface

The boiling curve (Fig 4.5), measured heat transfer coefficient (Fig 4.6) and pressure drop (Fig 4.7) are shown below for all experiments conducted at an inlet temperature of 30 °C. Although the nominal mass flux for each run is 150, 350 or 550 kg/m^{2}s, the actual mass flux for a given experiment is generally within ±10 kg/m^{2}s of the nominal value and the measured mass flux for each experiment is given in Appendix E. The tabulated experimental results for every experiment are presented in Appendix F.

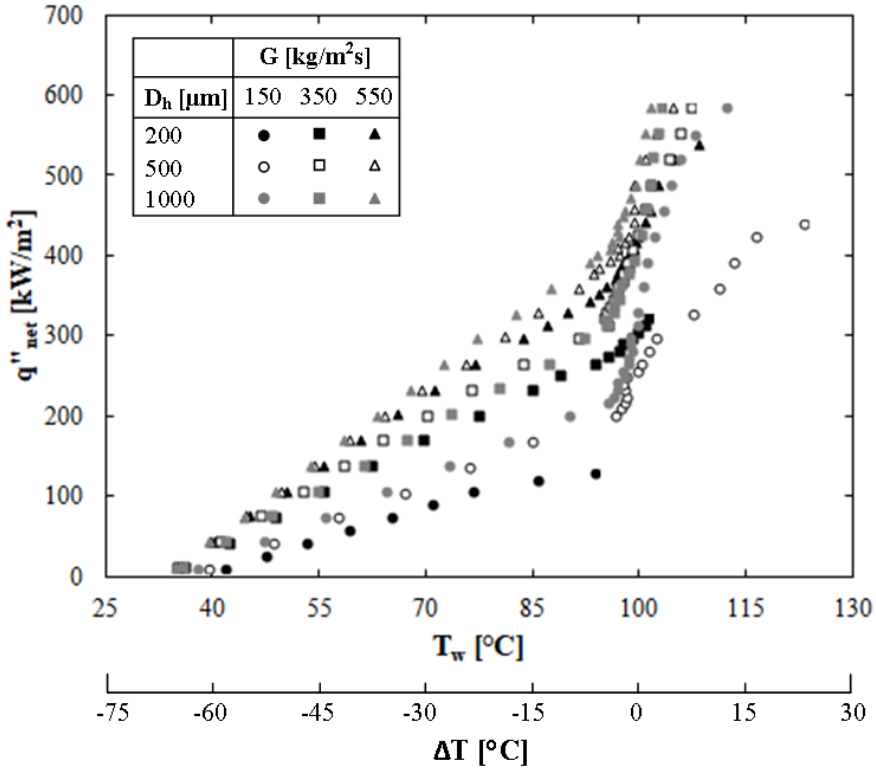

Fig. 4.5. Boiling curves for water on the smooth surface, T_i = 30 °C. $\Delta T = T_w - T_{sat}$.

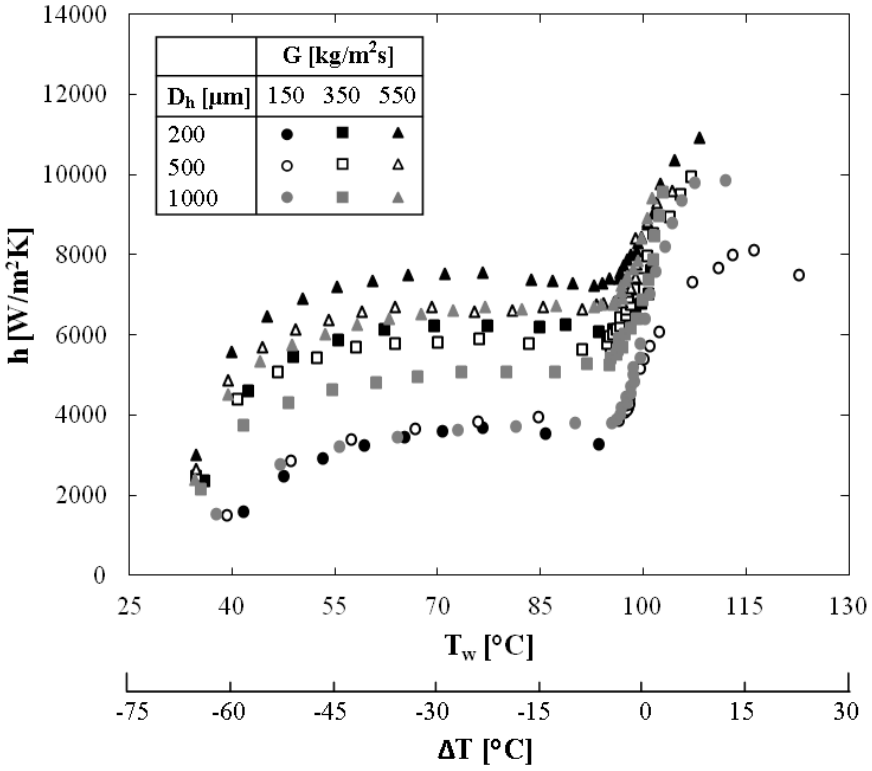

Fig. 4.6. Heat transfer coefficient for water on the smooth surface, T_i = 30 °C.

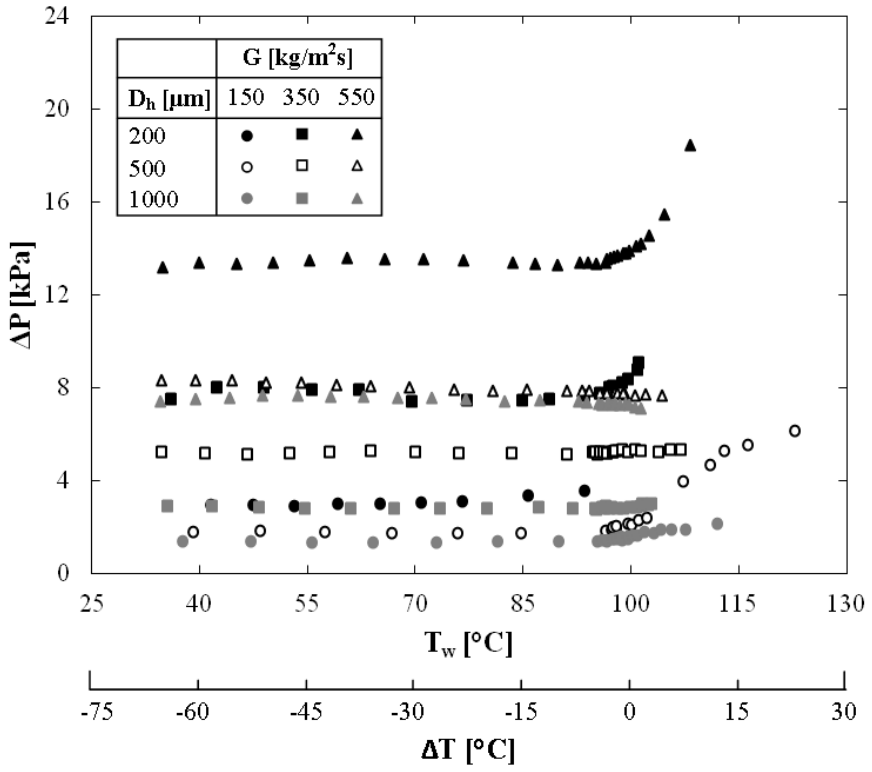

Fig. 4.7. Pressure drop for water on the smooth surface, T_i = 30 °C.

The boiling curves are also presented to view the effect of the mass flux (Fig 4.8) and the hydraulic diameter (Fig 4.9). The initiation of boiling, also known as the onset of nucleate boiling (ONB), is indicated by a change in the slope of the boiling curve as the heat transfer mechanism shifts from single-phase to two-phase forced convection. It can be seen, therefore, that boiling starts with little or no surface superheat at all hydraulic diameters and mass fluxes.

Prior to the ONB, increasing the mass flux increases the slope of the boiling curve for each gap (Fig 4.8). The increased slope is a result of higher heat transfer coefficients for larger mass fluxes (Fig 4.10). At G = 150 kg/m^{2}s, the boiling curves for D_h = 500 and 1000 μm are nearly equivalent in the single-phase region but the boiling curve for D_h = 200 μm shifts downward to higher wall temperatures (Fig 4.9a). For G = 350 and 550 kg/m^{2}s, the single-phase results are nominally equivalent for all D_h (Fig 4.9b and c).

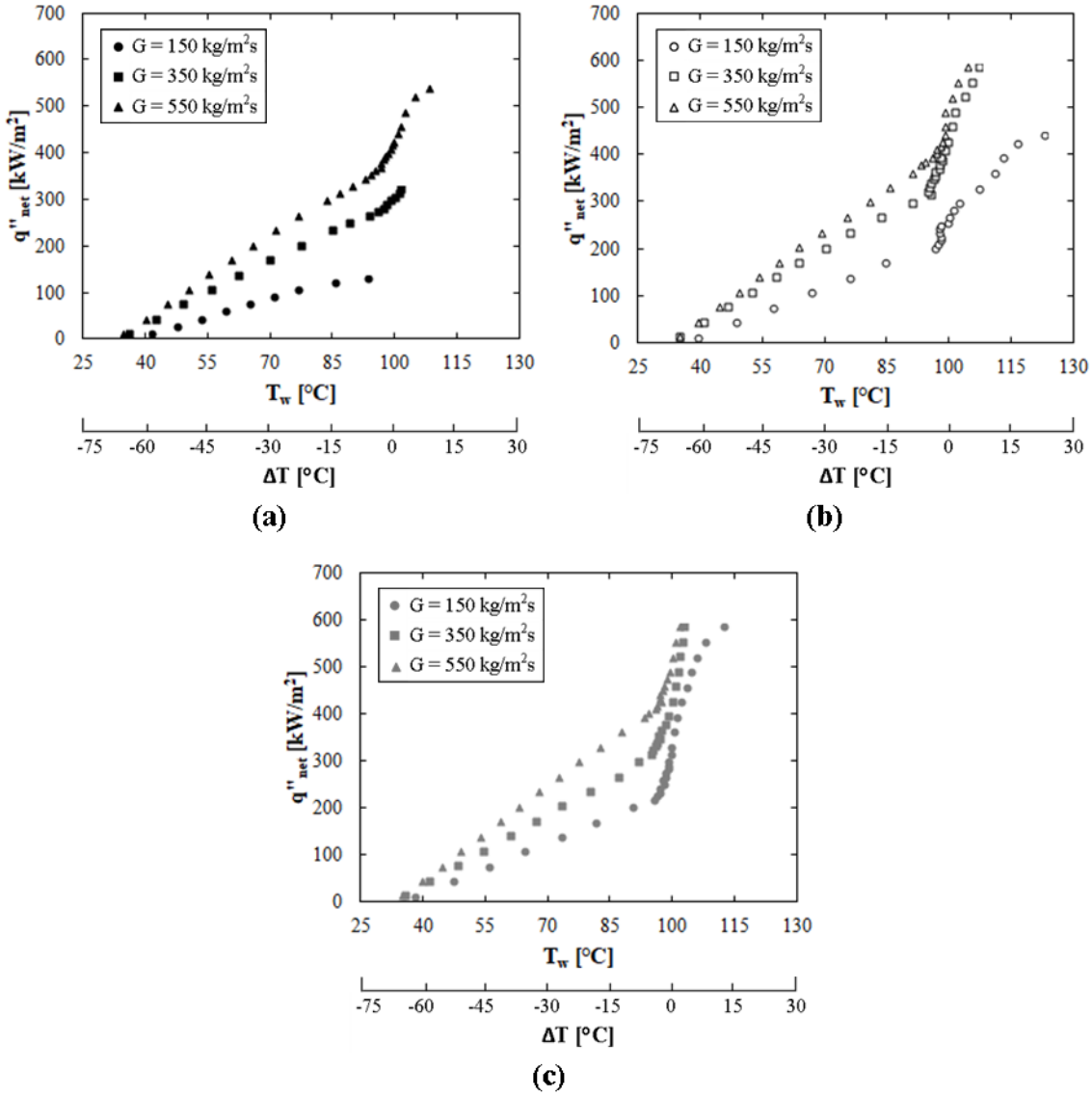

Fig. 4.8. Boiling curves for water on a smooth surface, T_i = 30 °C. (a) - (c) are for D_h = 200, 500 and 1000 µm, respectively.

For each gap size and mass flux, the two-phase results are nearly equivalent except when the critical heat flux (CHF) is approached or reached. The approach to CHF is demonstrated by the slope of the boiling curve decreasing, with the boiling curve shifting toward significantly higher wall temperatures with increasing heat flux. For the smallest gap, critical heat flux (CHF) is reached at relatively low wall temperatures, with CHF occurring at the ONB in the D_h = 200 µm gap at G = 150 kg/m^{2}s and at mean wall

temperatures less than 110 °C for G = 350 or 550 kg/m^{2}s (Fig 4.8a). Increasing D_h delays the approach to CHF. This is seen most clearly in Fig 4.9a, where CHF is achieved at the ONB for D_h= 200 µm and at ~450 kW/m^2 for D_h = 500 µm. For D_h = 1000 µm, CHF is approached but does not occur in the range of heat flux applied.

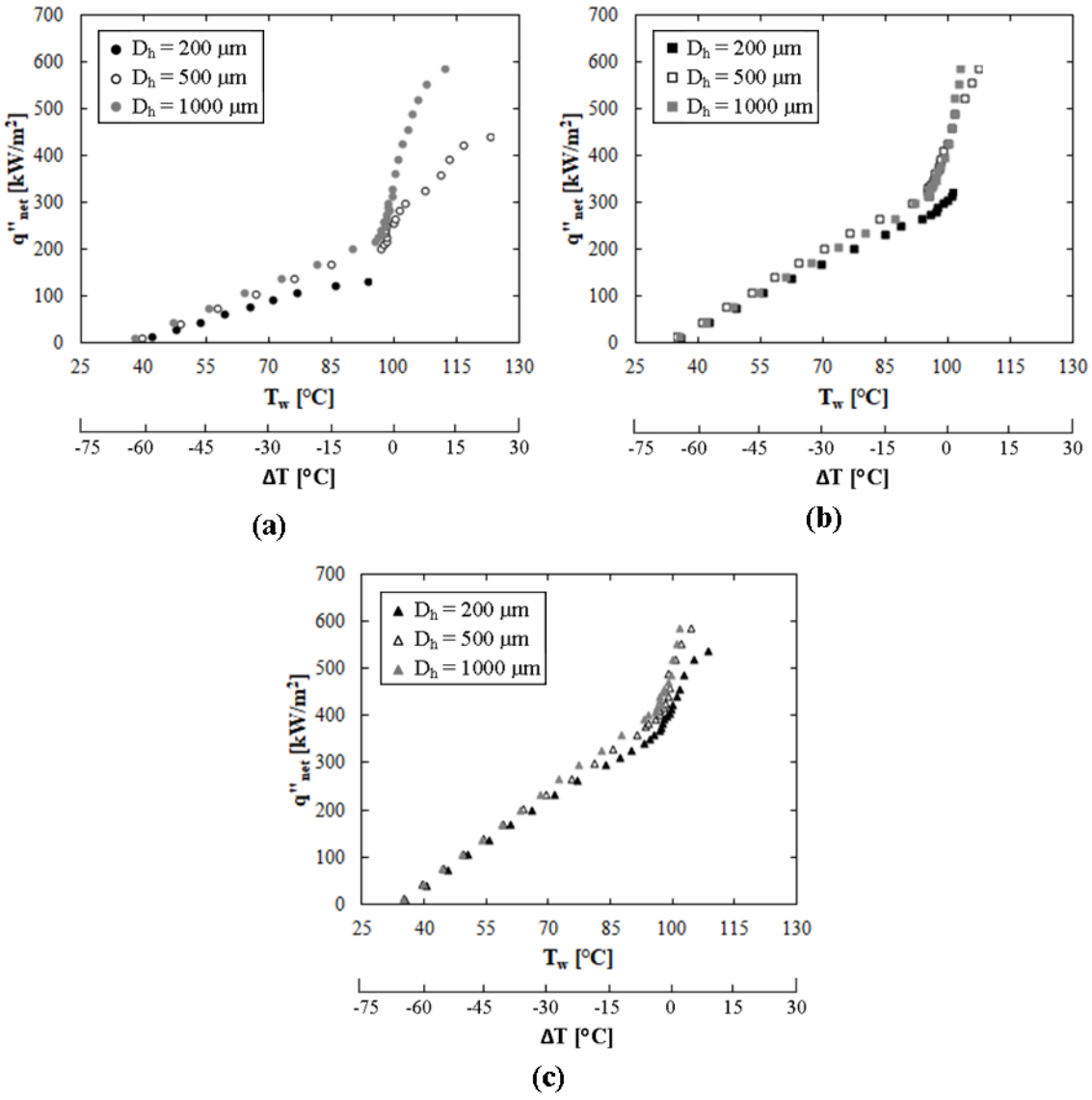

Fig. 4.9. Boiling curves for water on a smooth surface, T_i = 30 °C. (a) - (c) are for G = 150, 350 and 550 kg/m^{2}s, respectively.

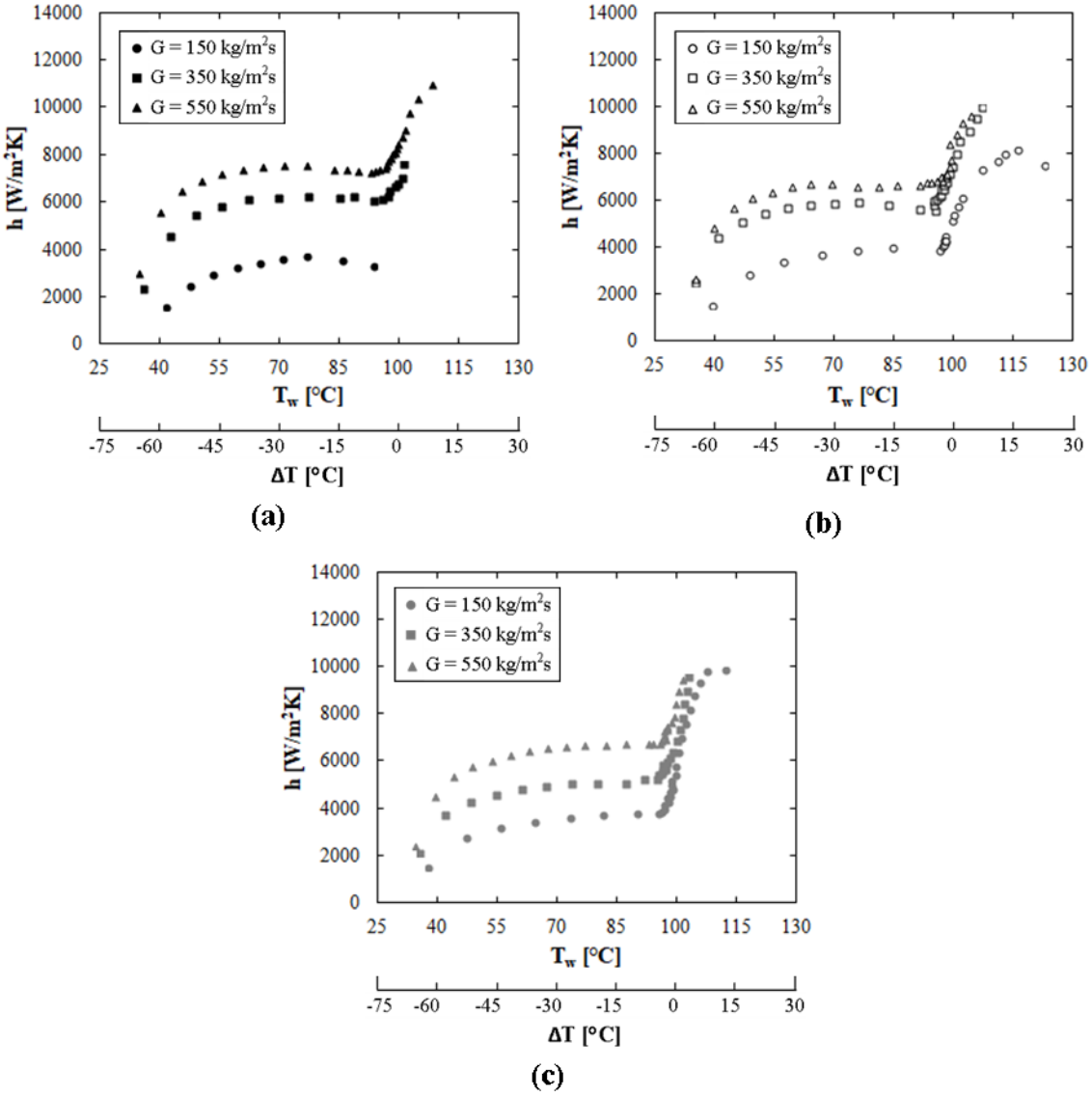

Fig. 4.10. Heat transfer coefficient for water on a smooth surface, T_i = 30 °C. (a) - (c) are for D_h = 200, 500 and 1000 µm, respectively.

Each heat transfer coefficient curve demonstrates 3 - 4 regions. First, the curve has a developing region where the h increases with increasing wall temperature. Second, the curve levels off and h stays fairly constant until boiling initiates. Following ONB, h increases dramatically. Finally, in the experiments in which CHF is approached or achieved, the curve levels out a second time as CHF is approached.

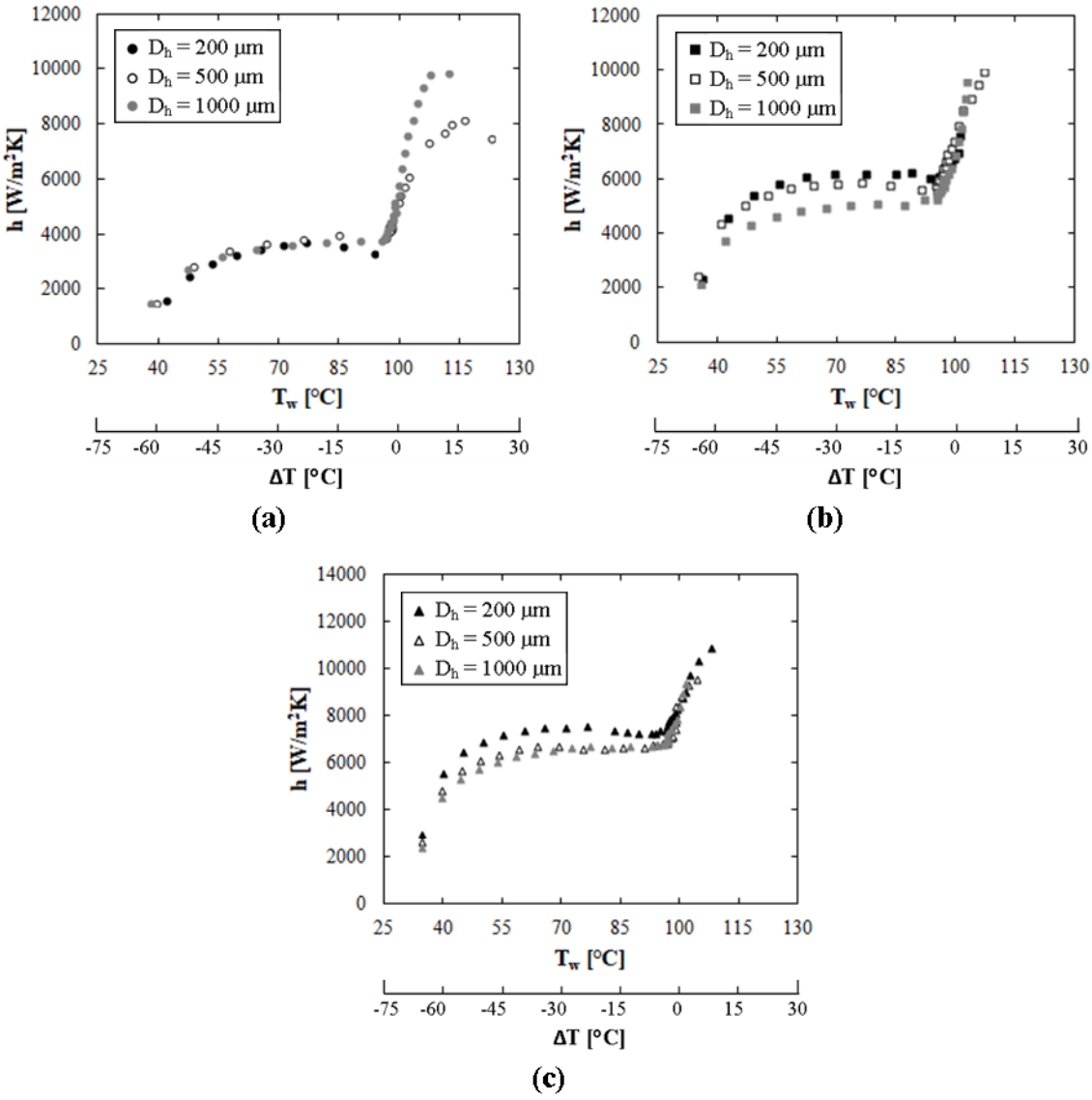

Fig. 4.11. Heat transfer coefficient for water on a smooth surface, T_i = 30 °C. (a) - (c) are for G = 150, 350 and 550 kg/m^{2}s, respectively.

As noted before, the heat transfer coefficient curves shift upward with increasing G at each D_h. However, the curves approach one another at each D_h once boiling initiates, except where CHF is approached (Fig 4.10). For G = 150 kg/m^{2}s, the h curves for all D_h are nominally the same until CHF is approached (Fig 4.11a). However, for G = 350 and 550 kg/m^{2}s, decreasing D_h leads to an increase in h in single-phase flow (Fig 4.11b and c). For example, at G = 350 kg/m^{2}s, decreasing D_h from 1000 μm to 200 μm increases h

by nearly 25%. Because the boiling curves are nearly equivalent for constant G but h increases with decreasing D_h, these results may suggest that the difference between the wall temperature and fluid temperature decreases with decreasing gap size.

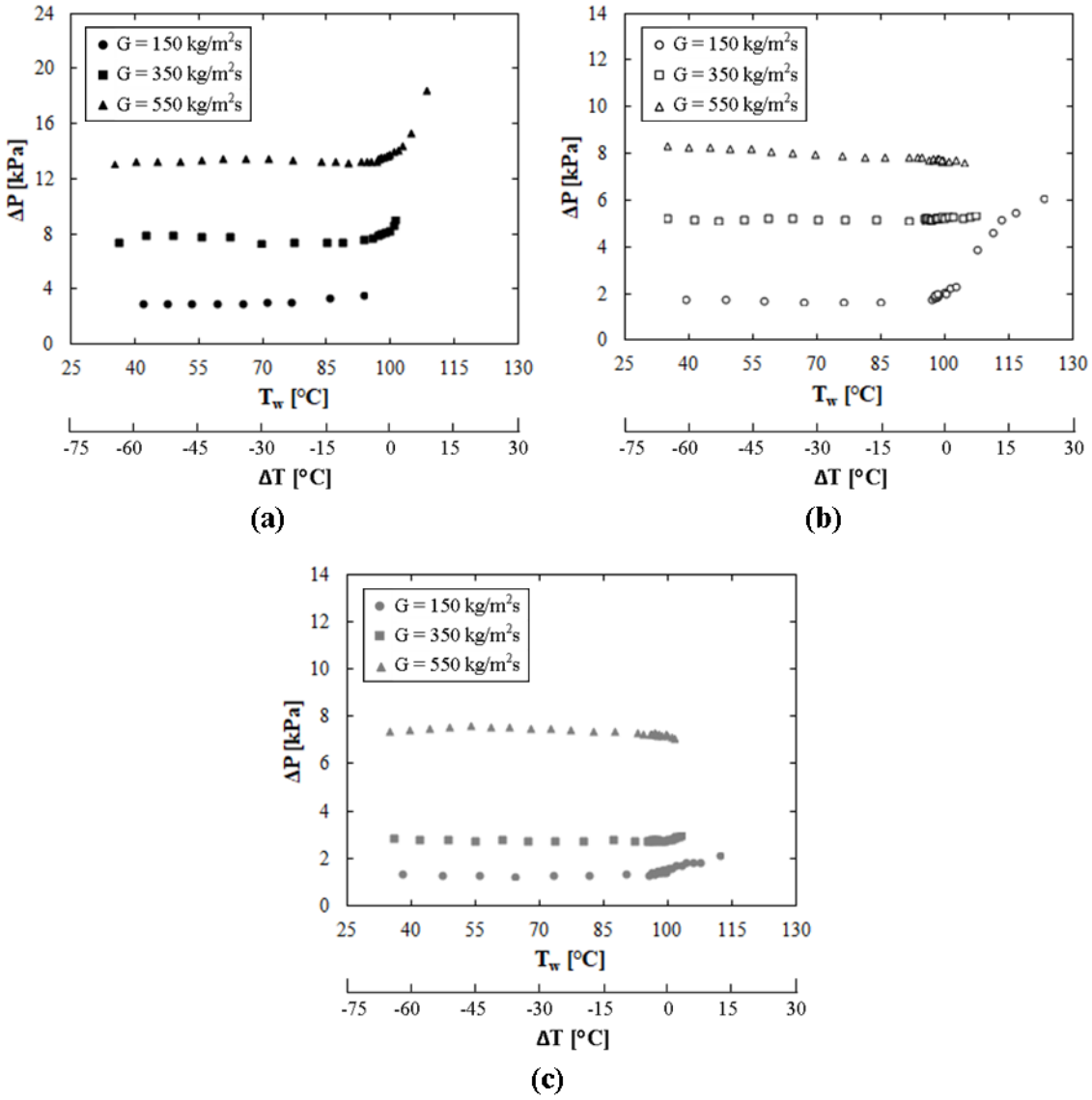

Fig. 4.12. Pressure drop for water on a smooth surface, T_i = 30 °C. (a) - (c) are for D_h = 200, 500 and 1000 µm, respectively.

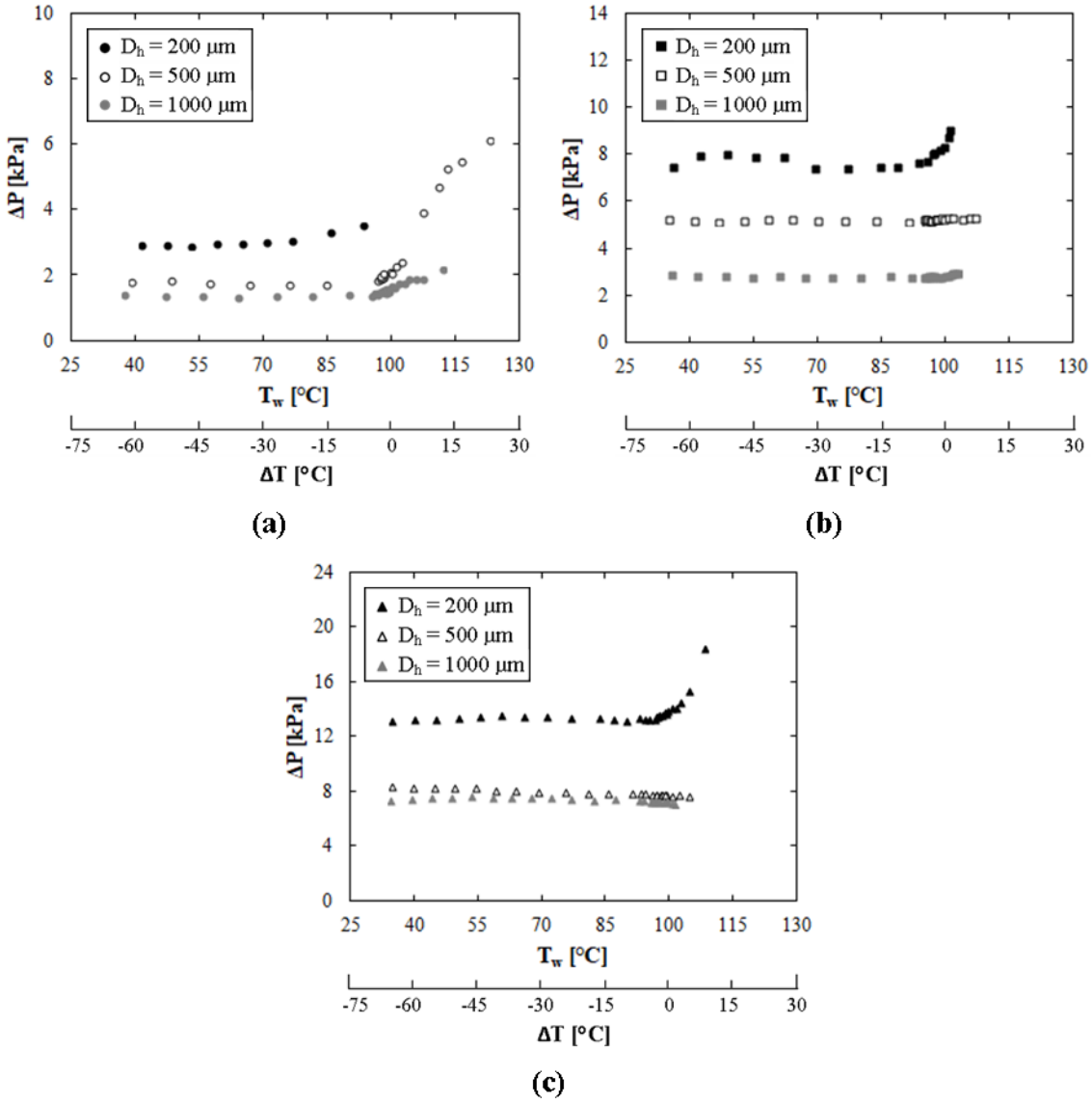

Fig. 4.13. Pressure drop for water on a smooth surface, T_i = 30 °C. (a) - (c) are for G = 150, 350 and 550 kg/m^{2}s, respectively.

The pressure drop measurements demonstrate that with increasing wall temperature, the pressure drop stays constant or decreases slightly prior to the ONB (Fig 4.12), possibly due to the slight decrease in dynamic viscosity and density as the film temperature increases. Once boiling initiates, the pressure drop is most strongly affected at lower G. This is not clearly seen in Fig 4.12a due to the early approach to CHF at all

G. However, Fig. 4.12b and c show that the pressure drop increases at the initiation of boiling for G = 150 kg/m^{2}s but stays constant for G = 350 and 550 kg/m^{2}s.

The pressure drop also shows a strong correlation with D_h (Fig. 4.13). In single-phase flow, decreasing D_h increases the pressure drop. At lower D_h, the pressure drop also increases dramatically once boiling initiates. However, the effect of boiling on the pressure drop decreases with increasing D_h and the pressure drop only slightly increases when boiling begins for G = 150 kg/m^{2}s in the 1000 μm gap. For G = 350 and 550 kg/m^{2}s, the pressure drop stays constant at the initiation of boiling for D_h = 500 and 1000 μm.

The heat transfer coefficient is presented in non-dimensional form via the Nusselt number in Fig. 4.14. Previous studies have shown that in flow boiling, the Nusselt number is a function of the Reynolds and Boiling numbers [13, 38] so these two parameters are used here to account for the effect of the hydraulic diameter, mass flux, applied heat flux, latent heat and other properties. It is assumed that the Prandtl number should also be considered but all experiments were conducted with water so the Prandtl number is not included in this analysis. For the two-phase data, it is clear that the Nusselt number is almost linearly dependent on ReBl and that the hydraulic diameter and mass flux are well accounted for in the Reynolds and Boiling numbers (Fig. 4.14). The data points that do not follow this trend are instances where CHF was approached or reached.

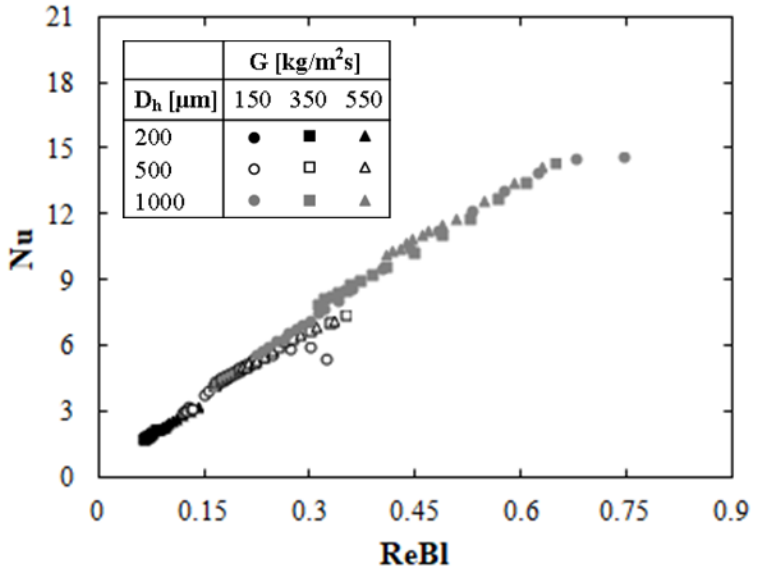

Fig. 4.14. Nusselt number as a function of the Reynolds and Boiling numbers for two-phase heat transfer on the smooth surface. T_i = 30 °C.

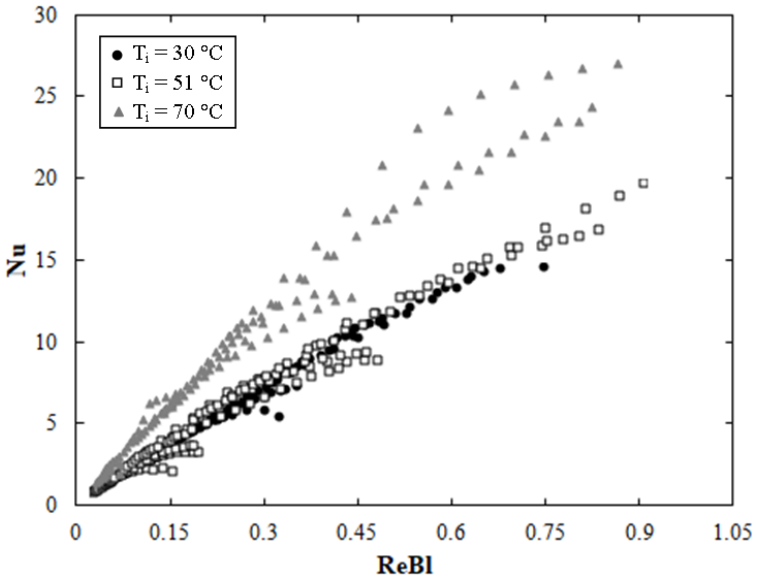

Fig. 4.15. Nusselt number as a function of the Reynolds and Boiling numbers at various inlet temperatures.

Data sets were also generated at inlet temperatures of 51 and 70 °C to study the effect of the inlet temperature. The trends in these data sets largely follow those discussed above in the 30 °C inlet temperature data set so the heat transfer coefficient is only presented here in non-dimensional form (Fig. 4.15). The single-phase data is neglected in Fig. 4.15 but the entire data sets are tabulated in Appendix F.

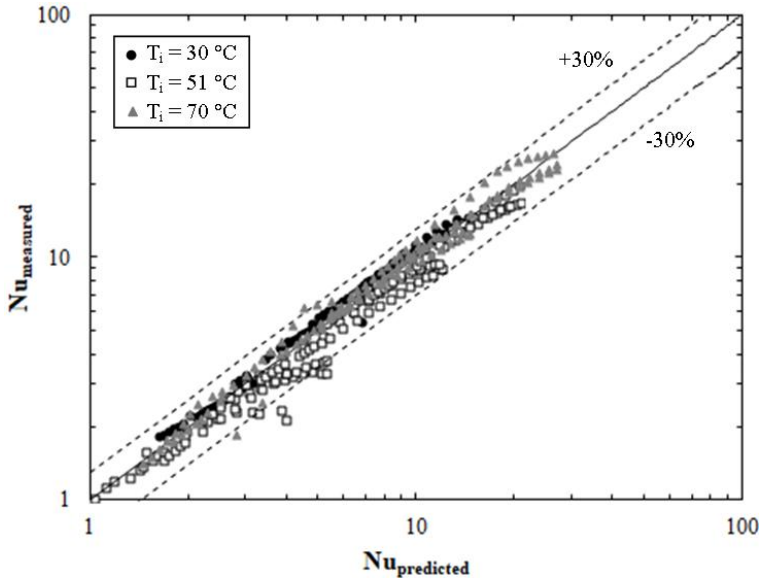

Fig. 4.16. Comparison between the measured Nusselt number and the Nusselt number predicted by Eqn. (4.8). The solid line represents equivalence between the measured and predicted Nusselt numbers.

Figure 4.15 shows that the boiling results have a strong dependence on inlet temperature. Although the 30 and 51 °C data sets show similar measured Nusselt numbers, as the inlet temperature continues to increase, the Nusselt number increases dramatically. This is a result of boiling occurring at lower heat fluxes and the smaller difference between the wall and fluid temperatures. The 51 and 70 °C data sets also show an almost linear dependence on ReBl. If the Jakob number is used to account for the level of subcooling, the experimental data can be correlated by the Jakob, Reynolds, Boiling and Nusselt numbers as parameters, resulting in,

$$Nu = 4.04Ja^{-0.615}Re^{0.909}Bl^{0.866} \tag{4.8}$$

There is very good agreement between the measured Nusselt number and that predicted by Eqn. (4.8) (Fig. 4.16), with 98% of the boiling data falling within ±30% of the predicted Nusselt number and 83% of the data within ±15%. The majority of the data that falls outside of these bounds represents data where CHF is approached.

4.2 Emulsions on the smooth surface

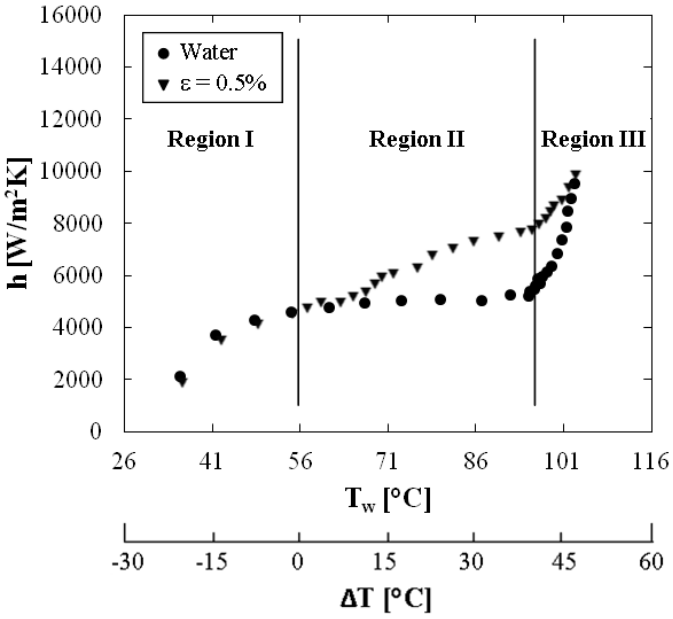

Fig. 4.17. Typical heat transfer coefficient curves for emulsions compared to those for water. T_i = 30 °C, D_h = 1000 μm, G = 350 kg/m^{2}s. $\Delta T = T_w - T_{sat}$.

For flow boiling of dilute emulsions, the heat transfer typically demonstrates three regions based on the wall temperature (Fig. 4.17). In region I, the wall temperature is lower than the saturation temperature of the dispersed component- 56 °C for FC-72- and single-phase heat transfer is present in both components. In this region, measured heat transfer coefficients are typically similar to those for water at the same experimental conditions. However, emulsion heat transfer coefficients can be lower than those for water depending on the volume fraction, flow rate, and gap size.

In region II, the wall temperature is between the saturation temperature of the dispersed and continuous components. In this region, the dispersed component will start to boil at wall temperatures slightly above its saturation temperature, with a corresponding shift in the slope of the boiling and heat transfer coefficient curves. Although in general the heat transfer coefficient increases with increasing wall

temperature in this region, and FIg. 4.17 shows much higher heat transfer coefficients for the emulsion than water, it is possible to have measured heat transfer coefficients lower than water at the same wall temperature. Depending on the volume fraction, mass flux and gap size, the emulsion heat transfer coefficient in this region can be higher or lower relative to water over the whole range of wall temperature, or less than water at lower wall temperatures and greater than water at higher wall temperatures. Thus, the heat transfer results are quite complex in this region.

In region III, part of the wall has reached the saturation temperature of the continuous component and boiling is present in both the dispersed and continuous components. This is signified by another shift in the slope of the boiling and heat transfer coefficient curves. Because the dispersed component accounts for less than 5% of the volume in a dilute emulsion, the heat transfer in this region is typically dominated by boiling of the continuous component.

The following figures show more fully the impact that the volume fraction, gap size and mass flux have on heat transfer and pressure drop. At $G = 350$ kg/m^{2}s and $D_h = 200$ μm, the emulsion boiling curves all shift to higher wall temperatures relative to water (Fig. 4.18a), indicating a decrease in heat transfer for the emulsion. For $T_w < 80$ °C, h is independent of the volume fraction and ~30% lower than that for water (Fig. 4.19a). At higher wall temperatures, h increases for the 0.1% and 0.5% emulsions but is still much less than that for water.

For $D_h = 500$ μm, the boiling curve for the 0.1% emulsion shifts to slightly lower wall temperatures (Fig. 4.18b), with a corresponding increase in h compared to water as the wall temperature increases (Fig. 4.19b). The 1% emulsion shows decreased heat transfer

but the boiling curve and h for the 0.5% and 2% emulsions are nearly the same as those for water. For D_h = 1000 μm, the boiling curve shifts to lower wall temperatures for all ε, with the largest shift occurring at the lower volume fractions (Fig. 4.18c). Thus, h is higher compared to water in all emulsion trials at this gap size (Fig. 4.19c). For the 0.1% emulsion, h is more than 50% higher than water at the same experimental condition.

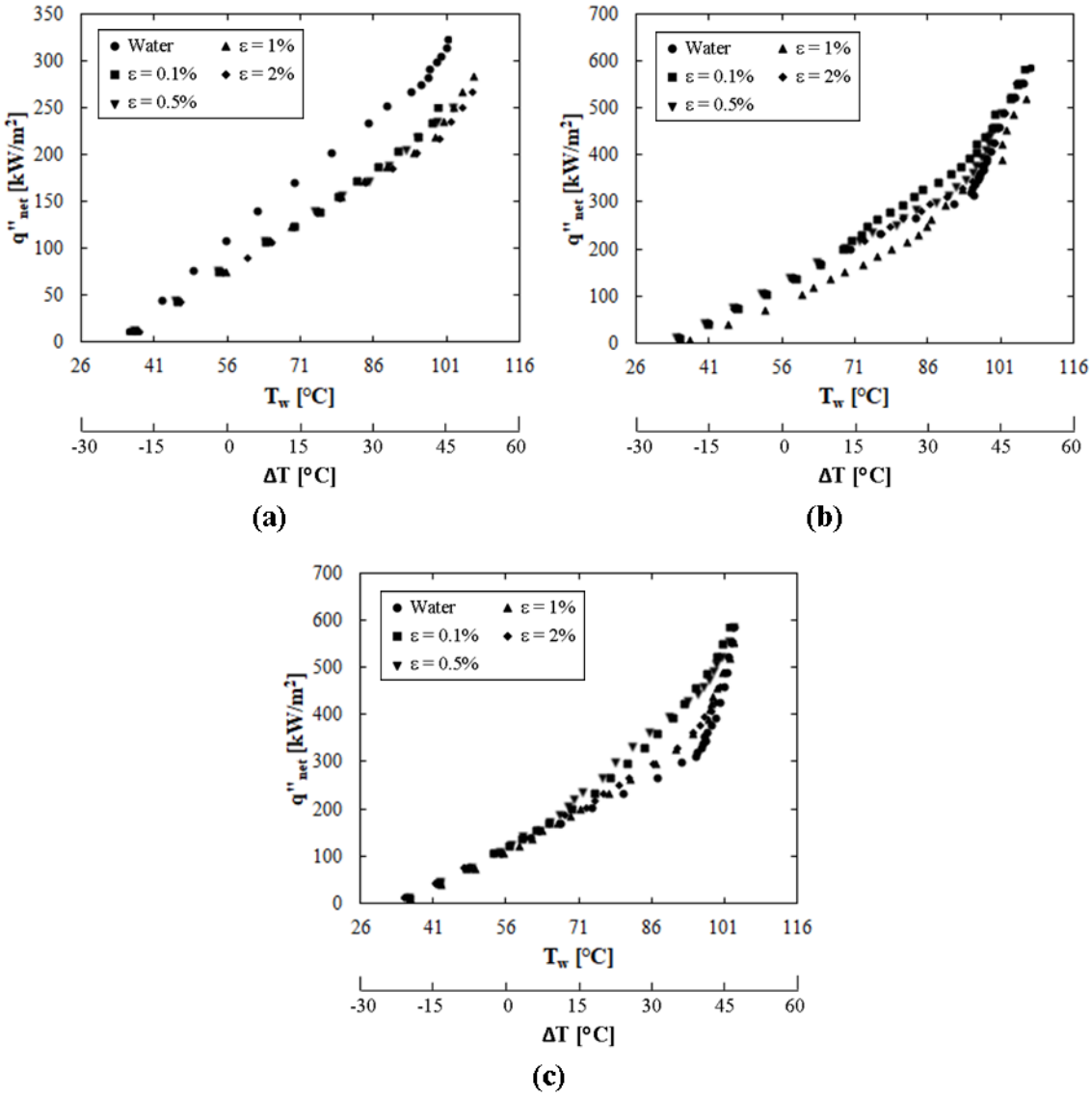

Fig. 4.18. Boiling curves for emulsions on the smooth surface, T_i = 30 °C, G = 350 kg/m^{2}s. (a) - (c) are for D_h = 200, 500 and 1000 μm, respectively. $\Delta T = T_w - T_{sat}$.

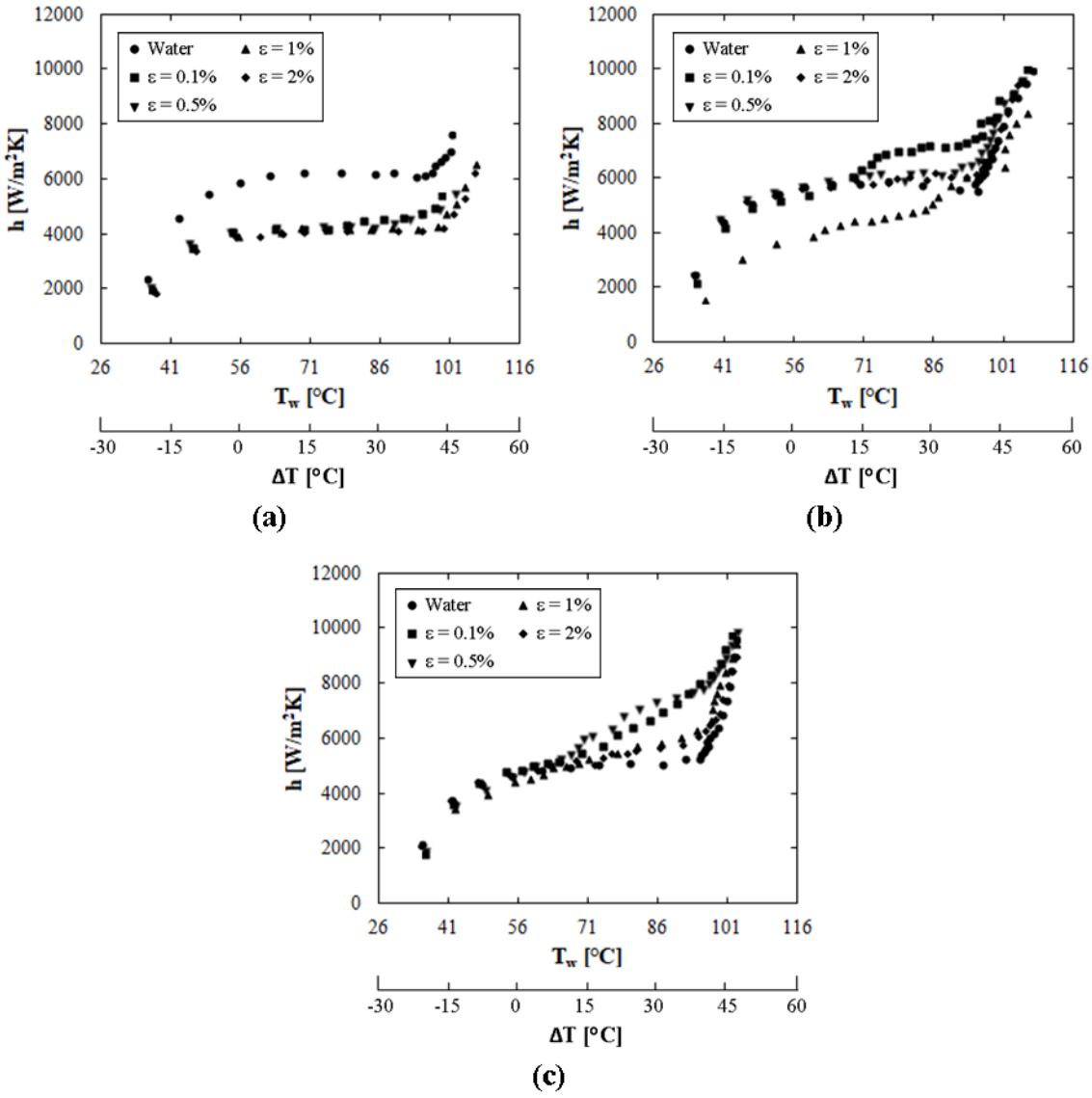

Fig. 4.19. Heat transfer coefficient for emulsions on the smooth surface, T_i = 30 °C, G = 350 kg/m^{2}s. (a) - (c) are for D_h = 200, 500 and 1000 µm, respectively.

Though the heat transfer in the flowing emulsions is, at times, similar to that for water, the pressure drop is always affected by the presence of the dispersed component. The pressure drop increases with increasing volume fraction, regardless of gap size (Fig. 4.20). The 2% emulsion pressure drop is generally 3-5 kPa higher than that for water. However, because the dispersed component constitutes less than 5% of the total volume, when it starts to boil, the pressure drop does not increase (e.g. Fig. 4.19c and Fig. 4.20c

where h increases with increasing wall temperature and the pressure drop stays constant). In contrast, when the continuous component starts to boil, the pressure drop can increase dramatically (Fig. 4.20a). Although the pressure drop is slightly higher for the emulsions at all T_w, for the range of T_w where the emulsions exhibit increased heat transfer compared to water, there is no associated additional pressure penalty.

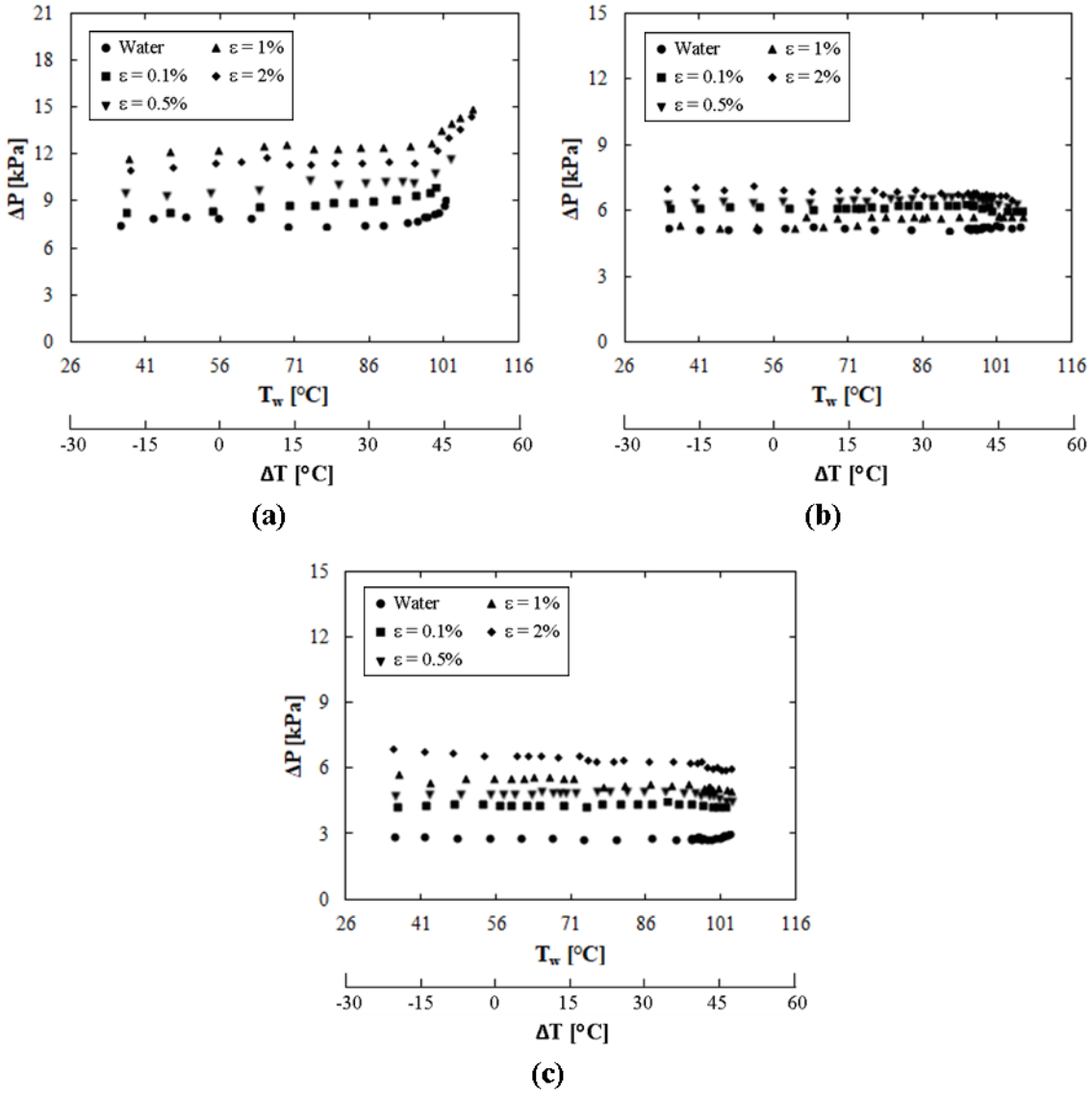

Fig. 4.20. Pressure drop for emulsions on the smooth surface, T_i = 30 °C, G = 350 kg/m^{2}s. (a) - (c) are for D_h = 200, 500 and 1000 µm, respectively.

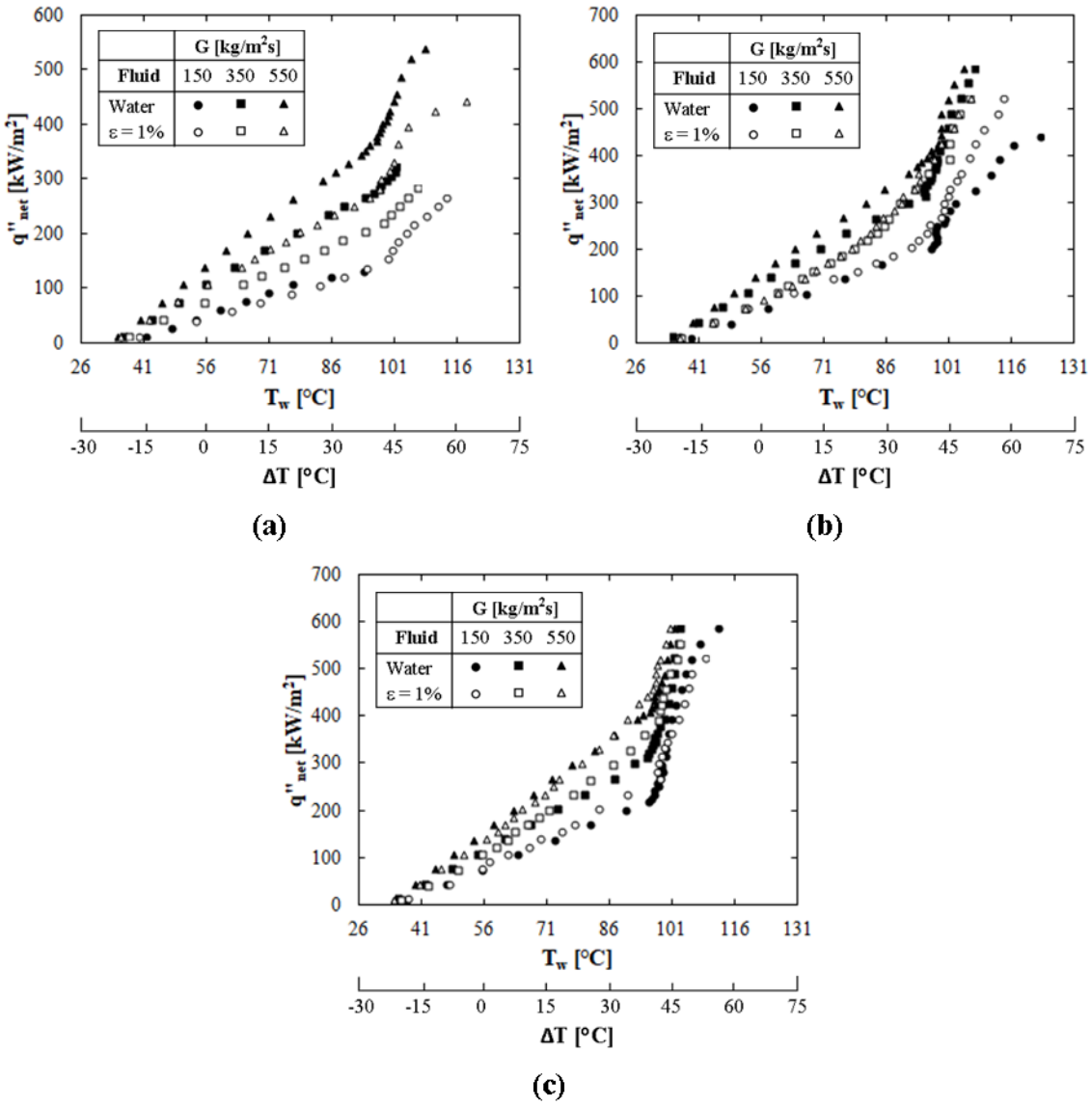

Fig. 4.21. Boiling curves for water and 1% emulsions on the smooth surface, T_i = 30 °C. (a) - (c) are for D_h = 200, 500 and 1000 µm, respectively.

The mass flux and gap size also strongly affect the emulsion heat transfer and this is shown for a fixed ε in the following figures. Similar to water, the emulsion boiling curves shift leftward with increasing G. However, for the 200 and 500 µm gaps, the boiling curve shifts to higher wall temperatures for G = 350 and 550 kg/m^{2}s compared to water (Fig. 4.21a and b). This is a result of the emulsion experiments having a

significantly lower heat transfer coefficient (Fig. 4.22a and b). The heat transfer coefficient is fairly constant and shows little evidence of boiling of the dispersed phase.

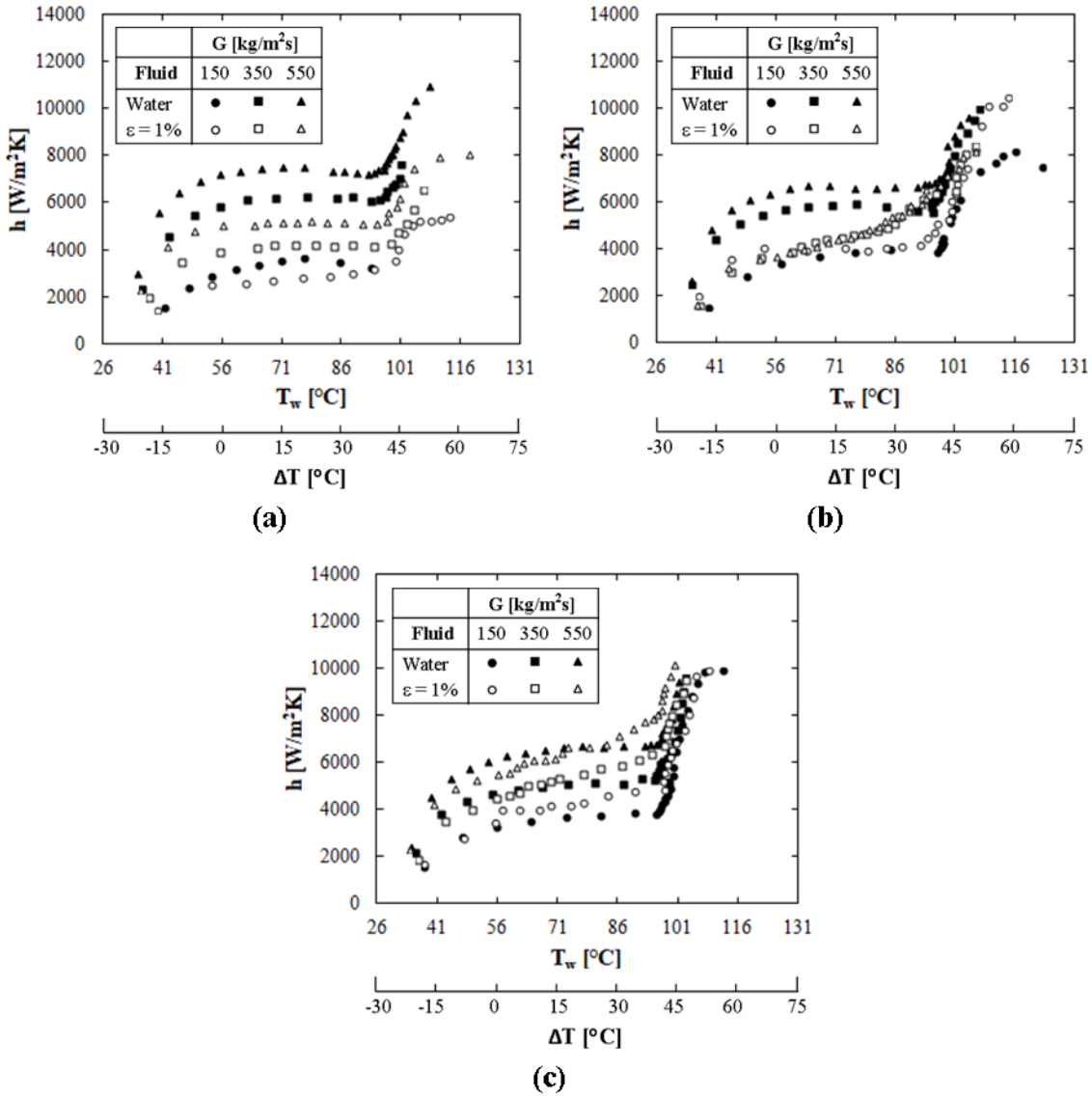

Fig. 4.22. Heat transfer coefficient for water and 1% emulsions on the smooth surface, T_i = 30 °C. (a) - (c) are for D_h = 200, 500 and 1000 μm, respectively.

For G = 150 kg/m^{2}s, the boiling curve is almost equivalent to that of water for D_h = 200 μm and shifts to slightly lower wall temperatures for D_h = 500 μm. For the 200 μm gap, the emulsion heat transfer coefficient is less than that for water but it does increase slightly with increasing T_w (Fig. 4.22a). For D_h = 500 μm, the heat transfer coefficient is

slightly higher than that for water at higher wall temperatures. Interestingly, CHF is reached in these two water experiments but CHF is significantly delayed in the corresponding emulsion experiments. For D_h = 1000 μm, the boiling curves shift to lower T_w for all G, with the largest shift occurring for G = 150 kg/m^{2}s and decreasing with increasing G (Fig. 4.21c). The 150 and 350 kg/m^{2}s mass flux experiments demonstrate higher emulsion heat transfer coefficients compared to water for T_w between the saturation temperatures of the two fluids (Fig. 4.22c). At G = 550 kg/m^{2}s, h increases with increasing T_w and becomes larger than water at ~T_w = 75 °C.

The effect of D_h on the boiling curve and heat transfer coefficient is shown in Figs. 4.23 and 4.24. At G = 150 kg/m^{2}s, the emulsion boiling curves are almost equivalent to those for water for D_h = 200 and 500 μm and the boiling curve shifts to lower T_w for D_h = 1000 μm (Fig. 4.23a). This corresponds to higher h compared to water for the 500 and 1000 μm gaps and lower h for the 200 μm gap (Fig. 4.24a). For G = 350 and 550 kg/m^{2}s, the boiling curve shifts to higher T_w for D_h = 200 and 500 μm and slightly lower T_w for the 1000 μm gap (Fig. 4.23b and c). Thus, the heat transfer coefficient is decreased for the 200 and 500 μm gaps. Interestingly, the heat transfer coefficient increases with decreasing gap size when boiling water but the reverse is true for the emulsions, with the highest h occurring for D_h = 1000 μm at each mass flux.

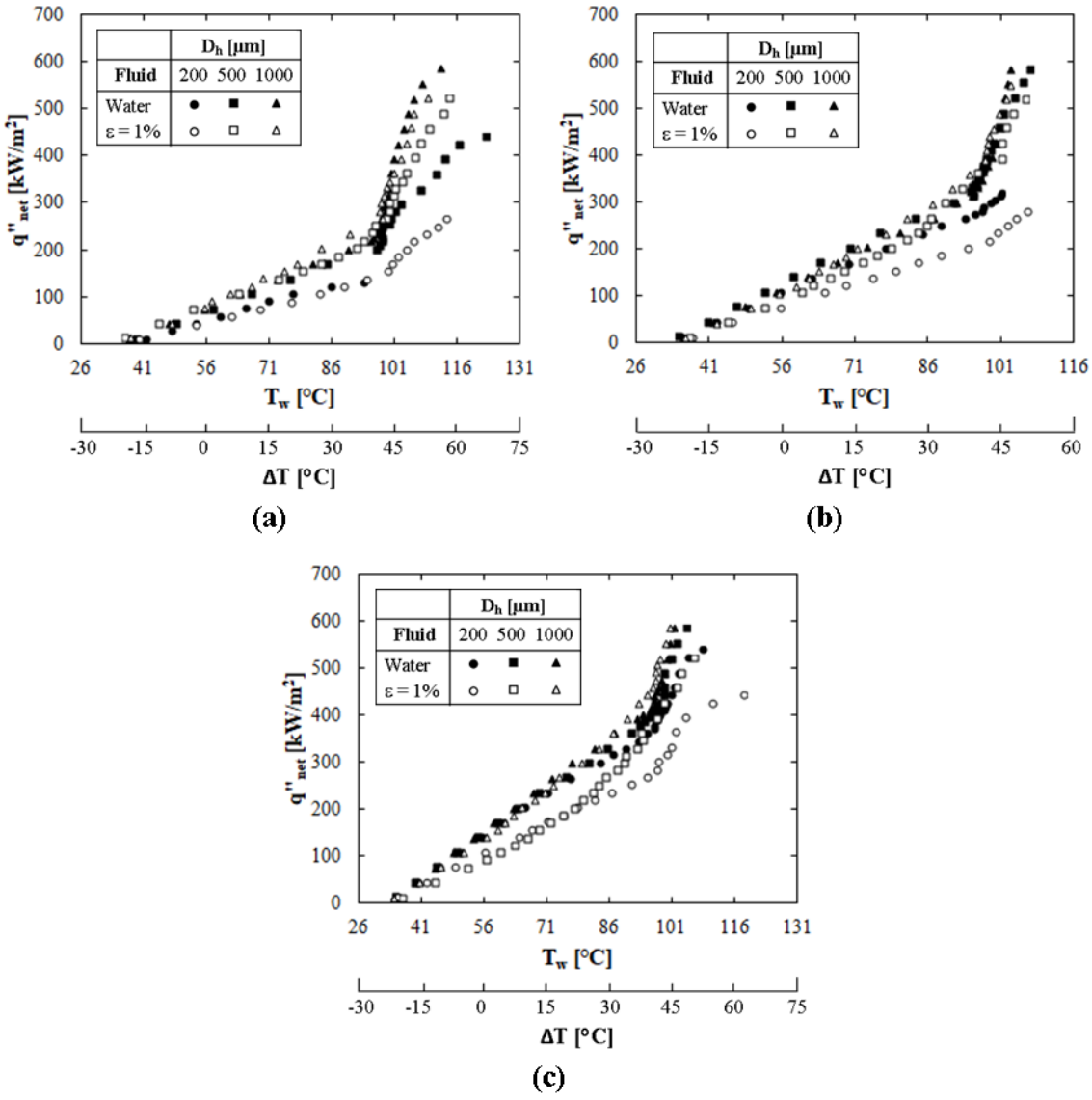

Fig. 4.23. Boiling curves for water and 1% emulsions on the smooth surface, T_i = 30 °C. (a) - (c) are for G = 150, 350 and 550 kg/m^{2}s, respectively.

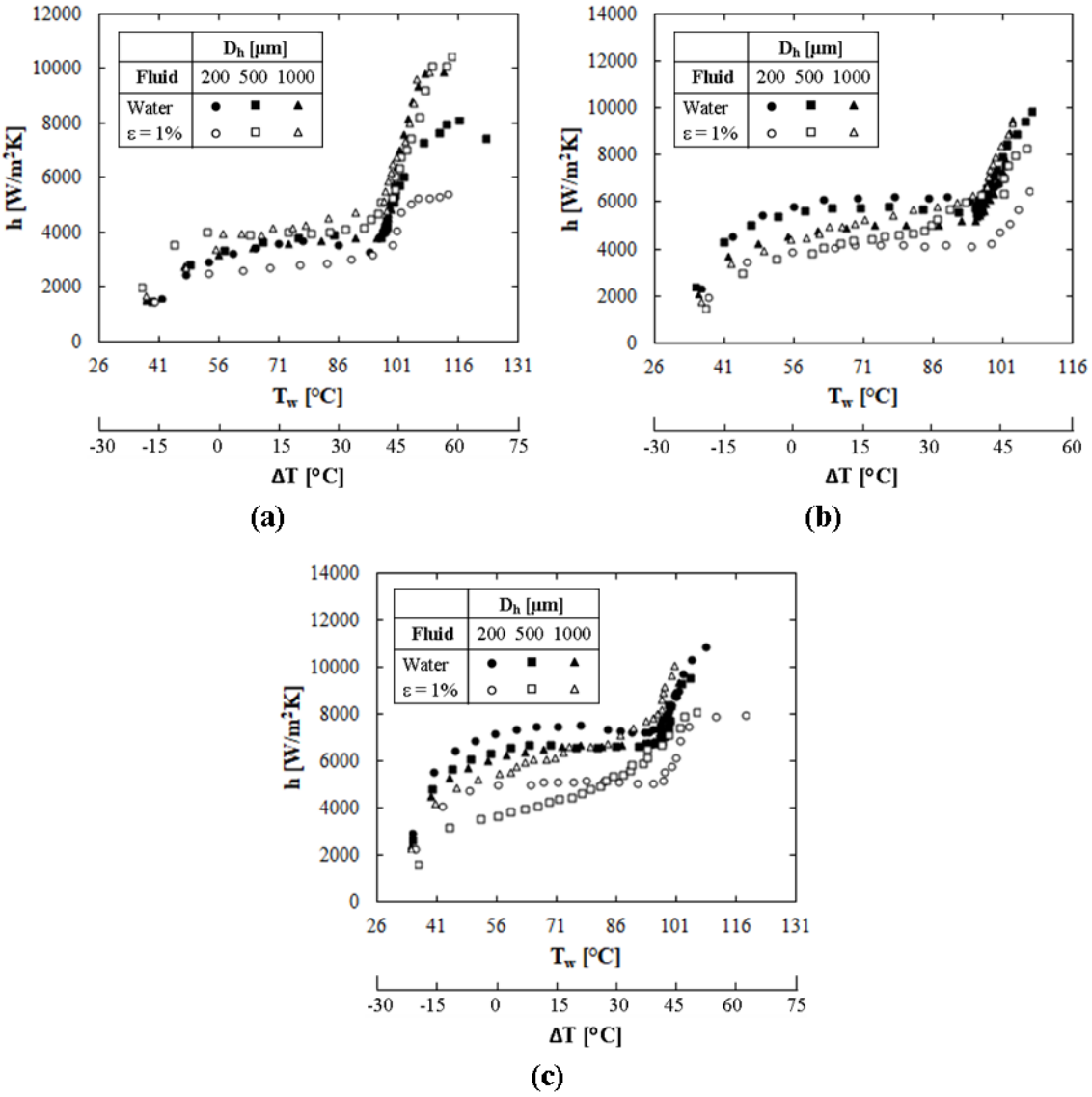

Fig. 4.24. Heat transfer coefficient for water and 1% emulsions on the smooth surface, T_i = 30 °C. (a) - (c) are for G = 150, 350 and 550 kg/m^{2}s, respectively.

Figures 4.25 and 4.26 demonstrate that the pressure drop for the 1% emulsion is almost always larger than that measured for water. The water and emulsions exhibit the same trend of increasing pressure drop with increasing G (Fig. 4.25) and decreasing D_h (Fig. 4.26). In general, the measured pressure drop is similar for D_h = 500 and 1000 μm for both the emulsions and water (Fig. 4.26). However, the emulsions demonstrate a wider range of pressure drop when viewing the pressure drop as a function of D_h, where

the difference between the pressure drop for D_h = 200 and 1000 μm at each mass flux is greater for the emulsions than for water.

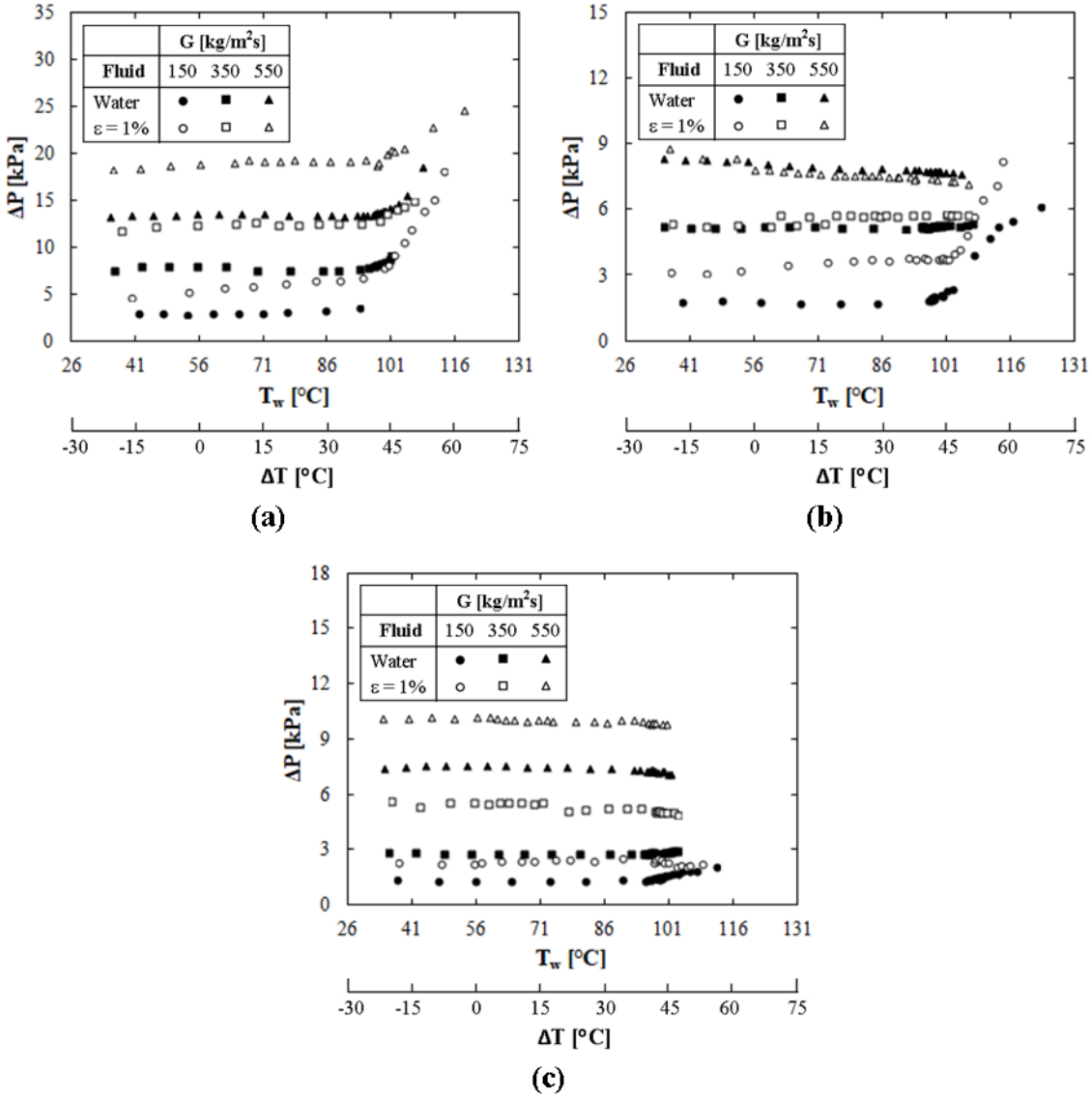

Fig. 4.25. Pressure drop for water and 1% emulsions on the smooth surface, T_i = 30 °C. (a) - (c) are for D_h = 200, 500 and 1000 μm, respectively.

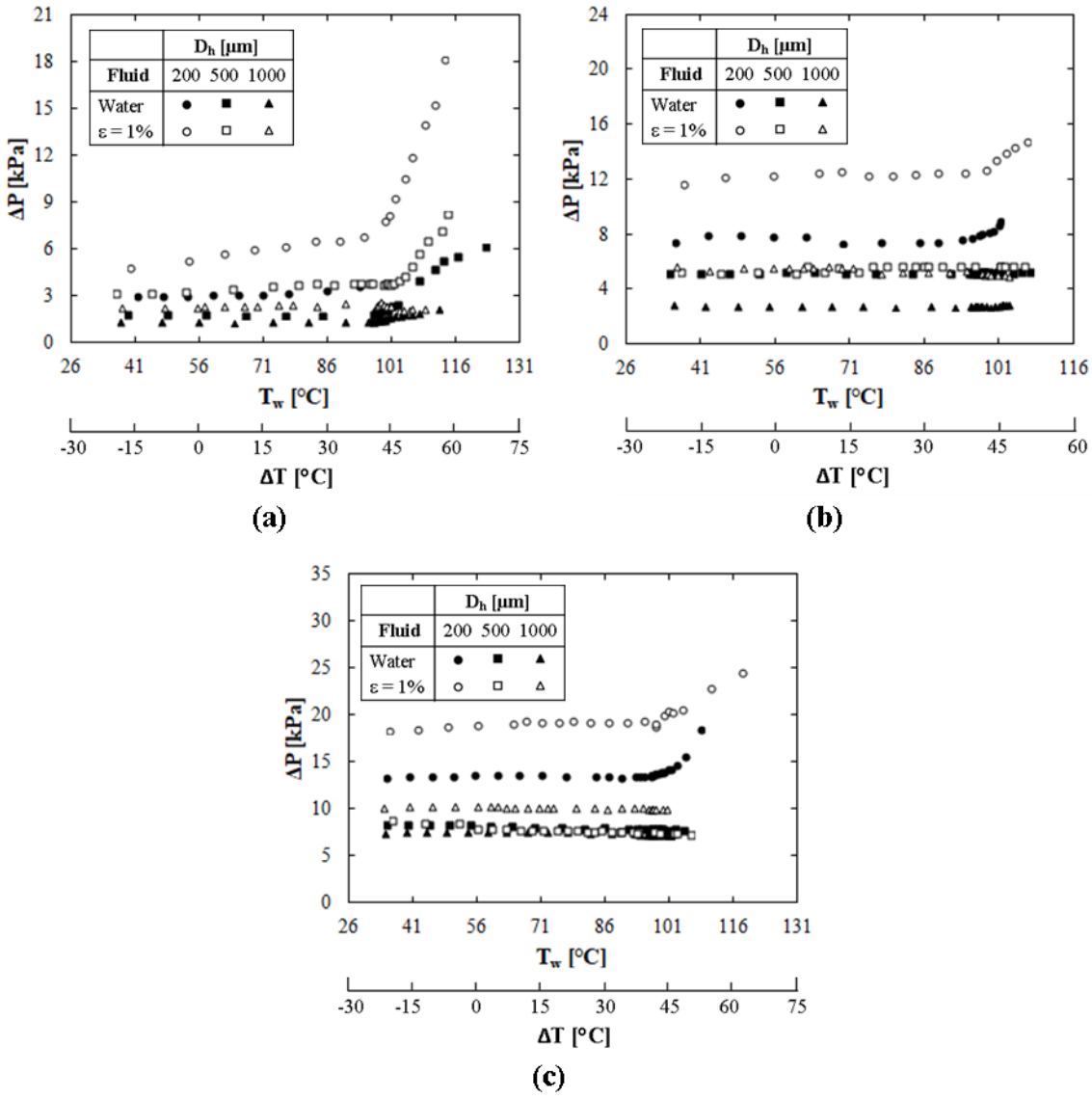

Fig. 4.26. Pressure drop for water and 1% emulsions on the smooth surface, T_i = 30 °C. (a) - (c) are for G = 150, 350 and 550 kg/m^{2}s, respectively.

In Fig. 4.27, the water and 1% emulsion data for D_h = 500 μm and G = 150 kg/m^{2}s are presented in comparison with that of Janssen and Kulacki [107] and Morshed et al. [108]. These two studies offer a limited comparison for similar experimental conditions. Flow boiling was also studied by Gasanov and Bulanov [104] and Bulanov, Skripov and Khmylnik [105]. Comparison with these studies is not feasible due to significant differences in the hydraulic diameter, heater geometry and mass flux.

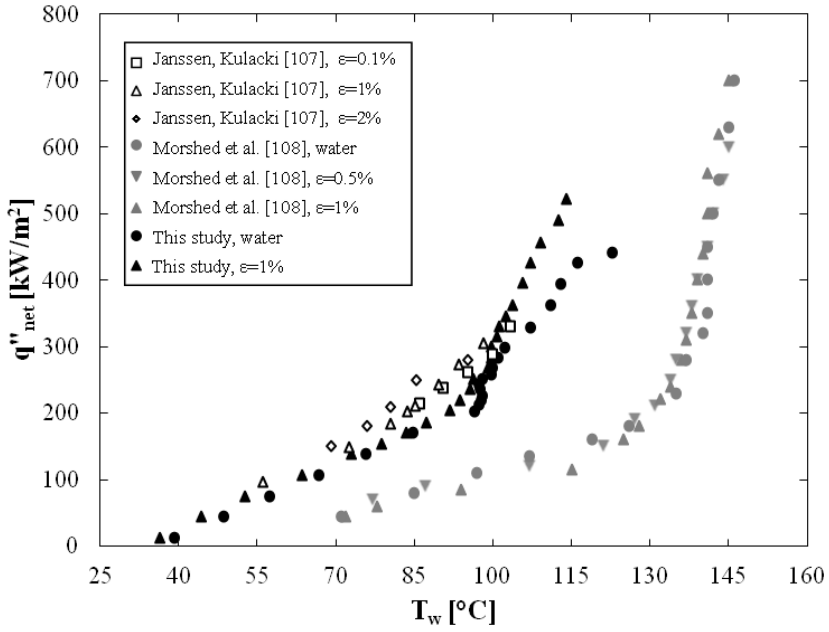

Fig. 4.27. Comparison of D_h = 500 μm, G=150 kg/m^{2}s emulsion boiling data with that of Janssen and Kulacki [107] (D_h = 500 μm, G = 133 kg/m^{2}s) and Morshed et al. [108] (D_h = 672 μm, G = 129 kg/m^{2}s).

It can be seen in Fig. 4.27 that the results of this study and that of Janssen and Kulacki are similar. The boiling curves measured by Morshed et al. are shifted to much higher wall temperatures for a nearly identical inlet temperature of 25 °C, and the boiling curves are relatively insensitive to ε. The Janssen data show continuously increasing heat transfer performance with increasing ε, which is not shown in the data of this study at the higher flowrate of G = 350 kg/m^{2}s. The emulsion data in this investigation show higher heat transfer for lower G so it is possible that for varying ε, a trend similar to Janssen's would be measured on this experimental setup at a lower mass flux of 150 kg/m^{2}s.

Because Morshed et al. measure a boiling curve for water that is also shifted to much higher wall temperatures than those measured here, it can be supposed that the difference in results for both water and emulsions is due to a difference in the experimental setup. It is likely that this is being caused by two factors. First, Janssen and Kulacki and this study both employ long flow development lengths upstream and exit lengths downstream

of the heated section, whereas the entrance and exit of the channel are placed just upstream and downstream of the heated section in Morshed et al.'s apparatus. Second, though the hydraulic diameter is similar, Morshed et al. use a channel that is 0.36mm × 5 mm in cross section, making their channel much narrower than that employed here (25.4 mm wide) or in Janssen and Kulacki's experiments (30 mm). Thus, their channel may be experiencing confinement effects that are not demonstrated for boiling in the wider gaps.

4.3 Water on the porous surfaces

Boiling curves, the measured heat transfer coefficient and pressure drop for water on each porous surface are shown in Figs. 4.28 - 4.31. Many of the trends discussed above for water on the smooth surface are also demonstrated on the porous surfaces, including the lack of superheat at ONB, the boiling curve shifting to the left for increasing mass flux and D_h, and increasing pressure drop for increasing G and D_h. As well, transition to CHF occurs at lower heat fluxes for lower G and D_h on the porous surfaces.

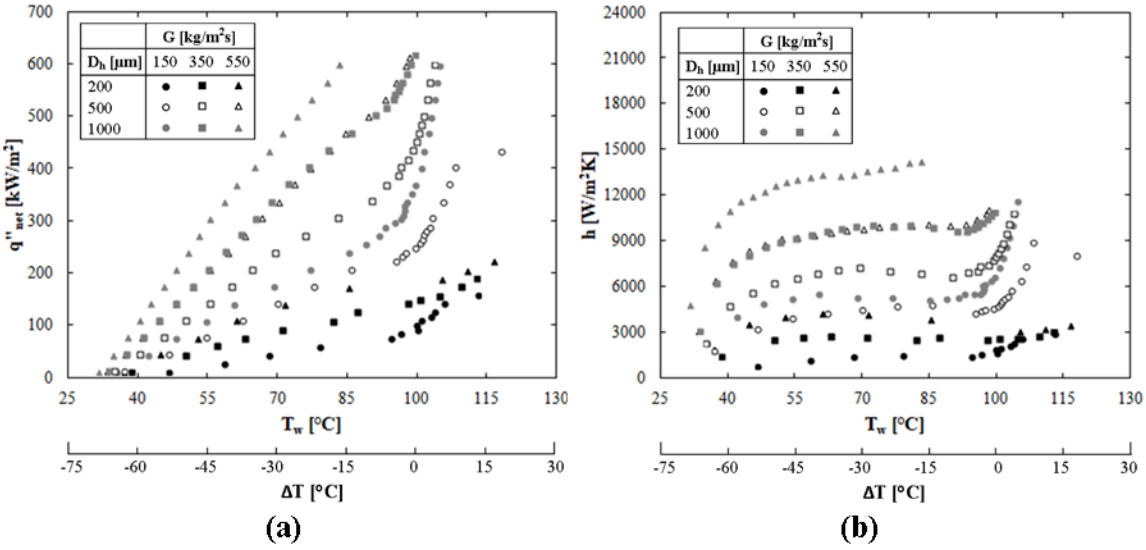

Fig. 4.28. (a) Boiling curve and (b) heat transfer coefficient for water on Porous Surface 1, T_i = 30 °C. $\Delta T = T_w - T_{sat}$.

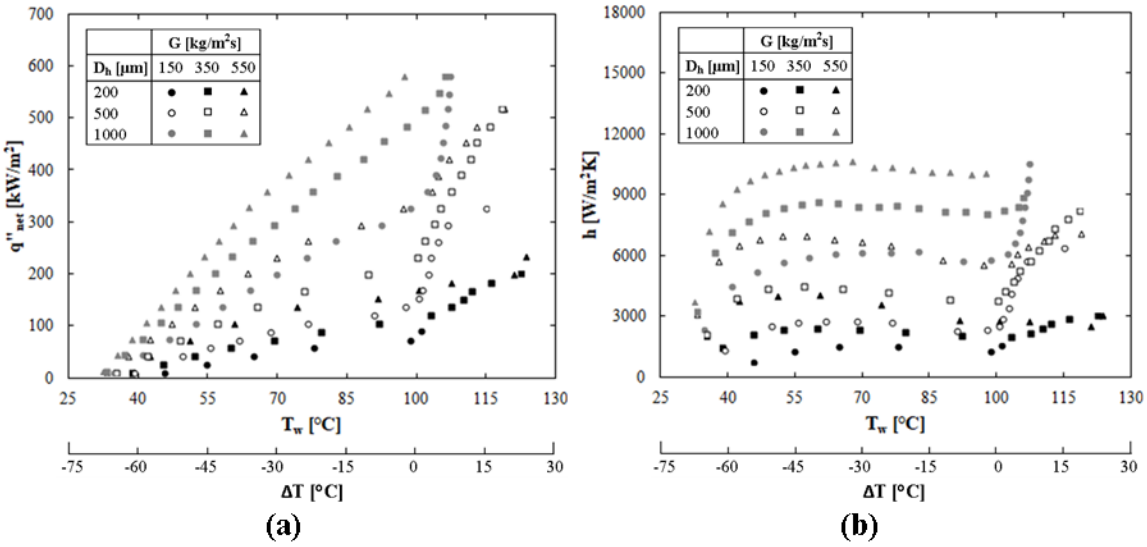

Fig. 4.29. (a) Boiling curve and (b) heat transfer coefficient for water on Porous Surface 2, T_i = 30 °C.

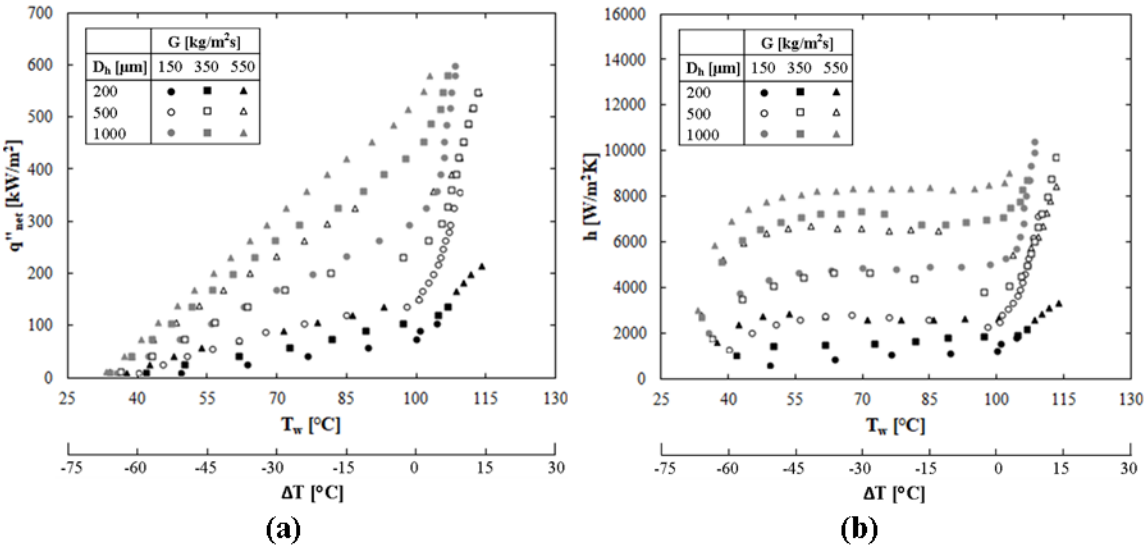

Fig. 4.30. (a) Boiling curve and (b) heat transfer coefficient for water on Porous Surface 3, T_i = 30 °C.

However, the heat transfer behavior on the porous surfaces does show some pronounced differences compared to the smooth surface. On the smooth surface, the heat transfer coefficient increased with decreasing hydraulic diameter in the single-phase region. After ONB, the boiling curves were seen to almost collapse to one curve prior to transition to CHF. On the porous surfaces, h decreases dramatically with decreasing D_h

in the single-phase region. After ONB, some curves do seem to approach each other but all curves for D_h = 200 μm and the G=150 kg/m^{2}s, D_h = 500 μm curves shift to higher wall temperature and often early transition to CHF. For D_h = 1000 μm, h is so high that boiling is not achieved in the range of heat flux studied in some cases, so it is difficult to tell if the curves would collapse for D_h = 500 and 1000 μm after ONB.

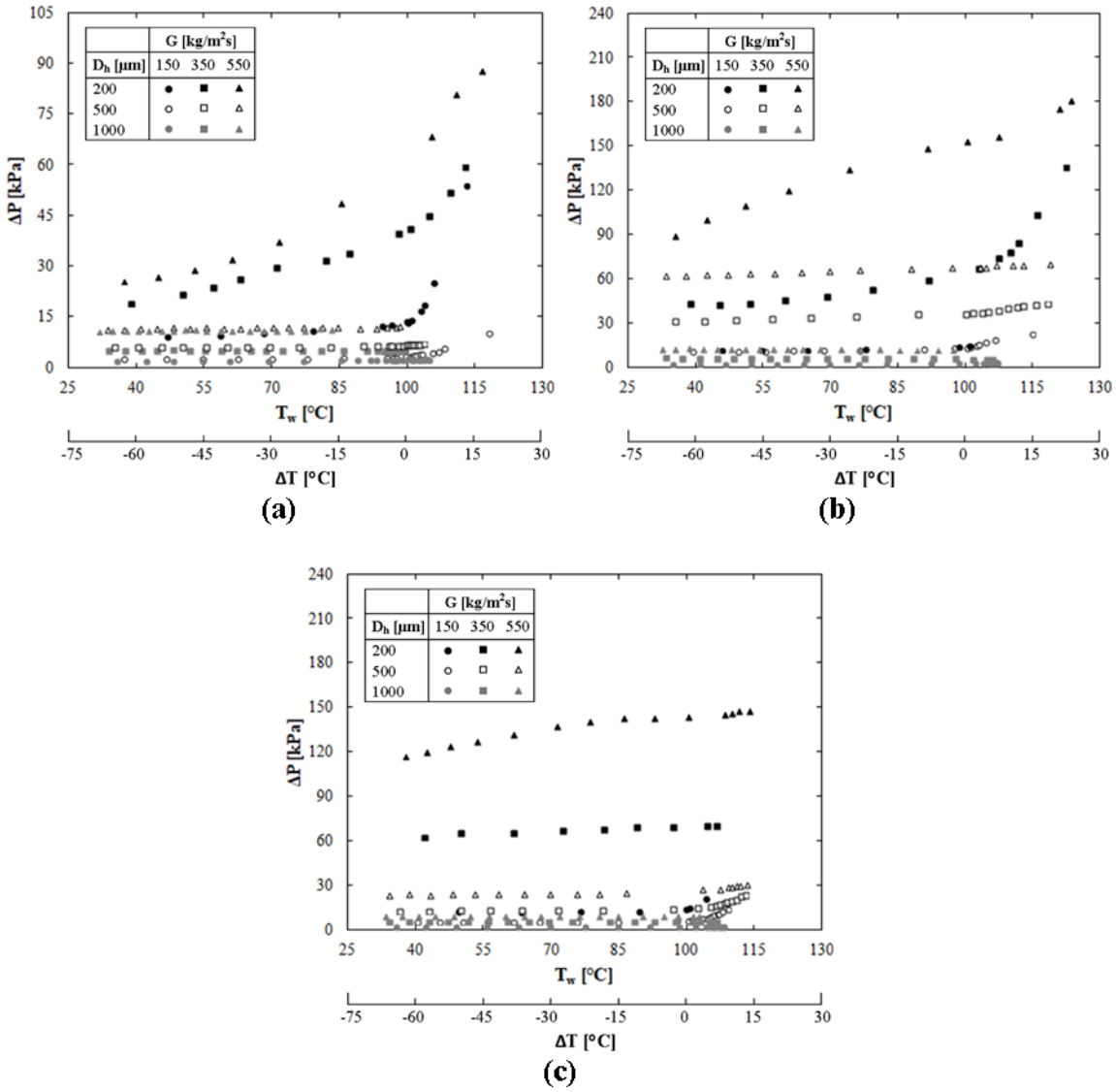

Fig. 4.31. Pressure drop on (a) Porous Surface 1, (b) Porous Surface 2, and (c) Porous Surface 3. T_i = 30 °C.

In the larger gaps, the pressure drop is relatively insensitive to the presence of boiling. In the 200 μm gap, unlike single-phase flow on the smooth surface, the pressure drop

increases prior to the initiation of boiling. This is especially pronounced on Surfaces 1 and 2, where the increase in pressure drop is as large as 200% in some cases. Porous Surface 3 does demonstrate an increase of the pressure drop in the single-phase region, but the increase is less dramatic for this surface.

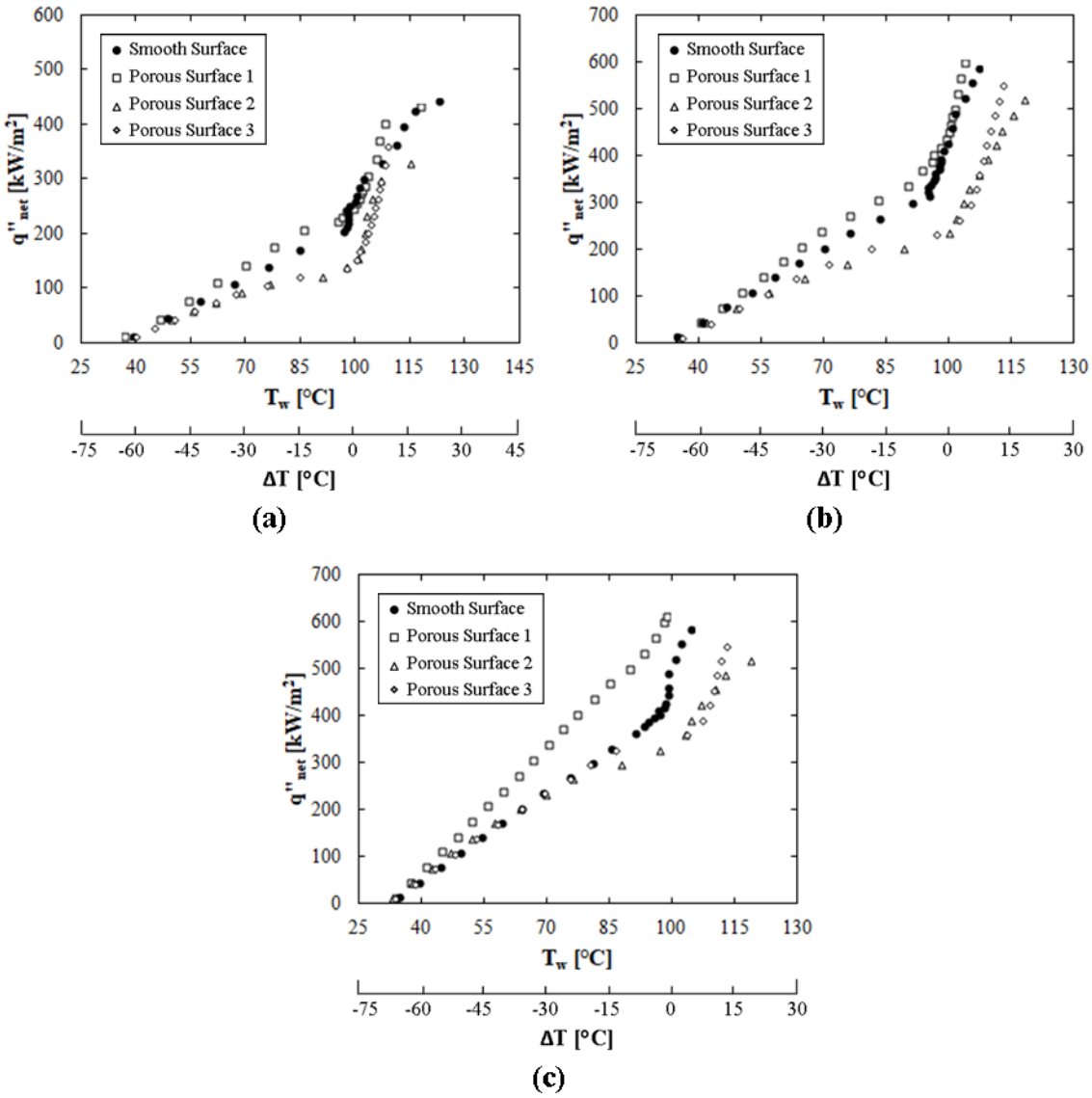

Fig. 4.32. Boiling curves for water on smooth and porous surfaces, D_h = 500 μm, T_i = 30 °C. (a) - (c) are for G = 150, 350, and 550 kg/m^{2}s, respectively.

A comparison of the smooth and porous surfaces' boiling curves and heat transfer coefficient are shown in Figs. 4.32 and 4.33, respectively, as a function of mass flux. It is

shown that Porous Surface 1 exhibits a higher single-phase heat transfer coefficient at every mass flux. This corresponds to a shift of the boiling curve to lower wall temperatures. After ONB, the boiling curve and heat transfer coefficient for the smooth surface and Porous Surface 1 collapse onto one curve. For G = 150 kg/m^{2}s, both the smooth surface and Porous Surface 1 transition to CHF.

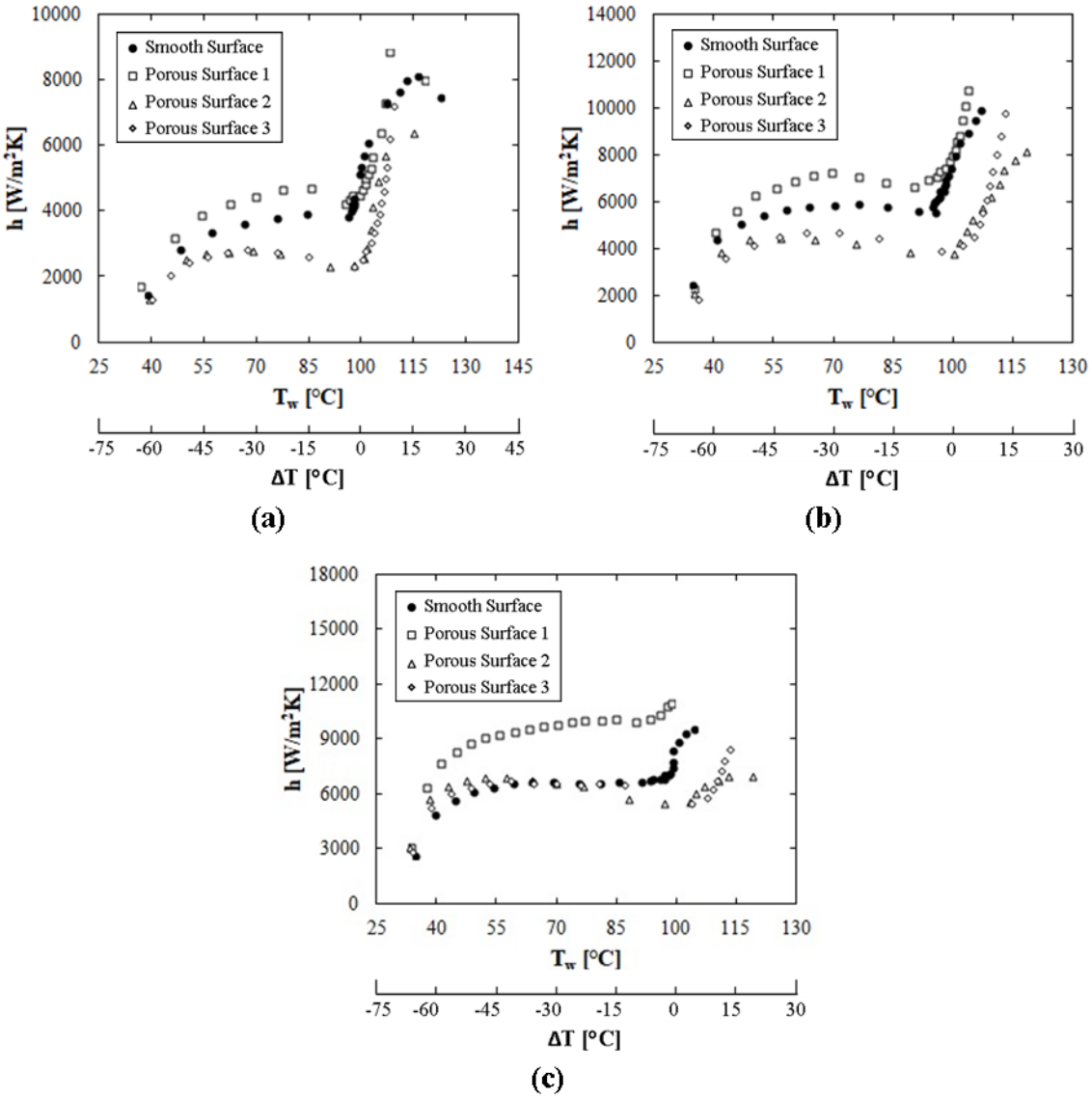

Fig. 4.33. Heat transfer coefficient for water on smooth and porous surfaces, D_h = 500 μm, T_i = 30 °C. (a) - (c) are for G = 150, 350, and 550 kg/m^{2}s, respectively.

The boiling curve for Porous Surfaces 2 and 3 follow the same path as the smooth surface and Surface 1 for $T_w < 55$ °C. At higher temperatures, the boiling curve for Surfaces 2 and 3 shift to the right, with a corresponding decrease in the heat transfer coefficient and an earlier transition to CHF. It seems this effect diminishes with increasing G.

The boiling curve and h as a function of D_h are shown in Figs. 4.34 and 4.35.

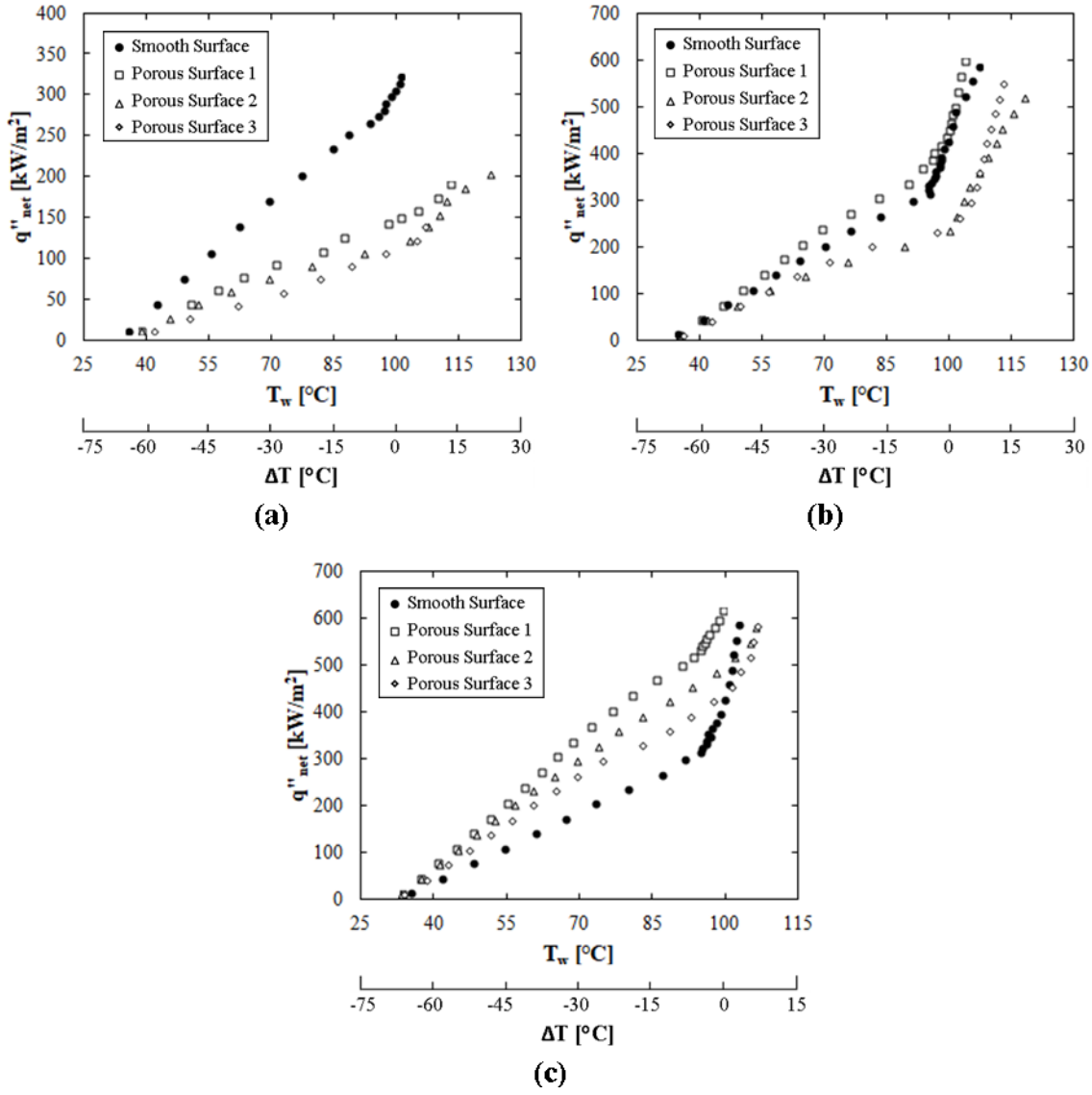

Fig. 4.34. Boiling curves for water on smooth and porous surfaces, G = 350 kg/m^{2}s, T_i = 30 °C. (a) - (c) are for D_h = 200, 500, and 1000 μm, respectively.

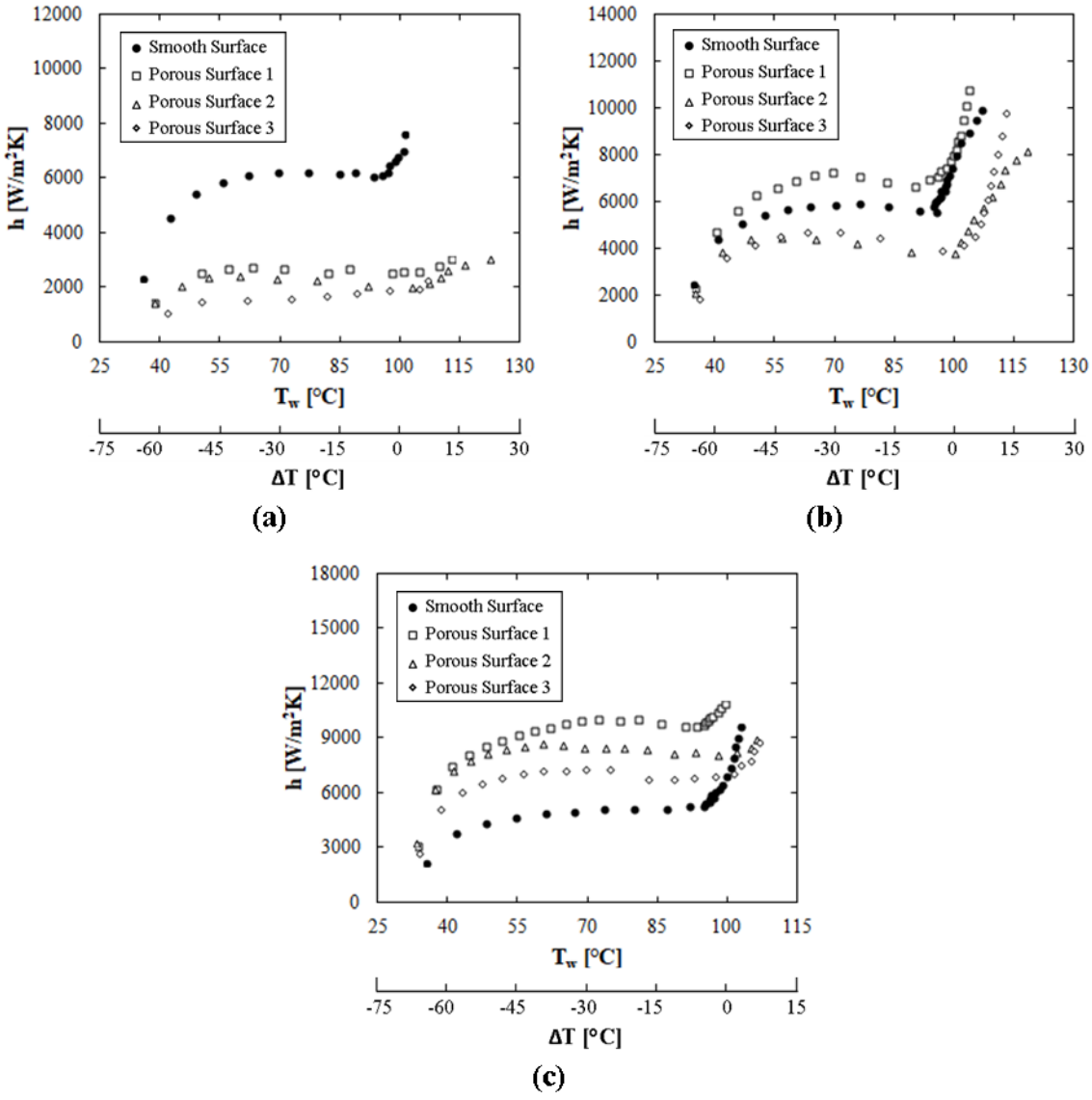

Fig. 4.35. Heat transfer coefficient for water on smooth and porous surfaces, G = 350 kg/m^{2}s, T_i = 30 °C. (a) - (c) are for D_h = 200, 500, and 1000 μm, respectively.

At the lowest gap size, the porous surfaces all exhibit diminished heat transfer compared to the smooth surface, causing transition to CHF at a much lower heat flux than that for the smooth surface. As the gap size increases, the porous surfaces demonstrate increasing heat transfer with respect to the smooth surface. At D_h = 500 μm, Porous Surface 1 exhibits a higher heat transfer coefficient than the smooth surface. At D_h = 1000 μm, all three surfaces demonstrate better heat transfer than the smooth surface. In

general, Porous Surfaces 2 and 3 show similar heat transfer results, though Porous Surface 2 seems to transition to CHF earlier than Surface 3.

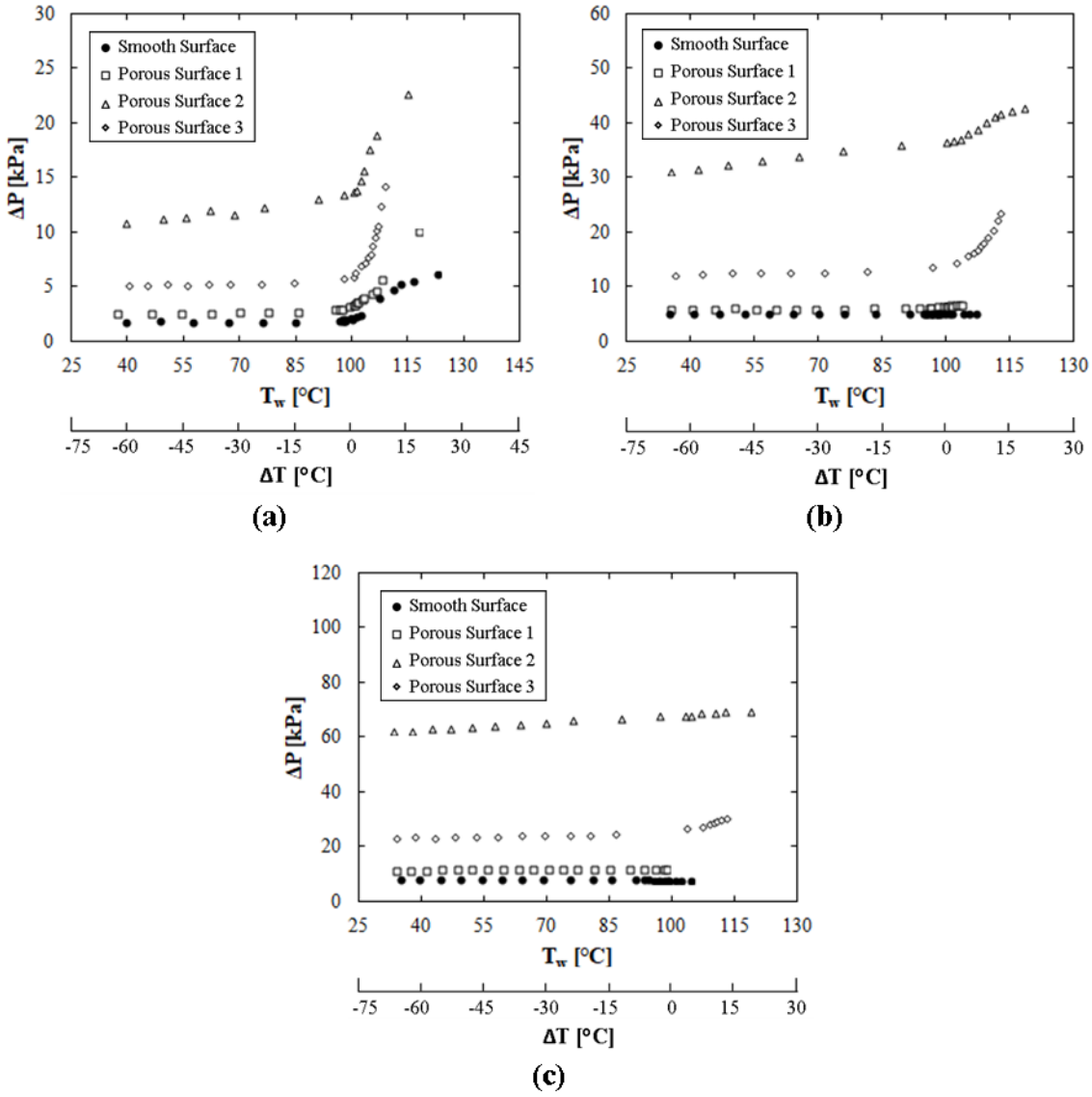

Fig. 4.36. Pressure drop for water on smooth and porous surfaces, D_h = 500 μm, T_i = 30 °C. (a) - (c) are for G = 150, 350, and 550 kg/m^{2}s, respectively.

The pressure drop for each surface as a function of mass flux and hydraulic diameter are shown in Figs. 4.36 and 4.37, respectively. For D_h = 500 μm, the pressure drop on Porous Surface 1 is almost equivalent to that for the smooth surface over the range of mass flux studied (Fig. 4.36). The pressure drop on Porous Surface 2 is almost always

the largest measured, with the measured pressure drop being up to 8 times larger than that for the smooth surface at the same wall temperature. Though the pressure drop for Porous Surface 1 is nearly equivalent to the smooth surface case for D_h = 500, for the 200 and 1000 μm gaps, the pressure drop is much larger for Porous Surface 1 than the smooth surface.

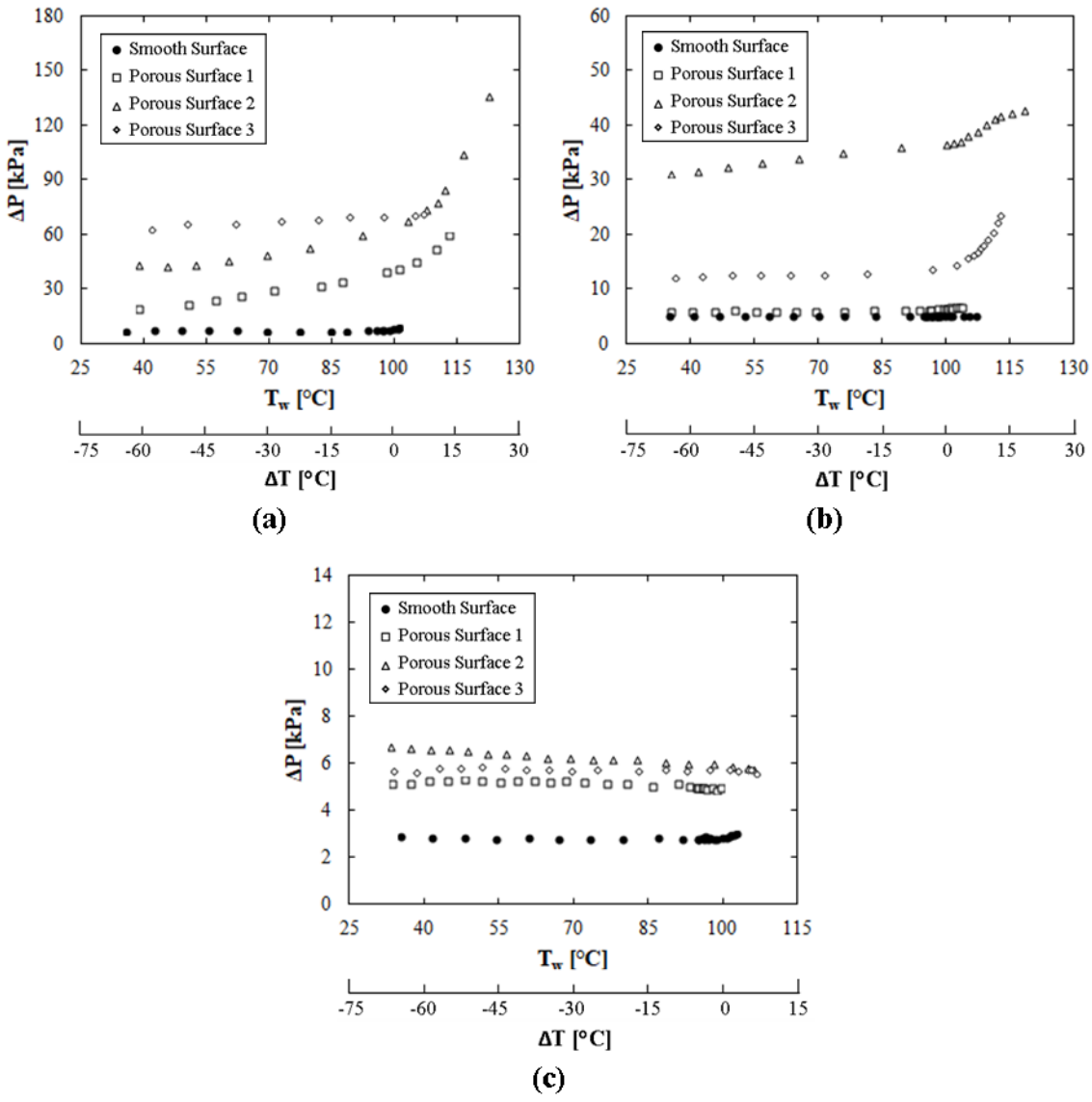

Fig. 4.37. Pressure drop for water on smooth and porous surfaces, G = 350 kg/m^{2}s, T_i = 30 °C. (a) - (c) are for D_h = 200, 500, and 1000 μm, respectively.

For flow over the top of a porous wall, there are two ways that the porous surface can increase the pressure drop (or decrease momentum). First, the presence of the porous surface increases the roughness of the wall. Second, flow at the pore scale serves as a sink of momentum from viscous and inertial losses in the porous structure. From the top views in Figs. 3.10 - 3.12, we see that Porous Surface 1 has a more packed structure and lower porosity than Surfaces 2 and 3. This results in Surfaces 2 and 3 appearing as "rougher" structures to the flow over the wall. If we compare the side views for Surfaces 2 and 3, we can see that Surface 2 has a more open pore structure and Surface 3 is more densely packed. Thus, Porous Surface 2 should have more flow through the surface than Porous Surface 3, increasing the pressure losses at the pore scale for Porous Surface 2.

4.4 Emulsions on the porous surfaces

The boiling curves and measured heat transfer coefficient as a function of ε and gap size on Porous Surface 1 are shown in Fig. 4.38. For D_h = 200 μm, the emulsions all display decreased heat transfer compared to water, with a shift of the boiling curve to higher wall temperatures and transition to CHF at very low heat fluxes (Fig. 4.38a). For D_h = 500 μm, the 0.1% emulsion shows a slight shift of the boiling curve to the right below the boiling point of the continuous component. At ~100 °C, a further diminishment in heat transfer is seen and CHF is approached. For higher ε, the boiling curve is shifted to even higher wall temperatures. It appears as though CHF is independent of ε on Porous Surface 1. For D_h = 1000 μm, there is a shift in the boiling curve to lower T_w for all ε. However, the heat transfer coefficient for the emulsions is lower than that of water at the same wall temperature, indicating that the difference in temperature between the wall and fluid is higher for the emulsions than water.

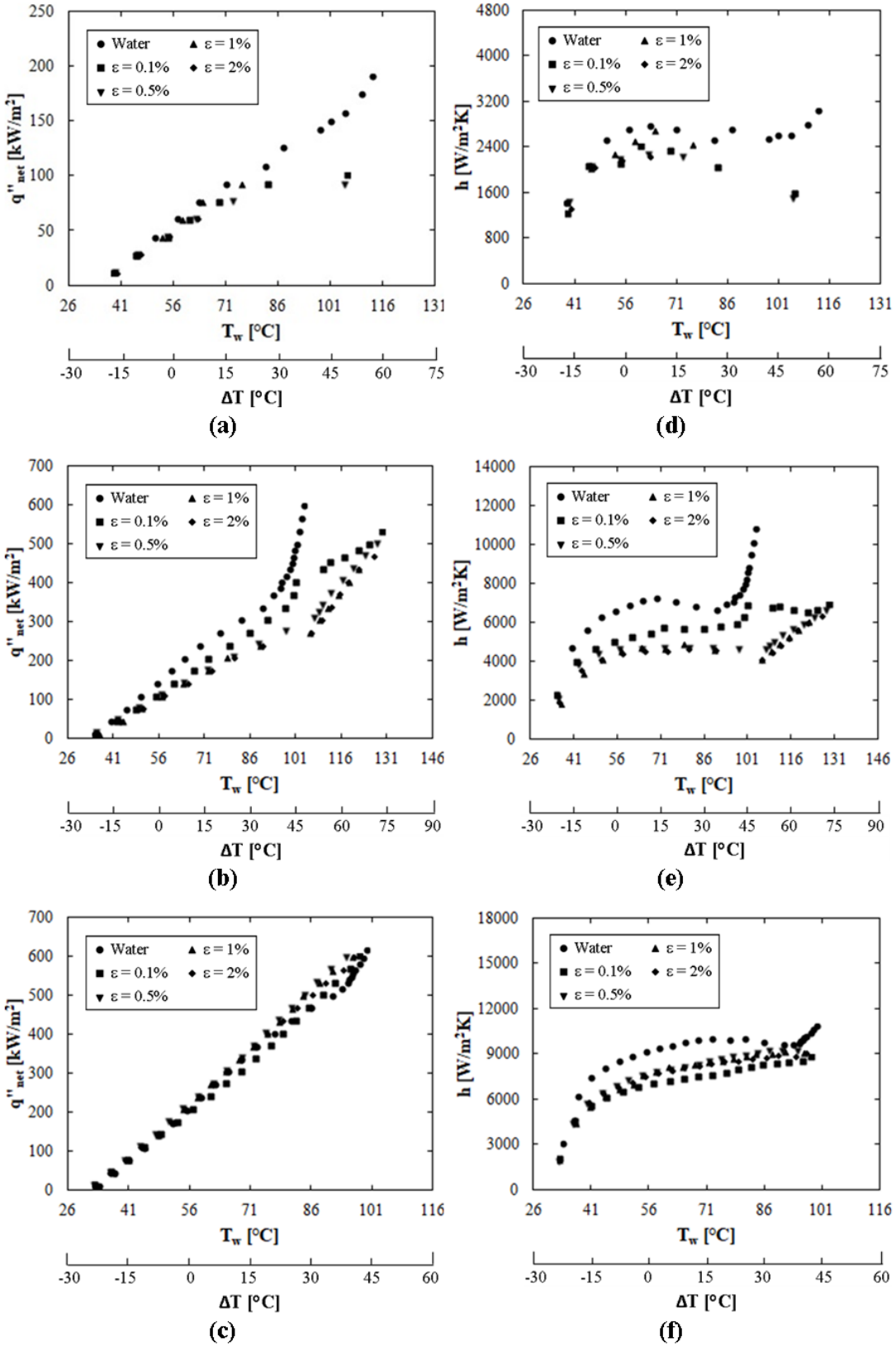

Fig. 4.38. (a) - (c) Boiling curves and (d) - (f) heat transfer coefficient for emulsions on Porous Surface 1 with D_h = 200, 500, and 1000 μm. T_i = 30 °C, G = 350 kg/m^{2}s.

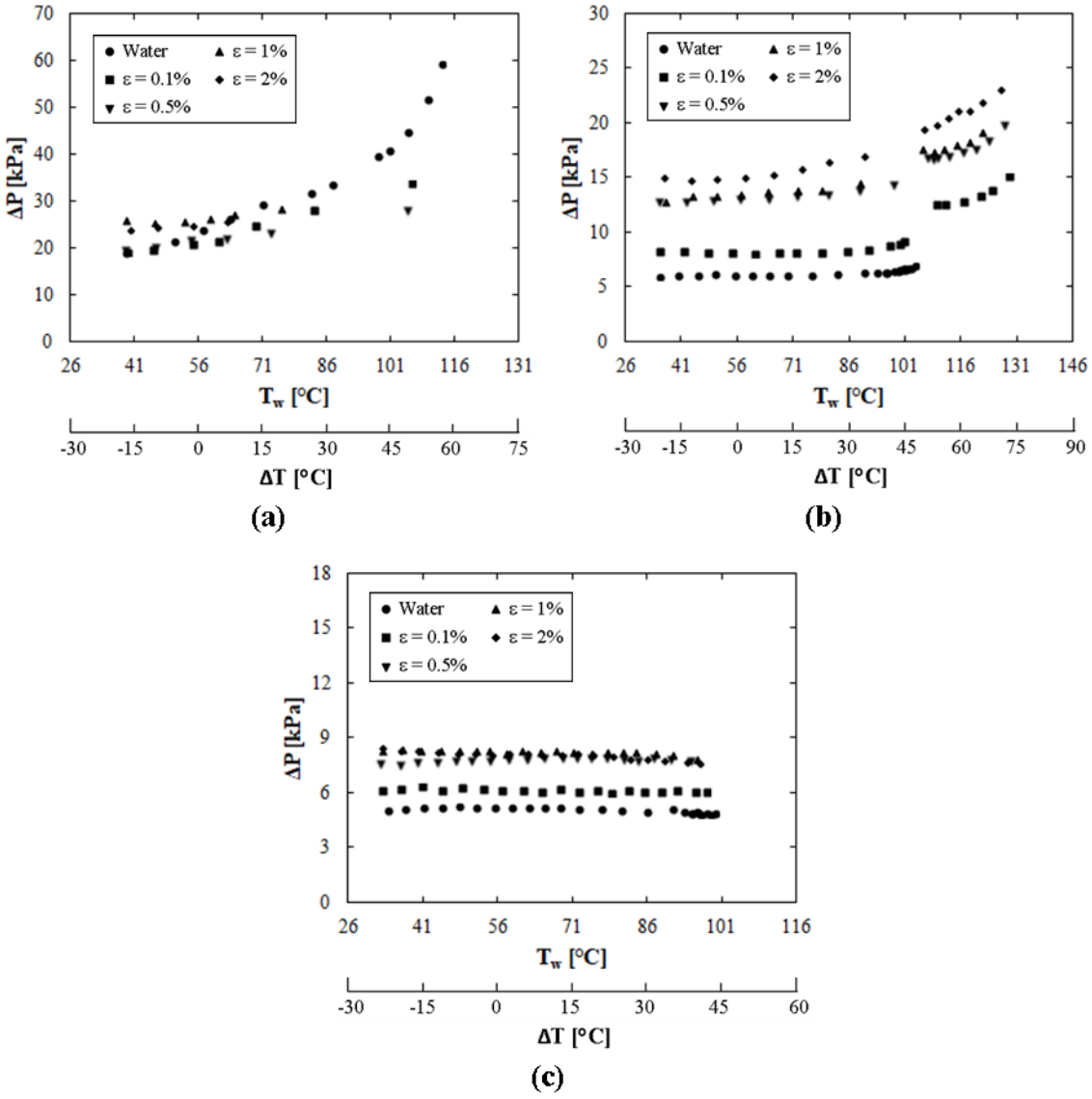

Fig. 4.39. Pressure drop for emulsions on Porous Surface 1, T_i = 30 °C, G = 350 kg/m^{2}s. (a) - (c) are for D_h = 200, 500 and 1000 µm, respectively.

The corresponding pressure drops for Surface 1 are shown in Fig. 4.39. For the smallest gap, the pressure appears to be relatively insensitive to ε, though CHF occurs so early in this gap that this conclusion is uncertain. For D_h = 500 and 1000 µm, the pressure drop increases with increasing ε and the emulsions demonstrate a larger increase in pressure drop after 100 °C than water. The effect of ε on pressure drop seems to diminish with increasing D_h after 500 µm.

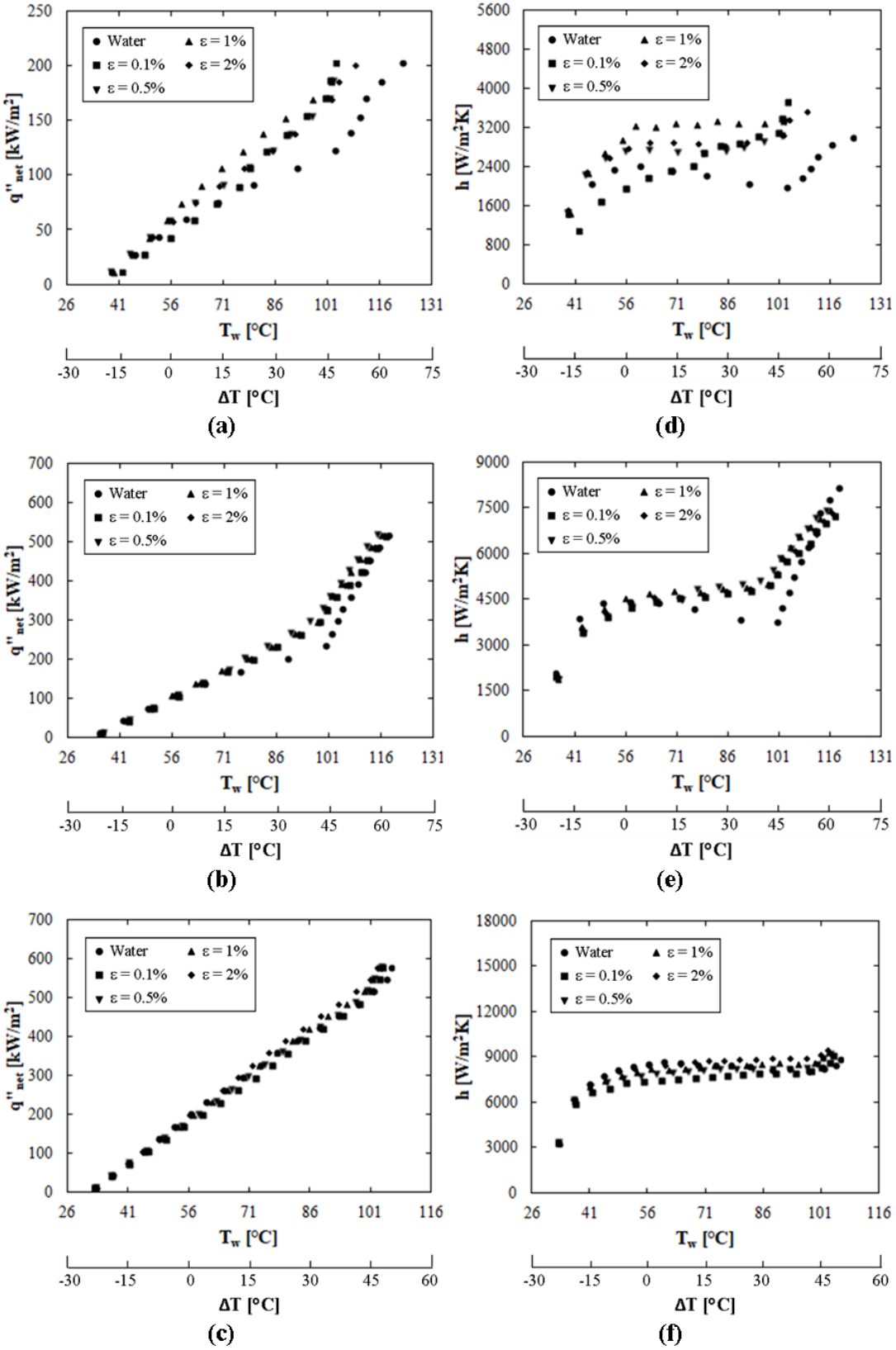

Fig. 4.40. (a) - (c) Boiling curves and (d) - (f) heat transfer coefficient for emulsions on Porous Surface 2 with D_h = 200, 500, and 1000 μm. T_i = 30 °C, G = 350 kg/m^{2}s.

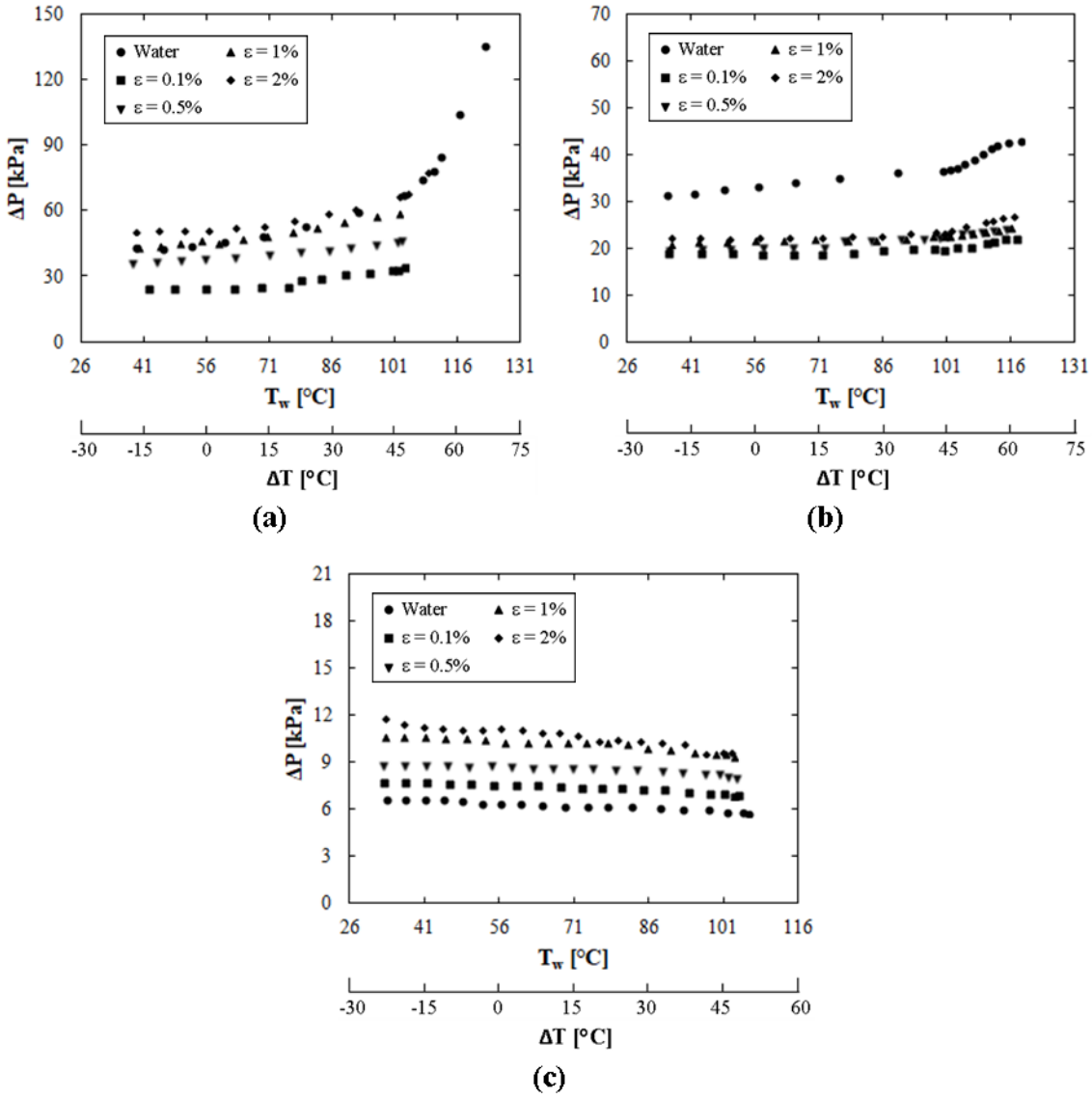

Fig. 4.41. Pressure drop for emulsions on Porous Surface 2, T_i = 30 °C, G = 350 kg/m^{2}s. (a) - (c) are for D_h = 200, 500 and 1000 µm, respectively.

The boiling curves and heat transfer coefficient for Porous Surface 2 are shown in Fig. 4.40. On this surface, the emulsions increase heat transfer for the majority of the experiments shown. The largest increases in heat transfer are seen for D_h = 200 µm, where the emulsions shift the boiling curve to lower T_w and increase h. The largest heat transfer coefficient is measured for ε = 1%. For this gap size, a large increase in the heat transfer coefficient is shown after boiling of the disperse component commences for ε =

0.1%. For $\varepsilon = 0.5$, 1 and 2%, the increase in h for $56\ ^\circ < T_w < 100\ ^\circ C$ is more moderate and the increased benefit compared to water with increasing T_w is primarily due to the decrease in the water heat transfer coefficient.

A similar moderate increase in the heat transfer coefficient over this range of wall temperatures is seen for all ε at $D_h = 500\ \mu m$. Again, the primary increase in heat transfer compared to water comes as a result of a diminishing h with increasing T_w for water. For $D_h = 1000\ \mu m$, the emulsions shift the boiling curve slightly to the left and result in slightly higher heat transfer coefficients, with the largest heat transfer coefficients measured for $\varepsilon = 2\%$.

The increase in heat transfer on Porous Surface 2 is likely a result of the open pore network on both the top and interior of the porous surface. This open pore network would allow FC-72 droplets to flow down into the porous structure and nucleate bubbles within the confined space there. After nucleation, the resulting vapor would also flow out of this porous structure more easily than in a structure that is more densely packed, either at the top of the surface (like Surface 1) or in the interior of the surface (like Surface 3).

For a subset of the data on this surface, improved heat transfer and a decrease in the pressure drop are measured for boiling emulsions (Fig. 4.41). This is demonstrated for $D_h = 200$ and $500\ \mu m$, where the pressure drop measured for $\varepsilon = 0.1\%$ is significantly lower than that for water. At $D_h = 200\ \mu m$, the pressure drop for $\varepsilon = 1$ and 2% are comparable to that for water; at $D_h = 500\ \mu m$, the measured pressure drop for water is much higher than the emulsions over the full range of ε. At $D_h = 1000\ \mu m$, where the heat transfer benefit is the lowest, the pressure drop for all emulsion cases is higher than that for water. At all gap sizes, the pressure drop increases with increasing ε after 0.1%.

For heat transfer on Porous Surface 3, at D_h = 200 μm, the boiling curve and h for ε = 0.5 and 1% are fairly similar to those for water (Fig. 4.42a and d). For ε = 0.1%, heat transfer is diminished compared to water. The 2% emulsion case shows a much higher heat transfer coefficient than water over the full range of wall temperatures. Thus, h increases with increasing ε up to 2% at this gap size.

For D_h = 500 μm, the boiling curve and heat transfer coefficient are similar to water at low T_w for all ε (Fig. 4.42b and e). For T_w > 80 °C, the water case shows a slight shift of the boiling curve to higher T_w and a decrease in h. For this same range of T_w, the emulsion cases demonstrate a slightly increasing heat transfer coefficient with increasing T_w, but the primary benefit compared to water comes as a result of the diminishing water heat transfer coefficient. For the 1000 μm gap, the boiling curves for water and all emulsions are similar (Fig. 4.42c). The water heat transfer coefficient is slightly higher at lower T_w, but h for the emulsions is slightly higher for T_w > 70 °C as a result of increasing h for the emulsions as the disperse component boils (Fig. 4.42f).

The pressure drop on Porous Surface 3 is shown in Fig. 4.43. It can be seen that for D_h = 200 and 1000 μm, the pressure drop is larger for the emulsions than for water at all ε. The pressure drop for ε = 2% in the 200 μm displays interesting behavior. Rather than increasing steadily with increasing T_w, the pressure drop dramatically increases suddenly at T_w = 71 °C. Comparison with Fig. 4.42 shows that this coincides with a significant increase in heat transfer. The pressure drop for ε = 2% is also much greater than that for ε = 0.1, 0.5 or 1% at this gap size. For D_h = 500 μm, the pressure drop for ε = 0.1% is lower than for water and ε = 0.5, 1 and 2% display equivalent or larger pressure drops than water. The pressure drop increases with increasing ε for every gap size.

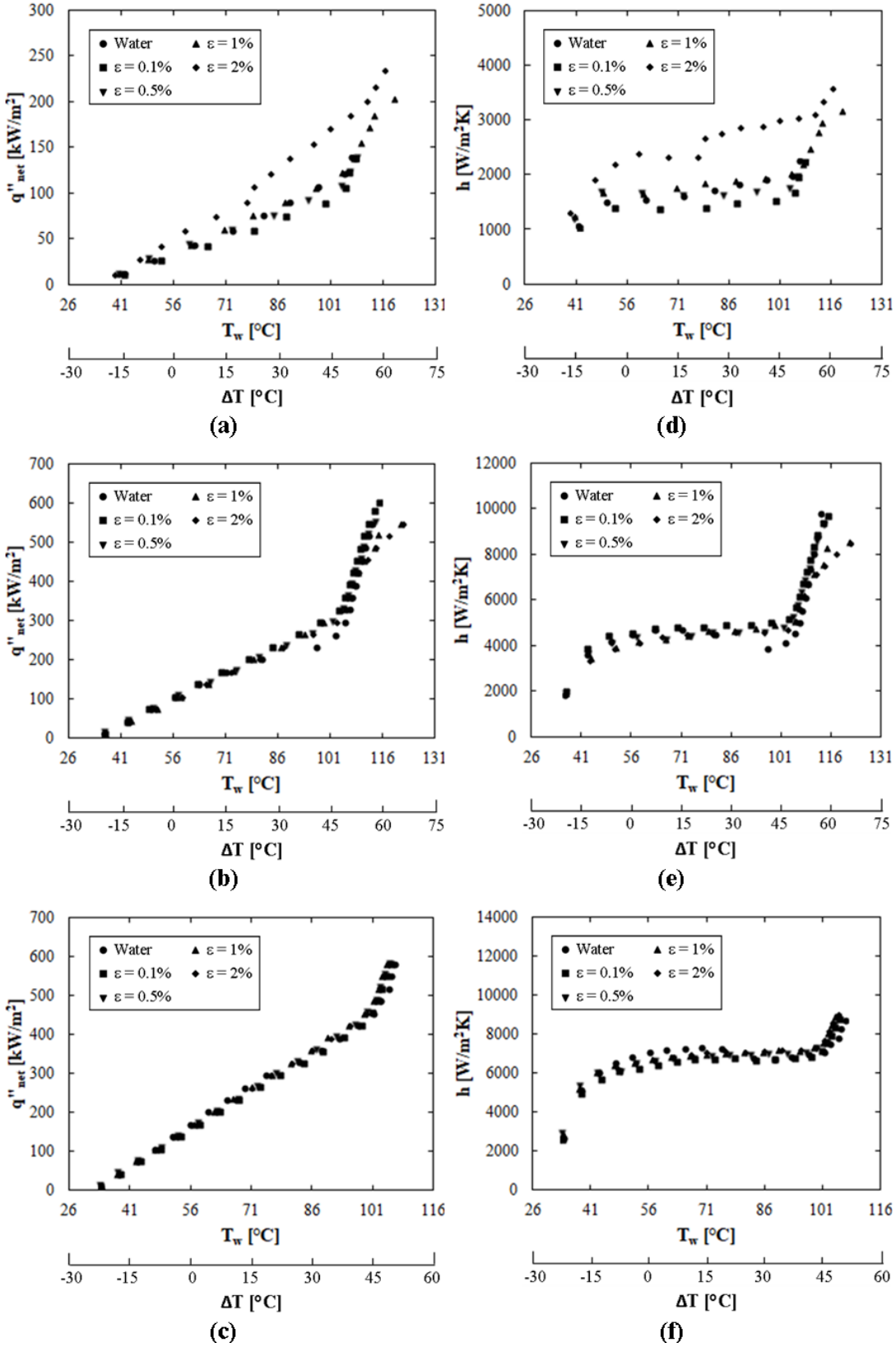

Fig. 4.42. (a) - (c) Boiling curves and (d) - (f) heat transfer coefficient for emulsions on Porous Surface 3 with D_h = 200, 500, and 1000 μm. T_i = 30 °C, G = 350 kg/m^{2}s.

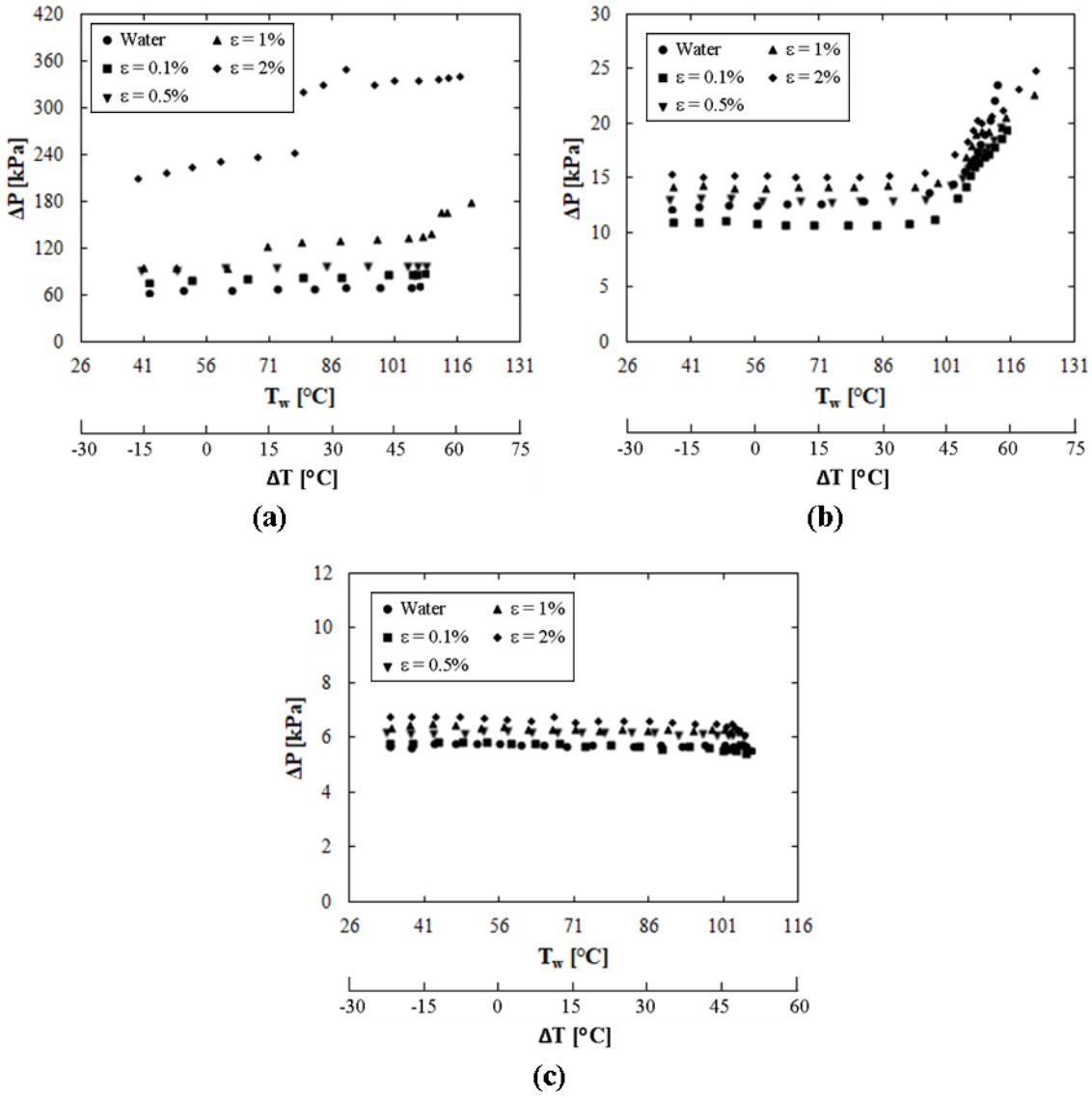

Fig. 4.43. Pressure drop for emulsions on Porous Surface 3, T_i = 30 °C, G = 350 kg/m^{2}s. (a) - (c) are for D_h = 200, 500 and 1000 µm, respectively.

Comparisons of the heat transfer on the smooth and microporous surfaces are shown as a function of mass flux in Fig. 4.44 and gap size in Fig. 4.45. It can be seen that for the 500 µm gap size across the range of mass flux studied, Porous Surface 1 consistently has the highest heat transfer coefficients for boiling of water and the lowest heat transfer coefficients for boiling emulsions (Fig. 4.44). For G = 150 kg/m^{2}s, the boiling curve for Surface 2 shifts to slightly lower T_w than that for Surface 3, but Surface 2 transitions to

CHF at a slightly lower heat flux. At this mass flux, all three surfaces have diminished emulsion boiling heat transfer compared to the smooth surface. At G = 350 kg/m^{2}s, Porous Surfaces 2 and 3 show very similar heat transfer behavior. Up to T_w = 86 °C, all four surfaces have nearly equivalent boiling curves and heat transfer coefficients for the 1% emulsion. For T_w > 86 °C, Porous Surface 1 demonstrates a shift of the boiling curve to higher T_w and the boiling curve for the smooth surface shifts to the left. For G = 550 kg/m^{2}s and T_w < 86 °C, the three porous surfaces all show higher heat transfer than the smooth surface. For T_w > 86 °C, Porous Surfaces 1 and 3 shift to higher T_w, with a greater shift occurring for Surface 1, and Porous surface 2 and the smooth surface have approximately the same heat transfer coefficient and boiling curve.

For D_h = 200 μm and G = 350 kg/m^{2}s, the three porous surfaces all show diminished heat transfer with respect to the smooth surface for boiling of emulsions (Fig. 4.45a and d). Surface 1 transitions to CHF at a very low heat flux and Surface 3 demonstrates a shift in the boiling curve to significantly higher wall temperatures. Surfaces 2 and 3 transition to CHF at approximately the same heat flux. For D_h = 1000 μm, all three porous surfaces show increased heat transfer compared to the smooth surface. For Surface 1, the boiling curve shifts to much lower T_w. More moderate decreases in T_w are seen for Surfaces 2 and 3, with a slightly larger decrease in T_w measured for Surface 2. Thus, it appears the porous surfaces have better heat transfer performance compared to the smooth surface with increasing gap size. At D_h = 1000 μm, the emulsions also provided better cooling performance than water on every surface.

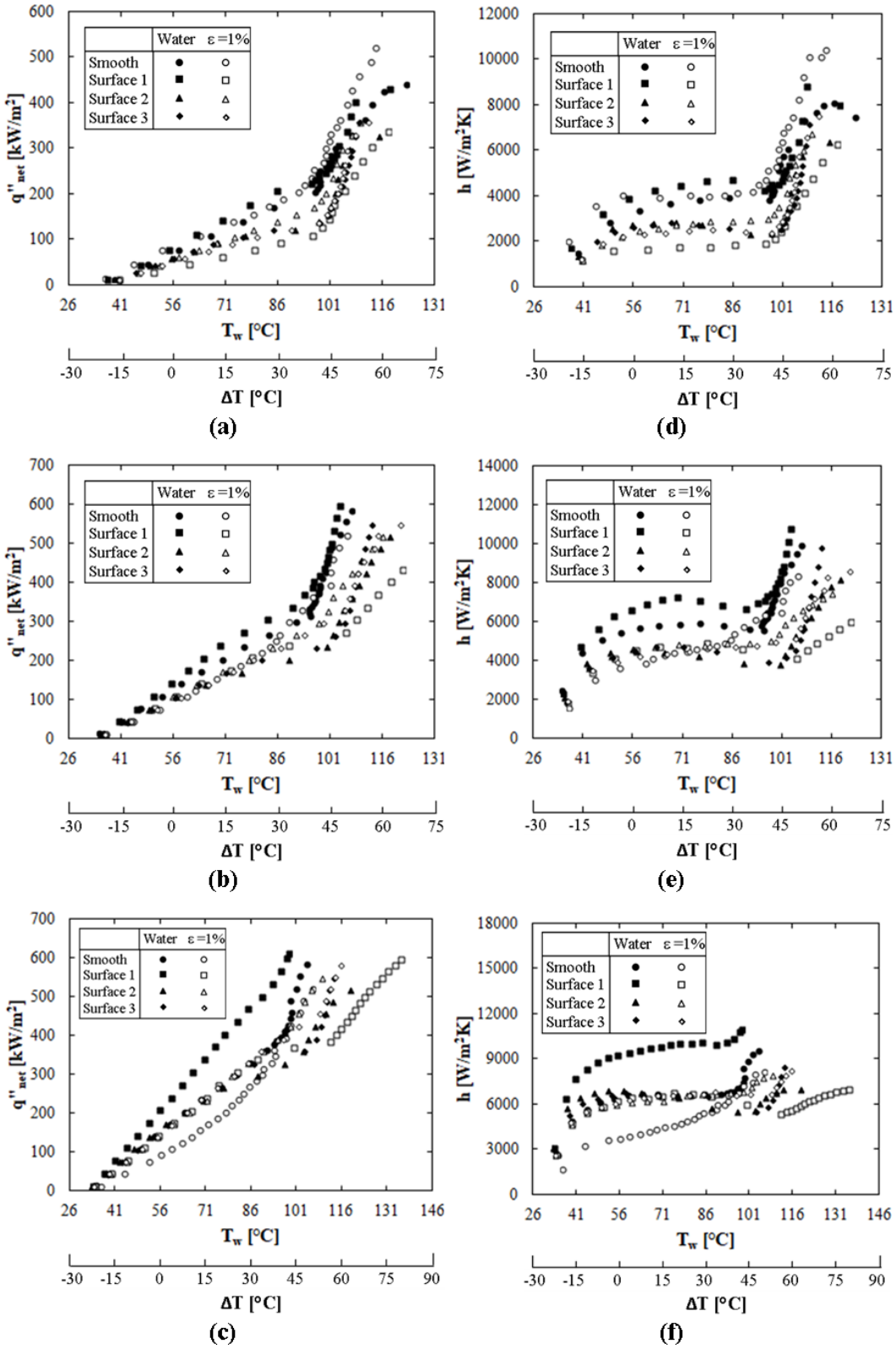

Fig. 4.44. (a) - (c) Boiling curves and (d) - (f) heat transfer coefficient for water and 1% emulsions on smooth and microporous surfaces with G = 150, 350, and 550 kg/m^{2}s, respectively. T_i = 30 °C, D_h = 500 μm.

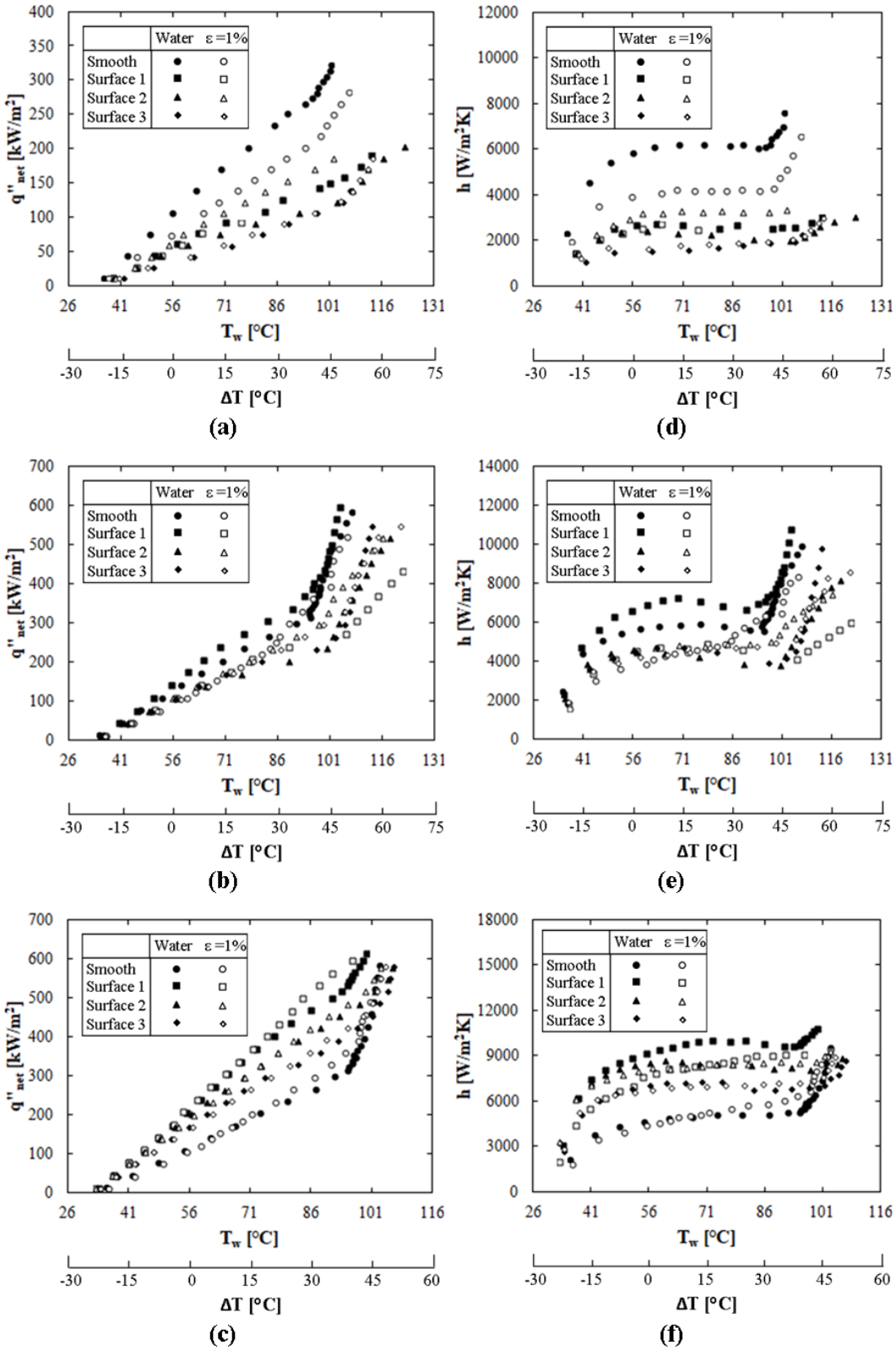

Fig. 4.45. (a) - (c) Boiling curves and (d) - (f) heat transfer coefficient for water and 1% emulsions on smooth and microporous surfaces with D_h = 200, 500, and 1000 μm, respectively. T_i = 30 °C, G = 350 kg/m^{2}s.

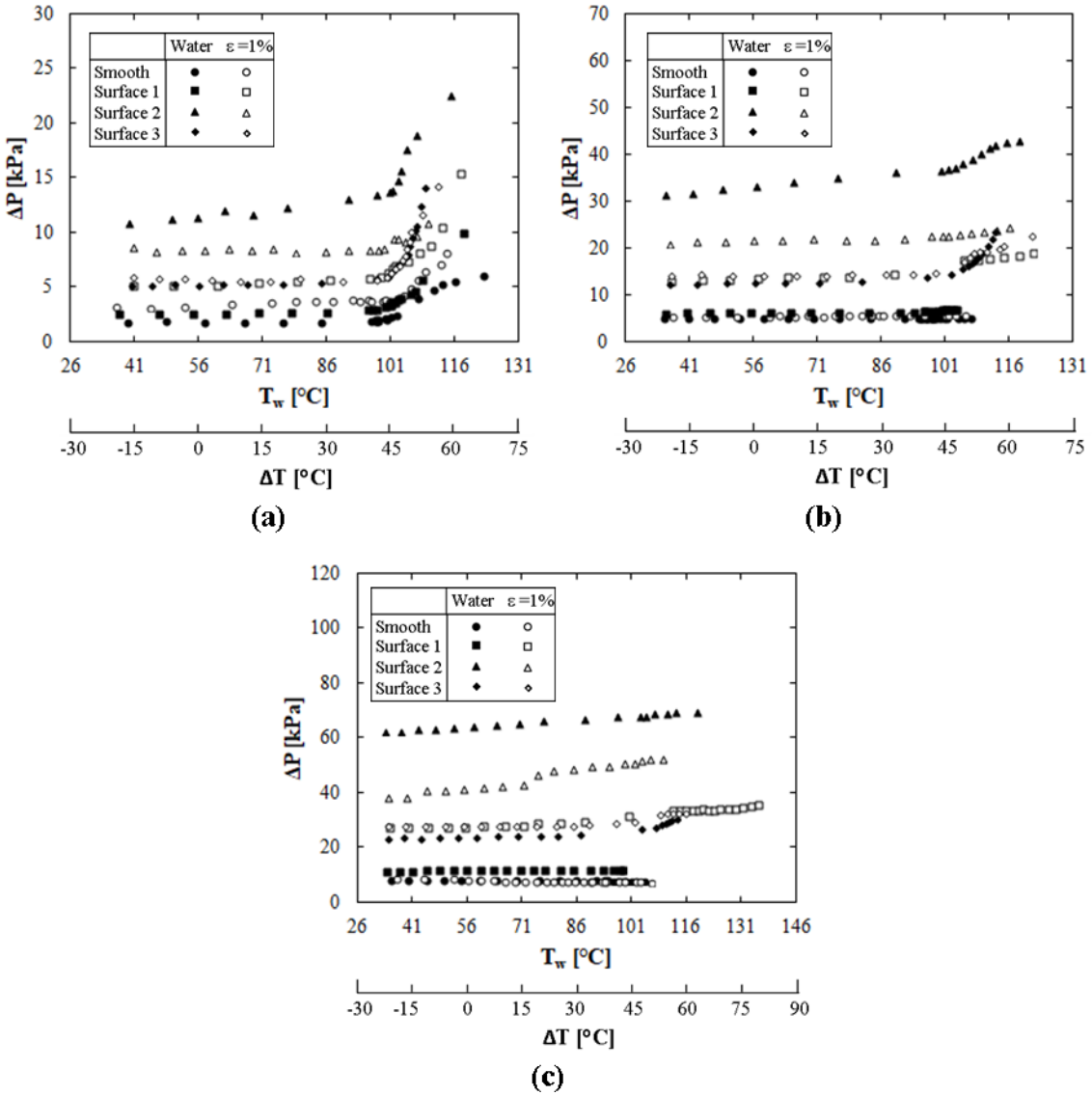

Fig. 4.46. Pressure drop for water and 1% emulsions on the smooth and microporous surfaces, D_h = 500μm, T_i = 30 °C. (a) - (c) are for G = 150, 350 and 550 kg/m^{2}s, respectively.

The measured pressure drop for each surface are presented as a function of mass flux in Fig. 4.46 and gap size in Fig. 4.47. Similar to what was noted for boiling water on the porous surfaces, Porous Surface 2 consistently had the highest pressure drop in the emulsion boiling data set. At D_h = 500 μm, Porous Surfaces 1 and 3 displayed similar pressure drop behavior over the range of G tested (Fig. 4.46). For D_h = 200 μm, Porous

Surface 3 had the highest measured pressure drop, with a step increase displayed at T_w ~ 71 °C (Fig. 4.47a). This step increase was not coincident with an increase in heat transfer as occurred with the 2% emulsion on this surface. For D_h = 500 μm, Porous Surfaces 1 and 3 display a similar measured pressure drop (Fig. 4.47b), and that for Surface 1 was slightly higher in the 1000 μm gap (Fig. 4.47c).

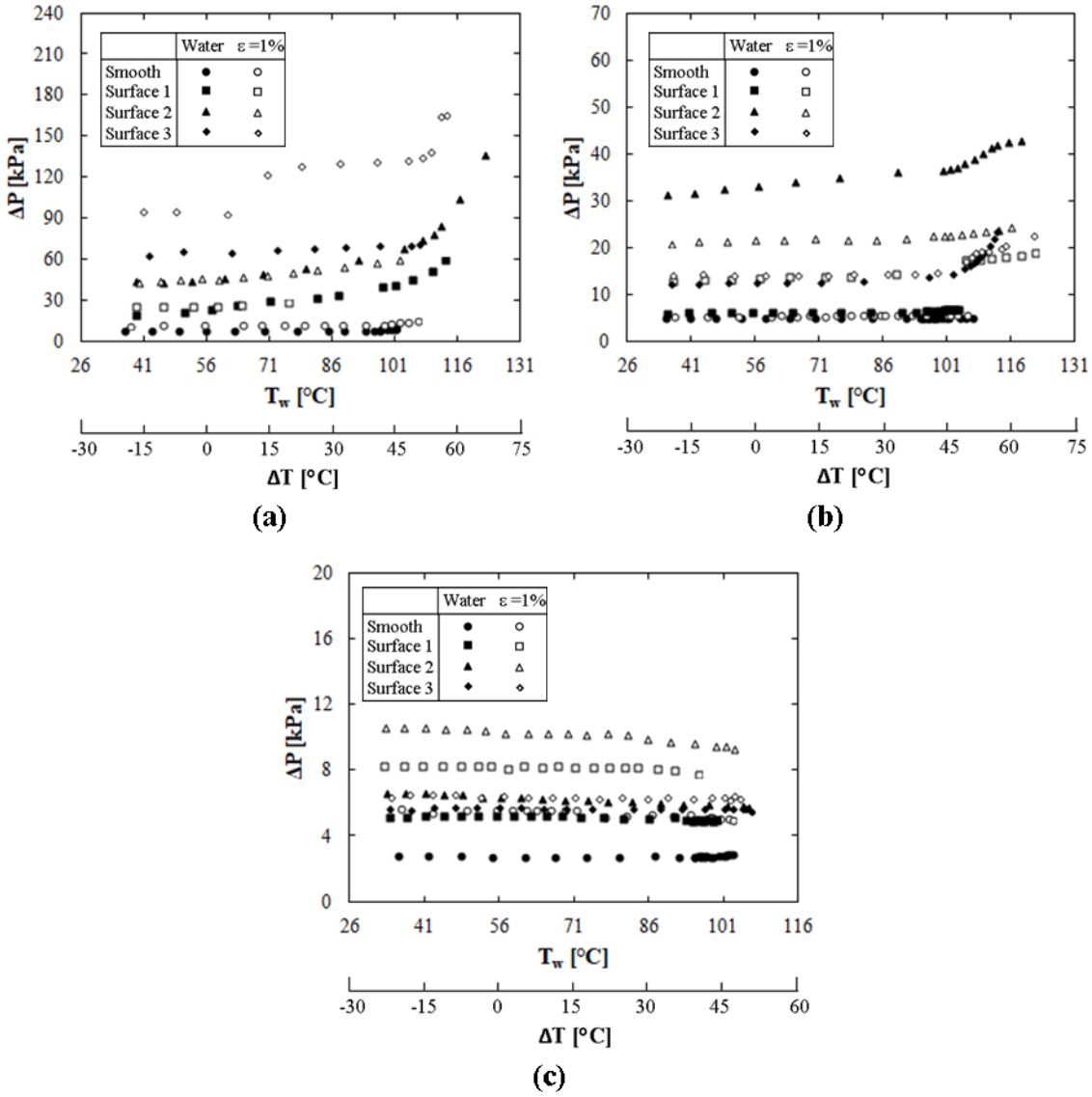

Fig. 4.47. Pressure drop for water and 1% emulsions on the smooth and microporous surfaces, G = 350 kg/m^{2}s, T_i = 30 °C. (a) - (c) are for D_h = 200, 500 and 1000 μm, respectively.

5. Physical Mechanisms and Correlation

For single-component single-phase flows, differential equations governing the fluid motion can be derived from mass and momentum balances on a differential fluid element. For viscous Newtonian fluids, this approach leads to the Navier-Stokes equations. For most single-phase flows, fluid motion and energy can be decoupled such that the equations of motion can be solved for the fluid velocity, as well as density or pressure, and then these results can be inserted into the energy equation to determine energy, or temperature.

For multiphase flows, a similar approach can be applied to determine the equations of motion and energy. However, care must be taken to account for the interaction between phases and changes in mass, momentum and energy for a given phase that arise due to the phase-change process, which leads to additional terms in both equations. Taking these additional terms into account, the mass, momentum and energy equations for the k^{th} phase are [117],

$$\frac{\partial(\alpha_k \rho_k)}{\partial t} + \nabla \cdot \left(\alpha_k \rho_k \vec{U}_k\right) = \underbrace{\Gamma_k}_{1} \tag{5.1}$$

$$\frac{\partial\left(\alpha_k \rho_k \vec{U}_k\right)}{\partial t} + \nabla \cdot \left(\alpha_k \rho_k \vec{U}_k \vec{U}_k\right) = \underbrace{\Gamma_k \vec{U}_{kj}}_{2} + \underbrace{\nabla \cdot (\alpha_k \boldsymbol{T}_k)}_{3} + \underbrace{\alpha_k \rho_k \vec{b}_k}_{4} + \underbrace{\vec{\boldsymbol{M}}_k}_{5} \tag{5.2}$$

$$\begin{aligned} \alpha_k \rho_k \left(\frac{\partial e_k}{\partial t} + \vec{U}_k \cdot \nabla e_k\right) = {} & \underbrace{\alpha_k \boldsymbol{T}_k : \nabla \vec{U}_k}_{6} - \underbrace{\nabla \cdot (\alpha_k \vec{q}_k)}_{7} + \underbrace{\alpha_k \rho_k B_k}_{8} + \\ & \underbrace{E_k}_{9} + \underbrace{\Gamma_k \left(e_{kj} - e_k - \frac{1}{2}\vec{U}_k \cdot \vec{U}_k + \vec{U}_{kj} \cdot \vec{U}_k\right)}_{10} \end{aligned} \tag{5.3}$$

Similar to the single-component transport equations, the left side of Eqns. (5.1) - (5.3) contain terms for the time rate of change and advection of mass, momentum and internal energy, respectively. These equations govern transport for the k^{th} phase and are scaled by

the volume fraction α_k. Although the time rate of change and advection terms are fairly standard, the source terms require some elaboration. Therefore, a brief discussion of the terms labeled 1 - 10 follows.

In Term 1, Γ_k represents the rate of production of phase k due to phase change. As Term 2 also involves this symbol, it is the rate of production of momentum for phase k due to mass production from the j^{th} phase. In this term, $\vec{U}_{kj}$ is the relative velocity between phases j and k. Term 3 is the sink of momentum due to traction, where $\mathbf{T}_k$ is the traction tensor. For most multiphase flows of engineering interest, the constituent fluids are Newtonian such that the components of the traction tensor are [118],

$$\boldsymbol{T}_{ij} = -P\delta_{ij} + 2\mu S_{ij} + (\mu_v - \frac{2}{3}\mu)\nabla \cdot \vec{U}\delta_{ij} \tag{5.4}$$

$$S_{ij} = \frac{1}{2}\left(\frac{\partial u_i}{\partial x_j} + \frac{\partial u_j}{\partial x_i}\right) \tag{5.5}$$

where δ_{ij} is the Kronecker delta. The traction tensor includes the effect of pressure and viscosity. Term 4 represents the body force present on phase k. For most applications, the only body force present is that due to gravity. However, there may be other body forces (e.g., electromagnetic forces) that should be accounted for. Term 5 accounts for the force on phase k due to interactions with other phases.

In the energy equation, Term 6 represents the friction work done on phase k due to viscous effects. This term is frequently neglected in single-phase studies. Term 7 is the heat transfer done on phase k. It is common practice to rewrite the internal energy in terms of temperature so that Eqn. (5.3) becomes a differential equation for temperature of the k^{th} phase. If this is done, the constitutive equation for $\vec{q}_k$ in Term 7 is Fourier's law of conduction.

Terms 8 and 9 represent the work done on phase k due to body forces and interactions with other phases, respectively. Finally, as Term 10 involves Γ_k, this term accounts for the energy transferred to phase k via phase change. This term involves both internal energy and kinetic energy.

These equations can be solved numerically using traditional direct numerical simulation (DNS), large eddy simulation (LES), or Reynolds-averaged Navier-Stokes (RANS) techniques. Any of these techniques can be a valuable tool for studying the boiling process. However, constitutive equations for the traction tensor, pressure and heat transfer, and appropriate models to describe the phase change process and the interactions between phases must first be developed before any Computation Fluid Dynamics technique can be applied. Ultimately, these models require an understanding of the physical mechanisms governing the boiling process. Such understanding can come from carefully studying the experimental results for trends and drawing conclusions based on these trends. Therefore, an explanation of some physical mechanisms that may be at play in the experimental results described in the previous chapter is given below. Based on these mechanisms, non-dimensional numbers will also be suggested for correlation of the data and a correlation is presented.

To begin a discussion of possible mechanisms, let us consider the various factors that have been shown to affect boiling heat transfer in emulsions. Previous pool boiling experiments have demonstrated that the boiling process is affected by the fluids used in the emulsion, the mean droplet size- or size distribution- and the emulsion volume fraction (see Section 2.3). The use of additives to stabilize the emulsion also has an

impact on experimental results but the effect of various additives is not yet clear so this factor will not be included in this discussion.

Visualization experiments further indicate that boiling of the dispersed component occurs at a heated surface in pool boiling and these experiments may suggest that droplets of the dispersed component agglomerate on the surface to create a film. This seems to be consistent with the experimental results from this study so it is assumed here that flow boiling of the dispersed component also takes place at the wall.

The experimental results herein show that, depending on the specific combination of volume fraction, mass flux, gap height and heat flux, heat transfer is either impaired or improved compared to the single-component heat transfer. In general, heat transfer decreases for increasing mass flux, decreasing gap height and increasing volume fraction. After the emulsion starts boiling, the heat transfer coefficient generally increases, though it can be lower than that for a single component flow at the same experimental condition over a broad range of wall heat flux. These results suggest that at least two heat transfer mechanisms are taking place, one that decreases and one that increases heat transfer.

Consider an emulsion of volume fraction ε flowing at a mass flux of G in a gap of height H. To be consistent with the experimental results, the flow is hydrodynamically fully-developed and above a surface being heated from below with a constant heat flux q", which causes a thermal boundary layer to develop. Finally, consideration here is restricted to the smooth surface.

In this study, the disperse component has a higher density than the continuous component so droplets in the middle of the gap will tend to settle toward the wall. As a droplet settles from a region of higher velocity to lower velocity, it will experience drag

due to its velocity being higher than the local velocity. This drag force will decrease the inertia of the droplet and the droplet will fall further toward the heated wall. As the droplet migrates toward the heated wall, it is possible that heating from the wall will cause rotation within the droplet, resulting in a Magnus lift force upon the droplet [119]. Thus, whether an individual droplet comes into contact with the heated surface is set by a balance of these forces. Note that these forces would also be present if the flow was not fully-developed and a hydraulic boundary layer is growing. However, the magnitude of these forces may change, e.g. a larger drag force may be felt due to a greater difference between the droplet velocity and the local flow velocity as it enters the boundary layer.

As droplets contact the surface, they can agglomerate and form a film over portions of the surface. In the film, the primary heat transfer mechanism will be conduction. If the disperse phase has a lower thermal conductivity than the continuous phase as in the present investigation, the presence of this film will decrease heat transfer to the portion of the surface below the film. However, if the surface temperature is high enough to cause nucleation within the film, some of the disperse phase will boil on the surface and the vapor will rise into the bulk of the flow. This will cause increased mixing in the flow, thereby increasing heat transfer. Thus, the overall impact on heat transfer is governed by the number of droplets deposited on the surface, n_d, the surface area covered by the film, A_o, the number of droplets that boil on the surface, n_b (or, rather, the amount of liquid volume released that would make up n_b droplets) and the surface area that is exposed to the bulk flow and can be cooled via mixing, A_e. This geometry is shown in Fig. 5.1, though the droplets, bubbles and film thickness are not to scale compared to the gap height.

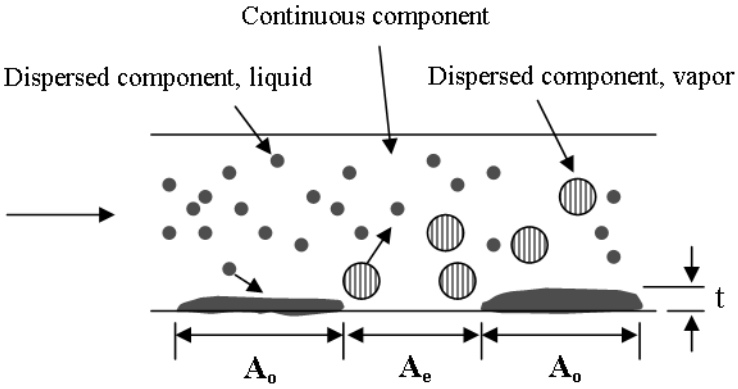

Fig. 5.1. Droplet deposition and release geometry.

Because there are two heat transfer mechanisms at play, the overall heat transfer coefficient can be determined by adding their effects, as was done by Chen [120]. Chen utilized superposition to combine the macroconvective and microconvective heat transfer coefficients to determine an overall heat transfer coefficient for the entire surface. In this case, however, the two mechanisms affect different portions of the wall so the heat transfer coefficient for each mechanism must also be scaled by the surface area for which it applies.

$$hA = h_{film}A_o + h_{mix}A_e \tag{5.6}$$

The heat transfer coefficient in the film is given by the thermal conductivity and the film thickness,

$$h_{film} = \frac{k_d}{t} \tag{5.7}$$

Here, k_d is an order of magnitude lower than k_c (see Appendix A) so conduction through the film of droplets will limit the amount of total heat transfer from the surface. The heat transfer coefficient h_{mix} would account for heat transfer in the continuous component due to the bulk fluid flow and a component associated with additional mixing caused by

vapor release from the heated surface. Areas A_o and A_e can be written in terms of the droplet diameter, d, as well as n_d, n_b and t,

$$A_o = \frac{\pi n_d d^3}{6t} \tag{5.8}$$

$$A_e = A_i + \frac{\pi n_b d^3}{6t} \tag{5.9}$$

where A_i is the area initially exposed, not exposed as a result of bubble release from the surface. It is expected that n_d and n_b are proportional to ε and dependent on various system and flow parameters, e.g. D_h, G, μ_c. We may suppose that t is proportional to d and possibly ε if the layer is more than one droplet thick.

Closure of a model of this form requires determination of the heat transfer coefficient h_{mix}, as well as the effect that heat transfer and various flow parameters have on n_d and n_b. It is not the intent here to close this model but to gain an understanding of mechanisms to determine appropriate parameters for correlation of the emulsion data. It is shown below that the correlation developed based on these mechanisms fits the experimental data very well. This suggests that the mechanisms discussed above are prevalent in flow boiling of emulsions and that closure of a model of this form may be a worthwhile endeavor.

These mechanisms suggest several system properties that can be used to correlate the emulsion boiling data: k_d, d, D_h, μ_c, ρ_d/ρ_c, G, h_{fg}, $C_{p,c}$, ε, q", h. Though strict similitude may not hold in this system, these parameters suggest that seven nondimensional numbers are necessary to correlate the data. Seven nondimensional numbers that represent the physical mechanisms discussed above are,

$$\frac{hD_h}{k_d} \qquad \frac{GD_h}{\mu_c} \qquad \frac{q''}{Gh_{fg_d}} \qquad \frac{1}{1+\varepsilon} \qquad \frac{\rho_d}{\rho_c} \qquad \frac{GC_p d}{k_d} \qquad \frac{d}{D_h} \tag{5.10}$$

The first three terms look similar to the Nusselt, Reynolds and Boiling numbers that are often used to correlate single- and two-phase convection data. Note, however, that the first and third terms use the thermal conductivity and latent heat of the disperse component and the second term uses the viscosity of the continuous component. These terms do not use mixture properties because the properties of these specific components are deemed to be more important than each respective property for the other component. The form of the fourth term is chosen to account for ε seeming to have a large effect on the heat transfer results at low values and the effect diminishes asymptotically as ε increases.

The fifth and sixth terms may be the most significant parameters in this group. The density ratio will govern how many droplets contact the heated surface, and it can be supposed that the heat transfer mechanisms may differ if the disperse component has a lower density than the continuous component. It is possible that in that case, boiling will be caused by superheated droplets coming into the thermal boundary layer, with nucleation happening via a mixture of interactions between neighboring droplets and bubbles. If boiling occurs at the wall in this case, droplet deposition may primarily be due to turbulence caused either by the boiling process or in the bulk flow if the flow is turbulent. The sixth term accounts for the sensible heat transfer to the continuous component advected away from the surface compared to the conduction heat transfer through the film of droplets.

If the smooth surface data is correlated based on these parameters, the following correlation results,

$$h = 0.0067\frac{k}{D_h}\left(\frac{1}{1+\varepsilon}\right)^{3.42}\left(\frac{d}{D_h}\right)^{-2.37}\left(\frac{GD_h}{\mu_c}\right)^{-1.48}\left(\frac{q''}{Gh_{fg_d}}\right)^{0.84}\left(\frac{GC_p d}{k_d}\right)^{2.24} \qquad (5.11)$$

Note that the correlation does not include the density ratio because only one combination of fluids was used in this study. This correlation fits the data very well, with 95.7% of the experimental data falling within ±10% of the predicted value. The data is plotted against the prediction in Fig. 5.2.

It can be argued that the data fits the correlation so well because many parameters were used and one should expect to get a better fit with an increasing number of parameters. However, various reasons account for the necessity of including all of these parameters. First, all of the properties used in the parameters are significant due to the consideration of the physical mechanisms above. Second, the p-value (a statistical parameter used to determine whether a given variable is significant in correlating data) for every parameter demonstrates that each has a strong correlation with the experimental data. Finally, it may be expected that the last two parameters in Eqn. (5.10) would show the least correlation with the experimental data. Though these may be two of the most important parameters to include, they each have only three values that appear in the data set, with additional minor variation due to the effect of temperature on the properties. Their effect on the correlation was examined by neglecting them and correlating the data a second time. The resulting correlation fit the data considerably worse than Eqn. (5.11). This correlation, along with other correlations considered, is given in Appendix G.

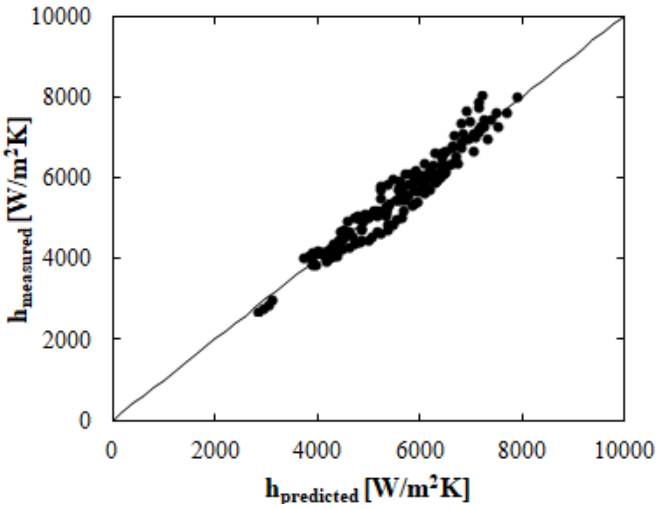

Fig. 5.2. Comparison between the measured emulsion heat transfer coefficient and that predicted by Eqn. (5.11). The solid line represents equivalence between the measured and predicted values.

The data can also be analyzed with respect to the heat transfer coefficient for water at the same wall temperature and experimental condition to determine when the emulsions result in higher heat transfer. This data was correlated as well, resulting in,

$$\frac{h-h_0}{h_0} = 0.045\left(\frac{1}{1+\varepsilon}\right)^{4.15}\left(\frac{d}{D_h}\right)^{-1.46}\left(\frac{GD_h}{\mu_c}\right)^{-1.46}\left(\frac{q''}{Gh_{fg_d}}\right)^{0.76}\left(\frac{GC_p d}{k_d}\right)^{1.73} - 1 \qquad (5.12)$$

The experimental data shows more scatter with respect to Eqn. (5.12) (Fig. 5.3), with 36.4% of the experimental data falling within ±15% of the predicted value and 58.7% within ±30%. However, the correlation captures the trend of the experimental data well. Though these correlations do a relatively good job of matching the experimental data, it should be cautioned that they should not be used for design. As they only represent one combination of droplet diameter, disperse component and continuous component, they are merely used to demonstrate the validity of these specific nondimensional parameters in correlating the emulsion boiling data. In Eqns. (5.11) and (5.12), the absolute volume fraction rather than percentage was used for ε. Disperse component properties were

determined at the saturation temperature. Continuous component properties were determined at the film temperature.

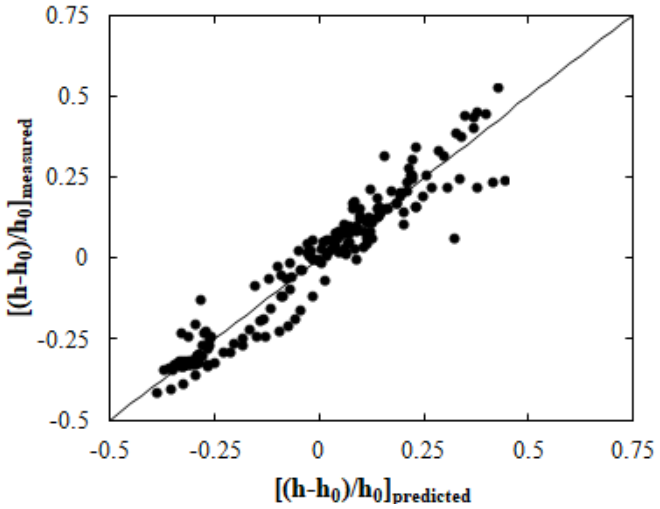

Fig. 5.3. Comparison between the measured ratio of the emulsion and water heat transfer coefficients and the ratio predicted by Eqn. (5.12). The solid line represents equivalence between the measured and predicted values.

6. Conclusion

This investigation has resulted in a wide variety of conclusions regarding boiling heat transfer of water and FC72/water emulsions on smooth and microporous surfaces. For water on the smooth surfaces, the single-phase heat transfer coefficient increases with increasing mass flux and decreasing gap size. After the onset of nucleate boiling (ONB) and prior to transition to the critical heat flux (CHF), the heat transfer curves collapse to one curve. CHF increases with increasing gap size and increasing mass flux. The effects of the liquid subcooling, applied heat flux, mass flux, and gap size on the two-phase heat transfer coefficient are correlated well using the Nusselt, Jakob, Reynolds and Boiling numbers, with 98% of the experimental data falling within ±30% of the Nusselt number predicted by Eqn. (4.8).

For boiling of emulsions on the smooth surface, increasing the volume fraction up to 0.1 or 0.5% enhances cooling in some cases, but increasing ε further to 1 or 2% provides no additional benefit and decreases heat transfer in some experiments. The emulsion improves heat transfer compared to water for larger gap sizes and lower mass fluxes. With decreasing gap size and increasing mass flux, the presence of the emulsion progressively decreases heat transfer compared to water. In almost all experiments, the heat transfer coefficient for the emulsion increases with increasing wall temperature.

Based on these observations, it is posited that two mechanisms for heat transfer exist when boiling emulsions, one that impairs and one that enhances heat transfer. The thermal conductivity of FC-72 is an order of magnitude lower than that of water, so if a film of the FC-72 disperse component covers a significant portion of the wall, heat transfer will be limited by conduction in this film. As the wall temperature increases,

FC-72 on the wall will boil and release from the wall, thereby increasing the portion of the wall exposed to the bulk flow and increasing heat transfer to the exposed portion of the wall via enhanced mixing.

Based on these two mechanisms and the experimental observations, various flow and system parameters are identified as important to the heat transfer behavior. From them, seven non-dimensional numbers are formed and used to correlate the emulsion heat transfer coefficient. Three of these terms look similar to the Nusselt, Reynolds and Boiling numbers, though they utilize various disperse and continuous component properties, depending on which component is deemed to be more important for that parameter. The volume fraction in the form $1/(1+\varepsilon)$, the ratio of dispersed and continuous component densities, and the ratio of the droplet diameter to hydraulic diameter are also used. The final parameter used in the correlation is a new non-dimensional number to account for the ratio of conduction in the disperse component film and the sensible heat advected away from the wall, GC_pd/k_d.

Using these parameters (except for ρ_d/ρ_c due to lack of variability in this investigation), correlations are developed for the emulsion heat transfer coefficient and the ratio $(h-h_0)/h_0$, where h_0 is the water heat transfer coefficient at the same experimental condition. A very good fit is seen for h, with 95.7% of the experimental data falling within ±10% of the correlation, Eqn. (5.11). For the heat transfer coefficient ratio, 58.7% of the experimental data falls within ±30% of the predicted value, though the correlation captures the trend of the data well.

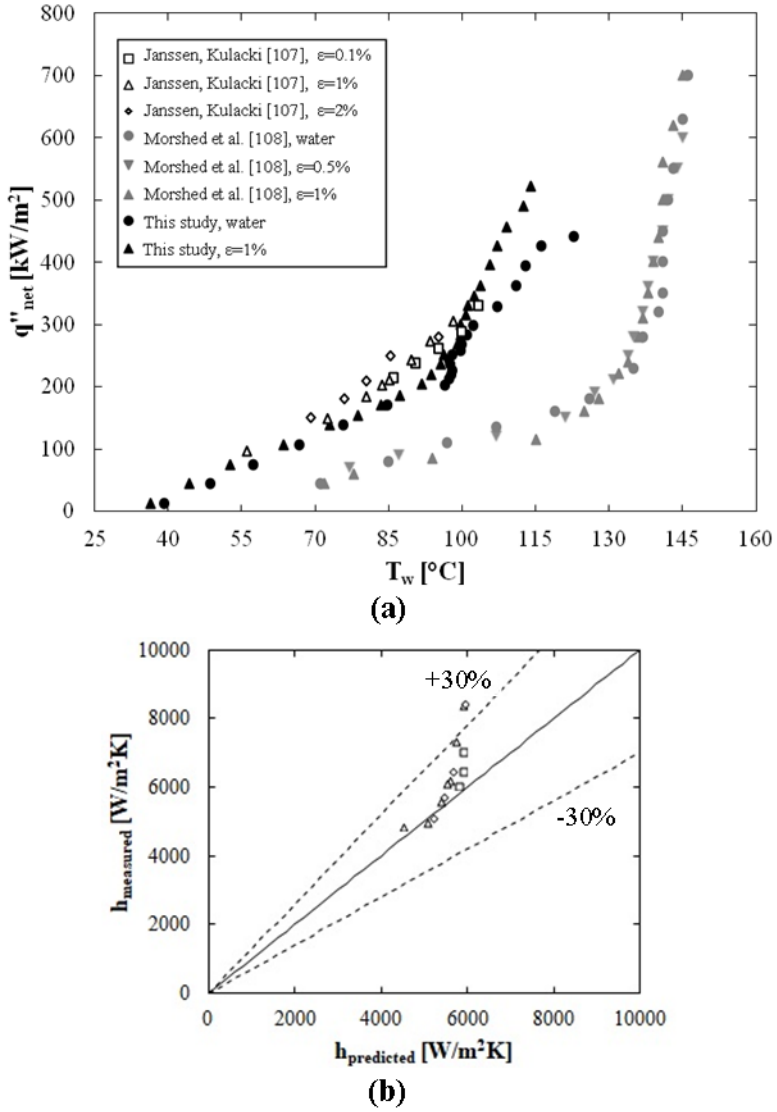

Fig. 6.1. (a) Comparison of D_h = 500 μm, G=150 kg/m^{2}s emulsion boiling data with that of Janssen and Kulacki [107] in a 500 μm gap and Morshed et al. [108] in a 672 μm gap. (b) Heat transfer coefficient measured in [107] compared to that predicted by Eqn. (5.11). The solid line represents equivalence between measured and predicted values.

In Section 4.2, comparison is made between the results of this study and those of Janssen and Kulacki [107] and Morshed et al. [108] where there is crossover between this data set and those, and that comparison is shown again in Fig. 6.1a. The only data points that intersect here are those for water and ε = 1% in the 500 μm gap at G = 150 kg/m^{2}s. It was noted that the data of Janssen and Kulacki show increasing heat transfer for increasing ε up to 2% at G = 133 kg/m^{2}s. This trend is not seen for that range of ε at G =

350 kg/m^{2}s in this investigation. However, decreasing mass flux increases emulsion heat transfer, so it is possible that this trend would be captured by the correlation developed. A comparison between the heat transfer coefficient measured by Janssen and Kulacki [107] and that predicted by Eqn. (5.11) is shown in Fig. 6.1b.

Equation (5.11) predicts the data of Janssen and Kulacki [107] well with the majority of the data falling within ±30% of the predicted value. For moderate heat fluxes, the measured h and that predicted by Eqn. (5.11) compare very favorably. For $\varepsilon = 1$ and 2%, as the heat flux increases, Eqn. (5.11) predicts a consistently lower heat transfer coefficient than that measured by Janssen and Kulacki.

For boiling of water on the porous surfaces, many of the trends seen for boiling on the smooth surface are also present for the porous surfaces. However, on the porous surfaces, the single-phase heat transfer coefficient decreases with decreasing gap size and the boiling curves do not collapse to one curve following ONB. The porous surfaces show enhanced heat transfer relative to that of the smooth surface with increasing mass flux and gap size. For $D_h = 200$ μm, heat transfer is significantly reduced for each porous surface. The best heat transfer for the porous surfaces is consistently displayed on Porous Surface 1.

Measured pressure drop for the porous surfaces is generally higher than that for water on the smooth surface. The highest pressure drops are measured for Porous Surface 2. This is attributed to the increased roughness of the wall due to the large pores seen from the top view of the surface and increased momentum lost at the pore scale due to flow through the relatively open porous structure.

For boiling of emulsions on the porous surfaces, Surface 1 shows a mixture of enhanced and degraded heat transfer. For D_h = 200 and 500 μm, the heat transfer is lower for the emulsions than water. At D_h = 1000 μm, the boiling curves shift to lower T_w but h is lower than that for water. For Surface 2, the emulsions enhance heat transfer for the majority of the data set, and this is especially pronounced for smaller gaps. The emulsions also decrease the measured pressure drop on Porous Surface 2 for the cases where heat transfer is increased. Porous Surface 3 shows similar behavior for the emulsions and water for most of the data set.

The increase in heat transfer on Porous Surface 2 is likely a result of the open pore network on both the top and interior of the porous surface. This open pore network would allow FC-72 droplets to flow down into the porous structure and nucleate bubbles within the confined space there. After nucleation, the resulting vapor would also flow out of this porous structure more easily than in a structure that is more densely packed, either at the top of the surface (like Surface 1) or in the interior of the surface (like Surface 3).

The trends discussed for each surface are shown graphically for the heat transfer coefficient ratio $(h-h_0)/h_0$ in Figs. 6.2 - 6.5. These graphs demonstrate the regions where the emulsions provide enhanced or impaired heat transfer relative to water on each surface. It is important to note that the error bars on the graph do not correspond to uncertainty in the measured ratio. Rather, the lower error bar and upper error bar represent the minimum and maximum ratios measured for a full experiment. For example, the error bars shown for ε = 0.5% in Fig. 6.2c correspond to the maximum and minimum heat transfer coefficient ratio for the water and emulsion experiments compared in Fig. 4.17.

A map of all of the existing emulsion experiments is given in Fig. 6.6. The corresponding publications shown in the map are listed in Table 6.1. On this map, $D_h \rightarrow \infty$ corresponds to pool boiling experiments. Almost all of the data points on the map correspond to individual experiments, with the exception of those of Morshed. et al., that represent 1-3 mass fluxes for one value of ε in their microchannels and microgap, and various Bulanov and Gasanov points that were conducted for pool boiling experiments with multiple fluids at the same value of ε. This study, therefore, expands the existing data set greatly by studying variation in volume fraction, mass flux, hydraulic diameter, and surface condition.

From the trends in the experimental data and the existing experiments shown in Fig. 6.6, it is clear that more flow boiling experiments should be conducted at lower volume fractions ($\varepsilon < 0.5\%$) and larger gap sizes ($D_h \sim 1$ mm). Other areas of study that should be considered to increase understanding of boiling of emulsions and move closer toward their use in design are,

- Studying the droplet-wall interaction in more depth for individual and multiple droplets via visualization and computational fluid dynamics (CFD)
- The use of CFD for studying flow boiling of dilute emulsions. To date, little study has been made in this area for pool boiling
- Boiling of emulsions on structured walls, where the wall structure is tailored to the droplet size
- The use of dilute emulsions in impinging jets
- Experiments conducted specifically for studying the effect of emulsion properties on CHF

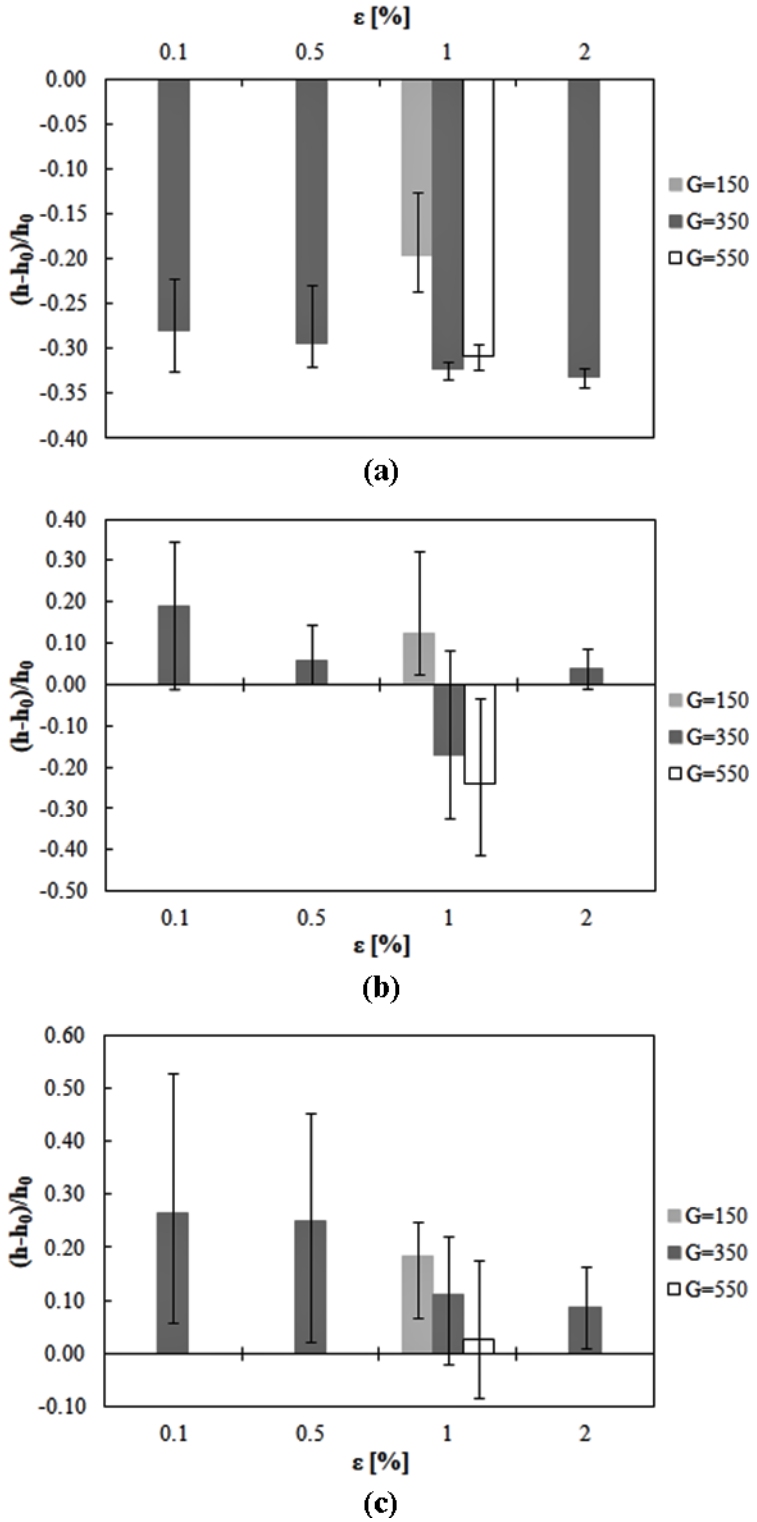

Fig. 6.2. Ratio of the emulsion heat transfer coefficient to that for water at the same wall temperature on the smooth surface. (a) - (c) are for D_h = 200, 500 and 1000 μm.

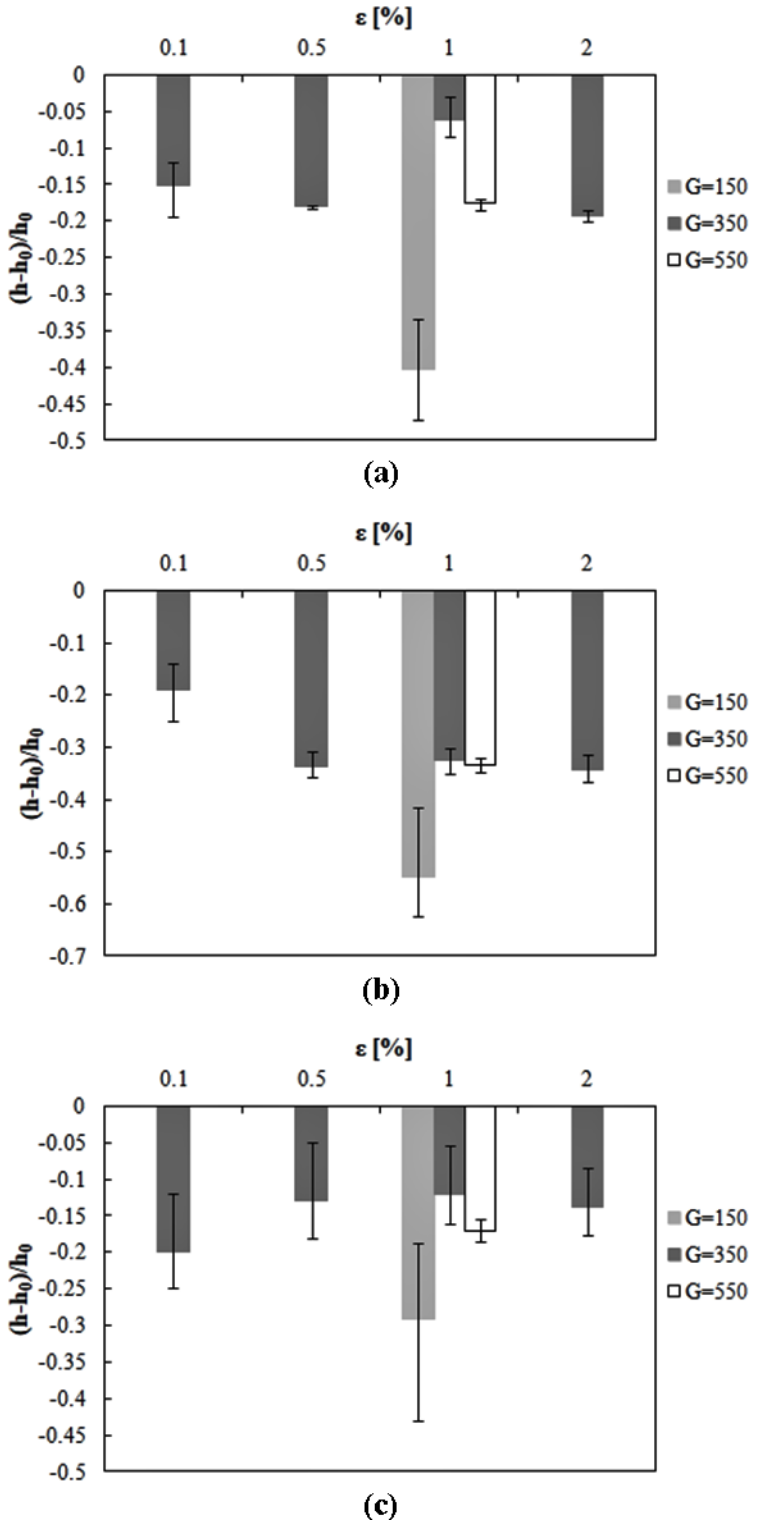

Fig. 6.3. Ratio of the emulsion heat transfer coefficient to that for water at the same wall temperature on Porous Surface 1. (a) - (c) are for D_h = 200, 500 and 1000 μm.

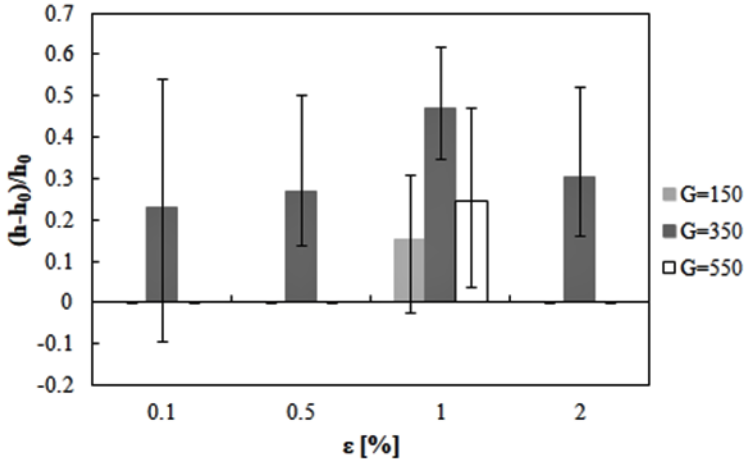

(a)

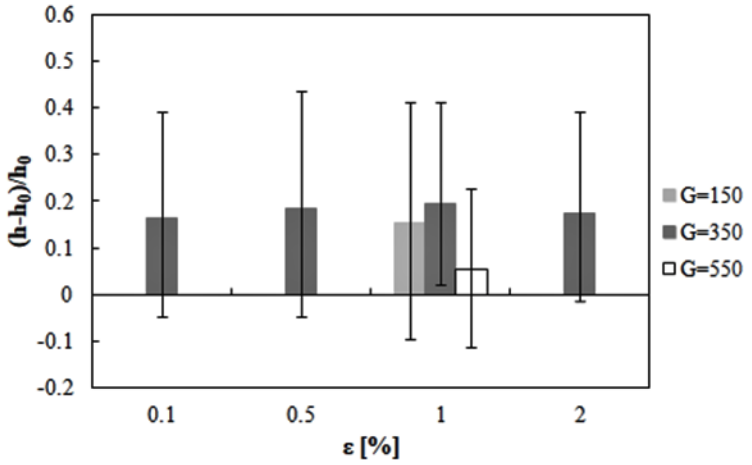

(b)

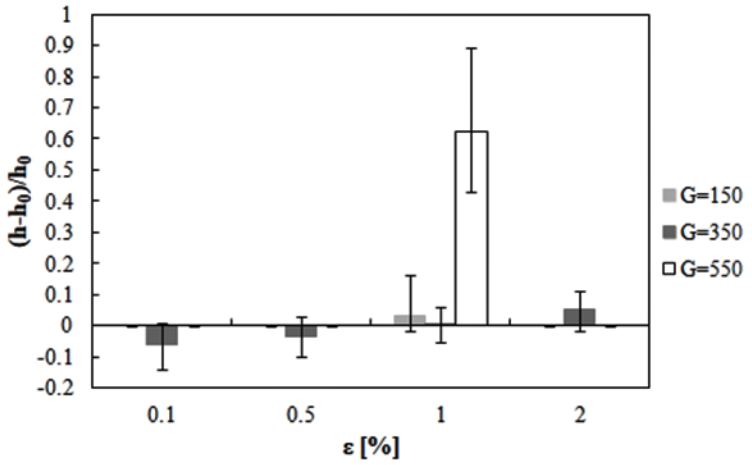

(c)

Fig. 6.4. Ratio of the emulsion heat transfer coefficient to that for water at the same wall temperature on Porous Surface 2. (a) - (c) are for D_h = 200, 500 and 1000 μm.

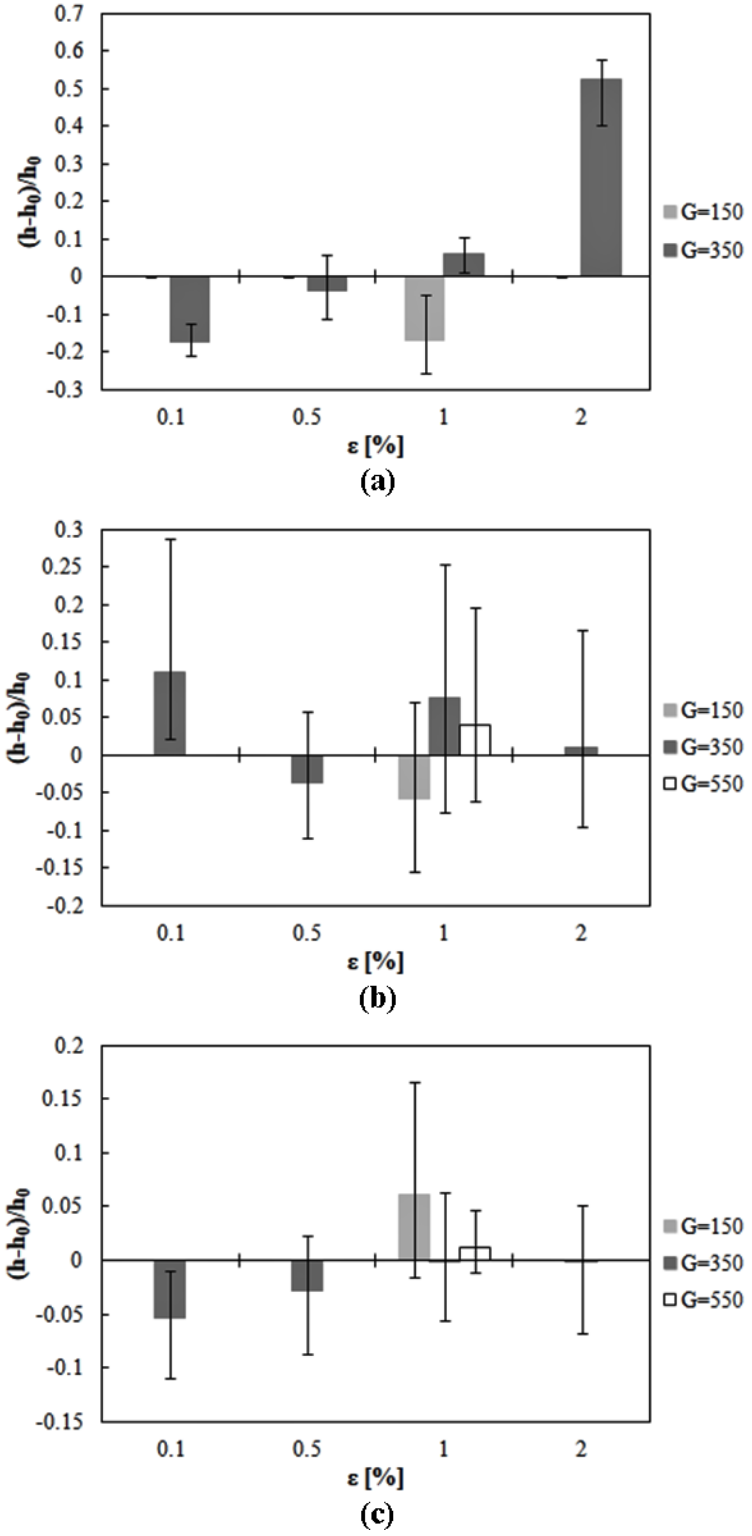

Fig. 6.5. Ratio of the emulsion heat transfer coefficient to that for water at the same wall temperature on Porous Surface 3. (a) - (c) are for D_h = 200, 500 and 1000 μm.

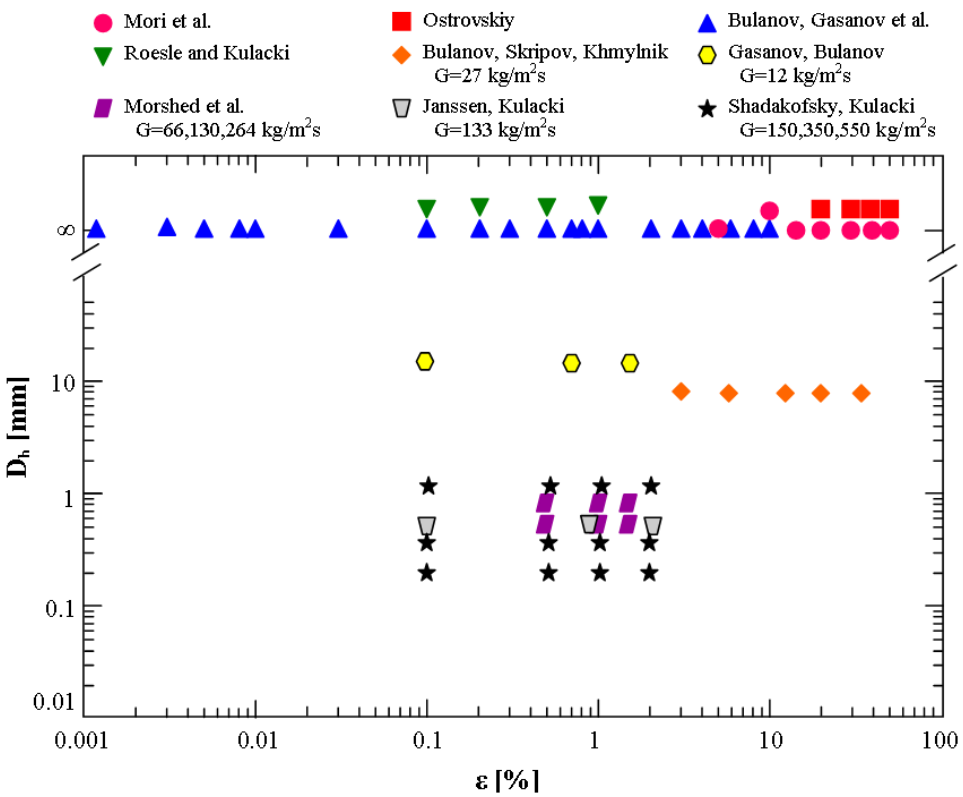

Fig. 6.6. Map of existing emulsion boiling experiments. The corresponding publications are listed in Table 6.1. $D_h \rightarrow \infty$ represents pool boiling results.

Table 6.1. Comparison of emulsion investigations

Paper	Fluids Studied	Volume Fractions Studied	Emulsion Bulk/Inlet Temperature	Heater Geometry	Notable Results
Mori, Inui amd Komotori [88]	Various; Sodium oleate, Span 80 and Tween 80 surfactants	5 - 50%	100 °C	Horizontal 0.2 mm DIA nickel wire	KF 96-in-water stabilized with Tween 80 boils at higher T_w than with Sodium oleate; KF 96/, Dodecane/ and Undecane/water emulsions boil at lower T_w than KF54-in- water; sudden foaming in the bulk fluid reported.
Bulanov, Skripov and Shuravenko [121]	Ether/glycerin	10%	20 °C	Vertical 0.2 mm DIA platinum wire	Boiling of 5 μm DIA droplets begin at T_w ~ 60 °C above T_s for ether; heat transfer coefficients ~ 3X higher compared to glycerin; fluctuations in heat transfer coefficient up to 30% of mean due to sequential sudden boiling and slow vaporization.
Bulanov, Skripov and Khmyl'nin [93]	Water/PMS300	0.8 - 3.2%	40 - 99 °C	Vertical 0.2 mm DIA platinum wire	Researchers report no effect of ε; at 40 °C bulk temperature, emulsions boiled at T_s for water; at 99 °C, heat transfer coefficient decreases until ($T_w - T$) = 40 °C and increases thereafter; this is attributed to water vapor wetting the wire.
Ostrovskiy [89]	Water/R113, water/benzene, water/butyl alcohol	20 - 80%	---	Vertical 6 mm DIA stainless steel tube	For all emulsions studied, the heat transfer coefficient approximately equal to that of the lower T_s component irrespective of ε; some variability is seen in water-in-benzene emulsions, with hat transfer coefficient decreasing with increasing fraction of benzene.
Bulanov, Skripov and Khmylnik [105]	Water/PES-4, diethyl ether/water	0 - 33% by weight	60 °C	8.4 mm inner DIA tube	For flow boiling of water-in-PES-4 emulsions, boiling begins at the saturation temperature of water; enhancement is measured up to ε = 33% but experimental scatter may account for variation in 12, 20 and 33% data sets.
Bulanov, Skripov, Gasanov and Baidakov [100]	Water/PES-5; sodium phosphate sodium hydroxide surfactants	0.1 - 8%	43.5 - 55 °C	0.05 and 0.1 mm DIA platinum wire	Little effect found with surfactant use on heat transfer coefficient; heat transfer coefficient depends on ε to ~1% and is independent of ε thereafter; heat transfer coefficient increases d with increasing T_w; nucleate boiling is observed up to T_w = 235 °C.

Gasanov, Bulanov and Baidakov [94]	Water/PES-5	0.1 - 8%	30 - 65 °C	0.05 and 0.1 mm DIA platinum wire	Boiling of 1-60 μm DIA droplets show increasing volume fraction increases heat transfer coefficient for $\varepsilon \leq 1\%$ then has little effect thereafter; increasing volume fraction decreases temperature overshoot at boiling onset.
Bulanov [98]	Water/PES-5, Freon-113/water, diethyl ether/water	---	---	---	Analytical model developed for boiling emulsions valid for various concentration and droplet distributions; comparison is given to experimental results for assumed values of nucleation rate and characteristic droplet time.
Bulanov and Gasanov [101]	Water/PES-5	0.10%	98 °C	Emulsion in contact with 125 °C flowing fluid	Emulsion is brought into direct contact with a pool of hot fluid; nucleation rate of bubbles is measured; authors posit that bubbles are nucleating via homogeneous nucleation on small floccules followed by chain activation.
Bulanov, Gasanov, and Turchaninova [122]	Various; activated carbon, zeolites and carbon surfactants	0.001 - 10%	20 - 72 °C	Vertical 0.05 and 0.1 mm DIA platinum wire	Authors provide tabulated values for h as a function of T_w for various experimental conditions, including emulsion fluids, temperature, volume fraction, use of surfactants and storage time.
Bulanov and Gasanov [95]	Various; activated carbon, zeolites and surfactants	1 - 10%	25 - 60 °C	Vertical 0.1 mm DIA platinum wire	Activated carbon decreases superheat in water-in-PES5 and increases it in n-pentane-in-glycerin; zeolites increase superheat in water-in-PES4; sodium hydrate and trisodium phosphate increase superheat in water-in-PES-5.
Bulanov and Gasanov [123]	Various	1%	36 - 60 °C	Vertical 0.05-0.2 mm DIA platinum wire	A short review of prior experimental results is provided regarding a boiling model and the effect of droplet size, use of adsorbents and use of surfactants.
Roesle and Kulacki [106]	FC-72/water	4 - 69%	24 - 32 °C	30 mm × 30 mm copper plate	Flow boiling experiments in 0.1 mm × 30 mm microgap conducted with $40 \leq G \leq 467$ kg/m^2-s; unsteady nature of experiments obscured heat transfer behavior; high volume of FC-72 inhibited heat transfer compared to pure water.

Bulanov, Gasanov and Muratov [110]	Pentane/water	1%	147 °C	---	Nucleation of bubbles are assumed occurs via a shock wave that initiates chain activation equations derived for the wave amplitude at distance R from droplet and the critical volume required to initiate chain activation.
Roesle and Kulacki [112]	FC-72/water, pentane/water, water/mineral oil	---	56 - 96 °C	---	Bubble growth is modeled after initiation for a single droplet in a continuous liquid, including the effect of surface tension; the density ratio and droplet size impact bubble growth rate and frequency of oscillations.
Roesle and Kulacki [90]	---	---	---	---	Euler-Euler differential equations for flow and temperature are presented; bubble nucleation rates are determined via chain boiling, droplet wall contact, droplet-bubble collisions and spontaneous nucleation mechanisms.
Rozentsvaig and Strashinskii [113]	Water/PES-5	---	---	---	The nucleation mechanism is modeled in two regimes of turbulent flow: droplet diameters greater than or less than the Kolmogorov scale of turbulence; favorable comparison is shown with limited experimental data
Rozentsvaig and Strashinskii [124]	Water/PES-5	---	---	---	Bubble nucleation of droplets is modeled with 1 μm and 100 μm DIA based on resonance between the turbulent fluctuations and surface waves on the droplet; qualitative agreement found with experiments is posited.
Bulanov and Gasanov [125]	Water/VM-1S, n-pentane/glycerol	0.1 - 10%	22 °C	Vertical wire	Authors develop a model to determine superheat at onset of boiling; superheat is found to be dependent on $\varepsilon^{-1/3}$, which fits data for water-in-VM1s and n-pentane-in-glycerol data.
Roesle and Kulacki [92]	FC-72/water, pentane/water	0.1 - 1%	25 °C	Horizontal 101 μm DIA copper wire	For FC-72-in-water, increasing ε decreases temperature overshoot, the reverse is found for pentane-in-water; emulsions exhibited similar h versus $(T_w - T_s)$ behavior water-in-R-113 and diethyl ether-in-water emulsions.

Roesle and Kulacki [102]	FC-72/water, pentane/water	0.1 - 1%	25 °C	Horizontal 101 µm diameter copper wire	Visualization is correlated to heat transfer; bubbles form on the wire; bubble diameter decreases with increasing heat flux; bubble diameter suggests wetting of liquid on wire or coalescence of bubbles.
Morshed, Paul, Fang and Khan [108]	FC-72/water	0.5 - 1%	25 °C	5 mm × 26 mm micro- channel	Experiments show increasing ε decreases single-phase heat transfer; no enhancement in two-phase heat transfer is measured; emulsions decrease axial temperature difference compared to water.
Gasanov and Bulanov [96]	Freon-11/water, pentane/water, water/VM-1S	1 - 5%	16 °C	0.05 and 0.1 mm DIA platinum wire	Though Freon-11 has a lower T_s than pentane, it boils at higher T_w; two regimes of boiling identified based on heat flux and fluid motion; analytical relation for the time required for bubble formation is presented.
Rozentsvaig and Strashinskii [126]	Water/PES-5, water/PMS-300	0.001 - 4%	---	Vertical 0.05 and 0.1 mm DIA platinum wire	Boiling is modeled as a linear combination of conduction in the viscous sublayer near a surface and latent heat exchange; comparison is made to experimental data and two distinct curves are demonstrated based on ε.
Rozentsvaig and Strashinskii [127]	Water/PES-5, water/PMS-300, water/VM-1S	0.001 - 2%	---	Vertical 0.05 and 0.1 mm DIA platinum wire	Authors use the model from [126] to determine the Nusselt number based on Reynolds number and compare predictions to experimental data; data show regimes of transition and developed turbulent boiling
Roesle, Lunde and Kulacki [128]	FC-72/water, pentane/water	0.1 - 0.5%	25 °C	Vertically oriented thin 1008 steel strip	In single-phase convection, the emulsions produce lower heat transfer coefficient than in water, decreasing with increasing ε; increasing ε decreases superheat; slightly larger superheats are measured for pentane-in-water than FC-72-in-water emulsions.
Gasanov and Bulanov [104]	Water/VO-1C	0.1 - 1.5%	24 °C	16 mm diam. pipe, 0.1 mm DIA platinum wire	For flow boiling at G = 12 kg/m^2-s, increasing droplet diameter shifts heat transfer coefficients to lower T_w; lower T_w is required to initiate boiling compared to pool boiling; increasing droplet diameter and ε decreases critical heat flux

Gasanov [103]	Pentane/water, pentane/glycerin	0.5 - 4%	22 °C	0.1 mm DIA platinum wire	High speed visualizations demonstrates pentane-in-water emulsions boil at wire surface; pentane-in-glycerin emulsions boil close to the kinetic limit of superheat so some bubbles formed in thermal boundary layer
Rozentsvaig and Strashinskii [129]	---	---	---	---	Unit and similarity analysis is performed to demonstrate the importance of the Weber and Euler numbers for droplet breakup; breakup is assumed dominated by turbulent kinetic energy.
Rozentsvaig and Strashinskii [130]	Parafinic base oil/water, naphthenic base oil/water	1 - 20%	---	1 μm gap between AA 1100 and AA 5182 rings	Authors modeled the use of oil-in-water emulsions for cooling and decreasing friction of high temperature machining applications; they develop an expression for the critical temperature for minimization of friction as a function of ε.
Janssen and Kulacki [107]	FC-72/water, pentane/water	0.1 - 2%	25 °C	30 mm × 30 mm flat plate	For boiling of FC-72-in-water at G = 100 kg/m^2-s, boiling initiates at superheats of ~20-30 °C; up to 60% increase in heat transfer coefficient over water is measured; pentane-in-water produces no enhancement over water.

References

[1] Tong, L.S., *Boiling Heat Transfer and Two-Phase Flow*, New York: Wiley, (1965).

[2] Collier, J.G., Thome, J.R., *Convective Boiling and Condensation (3rd ed.)*, Oxford: Oxford University Press, (1994).

[3] Westwater, J.W., "Things We Don't Know About Boiling Heat Transfer," *Theory and Fundamental Research in Heat Transfer*, J.A. Clark, New York: Pergamon Press, pp. 61-73, (1963).

[4] Lienhard, J.H., "Things We Don't Know About Boiling Heat Transfer: 1988," *Int. Comm. Heat Mass Trans.*, 15, pp. 401-428, (1988).

[5] Kandlikar, S.G., "History, Advances, and Challenges in Liquid Flow and Flow Boiling Heat Transfer in Microchannels: A Critical Review," *J. Heat. Trans.*, 134, pp. 134001- 1-15, (2012).

[6] Dhir, V.K., "Mechanistic Prediction of Nucleate Boiling Heat Transfer- Achievable or a Hopeless Task?," *J. Heat Trans.*, 128, pp. 1-12, (2006).

[7] Kim, J., "Review of nucleate pool boiling bubble heat transfer mechanisms," *Int. J. Multiphase Flow*, 35, pp. 1067-1076, (2009).

[8] Moghaddam, S., Kiger, K., "Physical mechanisms of heat transfer during single bubble nucleate boiling of FC-72 under saturation conditions-I. Experimental investigation," *Int. J. Heat Mass Trans.*, 52, pp. 1284-1294, (2009).

[9] Moghaddam, S., Kiger, K., "Physical mechanisms of heat transfer during single bubble nucleate boiling of FC-72 under saturation conditions-II. Theoretical analysis," *Int. J. Heat Mass Trans.*, 52, pp. 1295-1303, (2009).

[10] Bigham, S., Moghaddam, S., "Microscale study of mechanisms of heat transfer during flow boiling in a microchannel," *Int. J. Heat Mass Trans.*, 88, pp. 111-121, (2015).

[11] Bigham, S., Moghaddam, S., "Role of bubble growth dynamics on microscale heat transfer events in microchannel flow boiling process," *Appl. Phys. Lett.*, 107, pp. 244103- 1-5, (2015).

[12] Bigham, S., Moghaddam, S., "Physics of the Microchannel Flow Boiling Process and Comparison With the Existing Theories," *J. Heat Trans.*, 139, pp. 111503- 1-10, (2017).

[13] Brooks, C.S., Hibiki, T., "Wall nucleation modeling in subcooled boiling flow," *Int. J. Heat Mass Trans.*, 86, pp.183-196, (2015).

[14] Karayiannis, T.G., Mahmoud, M.M., "Flow boiling in microchannels: Fundamentals and applications," *Appl. Therm. Eng.*, 115, pp. 1372-1397, (2017).

[15] Kandlikar, S.G., "Fundamental issues related to flow boiling in minichannels and microchannels," *Exp. Therm. Fluid Sci.*, 26, pp. 389-407, (2002).

[16] Thome, J.R., "Boiling in microchannels: a review of experiment and theory," *Int. J. Heat Fluid Flow*, 25, pp. 128-139, (2004).

[17] Mudawar, I., "Two-Phase Microchannel Heat Sinks: Theory, Applications and Limitations," *J. Electron. Packag.*, 133, pp. 041002- 1-31, (2011).

[18] Saha, S.K., Celata, G.P., Kandlikar, S.G., "Thermofluid Dynamics of Boiling in Microchannels," In Y.I., Cho, G.A. Greene, Eds., *Advances in Heat Transfer. Vol. 43*, London: Elsevier, pp. 77-226, (2011).

[19] Kim, D.W., Rahim, E., Bar-Cohen, A., Han, B., "Thermofluid Characteristics of Two-Phase Flow in Micro-Gap Channels," *11th Intersociety Conference on Thermal and Thermomechanical Phenomena in Electronic Systems*, pp. 979-992, (2008).

[20] Bar-Cohen, A., Rahim, E., "Modeling and Prediction of Two-Phase Microgap Channel Heat Transfer Characteristics," *Heat Trans. Eng.*, 30(8), pp. 601-625, (2009).

[21] Kabov, O.A., Zaitsev, D.V., Chevedra, V.V., Bar-Cohen, A., "Evaporation and flow dynamics of thin, shear-driven liquid films in microgap channels," *Exp. Therm. Fluid Sci.*, 35, pp. 825-831, (2011).

[22] Bar-Cohen, A., Sheehan, J.R., Rahim, E., "Two-Phase Thermal Transport in Microgap Channels- Theory, Experimental Results, and Predictive Relations," *Microgravity Sci. Technol.*, 24, pp. 1-15, (2012).

[23] Harirchian, T., Garimella, S.V., "Effects of channel dimension, heat flux, and mass flux on flow boiling regimes in microchannels," *Int. J. Multiph. Flow*, 35, pp. 349-362, (2009).

[24] Harirchian, T., Garimella, S.V., "A comprehensive flow regime map for microchannel flow boiling with quantitative transition criteria," *Int. J. Heat Mass Trans.*, 53, pp. 2694-2702, (2010).

[25] Alam, T., Lee, P.S., Yap, C.R., Jin, L., "Experimental investigation of local flow boiling heat transfer and pressure drop characteristics in microgap channel," *Int. J. Multiph. Flow*, 42, pp. 164-174, (2012).

[26] Alam, T., Lee, P.S., Yap, C.R., Jin, L., Balasubramanian, K., "Experimental investigation and flow visualization to determine the optimum dimension range of microgap heat sinks," *Int. J. Heat Mass Trans.*, 55, pp. 7623-7634, (2012).

[27] Alam, T., Lee, P.S., Yap, C.R., Jin, L., "A comparative study of flow boiling heat transfer and pressure drop characteristics in microgap and microchannel heat sink and an evaluation of microgap heat sink for hot spot mitigation," *Int. J. Heat Mass Trans.*, 58, pp. 335-347, (2013).

[28] Alam, T., Lee, P.S., Yap, C.R., "Effects of surface roughness on flow boiling in silicon microgap heat sinks," *Int. J. Heat Mass Trans.*, 64, pp. 28-41, (2013).

[29] Alam, T., Lee, P.S., Jin, L., *Flow Boiling in Microgap Channels: Experiment, Visualization and Analysis*. *Springer Briefs in Applied Science and Technology, Thermal Engineering and Applied Science*, New York: Springer, (2014).

[30] Taitel, Y., "Flow Pattern Transition in Two Phase Flow," *Proceedings of the 9th International Heat Transfer Conference*, pp. 237-254, (1990).

[31] Yang, Y., Fujita, Y., "Flow Boiling Heat Transfer and Flow Pattern in Rectangular Channel of Mini-Gap," *2nd International Conference on Microchannels and Minichannels*, pp. 573-580, (2004).

[32] Lee, H.J., Lee, S.Y., "Heat transfer correlation for boiling flows in small rectangular horizontal channels with low aspect ratios," *Int. J. Multiphase Flow*, 27(12), pp. 2043-2062, (2001).

[33] Geisler, K.J.L, Bar-Cohen, A., "Confinement effects on nucleate boiling and critical heat flux in buoyancy-driven microchannels," *Int. J. Heat Mass Trans.*, 52, pp. 2427-2436, (2009).

[34] Kim, D.W., Rahim, E., Bar-Cohen, A., "Direct Submount Cooling of High-Power LEDs," *IEEE Trans. Compon. Packag. Technol.*, 33(4), pp. 698-712, (2010).

[35] Janssen, D.D., Dixon, J.M., Young, S.J., Kulacki, F.A., "Flow Boiling in a Short Narrow Gap Channel," *Proceedings of the ASME 2013 Summer Heat Transfer Conference*, pp. HT2013-17437- 1-13, (2013).

[36] Janssen, D.D., Dixon, J.M., Young, S.J., Kulacki, F.A., "Flow Boiling in an In-Line Set of Short Narrow Gap Channels," *J. Heat Trans.*, 137, pp. 111501- 1-12, (2015).

[37] Young, S.J., Janssen, D., Wenzel, E.A., Shadakofsky, B.M., Kulacki, F.A., "Electronics Cooling With Onboard Conformal Encapsulation," *2016 15th IEEE Intersociety Conference on Thermal and Thermomechanical Phenomena in Electronic Systems (ITherm)*, pp. 245-253, (2016).

[38] Young, S.J., Janssen, D., Wenzel, E.A., Shadakofsky, B.M., Kulacki, F.A., "Onboard Device Encapsulation With Two-Phase Cooling," *J. Therm. Sci. Eng. Appl.*, 10(2), pp. 021002- 1-13, (2018).

[39] Young, S.J., Janssen, D., Wenzel, E.A., Shadakofsky, B.M., Kulacki, F.A., "Multidevice Cooling With Flow Boiling in a Variable Microgap," *J. Therm. Sci. Eng. Appl.*, 10(6), pp. 061014- 1-8, (2018).

[40] Jacobi, A.M., Thome, J.R., "Heat Transfer Model for Evaporation of Elongated Bubble Flows in Microchannels," *J. Heat Trans.*, 124, pp. 1131-1136, (2002).

[41] Thome, J.R., Dupont, V., Jacobi, A.M., "Heat transfer model for evaporation in microchannels. Part I: presentation of the model," *Int. J. Heat Mass Trans.*, 47, pp. 3375-3385, (2004).

[42] Dupont, V., Thome, J.R., Jacobi, A.M., "Heat transfer model for evaporation in microchannels. Part II: comparison with the database," *Int. J. Heat Mass Trans.*, 47, pp. 3387-3401, (2004).

[43] Magnini, M., Thome, J.R., "An updated three-zone heat transfer model for slug flow boiling in microchannels," *Int. J. Multiphase Flow*, 91, pp. 296-314, (2017).

[44] Mikic, B.B., Rohsenow, W.M., "A new correlation of pool boiling data including the effect of heating surface characteristics," *J. Heat Trans.*, 91, pp. 245-250, (1969).

[45] Demiray, F., Kim, J., "Microscale heat transfer measurements during pool boiling of FC-72: effect of subcooling," *Int. J. Heat Mass Trans.*, 47, pp. 3257-3268, (2004).

[46] Harirchian, T., Garimella, S.V., "Microchannel size effects on local flow boiling heat transfer to a dielectric liquid," *Int. J. Heat Mass Trans.*, 51, pp. 3724-3735, (2008).

[47] Sheehan, J., Bar-Cohen, A., "Spatial and Temporal Wall Temperature Fluctuations in Two-Phase Flow in Microgap Coolers," *Proceedings of the ASME 2010 International Mechanical Engineering Congress & Exposition*, pp. IMECE2010-40227- 1-8, (2010).

[48] Bar-Cohen, A., Wang, P., "Thermal Management of On-Chip Hot Spot," *J. Heat Trans.*, 134, pp. 051017- 1-11, (2012).

[49] Kosar, A., Peles, Y., "Convective flow of refrigerant (R-123) across a bank of micro pin fins," *Int. J. Heat Mass Trans.*, 49, pp. 3142-3155, (2006).

[50] Kosar, A., Peles, Y., "Boiling heat transfer in a hydrofoil-based micro pin fin heat sink," *Int. J. Heat Mass Trans.*, 50, pp. 1018-1034, (2007).

[51] Lie, Y.M., Ke, J.H., Chang, W.R., Cheng, T.C., Lin, T.F., "Saturated flow boiling heat transfer and associated bubble characteristics of FC-72 on a heated micro-pin-finned silicon chip," *Int. J. Heat Mass Trans.*, 50, pp. 3862-3876, (2007).

[52] Krishnamurthy, S., Peles, Y., "Flow boiling of water in a circular staggered micro-pin fin heat sink," *Int. J. Heat Mass Trans.*, 51, pp. 1349-1364, (2008).

[53] Qu, W., Siu-Ho, A., "Experimental study of saturated flow boiling heat transfer in an array of staggered micro-pin-fins," *Int. J. Heat Mass Trans.*, 52, pp. 1853-1863, (2009).

[54] Ma, A., Wei, J., Yuan, M., Fang, J., "Enhanced flow boiling heat transfer of FC-72 on micro-pin-finned surfaces," *Int. J. Heat Mass Trans.*, 52, pp. 2925-2931, (2009).

[55] Chang, W.R., Chen, C.A., Ke, J.H., Lin, T.F., "Subcooled flow boiling heat transfer and associated bubble characteristics of FC-72 on a heated micro-pin-finned silicon chip," *Int. J. Heat Mass Trans.*, 53, pp. 5605-5621, (2010).

[56] Reeser, A., Bar-Cohen, A., Hetsroni, G., "High quality flow boiling heat transfer and pressure drop in microgap pin fin arrays," *Int. J. Heat Mass Trans.*, 78, pp. 974-985, (2014).

[57] Woodcock, C., Yu, X., Plawsky, J., Peles, Y., "Piranha Pin Fin (PPF)- Advanced flow boiling microstructures with low surface tension dielectric fluids," *Int. J. Heat Mass Trans.*, 90, pp. 591-604, (2015).

[58] Zhu, Y., Antao, D.S., Chu, K., Chen, S, Hendricks, T.J., Zhang, T., Wang, E., "Surface Structure Enhanced Microchannel Flow Boiling," *J. Heat Trans.*, 138, pp. 091501- 1-13, (2016).

[59] Alam, T., Li, W., Yang, F., Chang, W., Li, J., Wang, Z., Khan, J., Li, C., "Force analysis and bubble dynamics during flow boiling in silicon nanowire microchannels," *Int. J. Heat Mass Trans.*, 101, pp. 915-926, (2016).

[60] Alam, T., Khan, A.S., Li, W., Yang, F., Tong, Y., Khan, J., Li, C., "Transient force analysis and bubble dynamics during flow boiling in silicon nanowire microchannels," *Int. J. Heat Mass Trans.*, 101, pp. 937-947, (2016).

[61] Han, X., Fedorov, A., Joshi, Y., "Flow Boiling in Microgaps for Thermal Management of High Heat Flux Microsystems," *J. Electron. Packag.*, 138, pp. 040801- 1-12, (2016).

[62] Bigham, S., Fazeli, A., Moghaddam, S., "Physics of microstructures enhancement of thin film evaporation heat transfer in microchannels flow boiling," *Sci. Rep.*, 7, pp. 44745- 1-11, (2017).

[63] Fazeli, A., Moghaddam, S., "A New Paradigm for Understanding and Enhancing the Critical Heat Flux (CHF) Limit," *Sci. Rep.*, 7, pp. 5184- 1-12, (2017).

[64] Honda, H., Wei, J.J., "Enhanced boiling heat transfer from electronic components by use of surface microstructures," *Exp. Therm. Fluid Sci.*, 28, pp. 159-169, (2004).

[65] Patil, C.M., Kandlikar, S., "Review of the Manufacturing Techniques for Porous Surfaces Used in Enhanced Pool Boiling," *Heat Trans. Eng.*, 35(10), pp. 887-902, (2014).

[66] Shojaeian, M., Kosar, A., "Pool boiling and flow boiling on micro- and nanostructured surfaces," *Exp. Therm. Fluid Sci.*, 63, pp. 45-73, (2015).

[67] Burmeister, L.C., *Convective Heat Transfer (2nd ed.)*, New York: Wiley, (1993).

[68] You, S.M., Simon, T.W., Bar-Cohen, A., "A Technique for Enhancing Boiling Heat Transfer with Application to Cooling of Electronic Component," *IEEE Transactions on Components, Hybrids and Manufacturing Technology*, 15(5), pp. 823-831, (1992).

[69] O'Connor, J.P., You, S.M., "A painting technique to enhance pool boiling heat transfer in saturated FC-72," *J. Heat Trans.*, 117(2), pp. 387-393, (1995).

[70] Chang, J.Y., You, S.M., "Heater orientation effects on pool boiling of micro-porous-enhanced surfaces in saturated FC-72," *J. Heat Trans.*, 118(4), pp. 937-943, (1996).

[71] Chang, J.Y., You, S.M., "Boiling heat transfer phenomena from micro-porous and porous surfaces in saturated FC-72," *Int. J. Heat Mass Trans.*, 40(18), pp. 4437-4447, (1997).

[72] Ammerman, C.N., You, S.M., "Enhancing Small-Channel Convective Boiling Performance Using a Microporous Surface Coating," *J. Heat Trans.*, 123, pp. 976-983, (2001).

[73] Rainey, K.N., You, S.M., "Effects of heater size and orientation on pool boiling heat transfer from microporous coated surfaces," *Int. J. Heat Mass Trans.*, 44, pp. 2589-2599, (2001).

[74] Rainey, K.N., You, S.M., Lee, S., "Effect of Pressure, Subcooling, and Dissolved Gas on Pool Boiling Heat Transfer From Microporous Surfaces in FC-72," *J. Heat Trans.*, 125, pp. 75-83, (2003).

[75] Arik, M., Bar-Cohen, A., You, S.M., "Enhancement of pool boiling critical heat flux in dielectric liquids by microporous coatings," *Int. J. Heat Mass Trans.*, 50, pp. 997-1009, (2007).

[76] Sarwar, M.S., Jeong, Y.H., Chang, S.H., "Subcooled flow boiling CHF enhancement with porous surface coatings," *Int. J. Heat Mass Trans.*, 50, pp. 3649-3657, (2007).

[77] Liu, C., Yang, C., "Effect of coating layer thickness for boiling heat transfer on micro porous coated surface in confined and unconfined spaces," *Exp. Therm. Fluid Sci.*, 47, pp. 40-47, (2013).

[78] Liu, C., Yang, C., "Effect of space distance for boiling heat transfer on micro porous coated surface in confined space," *Exp. Therm. Fluid Sci.*, 47, pp. 163-171, (2013).

[79] El-Genk, M.S., Ali, A.F., "Enhanced nucleate boiling on copper micro-porous surfaces," *Int. J. Multiph. Flow*, 36, pp. 780-792, (2010).

[80] Parker, J.L., El-Genk, M.S., "Enhanced saturation and subcooled boiling of FC-72 dielectric liquid," *Int. J. Heat Mass Trans.*, 48, pp. 3736-3752, (2005).

[81] El-Genk, M.S., Parker, J.L., "Enhanced boiling of HFE-7100 dielectric liquid on porous graphite," *Energy Conversion and Management*, 46, pp. 2455-2481, (2005).

[82] El-Genk, M.S., Parker, J.L., "Nucleate boiling of FC-72 and HFE-7100 on porous graphite at different orientations and liquid subcooling," *Energy Conversion and Management*, 49, pp. 733-750, (2008).

[83] Bar-Cohen, A., McNeil, A., "Parametric effects of pool boiling critical heat flux in dielectric liquids," *ASME Pool and External Flow Boiling*, pp. 171-175, (1992).

[84] Shock, R.A.W., "Boiling in Multicomponent Fluids," In G.F. Hewitt, J.M. Delhaye and N. Zuber, Eds., *Multiphase Science and Techonology, Volume 1*, Washington D.C.: Hemisphere Publishing Corporation, pp. 281-386, (1982).

[85] Thome, J.R., "Boiling Heat Transfer in Binary Liquid Mixtures," In S. Kakac and M. Ishii, Eds., *Advances in Two-Phase Flow and Heat Transfer*, Dordrecht, Netherlands: Springer, pp. 275-319, (1983).

[86] Thome, J.R., "Enhanced Boiling of Mixtures, *Enhanced Boiling Heat Transfer*, Washington D.C.: Hemisphere Publishing Corporation, pp. 175-203, (1990).

[87] Stephan, K., "Heat Transfer During Boiling of Mixtures in Free Convection," In *Heat Transfer In Condensation and Boiling. International Series in Heat and Mass Transfer*, Berlin: Springer, pp. 262-284, (1992).

[88] Mori, Y.H., Inui, E., Komotori, K., "Pool Boiling Heat Transfer to Emulsions," *J. Heat Trans.*, 100, pp. 613-617, (1978).

[89] Ostrovskiy N.Y., "Free Convection Heat Transfer in the Boiling of Emulsions," *Heat Trans.- Sov. Res.*, 20(2), pp. 147-153, (1988).

[90] Roesle, M.L., Kulacki, F.A., "Boiling of Dilute Emulsions- Toward a New Modeling Framework," *Ind. Eng. Chem. Res.*, 49, pp. 5188-5196 (2010)

[91] Kandlikar, S.G., "Heat Transfer Mechanisms During Flow Boiling in Microchannels," *J. Heat Trans.*, 126, pp. 8-16, (2004).

[92] Roesle, M.L., Kulacki, F.A., "An experimental study of boiling in dilute emulsions, part A: Heat Transfer," *Int. J. Heat Mass Tran.*, 55, pp. 2160-2165 (2012).

[93] Bulanov, N.V., Skripov, V.P., Khmyl'nin, V.A., "Heat Transfer to Emulsion with Superheating of its Disperse Phase," *J. Eng. Phys. Thermophys.*, 46(1), pp. 1-3 (1984).

[94] Gasanov, B.M., Bulanov, N.V., Baidakov, V.G., "Boiling Characteristics of Emulsions with a Low-Boiling Dispersed Phase and Surfactants," *J. Eng. Phys. Thermophys.*, 70(2), pp. 179-181 (1997).

[95] Bulanov, N.V., Gasanov, B.M., "Special Features of Boiling of Emulsions with a Low-Boiling Dispersed Phase," *Heat Trans. Res.*, 38(3), pp. 259-273, (2007).

[96] Gasanov, B.M., Bulanov, N.V., "Effect of the Concentration and Size of Droplets of the Dispersed Phase of an Emulsion on the Character of Heat Exchange in a Boiling Emulsion," *High Temp.*, 52(1), pp. 86-92, (2014).

[97] Roesle, M.L., "Boiling of Dilute Emulsions." Thesis. University of Minnesota, (2010).

[98] Bulanov, N.V., "An Analysis of the Heat Flux Density under Conditions of Boiling Internal Phase of Emulsion," *High Temp.*, 39(3), pp. 462-469 (2001).

[99] Roesle, M.L., Kulacki, F.A., *Boiling Heat Transfer in Dilute Emulsions, Springer Briefs in Applied Science and Technology, Thermal Engineering and Applied Science*, New York: Springer, (2013).

[100] Bulanov, N.V., Skripov, V.P., Gasanov, B.M., Baidakov, V.G., "Boiling of Emulsions with a Low-Boiling Dispersed Phase," *Heat Trans. Res.*, 27(5-8), pp. 312-315 (1996).

[101] Bulanov, N.V., Gasanov, B.M., "Experimental Setup for Studying the Chain Activation of Low-Temperature Boiling Sites in Superheated Liquid Droplets," *Colloid J.*, 67(5), pp. 531-536, (2005).

[102] Roesle, M.L, Kulacki, F.A., "An experimental study of boiling in dilute emulsions, part B: Visualization," *Int. J. Heat Mass Trans.*, 55, pp. 2166-2172, (2012).

[103] Gasanov, B.M., "Boiling of emulsions with a low-boiling disperse phase. High-speed filming," *Int. J. Heat Mass Trans.*, 94, pp. 66-74, (2016).

[104] Gasanov, B.M., Bulanov, N.V., "Effect of the droplet size of an emulsions dispersion phase in nucleate boiling and emulsion boiling crisis," *Int. J. Heat Mass Trans.*, 88, pp. 256-260, (2015).

[105] Bulanov, N.V., Skripov, V.P., Khmylnik, V.A., "Heat Transfer to Emulsion with a Low-Boiling Disperse Phase," *Heat Trans. Res.*, 25(6), pp. 786-789, (1993).

[106] Roesle, M.L., Kulacki, F.A., "Characteristics of two-component two-phase flow and heat transfer in a flat microchannel," *Proceedings of the ASME Summer Heat Transfer Conference*, pp. 395-405, (2008).

[107] Janssen, D., Kulacki, F.A., "Flow boiling of dilute emulsions," *Int. J. Heat Mass Trans.*, 115, pp. 1000-1007, (2017).

[108] Morshed, A.K.M.M., Paul, T.C., Fang, R., Khan, J.A., "Flow Boiling Characteristics of Dilute Emulsion in Microchannel," *Proceedings of the ASME 2012 International Mechanical Engineering Congress & Exposition*, pp. 2085-2091, (2012).

[109] Avedisian, C.T., "Bubble Growth in Superheated Liquid Droplets," In N.P. Cheremisinoff, Ed., *Encyclopedia of Fluid Mechanics, Volume 3: Gas-Liquid Flows*, Houston, Texas: Gulf Publishing Company, pp. 130-190, (1986).

[110] Bulanov, N.V., Gasanov, B.M., Muratov, G.N., "Critical Volume and Chain Activation of Boiling Sites in Emulsions with Low-Boiling Dispersed Phase," *High Temp.*, 47(6), pp. 864-869, (2009).

[111] Mikic, B.B., Rohsenow, W.M., Griffith, P., "On Bubble Growth Rates," *Int. J. Heat Mass Trans.*, 13, pp. 657-666, (1970).

[112] Roesle, M.L., Kulacki, F.A., "Boiling of small droplets," *Int. J. Heat Mass Trans.*, 53, pp. 5587-5595, (2010).

[113] Rozentsvaig, A.K., Strashinskii, C.S., "Mechanisms of Boiling of an Emulsion with a Low-Boiling Disperse Phase in a Turbulent Flow of a Homogeneous Emulsion," *J. Eng. Phys. Thermophys.*, 83(3), pp. 486-495, (2010).

[114] Bulanov, N.V., Gasanov, B.M., "Characteristic Features of the Boiling of Emulsions Having a Low-Boiling Dispersed Phase," *J. Eng. Phys. Thermophys.*, 79(6), pp. 1130-1133, (2006).

[115] Janssen D.D., Mohs, W.F., Kulacki, F.A., "High Resolution Imaging of Frost Melting," *ASME Summer Heat Transfer Conference, Vol. 1*, HT2012-58061, pp. 491-507 (2012).

[116] Janssen, D., "Experimental Strategies for Frost Analysis," Thesis. University of Minnesota, (2011).

[117] Drew, D, Passman, S, *Theory of Multicomponent Fluids*, New York: Springer-Verlag, (1999).

[118] Kundu, P.K., Cohen, I.M., Dowling, D.R., *Fluid Mechanics (5th Edition)*, Massachusetts: Elsevier, (2012).

[119] Wenzel, E.A., Kulacki, F.A., Garrick, S.C., "Modeling and simulation of liquid-liquid droplet heating in a laminar boundary layer," *Int. J. Heat Mass Trans.*, 97, pp. 653-661, (2016).

[120] Chen, J.C., "Correlation for Boiling Heat Transfer to Saturated Fluids in Convective Flow," *Ind. Eng. Chem. Process Des. Dev.*, 5(3), pp. 322-329, (1966).

[121] Bulanov, N.V., Skripov, V.P., Shuravenko, N.A., "Heat Transfer to an Emulsion with High Superheating of its Disperse Phase," *J. Eng. Phys. Thermophys.*, 42(2), pp. 157-159, (1982).

[122] Bulanov, N.V., Gasanov, B.M., Turchaninova, E.A., "Results of Experimental Investigation of Heat Transfer with Emulsions with Low-Boiling Disperse Phase," *High Temp.*, 44(2), pp. 267-282, (2006).

[123] Bulanov, N.V., Gasanov, B.M., "Peculiarities of boiling of emulsions with a low-boiling disperse phase," *Int. J. Heat Mass Trans.*, 51, pp. 1628-1632, (2008).

[124] Rozentsvaig, A.K., Strashinskii, C.S., "Hydrodynamic Aspects of Boiling Up of a Disperse Phase in a Homogeneous Turbulent Flow of an Emulsion," *High Temp.*, 49(1), pp. 143-146, (2011).

[125] Bulanov, N.V., Gasanov, B.M., "Dependence of the Beginning of Chain Activation of Boiling Sites on Superheating of Droplets in the Dispersed Phase of the Emulsion," *High Temp.*, 49(2), pp. 213-216, (2011).

[126] Rozentsvaig, A.K., Strashinskii, C.S., "Model of the Heat Exchange in Boiling Emulsions with Low-Boiling Disperse Phase at the Solid Wall," *Contemp. Eng. Sci.*, 7, pp. 965-971, (2014).

[127] Rozentsvaig, A.K., Strashinskii, C.S., "Regimes of Heat Transfer During Boiling Emulsions with Low-Temperature Dispersed Phase," *Appl. Math. Sci.*, 9, pp. 5593-5601, (2015).

[128] Roesle, M.L., Lunde, D.L., Kulacki, F.A., "Boiling Heat Transfer to Dilute Emulsions From a Vertical Heated Strip," *J. Heat Trans.*, 137, pp. 041503-1-8, (2015).

[129] Rozentsvaig, A.K., Strashinskii, C.S., "Identification of Models of Transfer Processes in Complex Disperse Systems," *Appl. Math. Sci.*, 10, pp. 1151-1161, (2016).

[130] Rozentsvaig, A.K., Strashinskii, C.S., "Modeling of heat transfer conditions in cooling lubricant emulsions with low-boiling continuous media in narrow gaps," *Int. J. Heat Mass Trans.*, 102, pp. 555-560, (2016).

[131] Shah, R.K., London, A.L., "Laminar Flow Forced Convection in Ducts," In: *Advances in Heat Transfer*., New York: Academic Press, (1978).

[132] Ghiaasiaan, M.S., *Convective Heat and Mass Transfer*. Cambidge, UK: Cambridge University Press, (2011).

[133] Munson, B.R., Young, D.F., Okiishi, T.H., Huebsch, W.W., *Fundamentals of Fluid Mechanics (6th ed.)*. Hoboken, NJ, USA: Wiley, (2009).

[134] Bird, R.B., Stewart, W.E., Lightfoot, E.N., *Transport Phenomena (1st ed.)*. New York: Wiley, (1960).

[135] Prins, J.A., Mulder, J., Schenk, J., "Heat Transfer in Laminar Flow Between Parallel Plates," *Appl. Sci. Res., Sect. A*, 4(5), pp. 405-413, (1954).

[136] Cess, R.D., Shaffer, E.D., "Heat Transfer to Laminar Flow Between Parallel Plates With a Prescribed Wall Heat Flux," *Appl. Sci. Res., Sect. A*, 8(1), pp. 339-344, (1959).

[137] Arpaci, V.S., *Conduction Heat Transfer (Abridged Ed.)*. New York: Pearson Publishing, (1991).

[138] Bergman, T.L., Lavine, A.S., Incropera, F.P., Dewitt, D.P., *Fundamentals of Heat and Mass Transfer (7th ed.)*, New York: Wiley, (2011).

Appendices

A. FC-72 Tables of Properties

Table A1. Properties for FC-72 at 1 atm and 25 °C.

MW [kg/kmol]	338
T_{sat} [°C]	56
P_v [kPa]	30.9
h_{fg} [kJ/kg]	88
ρ [kg/m^3]	1680
μ [Ns/m^2]	64×10^{-5}
ν [m^2/s]	0.38×10^{-6}
C_p [J/kgK]	1100
k [W/mK]	0.057
σ [N/m]	0.01
n	1.251

Table A2. FC-72 properties as a function of temperature.

T [°C]	ρ [kg/m^3]	$\mu \times 10^5$ [Ns/m^2]	C_p [J/kgK]	k [W/mK]
0	1740	92.2	1014	0.060
5	1727	82.9	1022	0.059
10	1714	77.1	1030	0.059
15	1701	71.4	1037	0.058
20	1688	65.8	1045	0.058
25	1675	62.0	1053	0.057
30	1662	58.2	1061	0.057
35	1649	54.4	1068	0.056
40	1636	52.3	1076	0.056
45	1623	48.7	1084	0.055
50	1610	46.7	1092	0.055
55	1596	43.9	1099	0.054
60	1583	41.2	1107	0.053
65	1570	39.3	1115	0.053
70	1557	37.4	1123	0.052

B. Experimental Apparatus Drawings

Included below is a list of the parts used in the test section assembly. The detailed part drawings are also included for reference on the following pages.

Table B1. List of test section parts and drawing numbers.

Part	Drawing Number
Flow Test Section Assembly	A1
100 µm Gap Height Top	2
250 µm Gap Height Top	3
500 µm Gap Height Top	4
Base	5
Copper Plate (Plain Surface)	6
Garolite Heater Box	7

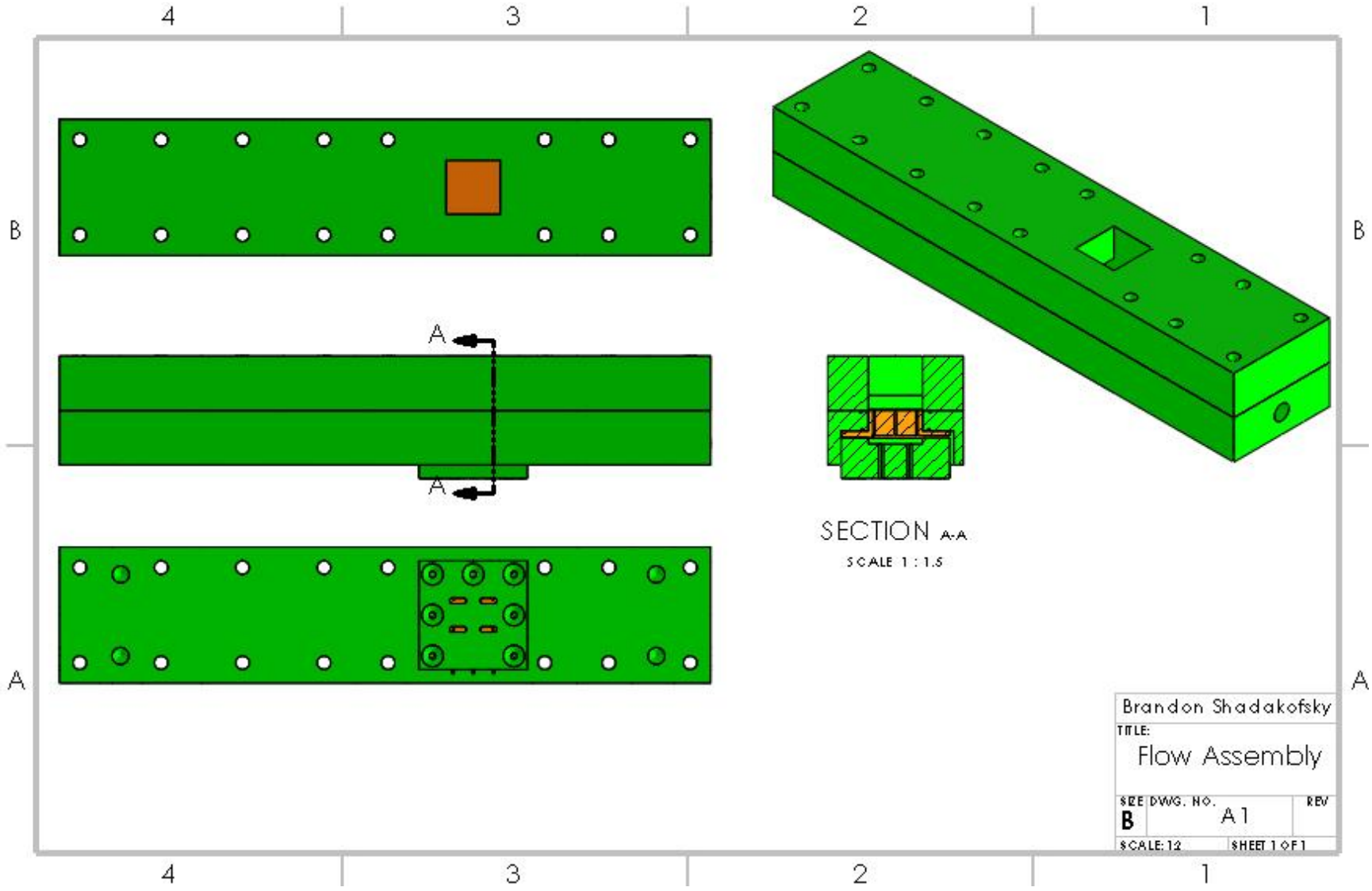
4
3
2
1
B
A
A
A
SECTION A-A
SCALE 1 : 1.5
Brandon Shadakofsky
TITLE:
Flow Assembly
SIZE
B
DWG. NO.
A1
REV
SCALE: 1:2
SHEET 1 OF 1

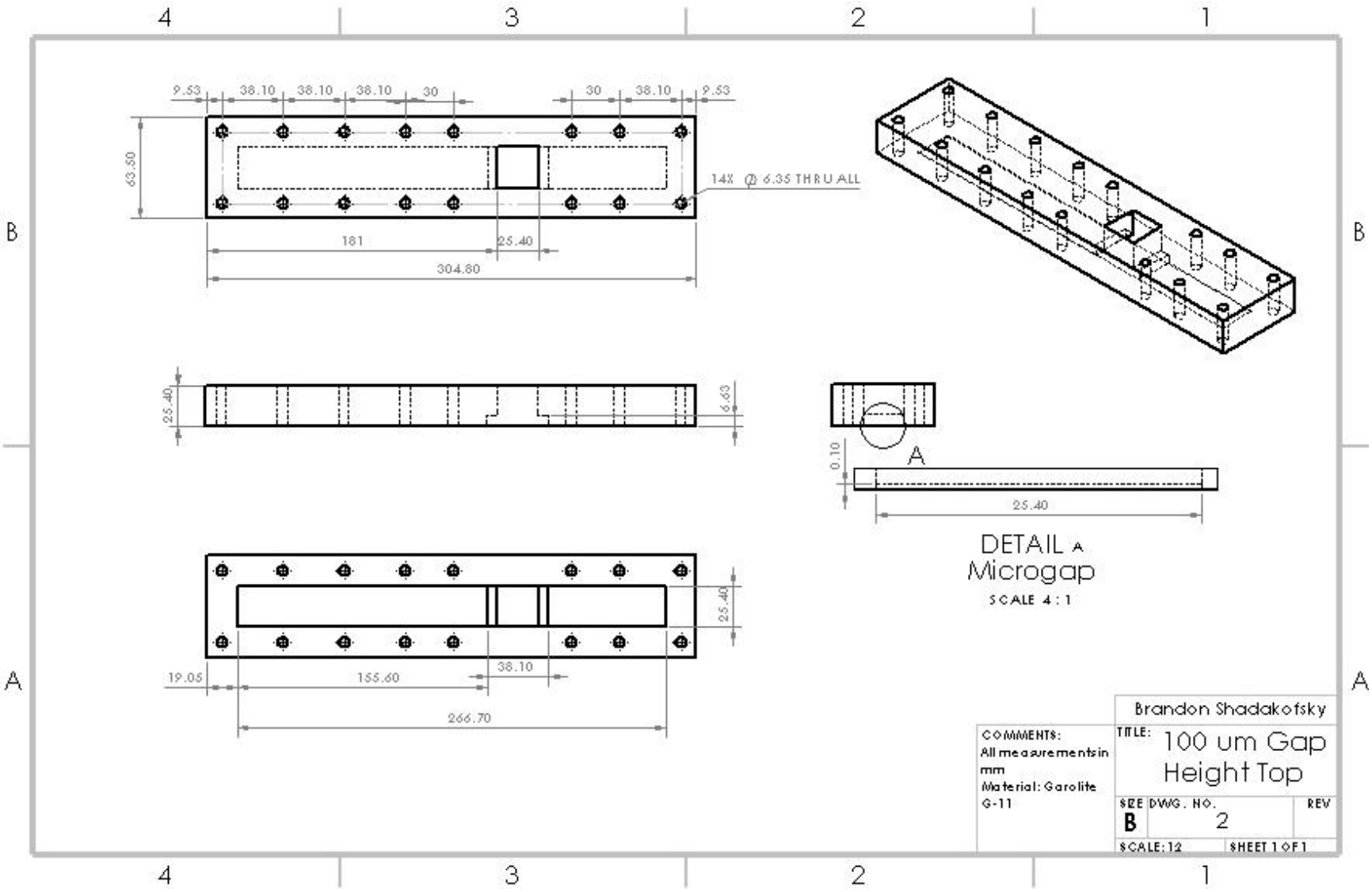
9.53
38.10
38.10
38.10
30
30
38.10
9.53
63.50
14X Ø 6.35 THRU ALL
181
25.40
304.80
25.40
6.63
0.10
A
25.40
DETAIL A
Microgap
SCALE 4 : 1
25.40
19.05
155.60
38.10
266.70
Brandon Shadakofsky
COMMENTS:
All measurements in mm
Material: Garolite G-11
TITLE: 100 um Gap Height Top
SIZE B
DWG. NO. 2
REV
SCALE: 1:2
SHEET 1 OF 1

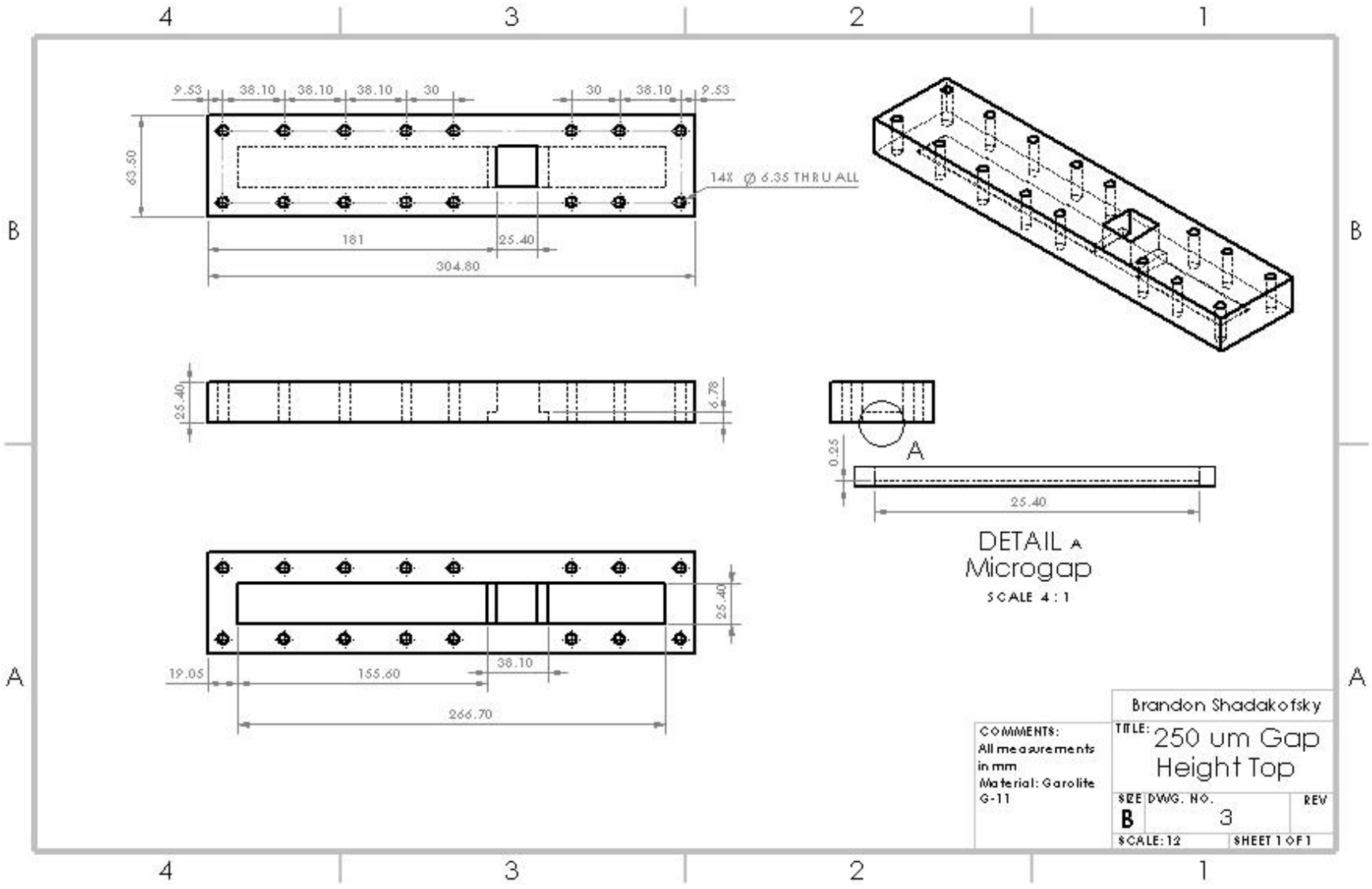
9.53
38.10
38.10
38.10
30
30
38.10
9.53
63.50
14X Ø 6.35 THRU ALL
181
25.40
304.80
25.40
6.78
0.25
A
25.40
DETAIL A
Microgap
SCALE 4 : 1
25.40
19.05
155.60
38.10
266.70
Brandon Shadakofsky
COMMENTS:
All measurements in mm
Material: Garolite G-11
TITLE: 250 um Gap Height Top
SIZE B
DWG. NO. 3
REV
SCALE: 1:2
SHEET 1 OF 1

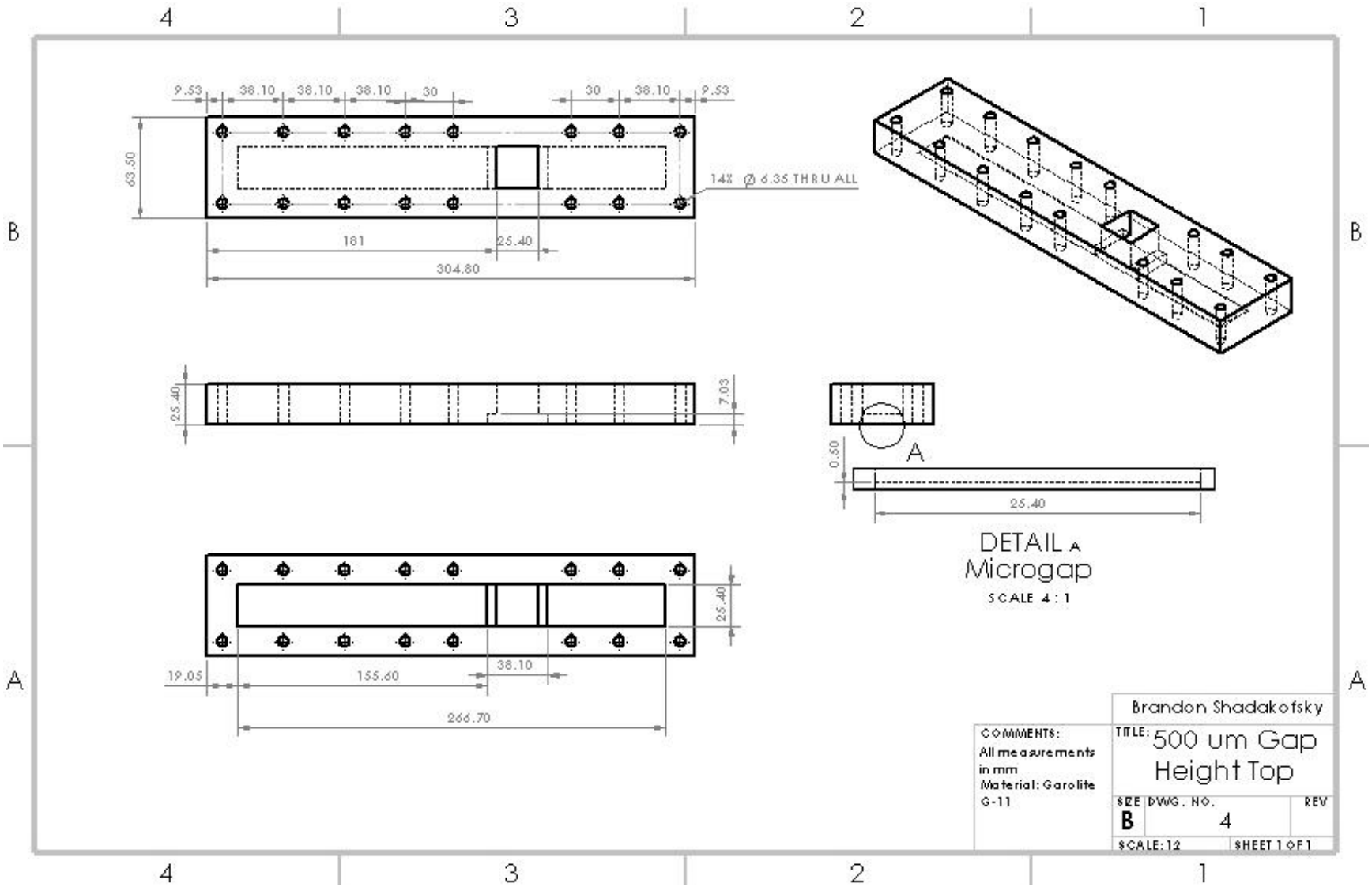
9.53
38.10
38.10
38.10
30
30
38.10
9.53
63.50
14X Ø 6.35 THRU ALL
181
25.40
304.80
25.40
7.03
0.50
A
25.40
DETAIL A
Microgap
SCALE 4 : 1
25.40
19.05
155.60
38.10
266.70
Brandon Shadakofsky
COMMENTS:
All measurements in mm
Material: Garolite G-11
TITLE: 500 um Gap Height Top
SIZE B
DWG. NO. 4
REV
SCALE: 1:2
SHEET 1 OF 1

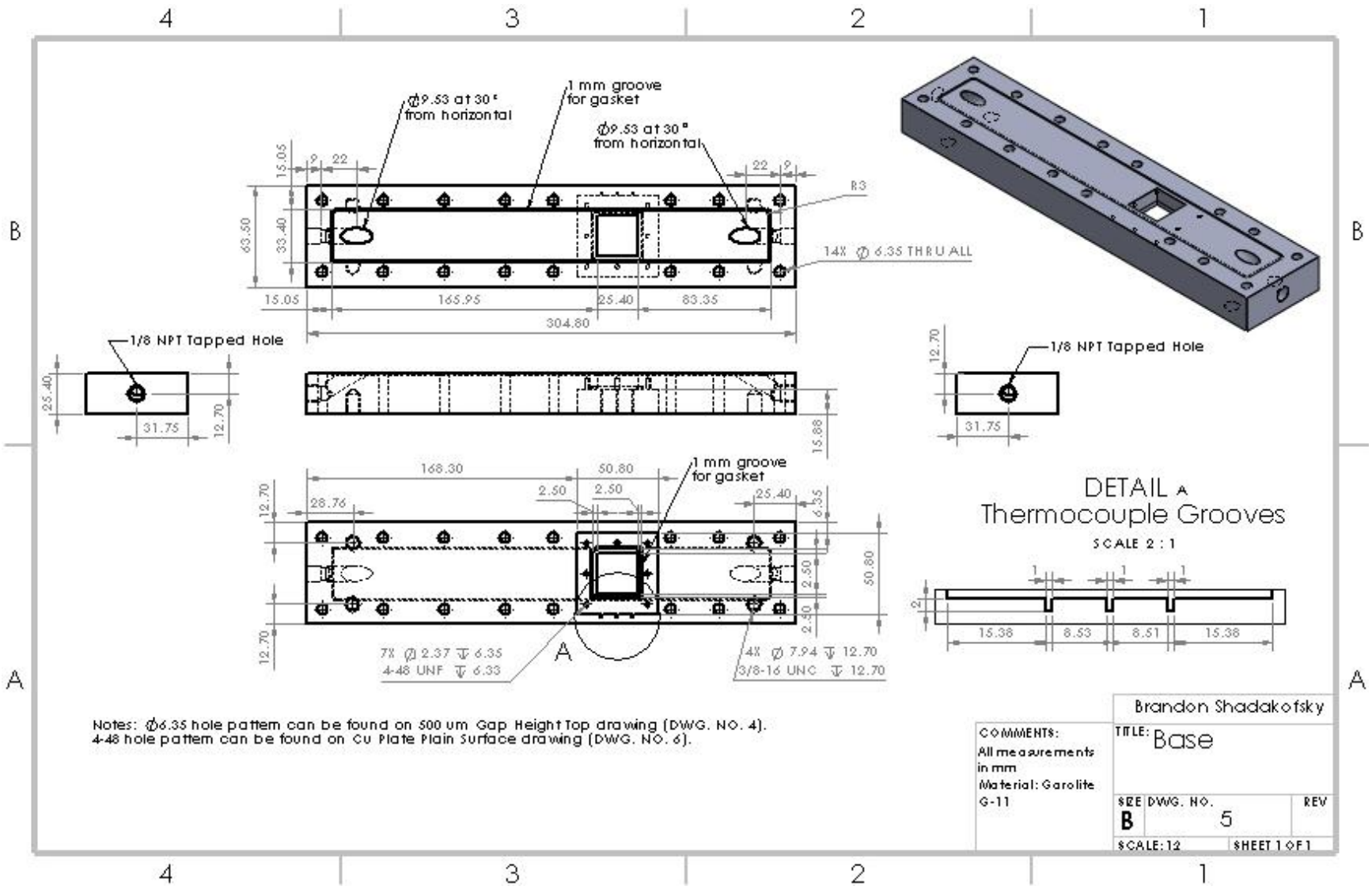
Ø9.53 at 30°
from horizontal
1 mm groove
for gasket
Ø9.53 at 30°
from horizontal
15.05
22
22
R3
63.50
33.40
14X Ø 6.35 THRU ALL
15.05
165.95
25.40
83.35
304.80
1/8 NPT Tapped Hole
25.40
31.75
12.70
15.88
1/8 NPT Tapped Hole
12.70
31.75
168.30
50.80
1 mm groove
for gasket
2.50
2.50
25.40
6.35
12.70
28.76
50.80
2.50
2.50
12.70
7X Ø 2.37 ↧ 6.35
4-48 UNF ↧ 6.33
A
4X Ø 7.94 ↧ 12.70
3/8-16 UNC ↧ 12.70
DETAIL A
Thermocouple Grooves
SCALE 2 : 1
1
1
1
2
15.38
8.53
8.51
15.38
Notes: Ø6.35 hole pattern can be found on 500 um Gap Height Top drawing (DWG. NO. 4).
4-48 hole pattern can be found on Cu Plate Plain Surface drawing (DWG. NO. 6).
COMMENTS:
All measurements
in mm
Material: Garolite
G-11
Brandon Shadakofsky
TITLE: Base
SIZE B
DWG. NO. 5
REV
SCALE: 1:2
SHEET 1 OF 1

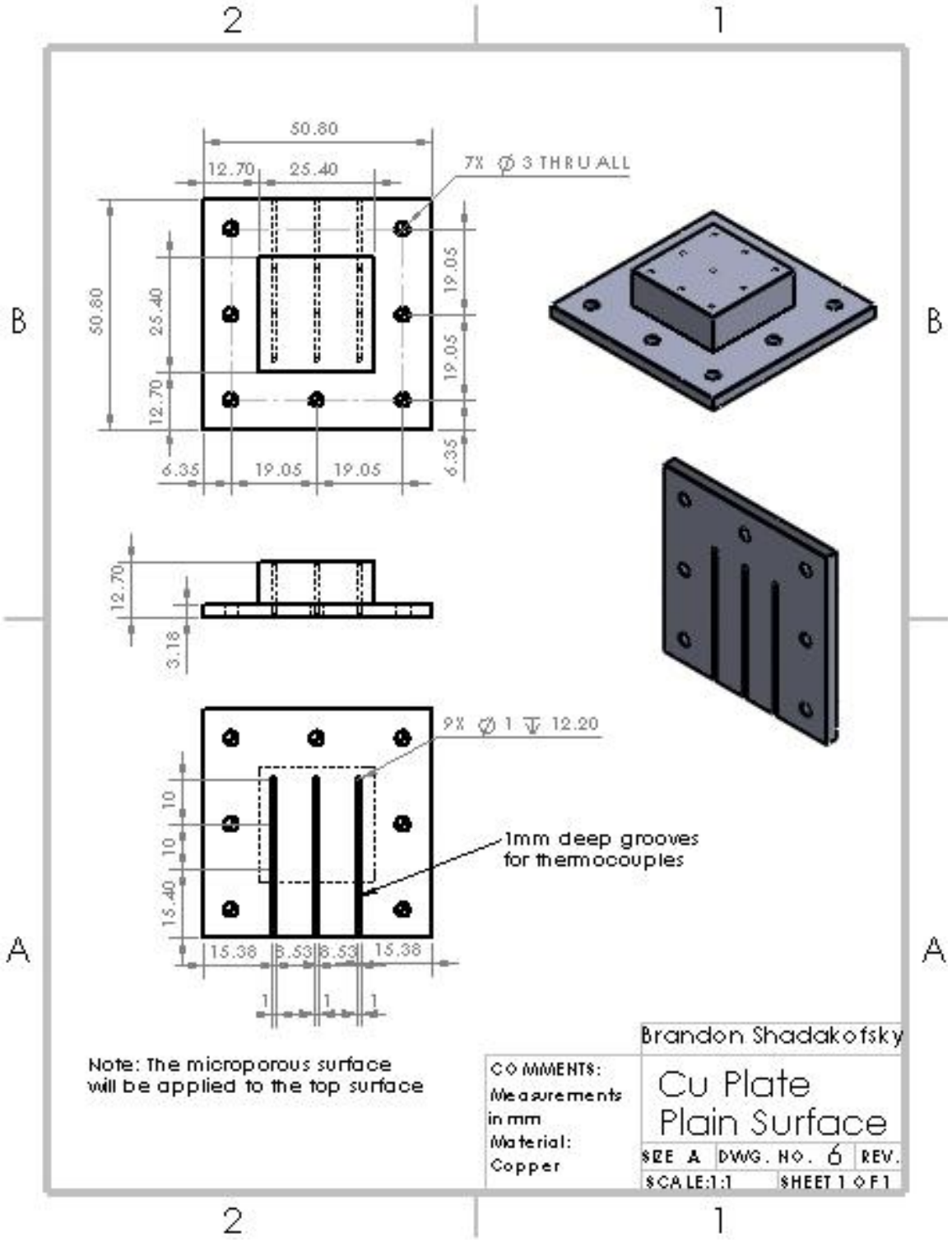
2
1
B
A
50.80
12.70
25.40
7X Ø 3 THRU ALL
19.05
19.05
6.35
19.05
19.05
6.35
12.70
3.18
9X Ø 1 ↧ 12.20
10
10
15.40
1mm deep grooves
for thermocouples
15.38
8.53
8.53
15.38
1
1
1
Note: The microporous surface
will be applied to the top surface
COMMENTS:
Measurements
in mm
Material:
Copper
Brandon Shadakofsky
Cu Plate
Plain Surface
SIZE A
DWG. NO. 6
REV.
SCALE:1:1
SHEET 1 OF 1

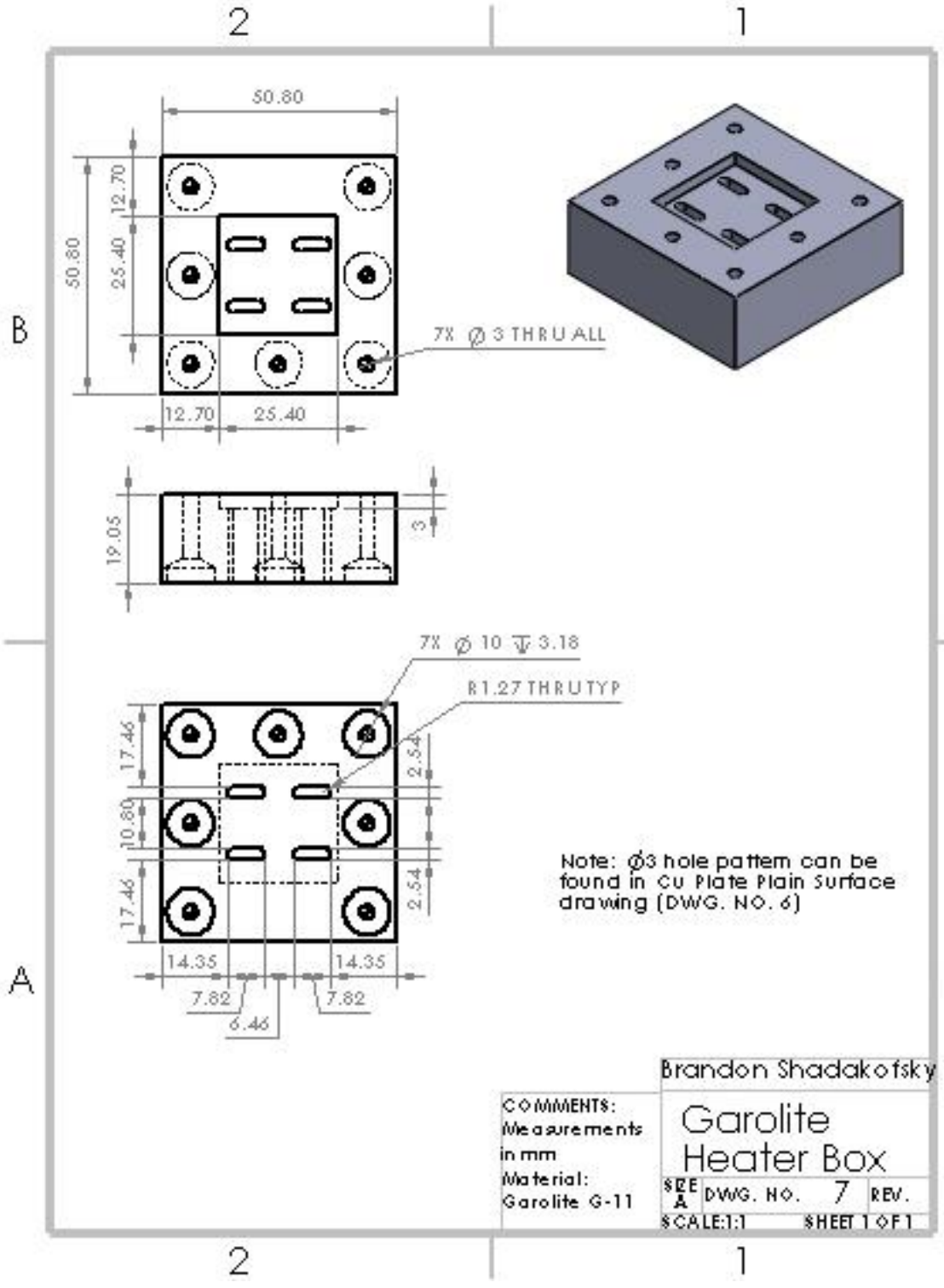
2
1
B
A
50.80
12.70
25.40
50.80
7X ⌀3 THRU ALL
12.70
25.40
19.05
3
7X ⌀10 ↧3.18
R1.27 THRU TYP
17.46
10.80
17.46
2.54
2.54
14.35
14.35
7.82
6.46
7.82
Note: ⌀3 hole pattern can be found in Cu Plate Plain Surface drawing (DWG. NO. 6)
Brandon Shadakofsky
COMMENTS:
Measurements in mm
Material:
Garolite G-11
Garolite Heater Box
SIZE A
DWG. NO. 7
REV.
SCALE:1:1
SHEET 1 OF 1

C. Single-Component, Single-Phase Analytical Solution

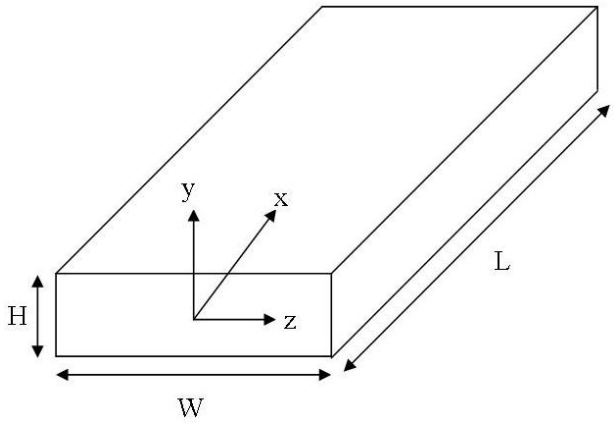

Fig. C1. Channel Geometry.

Consider laminar, steady, incompressible, hydrodynamically developed flow of a single component Newtonian fluid in the absence of body forces (other than gravity) through the horizontal rectangular channel shown in Fig. C1. Also, consider flow that is thermally developing and flow in the x-direction only. Conservation of mass and momentum for this flow are governed by the continuity and Navier-Stokes equations:

$$\frac{\partial \rho}{\partial t} + \rho \nabla \cdot \vec{U} = 0 \tag{C1}$$

$$\rho \frac{D\vec{U}}{Dt} = \rho \left(\frac{\partial \vec{U}}{\partial t} + \vec{U} \cdot \nabla \vec{U} \right) = \rho \vec{g} - \nabla P + \mu \nabla^2 \vec{U} \tag{C2}$$

If the velocity vector is $\vec{U} = (u, v, w)$, with $v = w = 0$, the continuity equation gives

$$\frac{\partial u}{\partial x} = 0 \tag{C3}$$

while the y- and z-momentum equations yield (neglecting the small hydrostatic pressure change in the y-direction)

$$\frac{\partial P}{\partial y} = \frac{\partial P}{\partial z} = 0 \tag{C4}$$

Lastly, the x-momentum equation yields

$$\frac{dP}{dx} = \mu\left(\frac{\partial^2 u}{\partial y^2} + \frac{\partial^2 u}{\partial z^2}\right) \tag{C5}$$

with the boundary conditions

$$\begin{aligned} &1) u\left(-{}^{H}/_{2}, z\right) = 0 \qquad 3) u\left(y, -{}^{W}/_{2}\right) = 0 \\ &2) u\left({}^{H}/_{2}, z\right) = 0 \qquad 4) u\left(y, {}^{W}/_{2}\right) = 0 \end{aligned} \tag{C6}$$

The solution to Eqn. (C5) with the boundary conditions shown is [131, 132]:

$$u(y,z) = -\frac{16\left({}^{W}/_{2}\right)^2}{\pi^3 \mu}\left(\frac{dP}{dx}\right) \sum_{n=1,3,5\ldots}^{\infty} \frac{1}{n^3}(-1)^{(n-1)/2}\left[1 - \frac{\cosh\left(\frac{n\pi y}{W}\right)}{\cosh\left(\frac{n\pi H}{2W}\right)}\right]\cos\left(\frac{n\pi z}{W}\right) \tag{C7}$$

where the pressure drop is obtained by [133]

$$\frac{dP}{dx} = -\frac{f}{D_h}\frac{\rho u_m^2}{2} \tag{C8}$$

and the friction factor can be approximated to within 0.5% by [131]

$$\begin{aligned} f * Re_{D_h} = 24\Bigg[1 - 1.3553\left(\frac{H}{W}\right) + 1.9467\left(\frac{H}{W}\right)^2 - 1.7012\left(\frac{H}{W}\right)^3 \\ +0.9564\left(\frac{H}{W}\right)^4 - 0.2537\left(\frac{H}{W}\right)^5\Bigg] \end{aligned} \tag{C9}$$

The mean velocity u_m is [132]

$$u_m = -\frac{16\left({}^{W}/_{2}\right)^2}{3\mu}\left(\frac{dP}{dx}\right)\left[1 - \frac{192}{\pi^5}\left(\frac{W}{H}\right)\sum_{n=1,3,5\ldots}^{\infty}\frac{1}{n^5}\tanh\left(\frac{n\pi H}{2W}\right)\right] \tag{C10}$$

or, if the flow rate is known a priori, the mean velocity can be determined by

$$u_m = \frac{Q}{HW} = \frac{G}{\rho} \tag{C11}$$

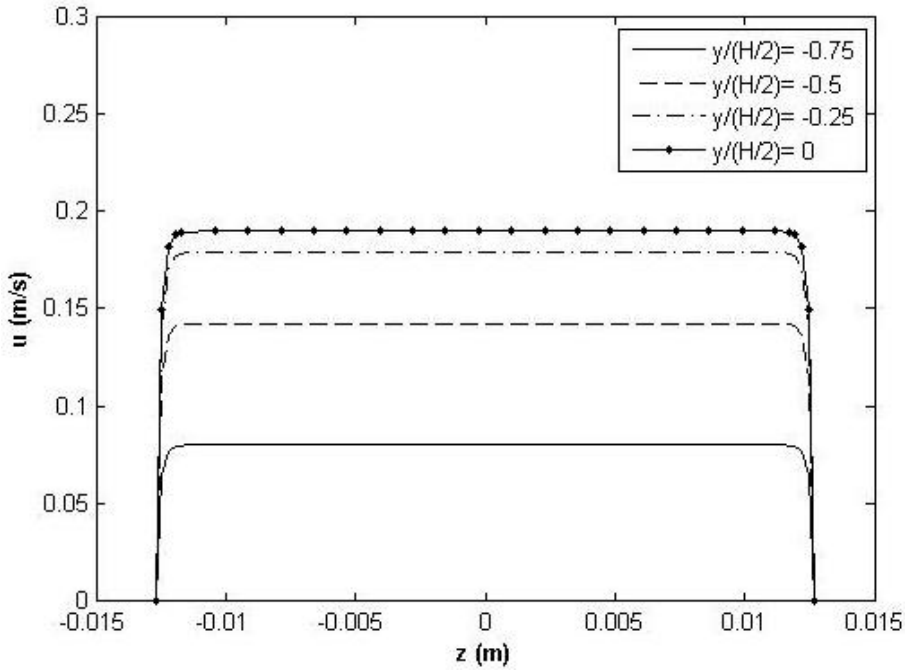

Fig. C2. Velocity profiles for D_h = 1000 μm, G = 500 kg/m^{2}s.

The velocity given by Eqn. (C7) is parabolic in both the y- and z-direction. The shape should become more flat in the z-direction and more parabolic in the y-direction for increasing aspect ratio W/H. If the aspect ratio is large enough, the rectangular channel can be assumed to be a pair of parallel plates. From Fig. C2, this assumption is valid for the smallest aspect ratio. Therefore, the channel can be assumed to be a parallel plate channel for all values of D_h being studied. The z-derivative then drops out of the x-momentum equation and the velocity solution is

$$u = -\frac{1}{2\mu}\left(\frac{dP}{dx}\right)\left(\frac{H^2}{4} - y^2\right) = \frac{3}{2}u_m\left[1 - \left(\frac{2y}{H}\right)^2\right] \tag{C12}$$

Now, the energy equation for developing thermal conditions is

$$k_f\left(\frac{\partial^2 T}{\partial x^2} + \frac{\partial^2 T}{\partial y^2}\right) = \rho C_p u\frac{\partial T}{\partial x} \tag{C13}$$

If the Peclet number is much greater than 1- as is the case for all values of Re_{D_h} being studied- conduction in the x-direction can be neglected and the energy equation reduces to Eqn. (C14) with the boundary conditions shown.

$$\frac{\partial^2 T}{\partial y^2} = \frac{\rho C_p}{k_f} u \frac{\partial T}{\partial x} = \frac{3}{2\alpha} u_m \left[1 - \left(\frac{2y}{H}\right)^2\right] \frac{\partial T}{\partial x} \tag{C14}$$

$$1)\ T(0,y) = T_i \qquad 2) - k_f \left.\frac{\partial T}{\partial y}\right|_{-H/2} = q_w'' \qquad 3) - k_f \left.\frac{\partial T}{\partial y}\right|_{H/2} = 0 \tag{C15}$$

Equation (C14) can be solved more easily by non-dimensionalizing T, x and y:

$$\theta = \frac{T - T_i}{\left(\frac{q_w'' D_h}{k_f}\right)} \qquad y^* = \frac{2y}{H} \qquad x^* = \frac{x}{D_h Re_{D_h} Pr} \tag{C16}$$

With the non-dimensionalization scheme shown, Eqns. (C14) and (C15) become

$$\frac{\partial^2 \theta}{\partial y^{*2}} = \frac{3}{32}(1 - y^{*2}) \frac{\partial \theta}{\partial x^*} \tag{C17}$$

$$1)\ \theta(0,y^*) = 0 \qquad 2)\ \left.\frac{\partial \theta}{\partial y^*}\right|_{-1} = -\frac{1}{4} \qquad 3)\ \left.\frac{\partial \theta}{\partial y^*}\right|_{1} = 0 \tag{C18}$$

Equation (C17) can be solved by sequentially applying superposition and separation of variables. Let the solution take the form $\theta = \theta_1 + \theta_2$, where θ_1 represents the fully-developed solution [132, 134]. θ_1 and θ_2 then are the solutions to the following differential equations:

$$\frac{\partial^2 \theta_1}{\partial y^{*2}} = \frac{3}{32}(1 - y^{*2}) \frac{\partial \theta_m}{\partial x^*} \tag{C19}$$

$$\frac{\partial^2 \theta_2}{\partial y^{*2}} = \frac{3}{32}(1 - y^{*2}) \frac{\partial \theta_2}{\partial x^*} \tag{C20}$$

θ_1 satisfies boundary conditions 2 and 3 above while θ_2 satisfies the boundary conditions

$$1)\ \theta_2(0,y^*) = -\theta_1(0,y^*) \qquad 2)\ \left.\frac{\partial\theta_2}{\partial y^*}\right|_{-1} = 0 \qquad 3)\ \left.\frac{\partial\theta_2}{\partial y^*}\right|_{1} = 0 \tag{C21}$$

An energy balance on the channel yields $\theta_m = 2x^*$, so Eqn. (C19) can simply be integrated twice to find θ_1. One of the two resulting constants can be determined by applying either boundary condition and the second constant can be determined by applying the definition of the mean temperature, Eqn. (C22), and using the energy balance result noted above.

$$T_m = \frac{1}{\dot{m}}\int \rho u T dA = \frac{1}{H u_m}\int u T dy \tag{C22}$$

Using separation of variables, θ_2 is expressed as $\theta_2 = X(x^*)Y(y^*)$. $X(x^*)$ is found to be

$$X(x^*) = C_1 \exp\left(-\frac{32}{3}\lambda^2 x^*\right) \tag{C23}$$

and $Y(y^*)$ is assumed to be a linear combination of eigenfunctions:

$$Y(y^*) = \sum_{n=1}^{\infty} C_{2,n} Y_n(y^*) \tag{C24}$$

Each eigenfunction is assumed to be represented by a power series [135 - 137]:

$$Y_n(y^*) = \sum_{m=0}^{\infty} a_m {y^*}^m \tag{C25}$$

The coefficients a_m can be solved for by plugging Eqn. (C25) into Eqn. (C20) and are given by the following recursive relationship.

$$a_0 = 1 \quad a_2 = -a_0\frac{\lambda_n^2}{2} \quad a_3 = -a_1\frac{\lambda_n^2}{6} \quad a_m = \frac{\lambda_n^2}{m(m-1)}(a_{m-4} - a_{m-2}) \tag{C26}$$

Note that this recursive relationship involves two parameters, a_0 and a_1. Without loss of generality, a_0 can be chosen to be 1 and BC 2 in Eqn. (C21) can be applied to determine a_1 in terms of a_0. The eigenvalues λ_n are found by applying BC 3 in Eqn. (C21) and the

constants C_1 and $C_{2,n}$ are combined to form one set of constants C_n, which are determined by applying BC 1 and the principal of orthogonality. C_n are given by

$$C_n = \frac{\int_{-1}^{1} Y_n(y^*) * \left[-\frac{3}{32}y^{*2} + \frac{1}{64}y^{*4} + \frac{1}{8}y^* + \frac{39}{2240}\right] dy^*}{\int_{-1}^{1} Y_n^2(y^*) dy^*} \tag{C27}$$

The first seven values of λ_n, a_1, C_n and the value of the eigenfunctions at the heated wall are shown in Table C1.

Table C1. Eigenvalues and constants evaluated from the power series solutions.

n	λ_n	a_1	C_n	$Y_n(-1)$
1	4.2872	2.3715	0.0687	-0.9052
2	8.3037	9.9307	-0.0301	0.4919
3	12.3106	11.2041	0.0304	-0.7426
4	16.3145	12.0152	-0.0299	0.9207
5	20.3171	12.5437	0.0291	-1.0578
6	24.3190	12.8984	-0.0281	1.1681
7	28.3232	13.1439	0.0272	-1.2529

The final temperature solution is then given by

$$T(x,y) = T_i + \frac{2Hq_w^{"}}{k_f}\left[\frac{3}{32}\left(\frac{2y}{H}\right)^2 - \frac{1}{64}\left(\frac{2y}{H}\right)^4 - \frac{1}{8}\left(\frac{2y}{H}\right) - \frac{39}{2240} + \frac{x}{HRe_{D_h}Pr} + \sum_{n=1}^{\infty} C_n Y_n(y) \exp\left(-\frac{32}{6HRe_{D_h}Pr}\lambda_n^2 x\right)\right] \tag{C28}$$

The local and average Nusselt number can be determined by evaluating the temperature distribution at the heated wall and utilizing the definition of the heat transfer coefficient:

$$h = \frac{q_w^{"}}{T_w - T_m} \tag{C29}$$

$$Nu(x) = \left[\frac{26}{140} + \sum_{n=1}^{\infty} C_n Y_n \left(-\frac{H}{2}\right) \exp\left(-\frac{32}{6HRe_{D_h}Pr}\lambda_n^2 x\right)\right]^{-1} \quad \text{(C30)}$$

$$\overline{Nu(x)} = \frac{1}{x}\int_0^x Nu(x')dx' \quad \text{(C31)}$$

Note that Eqn. (C30) demonstrates the well-known fully developed Nusselt number solution, Nu = 140/26, for one constant heat flux and one insulated wall [131].

D. One-Dimensional Conduction Resistance Model

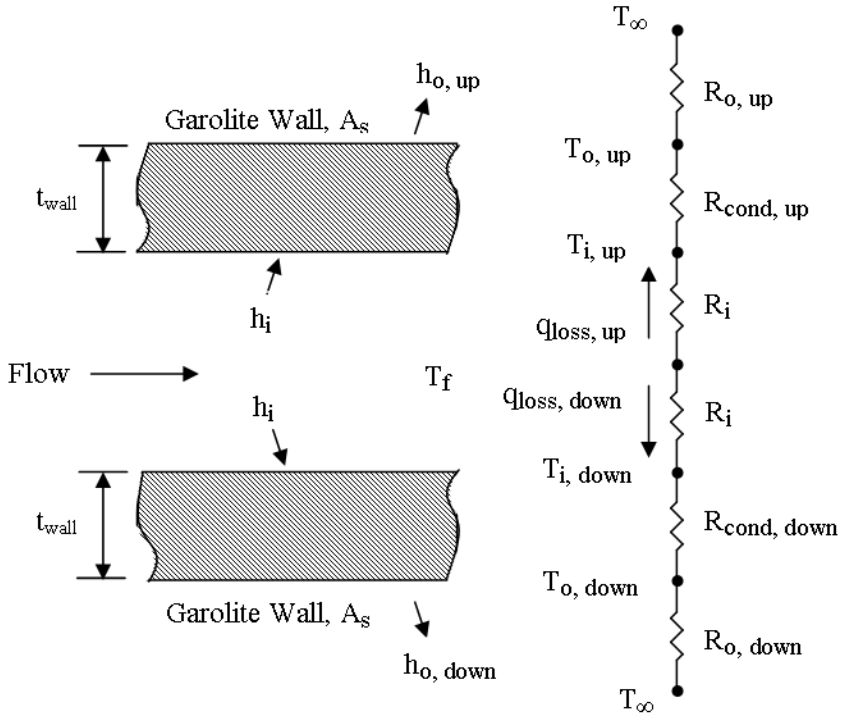

Fig. D1. Conduction resistance network in the microgap

As the fluid within the microgap heats, the gap will lose energy to the surroundings due to conduction through the microgap walls and convection to the surroundings. The actual amount of energy transferred to the fluid would be the supplied energy from the heaters minus the heat lost to the surroundings. Though conduction in the walls may be two- or three-dimensional, the low thermal conductivity of Garolite and the long conduction paths in the transverse and axial directions result in much smaller resistances to conduction heat transfer in the wall-normal direction. Thus, one-dimensional conduction is a good approximation for determining the heat lost to the surroundings.

Consider the conduction resistance model shown in Fig. D1. The hot fluid at temperature T_f will lose energy due to the conduction and convection resistances on the top and bottom walls. In each direction there are resistances to heat transfer that will limit the amount of energy transferred to the surroundings.

First, there is a resistance associated with convection heat transfer in the interior of the gap. It is assumed that the heat transfer coefficients on the inside top and bottom surfaces are equivalent. The resistance R_i associated with convection on the interior surfaces is

$$R_i = \frac{1}{h_i A_s} \tag{D1}$$

In single-phase flow, h_i is equal to the single-phase heat transfer coefficient. In two-phase flow, h_i is of $O(10^3 - 10^4)$. Next, there is a resistance associated with conduction through the Garolite wall. For conduction on the bottom surface, the resistance $R_{cond, down}$ is

$$R_{cond,down} = \frac{t_{wall}}{k_{wall} A_s} \tag{D2}$$

where k_{wall} is the thermal conductivity of Garolite and the Garolite walls are 1 inch thick. For the 200 μm and 500 μm gaps, $R_{cond, down} = R_{cond, up}$. However, the 1000 μm gap has a glass window installed for viewing the boiling process in the gap. In this gap, conduction occurs in parallel through both the glass and Garolite and the resulting resistance is

$$\frac{1}{R_{cond,up}} = \frac{1}{R_{glass}} + \frac{1}{R_{wall}} = \frac{k_g A_g}{t_g} + \frac{k_{wall}(A_s - A_g)}{t_{wall}} \tag{D3}$$

where k_g, A_g and t_g are the thermal conductivity, surface area and thickness of the glass window, respectively. Last, there is a resistance due to convection on the outer surface of the microgap. The resistance on the top and bottom surfaces have the same form as Eqn. (D1) but with the associated heat transfer coefficients $h_{o, up}$ and $h_{o, down}$. These heat transfer coefficients can be determined using correlations for natural convection on upward-facing and downward-facing heated plates that are available in most heat transfer references, e.g. [138].

At steady state, in each direction the heat that flows is equivalent through each resistance because the resistances are in series. The three resistances for each direction can be replaced by an equivalent resistance. For the heat lost through the bottom surface, $q_{loss,\ down}$, the heat lost and equivalent resistance are

$$q_{loss,down} = \frac{T_f - T_\infty}{R_{eq,down}} \tag{D4}$$

$$R_{eq,down} = R_i + R_{cond,down} + R_{o,down} \tag{D5}$$

The heat lost through the top surface has a similar form with the resistances associated with that heat flow. The total heat lost is given by

$$q_{loss} = q_{loss,down} + q_{loss,up} \tag{D6}$$

E. Measured Mass Flux for Each Experiment

All mass fluxes tabulated are in kg/m^2s.

Table E1. Mass flux for each experiment performed on the smooth surface. The inlet temperature for all emulsion runs is 30 °C.

Plain Surface			
	Hydraulic Diameter		
	200 µm	**500 µm**	**1000 µm**
Water, T_i = 30 °C	167, 345, 555	149, 348, 543	152, 347, 552
Water, T_i = 51 °C	164, 365, 566	163, 351, 549	147, 354, 558
Water, T_i = 70 °C	173, 358, 560	159, 347, 558	153, 357, 538
0.1% Emulsion	348	359	362
0.5% Emulsion	341	345	345
1% Emulsion	160, 356, 546	159, 357, 541	143, 345, 558
2% Emulsion	343	359	359

Table E2. Mass flux for each experiment performed on Porous Surface 1. The inlet temperature for all runs is 30 °C.

Porous Surface 1			
	Hydraulic Diameter		
	200 µm	**500 µm**	**1000 µm**
Water	161, 360, 555	156, 352, 546	158, 351, 548
0.1% Emulsion	357	360	346
0.5% Emulsion	348	349	346
1% Emulsion	162, 350, 547	156, 349, 559	157, 359, 553
2% Emulsion	349	341	341

Table E3. Mass flux for each experiment performed on Porous Surface 2. The inlet temperature for all runs is 30 °C.

Porous Surface 2			
	Hydraulic Diameter		
	200 µm	**500 µm**	**1000 µm**
Water	164, 346, 548	156, 349, 560	154, 356, 560
0.1% Emulsion	354	355	354
0.5% Emulsion	350	352	354
1% Emulsion	162, 354, 552	163, 355, 541	163, 352, 550
2% Emulsion	350	350	352

Table E4. Mass flux for each experiment performed on Porous Surface 3. The inlet temperature for all runs is 30 °C.

Porous Surface 3			
	Hydraulic Diameter		
	200 µm	**500 µm**	**1000 µm**
Water	163, 353, 550	159, 344, 548	162, 360, 551
0.1% Emulsion	344	351	345
0.5% Emulsion	351	344	345
1% Emulsion	159, 356	157, 350, 553	157, 355, 561
2% Emulsion	356	345	345

F. Tabulated Experimental Results

Table F1. Experimental data for water on the plain surface, D_h = 200 µm, T_i = 30 °C.

D_h = 200 µm															
G = 150 kg/m^{2}s					G = 350 kg/m^{2}s					G = 550 kg/m^{2}s				
q [W]	q"$_{net}$ [kW/m^2]	h [W/m^{2}K]	ΔP [kPa]	T_w [°C]	q [W]	q"$_{net}$ [kW/m^2]	h [W/m^{2}K]	ΔP [kPa]	T_w [°C]	q [W]	q"$_{net}$ [kW/m^2]	h [W/m^{2}K]	ΔP [kPa]	T_w [°C]
20.6	12.11	1578	2.93	41.6	20.5	11.93	2358	7.51	35.9	20.6	12.08	2987	13.17	34.8
30.8	28.34	2456	2.96	47.5	40.6	43.85	4586	7.98	42.4	40.8	44.15	5570	13.35	40.0
40.7	44.07	2912	2.91	53.3	60.6	75.74	5455	8.01	48.9	61.0	76.36	6462	13.32	45.2
51.0	60.50	3231	3.00	59.2	80.7	107.67	5855	7.91	55.6	80.8	107.94	6909	13.37	50.3
61.0	76.37	3432	3.00	65.1	100.7	139.51	6118	7.91	62.2	100.6	139.45	7190	13.46	55.3
70.9	92.13	3588	3.03	70.8	120.2	170.60	6217	7.41	69.6	120.7	171.30	7352	13.57	60.6
80.4	107.18	3674	3.07	76.6	140.3	202.60	6231	7.44	77.3	140.2	202.46	7479	13.52	65.7
89.8	122.17	3547	3.34	85.7	160.4	234.50	6201	7.46	84.9	160.3	234.39	7524	13.49	71.1
94.8	130.08	3279	3.52	93.5	171.1	251.59	6255	7.48	88.7	179.9	265.61	7541	13.44	76.7
					180.5	266.56	6069	7.65	93.6	200.3	298.02	7358	13.37	83.6
					185.4	274.37	6141	7.74	95.6	210.8	314.73	7336	13.31	86.7
					190.5	282.43	6251	8.01	97.0	220.0	329.36	7286	13.25	89.7
					195.7	290.68	6498	8.06	97.5	229.4	344.32	7230	13.37	92.9
					200.8	298.81	6650	8.20	98.8	235.0	353.23	7279	13.34	94.0
					204.8	305.18	6784	8.35	99.7	240.6	362.14	7387	13.33	95.1
					210.2	313.77	7012	8.75	100.8	246.1	370.89	7395	13.35	96.5
					215.6	322.36	7604	9.07	101.1	250.4	377.73	7552	13.50	96.7
										256.3	387.12	7719	13.55	97.2
										260.6	393.96	7866	13.61	97.7
										265.2	401.28	7991	13.67	98.2
										269.6	408.28	8079	13.78	99.0
										275.6	417.83	8281	13.76	99.3
										280.3	425.31	8431	13.88	99.7
										291.2	442.65	8755	14.09	100.7
										300.4	457.29	9036	14.16	101.4
										320.3	488.95	9765	14.51	102.5
										340.5	521.10	10358	15.43	104.7
										351.4	538.44	10922	18.45	108.2

Table F2. Experimental data for water on the plain surface, D_h = 500 μm, T_i = 30 °C.

D_h = 500 μm															
G = 150 kg/m^{2}s					G = 350 kg/m^{2}s					G = 550 kg/m^{2}s				
q [W]	q"$_{net}$ [kW/m^2]	h [W/m^{2}K]	ΔP [kPa]	T_w [°C]	q [W]	q"$_{net}$ [kW/m^2]	h [W/m^{2}K]	ΔP [kPa]	T_w [°C]	q [W]	q"$_{net}$ [kW/m^2]	h [W/m^{2}K]	ΔP [kPa]	T_w [°C]
20.7	12.24	1490	1.80	39.2	20.9	12.54	2457	5.21	34.7	21.3	13.25	2642	8.31	34.7
40.6	43.93	2841	1.83	48.5	40.8	44.25	4391	5.16	40.7	40.7	44.07	4852	8.30	39.5
60.3	75.28	3386	1.76	57.4	60.7	75.82	5066	5.14	46.6	61.0	76.37	5678	8.29	44.5
80.3	107.08	3659	1.70	66.7	80.8	107.86	5430	5.17	52.5	80.9	108.01	6122	8.22	49.3
100.3	138.86	3824	1.72	75.8	100.9	139.91	5677	5.23	58.1	100.7	139.49	6374	8.21	54.2
119.9	170.11	3948	1.71	84.7	120.1	170.39	5792	5.25	63.8	120.7	171.33	6579	8.09	59.0
140.3	202.49	3859	1.83	96.5	139.9	201.84	5813	5.20	70.0	140.3	202.52	6692	8.05	63.8
146.1	211.72	4051	1.87	97.3	160.1	233.99	5888	5.17	76.1	160.1	234.10	6700	7.98	69.1
150.7	219.15	4192	1.96	97.9	180.3	266.24	5767	5.16	83.4	180.6	266.66	6578	7.90	75.4
155.4	226.51	4433	1.92	97.9	200.5	298.34	5618	5.12	91.1	201.1	299.29	6614	7.85	80.8
161.1	235.63	4110	1.95	97.6	210.6	314.41	5554	5.13	95.3	220.1	329.52	6680	7.87	85.5
165.7	242.90	4253	1.97	97.5	215.6	322.36	5781	5.21	94.7	239.6	360.55	6633	7.84	91.2
170.6	250.70	4269	2.04	98.0	221.1	331.11	5940	5.22	95.0	250.9	378.53	6767	7.85	93.2
174.8	257.38	5143	2.11	99.6	225.3	337.80	6004	5.23	95.6	255.1	385.21	6796	7.84	94.2
181.1	267.42	5391	2.07	100.0	231.0	346.87	6132	5.19	96.2	260.7	394.12	6808	7.76	95.7
191.3	283.70	5732	2.29	101.0	235.1	353.39	6228	5.17	96.6	265.0	400.97	6809	7.73	96.9
200.9	298.97	6086	2.38	102.3	241.0	362.78	6425	5.19	96.7	271.2	410.83	7046	7.77	96.7
219.4	328.41	7318	3.93	107.2	245.4	369.78	6475	5.21	97.5	275.7	417.99	7073	7.78	97.8
240.7	362.30	7681	4.68	111.0	250.5	377.89	6648	5.24	97.4	280.2	425.15	7162	7.77	98.1
260.9	394.44	7996	5.25	113.1	255.6	386.01	6740	5.26	98.1	291.1	442.49	7418	7.69	98.9
280.3	425.31	8118	5.49	116.2	260.1	393.17	6933	5.24	97.8	301.4	458.88	7744	7.74	99.1
290.2	441.06	7488	6.10	122.8	270.0	408.92	7141	5.31	98.7	320.5	489.27	8407	7.75	99.0
					280.8	426.10	7410	5.22	99.5	340.1	520.46	8834	7.67	100.6
					301.2	458.56	7953	5.31	100.6	361.0	553.71	9294	7.71	102.1
					320.5	489.27	8524	5.27	101.4	380.4	584.58	9592	7.62	104.3
					340.8	521.57	8946	5.21	103.8					
					361.3	554.19	9506	5.30	105.4					
					380.3	584.42	9931	5.32	107.0					

Table F3. Experimental data for water on the plain surface, D_h = 1000 μm, T_i = 30 °C.

D_h = 1000 μm															
G = 150 kg/m^{2}s					G = 350 kg/m^{2}s					G = 550 kg/m^{2}s				
q [W]	q"$_{net}$ [kW/m^2]	h [W/m^{2}K]	ΔP [kPa]	T_w [°C]	q [W]	q"$_{net}$ [kW/m^2]	h [W/m^{2}K]	ΔP [kPa]	T_w [°C]	q [W]	q"$_{net}$ [kW/m^2]	h [W/m^{2}K]	ΔP [kPa]	T_w [°C]
20.5	11.98	1519	1.38	37.6	21.4	13.38	2138	2.90	35.5	21.0	12.79	2395	7.41	34.5
41.1	44.76	2768	1.35	47.1	40.7	44.06	3745	2.86	41.7	41.1	44.65	4507	7.48	39.4
60.6	75.67	3206	1.34	55.7	60.7	75.91	4310	2.83	48.2	60.9	76.20	5326	7.55	44.2
80.2	106.94	3457	1.30	64.2	80.7	107.70	4613	2.79	54.6	80.2	106.99	5751	7.62	48.8
100.7	139.56	3620	1.34	73.0	100.8	139.67	4810	2.81	61.0	100.5	139.29	6022	7.62	53.6
119.9	170.03	3715	1.35	81.4	120.5	171.02	4954	2.80	67.1	120.5	171.11	6248	7.59	58.3
140.1	202.17	3802	1.38	90.0	140.9	203.54	5055	2.78	73.4	140.2	202.39	6389	7.61	62.9
150.4	218.64	3784	1.36	95.4	160.5	234.74	5081	2.77	80.1	160.2	234.21	6508	7.52	67.6
155.1	226.12	3889	1.43	96.1	180.4	266.32	5062	2.83	87.1	180.6	266.69	6616	7.54	72.2
160.0	233.83	4009	1.38	96.6	200.7	298.66	5273	2.77	91.9	200.8	298.81	6686	7.47	77.0
165.5	242.68	4174	1.42	96.7	209.7	312.98	5254	2.80	95.0	219.8	329.05	6644	7.39	82.4
170.9	251.29	4287	1.47	97.6	215.3	321.89	5412	2.75	95.2	240.3	361.66	6708	7.43	87.3
175.4	258.37	4446	1.49	97.4	220.8	330.64	5497	2.83	96.1	260.0	393.01	6701	7.37	92.8
180.4	266.29	4544	1.51	98.1	225.8	338.59	5620	2.80	96.3	265.7	402.08	6745	7.32	93.9
185.4	274.37	4701	1.47	98.2	230.7	346.39	5702	2.79	97.0	270.7	410.03	6737	7.27	95.6
190.6	282.65	4834	1.43	98.8	235.0	353.23	5885	2.86	96.5	275.3	417.35	6843	7.26	96.0
196.0	291.11	5024	1.57	98.6	241.5	363.57	6003	2.84	97.3	280.4	425.47	6891	7.31	97.0
200.5	298.34	5175	1.52	98.6	250.2	377.42	6166	2.78	98.2	285.2	433.11	7077	7.32	96.7
210.6	314.41	5426	1.47	99.6	260.7	394.12	6393	2.78	99.0	290.0	440.74	7229	7.30	96.7
220.4	330.00	5777	1.56	99.5	280.6	425.79	6867	2.83	99.9	296.2	450.61	7348	7.24	97.5
240.9	362.62	6402	1.64	100.2	301.1	458.40	7377	2.85	100.8	300.8	457.93	7455	7.29	97.7
260.2	393.33	7006	1.62	100.9	320.3	488.95	7865	2.89	101.4	310.4	473.20	7648	7.22	98.5
280.0	424.83	7586	1.76	101.9	341.3	522.37	8473	2.97	101.6	320.0	488.48	7857	7.28	99.2
300.5	457.45	8188	1.73	103.2	360.5	552.92	8957	2.93	102.3	340.7	521.41	8416	7.24	99.7
320.6	489.43	8795	1.87	104.2	380.3	584.42	9558	2.99	102.8	360.9	553.55	8915	7.15	100.6
340.5	521.10	9346	1.88	105.6						380.7	585.06	9396	7.10	101.3
360.5	552.92	9807	1.88	107.5										
380.8	585.22	9854	2.15	112.1										

Table F4. Experimental data for water on the plain surface, D_h = 200 μm, T_i = 51 °C.

D_h = 200 μm															
G=150 kg/m^{2}s					G=350 kg/m^{2}s					G=550 kg/m^{2}s				
q [W]	q"$_{net}$ [kW/m^2]	h [W/m^{2}K]	ΔP [kPa]	T_w [°C]	q [W]	q"$_{net}$ [kW/m^2]	h [W/m^{2}K]	ΔP [kPa]	T_w [°C]	q [W]	q"$_{net}$ [kW/m^2]	h [W/m^{2}K]	ΔP [kPa]	T_w [°C]
21.3	13.24	1373	2.34	58.0	20.9	12.55	1568	5.52	56.7	21.1	12.84	2181	7.89	54.8
40.9	44.35	2452	2.38	70.6	41.0	44.49	3135	5.33	64.2	40.2	43.20	3679	7.48	62.1
60.7	75.82	2848	2.45	83.6	60.5	75.56	3783	5.14	73.0	60.3	75.23	4245	7.42	70.0
70.9	92.06	2800	2.73	93.2	80.0	106.61	4082	5.10	81.0	80.2	106.84	4558	7.21	77.5
80.0	106.57	2801	3.05	100.1	100.7	139.53	4259	4.63	91.3	100.6	139.38	4765	7.18	85.2
85.4	115.20	3151	3.32	100.4	110.3	154.74	4044	4.84	98.2	120.4	170.87	4909	7.18	92.2
90.5	123.38	3418	3.55	101.1	115.3	162.77	4144	4.82	100.1	130.4	186.74	4922	7.25	96.4
95.3	130.87	3774	3.80	101.9	121.3	172.34	4488	4.87	100.1	140.1	202.17	4901	7.13	100.9
101.2	140.29	4068	4.04	102.7	125.1	178.35	4594	5.05	100.8	145.3	210.43	5151	7.04	101.1
120.4	170.87	5359	5.75	105.1	131.2	188.09	4908	5.34	101.4	150.7	219.02	5386	7.05	101.3
141.0	203.62	6011	7.91	107.1	135.7	195.23	5125	5.43	101.9	155.5	226.75	5595	7.05	101.7
160.6	234.90	6507	10.14	108.8	141.4	204.33	5331	5.74	102.6	161.0	235.41	5796	7.19	102.3
180.6	266.64	7137	11.96	111.0	160.7	234.93	6238	6.32	104.3	180.3	266.20	6506	7.54	104.2
200.8	298.81	7363	13.30	113.0	180.7	266.82	7266	6.63	105.8	201.4	299.77	7301	7.83	106.2
221.4	331.59	7807	15.41	115.9	200.2	297.86	8385	7.72	107.4	220.7	330.48	8071	8.11	107.8
240.9	362.62	7841	16.73	120.0	220.0	329.36	8873	10.22	110.2	241.6	363.73	8957	8.90	109.5
260.8	394.28	7782	18.24	123.1	241.4	363.41	9399	12.47	111.8	261.0	394.60	9760	10.01	110.9
280.7	425.95	8015	20.17	127.7	260.5	393.80	9800	14.91	113.3	280.9	426.26	10542	12.08	112.9
300.8	457.93	7358	21.02	134.6	281.1	426.58	10309	17.46	115.2	300.6	457.61	11308	14.05	114.6
					300.7	457.77	10645	19.37	116.9	300.6	457.61	11275	14.20	114.7
					320.1	488.64	11047	21.69	118.1	319.9	488.32	11584	16.55	116.4
					340.8	521.57	11386	23.31	119.8	340.0	520.30	11970	19.06	117.9
					360.7	553.24	11447	25.80	122.5	361.1	553.87	12383	21.99	119.3
					380.7	585.06	11366	27.40	125.6	380.3	584.42	12708	24.15	120.6
					390.5	600.65	11311	29.02	127.2	390.4	600.49	12848	25.70	121.5

Table F5. Experimental data for water on the plain surface, D_h = 500 μm, T_i = 51 °C.

D_h = 500 μm															
G=150 kg/m^{2}s					G=350 kg/m^{2}s					G=550 kg/m^{2}s				
q [W]	q"$_{net}$ [kW/m^2]	h [W/m^{2}K]	ΔP [kPa]	T_w [°C]	q [W]	q"$_{net}$ [kW/m^2]	h [W/m^{2}K]	ΔP [kPa]	T_w [°C]	q [W]	q"$_{net}$ [kW/m^2]	h [W/m^{2}K]	ΔP [kPa]	T_w [°C]
21.2	13.06	1765	1.34	57.8	21.1	12.8	1898	2.86	55.6	20.9	12.5	2122	5.90	54.8
40.7	44.09	2733	1.39	68.8	40.4	43.5	3290	2.52	63.7	40.5	43.8	3723	5.98	61.2
60.5	75.58	2874	1.39	81.1	60.4	75.5	3843	2.45	71.7	60.8	76.0	4400	6.12	67.3
69.9	90.55	2736	1.50	89.5	80.6	107.6	4134	2.45	79.6	80.4	107.2	4701	5.95	73.5
81.1	108.40	3051	1.54	93.4	99.9	138.3	4036	2.01	91.9	100.4	139.0	4906	5.96	79.9
90.4	123.09	3056	1.65	99.3	110.7	155.5	4029	2.00	96.6	120.4	170.9	5083	5.94	85.8
95.1	130.70	3261	1.63	99.8	115.2	162.7	4018	1.96	99.0	140.4	202.6	5137	5.85	92.8
100.6	139.32	3546	1.69	99.9	120.5	171.0	4177	1.94	100.2	150.8	219.2	5229	6.00	95.4
105.6	147.39	3799	1.73	100.3	125.4	178.8	4357	2.03	100.6	160.1	234.0	5232	5.85	98.7
110.8	155.61	4040	1.77	100.8	130.3	186.7	4553	2.14	100.9	165.4	242.5	5278	5.83	100.2
120.9	171.60	4448	1.80	101.9	135.5	194.9	4691	2.16	101.8	171.0	251.4	5434	6.03	100.5
141.1	203.79	5382	1.93	103.3	141.2	204.0	4917	2.14	102.3	175.5	258.5	5624	5.94	100.6
161.0	235.41	6338	2.30	105.2	161.0	235.4	5697	2.19	103.6	180.5	266.5	5753	5.70	101.5
181.0	267.34	7249	2.92	107.1	181.2	267.6	6382	2.74	105.9	190.8	282.9	5986	5.77	102.5
200.7	298.66	8421	3.39	108.3	201.1	299.3	7296	3.10	107.0	201.5	299.9	6282	5.93	103.3
220.8	330.64	9509	4.00	109.7	220.6	330.3	8082	3.55	108.4	220.8	330.6	6823	5.94	104.6
241.2	363.10	9984	4.48	111.4	241.4	363.4	9005	4.03	109.8	240.3	361.7	7373	5.61	106.4
260.7	394.12	10478	4.62	112.8	260.9	394.4	9678	4.52	111.1	261.2	394.9	7950	5.72	107.4
280.6	425.79	10939	5.11	114.2	280.9	426.3	10430	4.95	112.2	281.3	426.9	8493	5.99	108.6
300.3	457.13	11260	5.53	116.0	300.9	458.1	11093	5.44	113.6	300.4	457.3	9056	5.87	109.7
320.8	489.75	11656	5.94	117.1	320.5	489.3	12027	6.03	114.9	320.8	489.8	9675	5.82	110.8
341.2	522.21	11996	6.38	118.8	340.7	521.4	12283	6.32	116.7	341.2	522.2	10255	6.14	112.0
360.3	552.60	11997	6.99	121.4	361.3	554.2	12515	6.90	118.6	360.2	552.4	10750	6.48	112.8
380.9	585.38	12231	7.30	123.1	380.3	584.4	12724	7.28	119.9	381.2	585.9	11204	6.80	114.5
391.4	602.08	12199	7.59	124.8	390.6	600.8	12848	7.49	120.8	391.3	601.9	11476	6.83	115.7

Table F6. Experimental data for water on the plain surface, D_h = 1000 μm, T_i = 51 °C.

D_h = 1000 μm															
G=150 kg/m^{2}s					G=350 kg/m^{2}s					G=550 kg/m^{2}s				
q [W]	q"$_{net}$ [kW/m^2]	h [W/m^{2}K]	ΔP [kPa]	T_w [°C]	q [W]	q"$_{net}$ [kW/m^2]	h [W/m^{2}K]	ΔP [kPa]	T_w [°C]	q [W]	q"$_{net}$ [kW/m^2]	h [W/m^{2}K]	ΔP [kPa]	T_w [°C]
20.7	12.2	1611	1.22	57.0	20.7	12.2	1897	2.90	55.0	20.6	12.1	2107	6.63	53.3
40.5	43.7	2673	1.21	67.3	40.2	43.3	3272	2.79	62.5	40.6	44.0	3849	6.65	59.0
60.1	74.9	3060	1.28	77.0	60.0	74.8	3809	2.73	69.5	60.6	75.8	4409	6.63	65.3
80.3	107.1	3323	1.25	85.7	80.4	107.3	4081	2.80	77.0	80.3	107.1	4620	6.63	71.5
99.8	138.0	3447	1.24	94.9	100.1	138.6	4217	2.88	84.3	100.7	139.5	4814	6.63	78.0
105.5	147.1	3491	1.27	97.6	120.9	171.6	4388	2.83	91.2	120.5	171.0	4957	6.61	84.0
110.4	155.0	3568	1.25	99.2	139.7	201.6	4440	2.89	98.2	140.9	203.4	5258	6.67	88.7
115.7	163.4	3818	1.29	99.1	145.4	210.6	4498	2.83	100.2	160.7	235.1	5384	6.74	94.3
120.5	171.0	3902	1.27	99.8	151.3	220.0	4738	2.80	100.0	170.8	251.0	5776	6.74	94.7
125.9	179.6	4034	1.32	100.0	155.6	226.9	4825	2.92	100.4	180.7	266.9	5851	6.70	97.0
130.2	186.5	4159	1.37	100.5	161.0	235.4	5018	2.85	101.0	191.2	283.6	6173	6.78	97.7
135.9	195.5	4320	1.36	101.1	166.0	243.4	5154	2.99	101.1	201.0	299.1	6348	6.81	99.0
141.1	203.8	4528	1.37	101.4	171.0	251.4	5332	2.91	101.5	210.5	314.2	6465	6.83	100.8
160.2	234.2	5184	1.41	102.3	181.4	267.9	5684	2.90	101.7	220.3	329.8	6668	6.85	101.7
181.1	267.5	5891	1.35	103.8	201.1	299.3	6203	2.78	103.6	240.8	362.5	7512	6.81	101.4
200.9	299.0	6601	1.47	105.4	221.5	331.8	6799	2.92	104.5	260.3	393.5	7894	6.84	103.3
220.4	330.0	7274	1.48	106.4	241.7	363.9	7484	2.84	105.6	281.1	426.6	8567	6.94	103.5
240.6	362.1	7935	1.61	107.7	261.3	395.1	7981	2.94	106.5	300.3	457.1	9008	6.90	104.8
261.6	395.6	8709	1.72	109.3	280.9	426.3	8637	2.88	107.7	321.9	491.5	9777	6.94	105.5
281.0	426.4	9352	1.84	110.5	300.9	458.1	9208	3.03	108.7	340.6	521.3	10199	7.06	106.9
300.9	458.1	9938	1.90	111.9	321.5	490.9	9810	3.02	109.8	361.4	554.3	10637	6.94	108.3
321.7	491.2	10745	2.04	113.1	341.9	523.3	10374	2.97	110.9	380.2	584.3	10905	6.89	110.0
340.3	520.8	11520	2.12	114.5	361.1	553.9	10720	3.25	112.3	391.5	602.2	11013	6.87	110.7
361.1	553.9	12335	2.23	116.1	380.1	584.1	11146	3.27	114.6					
380.5	584.7	12897	2.45	117.2	392.2	603.4	11418	3.30	115.3					
390.8	601.1	13401	2.48	118.2										

Table F7. Experimental data for water on the plain surface, D_h = 200 μm, T_i = 70 °C.

D_h = 200 μm															
G=150 kg/m^{2}s					G=350 kg/m^{2}s					G=550 kg/m^{2}s				
q [W]	q"$_{net}$ [kW/m^2]	h [W/m^{2}K]	ΔP [kPa]	T_w [°C]	q [W]	q"$_{net}$ [kW/m^2]	h [W/m^{2}K]	ΔP [kPa]	T_w [°C]	q [W]	q"$_{net}$ [kW/m^2]	h [W/m^{2}K]	ΔP [kPa]	T_w [°C]
20.9	12.51	1055	2.48	73.5	20.5	11.87	2934	8.57	71.3	20.6	12.16	3125	8.72	71.7
30.5	27.86	1723	2.66	80.7	30.8	28.24	4068	8.79	75.5	40.8	44.28	5015	8.93	78.2
40.3	43.37	1945	2.84	91.2	40.9	44.39	4419	8.89	79.6	60.7	75.93	5508	9.01	84.7
44.9	50.77	2643	3.03	95.3	50.7	60.02	4550	9.01	84.1	70.7	91.87	5708	9.20	87.7
					60.6	75.67	4487	9.11	89.2	80.8	107.86	5627	9.03	91.4
					70.3	91.24	4747	8.10	92.6	90.4	123.11	5948	9.12	94.1
					75.4	99.26	4658	8.16	95.2	95.0	130.39	5688	9.14	96.6
					80.2	106.84	4656	8.24	97.4	100.3	138.97	5917	9.08	97.7
					85.5	115.37	4825	8.33	99.2	105.3	146.93	5968	9.20	99.0
					90.2	122.87	5164	8.52	99.6	110.4	154.90	6313	9.41	99.7
					95.0	130.49	5529	8.79	100.3	115.2	162.66	6674	9.44	100.0
					100.0	138.48	5965	8.92	100.7	120.6	171.16	7036	9.71	100.8
					105.1	146.56	6444	9.16	101.0	124.9	178.08	7434	9.76	101.1
					110.8	155.61	7063	9.50	101.6	130.5	186.89	7849	10.02	101.6
					115.7	163.36	7753	9.55	101.8	140.6	203.01	8759	10.48	102.8
					121.0	171.84	8525	10.00	102.4	151.2	219.85	8723	15.04	111.8
					131.6	188.63	9228	10.54	103.9					
					140.1	202.19	9698	10.68	104.5					
					149.9	217.84	6416	14.15	116.7					

Table F8. Experimental data for water on the plain surface, D_h = 500 μm, T_i = 70 °C.

D_h = 500 μm															
G=150 kg/m^{2}s					G=350 kg/m^{2}s					G=550 kg/m^{2}s				
q [W]	q"$_{net}$ [kW/m^2]	h [W/m^{2}K]	ΔP [kPa]	T_w [°C]	q [W]	q"$_{net}$ [kW/m^2]	h [W/m^{2}K]	ΔP [kPa]	T_w [°C]	q [W]	q"$_{net}$ [kW/m^2]	h [W/m^{2}K]	ΔP [kPa]	T_w [°C]
20.4	11.81	2110	1.19	72.1	20.8	12.38	2452	3.24	72.7	20.8	12.38	2762	6.44	72.8
40.5	43.77	3373	1.30	81.9	40.8	44.19	4454	3.40	78.9	40.5	43.77	5214	6.58	77.6
50.7	60.02	3460	1.34	87.7	60.3	75.24	5021	3.39	85.3	60.5	75.61	6077	6.65	82.3
60.6	75.66	3681	1.35	92.5	70.2	91.08	5092	3.43	88.4	80.8	107.91	6434	6.74	86.8
65.4	83.39	3502	1.44	96.1	80.8	107.82	5284	3.42	91.7	100.4	138.99	6910	6.73	90.8
70.8	91.89	3636	1.46	98.0	89.9	122.31	5206	3.44	95.0	110.4	155.04	7011	6.79	93.2
75.7	99.73	4092	1.43	98.2	95.5	131.22	5334	3.44	96.6	120.0	170.22	7148	6.85	95.3
81.4	108.90	4488	1.47	99.1	100.4	139.05	5416	3.43	97.7	125.4	178.83	7232	6.87	96.2
85.6	115.56	4850	1.51	99.5	105.5	147.20	5609	3.42	98.4	130.8	187.44	7302	6.81	97.5
90.8	123.73	5243	1.56	100.0	110.6	155.36	5983	3.43	98.8	140.5	202.85	7684	6.81	98.4
95.1	130.55	5638	1.56	100.3	115.4	162.98	6212	3.49	99.1	145.1	210.22	7928	6.87	98.7
101.0	140.08	6204	1.67	100.7	120.9	171.62	6530	3.47	99.4	151.0	219.64	8155	6.86	99.2
106.1	148.13	7155	2.12	101.9	125.2	178.59	6870	3.50	99.6	155.9	227.36	8400	6.91	99.5
111.3	156.41	8474	2.53	102.3	130.8	187.45	7112	3.50	100.2	160.8	235.09	8661	6.92	99.7
120.9	171.62	8816	2.69	103.6	141.1	203.82	7650	3.58	100.7	170.6	250.83	9132	6.91	100.3
131.4	188.34	9102	3.13	105.0	151.1	219.66	8259	3.57	101.4	180.8	266.94	9673	6.87	100.8
139.9	201.98	9334	3.35	108.4	160.8	235.19	8788	3.51	101.9	200.8	298.81	10665	6.92	101.9
					180.8	267.01	10117	3.80	102.9	220.1	329.52	11565	7.08	103.0
					200.8	298.81	11228	4.46	104.2	240.5	361.98	12451	7.17	104.0
					220.1	329.52	12421	5.29	105.7	261.1	394.76	13278	7.21	105.3
					241.4	363.41	13767	6.12	106.9	281.1	426.58	14008	7.65	106.5
					260.6	393.96	15238	7.12	108.2	299.9	456.50	14776	8.04	107.5
					280.7	425.95	16702	7.86	108.9	321.0	490.07	15643	8.59	108.8
					301.0	458.25	17027	8.85	110.5	339.9	520.14	16353	9.15	109.9
					321.0	490.07	17584	9.67	111.7	360.9	553.55	17078	9.80	111.2
					340.4	520.94	17572	10.51	113.3					
					361.1	553.87	17381	11.50	115.3					

Table F9. Experimental data for water on the plain surface, D_h = 1000 μm, T_i = 70 °C.

D_h = 1000 μm															
G=150 kg/m^{2}s					G=350 kg/m^{2}s					G=550 kg/m^{2}s				
q [W]	q"$_{net}$ [kW/m^2]	h [W/m^{2}K]	ΔP [kPa]	T_w [°C]	q [W]	q"$_{net}$ [kW/m^2]	h [W/m^{2}K]	ΔP [kPa]	T_w [°C]	q [W]	q"$_{net}$ [kW/m^2]	h [W/m^{2}K]	ΔP [kPa]	T_w [°C]
20.4	11.79	2260	0.91	72.6	20.4	11.79	2388	2.54	73.8	20.5	11.90	3192	5.16	72.1
40.1	43.18	3569	0.94	80.8	40.2	43.31	4231	2.52	79.5	40.4	43.57	5325	5.15	76.9
50.6	59.89	3837	0.91	85.2	60.9	76.17	4813	2.59	85.6	60.4	75.36	5961	5.14	81.9
60.5	75.52	3869	0.92	89.8	80.6	107.58	5033	2.70	91.5	80.1	106.78	6297	5.17	86.6
70.2	91.03	3808	0.99	95.0	90.6	123.39	5040	2.72	94.9	99.8	138.16	6482	5.09	91.3
80.6	107.56	4015	0.99	98.4	95.3	131.00	5037	2.72	96.6	110.4	154.98	6555	5.10	93.7
85.2	114.80	4330	1.00	98.6	100.2	138.81	5118	2.72	97.9	119.9	170.12	6696	5.18	95.8
90.3	123.06	4688	1.05	98.8	105.3	146.81	5320	2.72	98.5	130.9	187.55	6981	5.11	97.3
95.1	130.68	4977	1.03	99.0	110.5	155.09	5563	2.67	98.8	140.1	202.20	7528	5.22	97.6
100.1	138.64	5232	0.97	99.6	115.3	162.69	5874	2.75	98.9	160.4	234.50	8324	5.24	99.1
105.1	146.59	5588	1.06	99.8	120.7	171.33	6158	2.72	99.1	181.0	267.34	9405	5.26	99.8
110.4	154.99	5984	1.01	99.9	125.1	178.40	6443	2.77	99.2	200.6	298.50	10299	5.18	100.8
115.7	163.41	6338	1.02	100.1	130.7	187.28	6753	2.73	99.4	220.1	329.52	11126	5.15	101.9
120.6	171.19	6679	1.04	100.3	135.3	194.55	7047	2.79	99.4	240.9	362.62	11892	5.29	103.0
124.9	178.11	6996	1.08	100.5	141.0	203.73	7354	2.76	99.7	261.2	394.92	12644	5.36	104.2
130.5	186.94	7359	0.97	100.8	145.7	211.13	7599	2.72	100.0	281.0	426.42	13316	5.35	105.4
140.8	203.38	8085	1.07	101.2	150.5	218.70	7790	2.73	100.3	300.1	456.81	13900	5.45	106.5
160.6	234.87	9451	1.16	102.3	160.7	235.03	8294	2.70	100.9	320.8	489.75	14666	5.44	107.5
180.6	266.66	10791	1.34	103.7	180.7	266.80	9365	2.74	101.9	341.2	522.21	15318	5.52	108.6
200.2	297.86	12200	1.50	104.7	200.8	298.81	10334	2.76	102.7	361.5	554.51	15938	5.59	109.8
220.1	329.52	14126	1.65	105.9	229.9	345.12	11789	2.78	103.5					
241.5	363.57	15710	1.80	106.6	240.6	362.14	12307	2.80	104.3					
260.6	393.96	16442	1.97	107.5	261.1	394.76	13284	2.92	105.1					
280.7	425.95	17064	2.00	108.6	281.3	426.90	14125	2.87	106.3					
301.0	458.25	17532	2.24	109.9	299.8	456.34	14641	3.04	107.6					
320.4	489.11	17895	2.19	111.2	320.7	489.59	15372	3.21	109.0					
340.3	520.78	18187	2.39	112.4	340.7	521.41	15928	3.33	110.5					
360.0	552.12	18356	2.52	113.9	359.9	551.96	16554	3.53	111.6					

Table F10. Experimental data for a 0.1% emulsion on the plain surface, G = 350 kg/m^{2}s, T_i = 30 °C.

D_h = 200 µm					D_h = 500 µm					D_h = 1000 µm				
G = 350 kg/m^{2}s					G = 350 kg/m^{2}s					G = 350 kg/m^{2}s				
q [W]	$q"_{net}$ [kW/m^2]	h [W/m^{2}K]	ΔP [kPa]	T_w [°C]	q [W]	$q"_{net}$ [kW/m^2]	h [W/m^{2}K]	ΔP [kPa]	T_w [°C]	q [W]	$q"_{net}$ [kW/m^2]	h [W/m^{2}K]	ΔP [kPa]	T_w [°C]
20.7	12.28	1980	8.30	37.0	20.4	11.82	2164	6.15	35.0	20.7	12.30	1836	4.24	36.1
40.4	43.52	3537	8.28	45.6	40.8	44.30	4215	6.15	40.9	40.9	44.36	3642	4.27	42.0
60.5	75.52	4072	8.42	54.2	61.3	76.87	4892	6.18	46.9	60.5	75.50	4374	4.34	47.6
80.5	107.40	4197	8.62	63.5	80.4	107.31	5186	6.22	52.8	80.6	107.59	4824	4.37	53.2
90.3	122.96	4193	8.70	69.6	100.5	139.19	5365	6.15	58.9	90.7	123.63	4866	4.33	56.6
100.6	139.40	4205	8.73	74.8	120.2	170.54	5724	6.09	63.8	100.6	139.38	5035	4.32	59.0
110.6	155.29	4362	8.88	78.6	141.0	203.62	6084	6.14	68.5	110.8	155.61	5114	4.26	62.1
121.0	171.76	4499	8.96	82.5	151.5	220.29	6331	6.12	70.3	120.3	170.66	5195	4.28	64.7
130.4	186.81	4565	8.97	86.6	160.4	234.50	6502	6.11	72.2	140.9	203.54	5493	4.30	69.5
140.7	203.17	4631	9.11	90.9	170.2	250.16	6766	6.10	73.5	160.6	234.84	5726	4.24	74.1
150.6	218.86	4761	9.34	95.0	180.1	265.85	6909	6.16	75.5	181.1	267.39	6146	4.36	77.2
160.5	234.64	4972	9.57	97.8	190.0	281.68	6992	6.10	78.0	200.2	297.86	6386	4.36	80.7
170.2	250.09	5406	9.87	99.1	199.8	297.22	6991	6.26	80.8	220.9	330.80	6671	4.34	84.3
					210.7	314.57	7130	6.23	83.0	240.3	361.66	6981	4.34	87.0
					220.3	329.84	7223	6.24	84.9	260.8	394.28	7310	4.46	90.1
					230.3	345.75	7155	6.24	88.1	279.9	424.67	7630	4.36	92.6
					240.5	361.98	7193	6.28	90.8	300.9	458.09	8022	4.38	95.0
					250.3	377.58	7308	6.25	92.7	320.0	488.48	8332	4.32	97.3
					260.8	394.28	7484	6.29	94.4	341.7	523.00	8741	4.26	99.4
					269.7	408.44	7561	6.25	96.0	360.3	552.60	9240	4.22	100.5
					280.6	425.79	8010	6.28	95.8	381.4	586.17	9738	4.22	101.9
					289.9	440.58	8111	6.13	97.6					
					301.0	458.25	8256	6.18	99.0					
					320.5	489.27	8880	6.03	99.8					
					340.5	521.10	9082	5.98	102.9					
					360.9	553.55	9534	6.01	104.5					
					379.9	583.79	9980	5.97	105.9					

Table F11. Experimental data for a 0.5% emulsion on the plain surface, G = 350 kg/m^{2}s, T_i = 30 °C.

D_h = 200 µm					D_h = 500 µm					D_h = 1000 µm				
G = 350 kg/m^{2}s					G = 350 kg/m^{2}s					G = 350 kg/m^{2}s				
q [W]	q"$_{net}$ [kW/m^2]	h [W/m^{2}K]	ΔP [kPa]	T_w [°C]	q [W]	q"$_{net}$ [kW/m^2]	h [W/m^{2}K]	ΔP [kPa]	T_w [°C]	q [W]	q"$_{net}$ [kW/m^2]	h [W/m^{2}K]	ΔP [kPa]	T_w [°C]
20.7	12.30	2045	9.46	36.7	20.6	12.06	2366	6.27	34.5	20.8	12.36	1897	4.73	35.9
40.7	44.14	3624	9.32	45.2	40.7	44.04	4415	6.31	40.1	40.6	43.85	3509	4.78	42.5
60.1	74.93	4045	9.46	54.1	60.8	76.04	5142	6.36	45.9	60.6	75.69	4120	4.78	48.9
80.0	106.64	4197	9.64	63.8	80.5	107.32	5412	6.33	51.7	80.6	107.62	4543	4.74	54.7
100.9	139.83	4237	10.25	74.0	100.6	139.32	5592	6.40	57.8	90.5	123.31	4746	4.79	57.3
110.5	155.15	4252	10.03	79.6	120.4	170.86	5827	6.32	63.2	100.8	139.70	4980	4.79	59.7
120.7	171.37	4221	10.11	85.0	140.8	203.38	5936	6.34	69.1	109.9	154.21	4964	4.79	63.0
130.7	187.20	4379	10.19	89.1	150.6	218.86	6007	6.41	71.9	120.6	171.16	5207	4.89	65.1
141.1	203.78	4501	10.16	92.6	160.6	234.91	6079	6.37	74.6	130.5	187.01	5377	4.83	67.2
150.1	218.08	4712	10.13	95.0	170.3	250.22	5839	6.48	79.5	140.8	203.28	5654	4.83	68.8
160.3	234.42	4886	10.71	99.0	180.1	265.94	6078	6.43	81.0	150.7	219.16	5944	4.83	70.0
170.4	250.38	5463	11.69	102.4	190.7	282.71	6147	6.51	83.7	160.3	234.41	6079	4.84	71.9
					200.3	298.02	6044	6.52	87.7	180.0	265.64	6312	4.87	76.0
					210.8	314.73	6120	6.54	90.3	200.4	298.18	6774	4.87	78.7
					221.0	330.96	6345	6.59	91.7	219.8	329.05	7046	4.88	82.0
					230.6	346.23	6387	6.59	93.9	239.6	360.55	7297	4.88	85.7
					240.4	361.82	6574	6.54	95.4	260.9	394.44	7458	4.93	89.9
					250.7	378.21	6873	6.53	96.0	280.7	425.95	7652	4.83	93.6
					260.8	394.28	7058	6.50	97.2	290.7	441.86	7745	4.83	95.7
					271.2	410.83	7354	6.35	98.0	300.8	457.93	7961	4.73	96.8
					280.7	425.95	7588	6.42	98.6	310.3	473.04	8169	4.84	97.9
					290.0	440.74	7910	6.40	98.8	320.7	489.59	8441	4.72	98.7
					301.1	458.40	8164	6.37	99.6	330.7	505.50	8684	4.73	99.4
					320.6	489.43	8662	6.26	101.1	340.6	521.25	8877	4.57	100.6
					340.7	521.41	9055	6.11	103.1	361.1	553.87	9352	4.47	102.0
					360.7	553.24	9537	6.24	105.0	380.6	584.90	9851	4.46	103.1

Table F12. Experimental data for a 1% emulsion on the plain surface, D_h = 200 μm, T_i = 30 °C.

D_h = 200 μm															
G = 150 kg/m^{2}s					G = 350 kg/m^{2}s					G = 550 kg/m^{2}s				
q [W]	q"$_{net}$ [kW/m^2]	h [W/m^{2}K]	ΔP [kPa]	T_w [°C]	q [W]	q"$_{net}$ [kW/m^2]	h [W/m^{2}K]	ΔP [kPa]	T_w [°C]	q [W]	q"$_{net}$ [kW/m^2]	h [W/m^{2}K]	ΔP [kPa]	T_w [°C]
20.7	12.22	1464	4.71	39.9	20.7	12.30	1977	11.70	37.6	20.8	12.38	2299	18.33	35.6
40.0	42.91	2497	5.24	53.3	40.4	43.61	3537	12.19	45.7	40.4	43.60	4135	18.42	42.2
50.4	59.49	2613	5.69	61.7	60.0	74.82	3916	12.31	55.4	60.3	75.29	4787	18.81	49.0
60.6	75.75	2724	5.93	68.6	80.5	107.32	4092	12.57	64.5	80.2	106.91	5018	18.87	56.0
70.2	91.04	2801	6.12	76.1	90.5	123.27	4228	12.63	69.0	100.8	139.75	5040	19.13	64.2
80.3	107.15	2871	6.45	83.0	100.9	139.83	4202	12.37	74.5	110.6	155.23	5140	19.33	67.4
90.0	122.58	3011	6.47	88.8	110.8	155.57	4204	12.34	79.3	120.9	171.72	5171	19.26	71.1
100.3	138.94	3171	6.78	94.3	120.5	170.97	4195	12.45	83.9	130.4	186.81	5161	19.20	75.0
110.4	154.90	3534	7.77	99.4	130.8	187.45	4243	12.49	88.6	140.5	202.79	5237	19.34	78.3
120.4	170.95	4061	8.14	100.3	140.2	202.46	4174	12.57	94.0	149.8	217.68	5159	19.29	82.4
130.2	186.53	4718	9.23	101.6	150.8	219.23	4297	12.75	98.3	160.0	233.94	5172	19.19	86.6
140.3	202.47	5062	10.51	103.9	160.8	235.17	4760	13.50	100.1	171.0	251.45	5107	19.19	91.2
150.6	218.89	5246	11.85	105.6	170.3	250.27	5137	13.98	102.2	180.5	266.53	5092	19.37	95.0
160.5	234.63	5238	13.92	108.6	180.7	266.90	5738	14.34	104.0	190.3	282.09	5212	18.74	97.5
170.6	250.78	5301	15.17	111.1	190.8	282.86	6548	14.85	106.4	201.5	299.93	5574	19.05	97.9
180.3	266.26	5386	18.05	113.3						210.6	314.41	5814	20.02	99.8
										220.3	329.84	6183	20.42	100.8
										241.5	363.57	6879	20.22	101.7
										261.2	394.92	7485	20.54	104.1
										280.1	424.99	7950	22.84	110.8
										290.3	441.22	8029	24.59	118.1

Table F13. Experimental data for a 1% emulsion on the plain surface, D_h = 500 μm, T_i = 30 °C.

D_h = 500 μm															
G = 150 kg/m^{2}s					G = 350 kg/m^{2}s					G = 550 kg/m^{2}s				
q [W]	q"$_{net}$ [kW/m^2]	h [W/m^{2}K]	ΔP [kPa]	T_w [°C]	q [W]	q"$_{net}$ [kW/m^2]	h [W/m^{2}K]	ΔP [kPa]	T_w [°C]	q [W]	q"$_{net}$ [kW/m^2]	h [W/m^{2}K]	ΔP [kPa]	T_w [°C]
20.8	12.33	1996	3.14	36.4	20.2	11.49	1554	5.34	37.0	20.6	12.01	1639	8.79	36.4
40.4	43.63	3557	3.11	44.4	40.3	43.39	3028	5.23	44.8	40.6	43.87	3201	8.39	43.9
60.2	75.12	4034	3.19	52.7	60.0	74.72	3606	5.30	52.2	60.8	76.06	3605	8.34	52.0
80.1	106.81	3933	3.45	63.5	80.0	106.64	3858	5.18	59.8	70.7	91.74	3695	7.86	56.2
100.1	138.56	4027	3.64	72.9	90.2	122.76	4106	5.73	62.2	80.7	107.64	3873	7.84	59.6
109.8	154.04	3955	3.69	78.7	100.1	138.62	4274	5.27	65.7	90.7	123.60	3991	7.76	63.0
120.6	171.19	4049	3.75	83.4	110.0	154.39	4417	5.63	68.6	100.2	138.75	4108	7.69	66.1
130.1	186.27	4129	3.65	87.3	120.3	170.66	4465	5.32	72.4	110.7	155.50	4294	7.71	68.9
140.9	203.46	4201	3.80	91.9	130.4	186.75	4569	5.70	75.2	120.7	171.29	4439	7.68	71.6
150.6	218.89	4479	3.74	93.6	140.3	202.55	4640	5.70	78.4	130.2	186.48	4501	7.59	74.8
160.8	235.12	4704	3.80	95.6	150.5	218.72	4742	5.68	81.4	140.7	203.12	4697	7.60	77.3
171.3	251.84	5102	3.75	96.3	159.8	233.63	4865	5.71	83.9	151.0	219.56	4874	7.60	79.5
181.1	267.50	5262	3.72	99.0	170.2	250.11	5065	5.67	85.6	161.0	235.52	4994	7.56	81.8
190.8	282.94	5598	3.76	99.7	180.2	266.09	5337	5.72	86.6	170.6	250.83	5225	7.56	83.4
201.3	299.61	6053	3.80	99.7	200.2	297.86	5747	5.69	89.3	181.2	267.69	5406	7.58	85.1
210.6	314.41	6374	3.72	100.7	219.9	329.21	6062	5.70	92.9	190.6	282.51	5442	7.55	87.7
220.3	329.84	6780	3.77	101.1	240.3	361.66	6352	5.75	96.1	200.9	298.97	5642	7.52	89.4
230.2	345.59	7066	3.98	102.6	259.8	392.69	6429	5.71	101.0	210.4	314.09	5901	7.51	89.9
240.7	362.30	7440	4.22	103.8	280.4	425.47	7065	5.76	101.2	220.5	330.16	5958	7.50	92.5
261.2	394.92	8255	4.84	105.7	300.5	457.45	7613	5.74	101.9	231.0	346.87	6162	7.46	93.7
281.1	426.58	9247	5.70	107.3	320.1	488.64	8040	5.76	103.5	241.4	363.41	6541	7.39	93.6
299.9	456.50	10122	6.47	109.1	340.4	520.94	8360	5.75	105.9	260.7	394.12	6729	7.44	97.4
320.5	489.27	10098	7.13	112.5						280.2	425.15	7148	7.36	98.9
340.5	521.10	10442	8.19	114.0						301.1	458.40	7447	7.35	102.0
										320.2	488.80	7925	7.36	103.0
										340.7	521.41	8156	7.17	106.2

Table F14. Experimental data for a 1% emulsion on the plain surface, D_h = 1000 µm, T_i = 30 °C.

D_h = 1000 µm															
G = 150 kg/m^{2}s					G = 350 kg/m^{2}s					G = 550 kg/m^{2}s				
q [W]	q"$_{net}$ [kW/m^2]	h [W/m^{2}K]	ΔP [kPa]	T_w [°C]	q [W]	q"$_{net}$ [kW/m^2]	h [W/m^{2}K]	ΔP [kPa]	T_w [°C]	q [W]	q"$_{net}$ [kW/m^2]	h [W/m^{2}K]	ΔP [kPa]	T_w [°C]
20.7	12.32	1660	2.28	37.8	20.8	12.38	1817	5.73	36.1	20.5	11.85	2308	10.11	34.3
40.3	43.47	2734	2.25	47.5	40.6	43.88	3475	5.39	42.6	40.9	44.41	4245	10.15	40.2
60.5	75.60	3379	2.22	55.3	60.6	75.69	3974	5.59	49.5	60.6	75.75	4899	10.27	45.5
70.8	91.89	3964	2.32	57.1	80.6	107.53	4455	5.58	55.4	80.8	107.88	5274	10.15	50.9
80.4	107.31	3982	2.37	61.6	90.3	123.03	4551	5.56	58.7	101.0	139.99	5525	10.21	56.2
90.0	122.49	3923	2.37	66.4	100.6	139.38	4716	5.59	61.4	110.6	155.34	5547	10.24	59.1
100.6	139.45	4162	2.35	69.4	111.0	155.88	4992	5.61	63.4	120.3	170.71	5805	10.14	60.7
110.5	155.14	4154	2.44	74.3	120.4	170.92	5044	5.63	66.4	130.2	186.53	5986	10.09	62.7
119.9	170.03	4261	2.46	77.6	130.2	186.50	5148	5.56	69.1	140.5	202.92	6121	10.11	64.9
140.3	202.49	4552	2.37	83.3	140.4	202.65	5310	5.59	71.3	150.8	219.27	6138	10.03	67.9
160.7	235.04	4740	2.54	90.0	160.1	234.01	5483	5.17	77.2	160.3	234.44	6199	10.08	70.3
180.6	266.66	4790	2.41	97.8	180.2	266.10	5727	5.24	81.4	170.6	250.71	6393	10.05	72.3
190.4	282.19	5185	2.33	97.3	200.6	298.50	5859	5.30	86.7	180.6	266.74	6627	10.02	73.7
200.7	298.66	5540	2.45	97.7	220.4	330.00	6061	5.27	91.0	200.6	298.50	6664	9.97	79.1
210.2	313.77	5871	2.57	98.3	240.6	362.14	6340	5.33	94.3	219.8	329.05	6802	9.97	83.3
221.4	331.59	6221	2.47	99.0	259.7	392.53	6707	5.11	97.5	239.9	361.03	7122	9.93	86.5
230.4	345.91	6518	2.31	99.5	271.8	411.78	7099	5.07	97.9	259.9	392.85	7440	10.10	89.9
240.3	361.66	6772	2.32	100.6	281.0	426.42	7404	5.18	98.2	280.7	425.95	7754	10.08	92.9
260.8	394.28	7339	2.07	102.5	290.2	441.06	7678	5.17	98.6	291.3	442.81	7895	9.99	94.8
280.6	425.79	8037	2.11	103.6	300.6	457.61	7966	5.05	99.2	300.5	457.45	8054	9.95	96.1
301.2	458.56	8735	2.08	104.9	321.1	490.23	8437	5.09	100.4	310.1	472.72	8256	9.83	96.9
320.9	489.91	9631	2.18	105.5	341.2	522.21	8929	5.06	101.9	321.5	490.86	8639	9.94	97.0
340.5	521.10	9858	2.20	108.7	360.6	553.08	9443	4.95	102.8	331.7	507.09	8960	9.95	97.2
										340.2	520.62	9215	9.92	97.8
										360.5	552.92	9665	9.87	99.3
										380.3	584.42	10139	9.82	100.3

Table F15. Experimental data for a 2% emulsion on the plain surface, G = 350 kg/m^{2}s, T_i = 30 °C.

D_h = 200 µm					D_h = 500 µm					D_h = 1000 µm				
G=350 kg/m^{2}s					G=350 kg/m^{2}s					G=350 kg/m^{2}s				
q [W]	q"$_{net}$ [kW/m^2]	h [W/m^{2}K]	ΔP [kPa]	T_w [°C]	q [W]	q"$_{net}$ [kW/m^2]	h [W/m^{2}K]	ΔP [kPa]	T_w [°C]	q [W]	q"$_{net}$ [kW/m^2]	h [W/m^{2}K]	ΔP [kPa]	T_w [°C]
20.6	12.12	1898	11.01	37.8	20.8	12.41	2481	7.03	34.6	20.9	12.55	2161	6.91	35.0
40.4	43.61	3444	11.25	46.3	40.7	44.00	4515	7.07	40.2	40.8	44.19	3806	6.82	41.3
60.6	75.77	3952	11.45	54.9	60.3	75.31	5171	6.98	45.8	60.5	75.60	4456	6.73	47.2
70.5	91.52	3959	11.60	59.9	80.4	107.19	5415	7.12	51.9	80.6	107.50	4771	6.63	53.4
81.0	108.23	4041	11.80	64.9	100.4	139.13	5675	6.99	57.7	100.6	139.30	4867	6.60	59.9
90.6	123.50	4088	11.37	69.5	119.6	169.63	5726	6.90	63.5	110.8	155.66	5058	6.65	62.3
100.6	139.43	4183	11.41	74.1	140.7	203.14	5957	6.98	69.1	120.4	170.87	5196	6.59	64.8
109.9	154.13	4160	11.47	78.8	150.3	218.41	5839	6.98	72.8	130.7	187.29	5210	6.57	68.1
120.1	170.35	4179	11.44	84.1	160.7	235.03	5866	6.97	76.1	140.5	202.93	5081	6.65	72.3
130.5	186.91	4153	11.54	89.5	170.3	250.33	6022	6.78	77.9	151.0	219.50	5317	6.42	74.1
140.5	202.89	4148	11.50	94.7	180.5	266.58	6074	6.91	80.7	160.6	234.84	5483	6.35	75.8
150.3	218.40	4272	12.31	99.4	190.3	282.09	5959	6.94	84.5	170.7	250.92	5480	6.37	79.1
161.1	235.63	4784	13.10	101.5	201.2	299.45	6203	6.72	86.1	180.5	266.58	5595	6.41	81.2
171.3	251.91	5340	13.68	103.9	210.0	313.45	6058	6.83	89.7	199.9	297.38	5694	6.34	86.3
181.0	267.25	6234	14.42	106.1	220.6	330.32	6072	6.78	92.9	219.7	328.89	5824	6.38	91.1
					230.0	345.28	6161	6.81	95.0	240.4	361.82	6119	6.31	94.5
					240.6	362.14	6371	6.81	96.3	251.0	378.69	6293	6.30	95.9
					250.8	378.37	6659	6.84	96.6	261.3	395.08	6526	6.34	96.9
					261.1	394.76	6871	6.69	97.9	270.3	409.40	6713	6.07	98.1
					270.2	409.24	7082	6.75	98.7	281.0	426.42	6942	6.06	99.0
					281.3	426.90	7355	6.74	99.5	301.4	458.88	7466	6.07	99.8
					300.1	456.81	7861	6.73	100.2	320.9	489.91	7950	5.95	100.9
					321.3	490.55	8389	6.71	101.6	341.1	522.05	8472	6.00	101.8
					341.4	522.53	8931	6.71	102.8	361.4	554.35	8975	6.05	102.7
					360.2	552.44	9422	6.53	103.8					

Table F16. Experimental data for water on Porous Surface 1, D_h = 200 µm, T_i = 30 °C.

D_h = 200 µm															
G = 150 kg/m^{2}s					**G = 350 kg/m^{2}s**					**G = 550 kg/m^{2}s**				
q [W]	**q"$_{net}$ [kW/m^2]**	**h [W/m^{2}K]**	**ΔP [kPa]**	**T_w [°C]**	**q [W]**	**q"$_{net}$ [kW/m^2]**	**h [W/m^{2}K]**	**ΔP [kPa]**	**T_w [°C]**	**q [W]**	**q"$_{net}$ [kW/m^2]**	**h [W/m^{2}K]**	**ΔP [kPa]**	**T_w [°C]**
20.1	11.51	744	9.04	46.8	20.42	12.064	1443.238	19.06	38.718	20.4	12.10	1834	25.61	37.1
30.3	28.11	1136	9.54	58.6	40.43	44.599	2536.937	21.694	50.327	40.8	45.27	3519	27.14	44.8
40.2	44.26	1369	10.23	68.1	51.13	61.996	2715.859	23.881	56.952	60.5	77.22	3973	28.92	52.9
50.4	60.81	1467	11.04	79.2	60.39	77.052	2773.46	26.319	63.132	80.5	109.77	4207	32.06	61.2
60.0	76.43	1403	12.29	94.6	70.06	92.775	2721.464	29.524	71.023	100.2	141.85	4145	37.35	71.5
65.3	84.99	1541	12.77	96.7	80.02	108.969	2525.037	31.845	82.089	120.2	174.25	3869	48.97	85.3
70.2	93.05	1613	13.15	100.1	90.58	126.138	2717.799	33.791	87.183	129.2	189.00	3049	68.60	105.2
75.5	101.65	1808	13.63	100.0	100.5	142.316	2559.486	39.608	97.985	140.0	206.56	3220	81.02	110.9
80.5	109.75	1955	14.12	100.9	105.3	150.104	2618.09	41.038	100.731	150.1	222.83	3434	87.78	116.5
85.0	117.03	2054	16.81	103.1	110.2	157.958	2613.053	44.729	104.861					
90.7	126.38	2241	18.42	103.8	120.5	174.704	2802.156	51.785	109.59					
100.5	142.19	2560	25.00	105.9	130.3	190.768	3043.027	59.257	112.859					
110.2	158.04	2832	53.65	113.2										

Table F17. Experimental data for water on Porous Surface 1, D_h = 500 µm, T_i = 30 °C.

D_h = 500 µm															
G = 150 kg/m^{2}s					G = 350 kg/m^{2}s					G = 550 kg/m^{2}s				
q [W]	q"$_{net}$ [kW/m^2]	h [W/m^{2}K]	ΔP [kPa]	T_w [°C]	q [W]	q"$_{net}$ [kW/m^2]	h [W/m^{2}K]	ΔP [kPa]	T_w [°C]	q [W]	q"$_{net}$ [kW/m^2]	h [W/m^{2}K]	ΔP [kPa]	T_w [°C]
20.3	11.80	1733	2.60	37.0	20.1	11.58	2294	5.97	35.0	20.4	12.02	3081	11.15	33.6
40.5	44.70	3218	2.53	46.5	40.1	44.03	4745	6.04	40.2	40.3	44.34	6359	11.38	37.3
60.8	77.69	3889	2.56	54.5	60.2	76.73	5650	6.04	45.5	60.2	76.73	7660	11.60	40.9
80.6	109.86	4239	2.62	62.3	80.0	108.97	6280	6.15	50.1	80.6	109.96	8319	11.77	44.7
100.3	141.96	4477	2.64	69.9	100.2	141.80	6568	6.06	55.3	100.3	141.89	8764	11.83	48.3
120.8	175.21	4678	2.68	77.7	120.3	174.40	6899	6.10	60.0	120.6	174.92	9117	11.78	51.9
140.1	206.59	4740	2.75	85.7	139.9	206.25	7131	6.09	64.6	139.9	206.38	9249	11.81	55.5
150.3	223.17	4259	2.91	95.4	159.9	238.77	7284	6.04	69.3	160.2	239.27	9387	11.76	59.4
155.5	231.74	4382	2.90	96.6	180.2	271.77	7078	6.07	76.0	180.3	272.06	9568	11.79	63.0
160.4	239.63	4497	2.90	97.4	200.5	304.86	6856	6.21	83.0	200.8	305.35	9699	11.81	66.6
165.0	247.19	4520	3.15	99.4	220.5	337.38	6651	6.27	90.1	220.3	337.05	9780	11.84	70.3
171.0	256.93	4701	3.34	100.5	240.0	369.08	6974	6.27	93.4	241.2	371.03	9921	11.85	73.8
176.1	265.20	4866	3.39	101.0	250.5	386.16	7054	6.35	95.8	259.9	401.44	10020	11.96	77.0
181.2	273.46	5034	3.56	101.3	260.0	401.60	7322	6.34	96.3	280.7	435.26	10018	11.91	81.2
185.1	279.76	5160	3.62	101.8	269.8	417.54	7464	6.40	98.0	300.8	467.94	10121	11.91	84.8
190.2	288.16	5331	3.83	102.6	280.7	435.26	7721	6.45	99.1	320.5	499.97	9979	11.73	89.6
200.7	305.18	5691	3.97	103.3	290.5	451.19	7998	6.56	99.8	340.0	531.67	10101	11.80	93.2
220.1	336.73	6389	4.33	105.6	299.8	466.31	8230	6.61	100.3	360.1	564.36	10373	12.09	95.6
240.8	370.38	7316	4.58	106.7	310.3	483.38	8561	6.65	100.8	380.5	597.52	10783	11.98	97.7
260.4	402.25	8854	5.73	108.1	320.1	499.32	8834	6.63	101.3	389.5	612.16	10999	12.14	98.4
278.5	431.68	8011	10.02	118.0	340.6	532.65	9494	6.70	102.1					
					360.3	564.68	10128	6.77	102.8					
					380.7	597.85	10802	6.90	103.7					

Table F18. Experimental data for water on Porous Surface 1, D_h = 1000 µm, T_i = 30 °C.

D_h = 1000 µm															
G = 150 kg/m^{2}s					G = 350 kg/m^{2}s					G = 550 kg/m^{2}s				
q [W]	q"$_{net}$ [kW/m^2]	h [W/m^{2}K]	ΔP [kPa]	T_w [°C]	q [W]	q"$_{net}$ [kW/m^2]	h [W/m^{2}K]	ΔP [kPa]	T_w [°C]	q [W]	q"$_{net}$ [kW/m^2]	h [W/m^{2}K]	ΔP [kPa]	T_w [°C]
20.8	12.65	2253	1.77	35.5	20.9	12.78	3113	5.10	33.7	20.5	12.21	4772	10.57	31.7
40.6	44.88	4037	1.76	42.1	40.9	45.38	6211	5.12	37.4	40.6	44.84	8626	10.79	34.7
60.2	76.78	4875	1.80	48.0	60.9	77.80	7473	5.20	41.0	61.1	78.17	10127	10.70	37.6
80.2	109.23	5206	1.88	54.5	80.4	109.57	8074	5.23	44.6	80.7	110.03	10973	10.73	40.3
100.2	141.75	5490	1.92	60.5	100.9	142.84	8618	5.25	48.2	100.4	142.17	11610	10.92	42.8
120.6	175.01	5278	1.96	69.1	120.0	174.04	8904	5.23	51.7	120.8	175.21	11886	10.74	45.6
140.8	207.73	5246	2.02	76.9	140.4	207.19	9206	5.19	55.2	140.3	206.91	12227	10.78	48.1
160.2	239.37	5123	2.10	85.1	160.7	240.12	9428	5.22	58.7	161.2	241.01	12617	11.08	50.7
170.7	256.37	5163	2.12	89.0	180.8	272.86	9622	5.24	62.1	180.2	271.87	12830	11.00	53.1
180.7	272.73	5241	2.19	91.7	200.2	304.37	9817	5.18	65.3	200.0	304.05	13052	10.96	55.5
190.8	289.12	5542	2.17	93.0	219.8	336.24	9972	5.20	68.5	220.5	337.38	13184	10.96	58.6
195.9	297.30	5514	2.17	95.0	240.9	370.55	10052	5.16	72.3	240.6	370.06	13332	10.93	61.2
201.0	305.67	5547	2.19	96.3	260.8	402.90	9976	5.12	76.8	261.0	403.23	13297	10.80	65.1
205.1	312.34	5638	2.15	96.9	281.0	435.75	10041	5.08	80.7	280.5	434.93	13378	10.88	68.1
210.5	321.12	5794	2.25	97.2	300.8	467.94	9854	5.00	85.8	300.8	467.94	13553	10.85	71.1
216.1	330.22	6033	2.24	97.1	321.2	501.11	9657	5.12	91.1	320.9	500.62	13732	10.90	74.0
220.2	336.89	6130	2.20	97.7	330.8	516.72	9674	4.97	93.3	340.6	532.65	13822	10.73	77.2
230.2	353.15	6345	2.19	98.9	340.6	532.65	9778	4.91	94.8	360.9	565.66	14172	11.34	80.5
240.9	370.55	6657	2.17	99.6	345.7	540.94	9942	4.93	95.1	381.5	599.15	14173	11.27	83.2
260.1	401.76	7218	2.15	100.7	350.6	548.91	9997	4.94	95.8					
280.2	434.44	7902	2.38	101.5	355.7	557.20	10166	4.94	96.1					
300.8	467.94	8596	2.06	102.3	360.5	565.01	10232	4.86	96.8					
320.4	499.81	9259	2.11	103.1	370.6	581.43	10413	4.93	97.9					
340.6	532.65	9999	2.24	103.7	380.7	597.85	10649	4.83	98.6					
361.1	565.98	10806	2.39	104.2	392.0	616.22	10877	4.91	99.5					
380.1	596.87	11569	2.33	104.8										

Table F19. Experimental data for a 0.1% emulsion on Porous Surface 1, G = 350 kg/m^{2}s, T_i = 30 °C.

D_h = 200 µm					D_h = 500 µm					D_h = 1000 µm				
G = 350 kg/m^{2}s					G = 350 kg/m^{2}s					G = 350 kg/m^{2}s				
q [W]	q"$_{net}$ [kW/m^2]	h [W/m^{2}K]	ΔP [kPa]	T_w [°C]	q [W]	q"$_{net}$ [kW/m^2]	h [W/m^{2}K]	ΔP [kPa]	T_w [°C]	q [W]	q"$_{net}$ [kW/m^2]	h [W/m^{2}K]	ΔP [kPa]	T_w [°C]
20.6	12.32	1246	19.03	39.0	20.5	12.24	2253	8.38	35.0	20.6	12.28	2118	6.17	32.7
30.2	27.97	2074	19.62	45.2	40.4	44.55	3969	8.31	41.8	40.5	44.73	4588	6.22	36.6
40.2	44.23	2118	20.88	54.4	60.1	76.65	4632	8.20	48.1	60.5	77.26	5589	6.33	40.7
50.6	61.05	2421	21.47	60.5	80.4	109.60	4991	8.18	54.6	80.3	109.41	6128	6.16	44.8
60.3	76.94	2345	24.91	69.3	100.8	142.79	5273	8.12	60.7	101.1	143.21	6566	6.29	48.9
70.1	92.78	2061	27.95	82.9	121.0	175.53	5403	8.13	67.2	120.5	174.84	6806	6.21	53.0
75.3	101.26	1605	33.70	105.8	140.5	207.24	5744	8.18	71.8	140.3	207.03	7061	6.10	56.9
					160.5	239.86	5699	8.20	78.8	160.9	240.52	7206	6.17	61.2
					180.3	271.97	5674	8.30	85.5	180.3	272.03	7375	6.06	65.0
					200.6	305.02	5816	8.49	91.3	200.1	304.21	7505	6.20	68.7
					220.2	336.89	5893	8.82	97.1	219.6	335.91	7637	6.08	72.3
					240.1	369.25	6279	9.02	99.7	240.8	370.38	7794	6.11	76.0
					260.1	401.76	6865	9.18	100.6	259.9	401.44	7996	6.00	78.9
					280.9	435.58	6738	12.58	109.5	280.2	434.44	8162	6.10	82.2
					291.4	452.65	6813	12.60	111.8	300.1	466.80	8300	6.07	85.3
					299.5	465.82	6616	12.84	116.7	321.2	501.11	8394	6.02	88.9
					310.2	483.22	6532	13.38	121.4	340.3	532.16	8506	6.14	91.9
					320.2	499.48	6639	13.95	124.6	361.2	566.14	8579	6.06	95.6
					339.8	531.35	6914	15.13	129.0	381.3	598.82	8828	6.09	97.9

Table F20. Experimental data for a 0.5% emulsion on Porous Surface 1, G = 350 kg/m^{2}s, T_i = 30 °C.

D_h = 200 µm					D_h = 500 µm					D_h = 1000 µm				
G = 350 kg/m^{2}s					G = 350 kg/m^{2}s					G = 350 kg/m^{2}s				
q [W]	q"$_{net}$ [kW/m^2]	h [W/m^{2}K]	ΔP [kPa]	T_w [°C]	q [W]	q"$_{net}$ [kW/m^2]	h [W/m^{2}K]	ΔP [kPa]	T_w [°C]	q [W]	q"$_{net}$ [kW/m^2]	h [W/m^{2}K]	ΔP [kPa]	T_w [°C]
20.4	12.06	1415	19.16	39.2	20.3	11.92	2068	12.64	35.4	20.4	12.08	1852	7.58	32.6
30.3	28.06	2035	20.00	46.0	40.8	45.15	3808	12.76	42.6	40.4	44.49	4329	7.51	36.5
40.3	44.40	2165	21.29	54.4	60.6	77.31	4345	12.79	49.6	60.4	77.09	5615	7.65	40.0
50.5	60.91	2263	21.82	62.6	80.8	110.17	4567	12.93	56.9	81.1	110.64	6314	7.62	44.0
60.5	77.22	2208	23.01	72.9	100.0	141.39	4587	13.01	64.5	100.9	142.90	6789	7.70	47.6
70.0	92.68	1474	27.93	105.1	120.4	174.67	4680	13.24	72.0	120.4	174.61	7225	7.72	50.8
					140.3	206.95	4642	13.41	80.6	140.7	207.60	7529	7.72	54.4
					160.2	239.29	4623	13.70	88.9	160.2	239.32	7711	7.78	58.1
					180.7	272.65	4582	14.22	98.0	180.8	272.76	7881	7.80	61.8
					200.6	305.02	4574	16.66	107.2	200.7	305.18	8089	7.89	65.3
					210.0	320.31	4770	16.64	108.6	221.4	338.84	8231	7.91	69.0
					221.1	338.35	4982	16.73	110.1	240.1	369.25	8418	7.88	71.9
					240.9	370.55	5346	16.87	112.8	260.8	402.90	8625	7.86	74.8
					260.9	403.06	5631	17.21	116.6	280.5	434.93	8762	7.91	78.0
					279.8	433.79	5888	17.52	120.3	299.7	466.15	8836	7.81	81.2
					300.0	466.64	6223	18.31	123.8	320.2	499.48	8973	7.73	84.3
					319.8	498.83	6619	19.78	127.9	340.2	532.00	9117	7.86	87.3
										361.4	566.47	9188	7.77	90.9
										380.8	598.01	9174	7.69	94.7

Table F21. Experimental data for a 1% emulsion on Porous Surface 1, D_h = 200 µm, T_i = 30 °C.

D_h = 200 µm															
G = 150 kg/m^{2}s					**G = 350 kg/m^{2}s**					**G = 550 kg/m^{2}s**				
q [W]	**q"$_{net}$ [kW/m^2]**	**h [W/m^{2}K]**	**ΔP [kPa]**	**T_w [°C]**	**q [W]**	**q"$_{net}$ [kW/m^2]**	**h [W/m^{2}K]**	**ΔP [kPa]**	**T_w [°C]**	**q [W]**	**q"$_{net}$ [kW/m^2]**	**h [W/m^{2}K]**	**ΔP [kPa]**	**T_w [°C]**
20.1	11.61	713	11.93	48.9	20.5	12.11	1428	26.03	38.9	20.3	11.87	1730	39.29	36.8
30.1	27.74	887	13.62	66.7	30.3	28.08	2026	25.44	45.7	30.8	28.99	2569	39.44	42.2
39.6	43.31	768	16.49	95.3	40.5	44.71	2286	25.65	52.7	40.5	44.73	2872	40.04	47.4
45.6	52.92	858	17.84	101.7	50.5	60.94	2499	26.14	58.6	50.3	60.57	3173	40.83	51.9
					60.5	77.23	2685	27.06	64.4	60.4	77.04	3372	41.49	56.7
					70.0	92.65	2450	28.24	75.6	70.3	93.23	3428	43.15	62.1
										80.9	110.40	3456	44.74	68.2
										90.9	126.58	3366	48.06	75.2

Table F22. Experimental data for a 1% emulsion on Porous Surface 1, D_h = 500 µm, T_i = 30 °C.

D_h = 500 µm															
G = 150 kg/m^{2}s					G = 350 kg/m^{2}s					G = 550 kg/m^{2}s				
q [W]	q"$_{net}$ [kW/m^2]	h [W/m^{2}K]	ΔP [kPa]	T_w [°C]	q [W]	q"$_{net}$ [kW/m^2]	h [W/m^{2}K]	ΔP [kPa]	T_w [°C]	q [W]	q"$_{net}$ [kW/m^2]	h [W/m^{2}K]	ΔP [kPa]	T_w [°C]
20.2	11.63	1150	5.16	40.5	20.5	12.26	1837	12.80	36.6	20.8	12.70	2638	27.49	34.3
30.8	28.96	1584	5.13	50.1	40.3	44.39	3387	13.32	44.0	40.5	44.68	4727	27.73	39.5
40.5	44.70	1631	5.18	60.4	60.4	77.12	4124	13.32	50.5	60.4	77.00	5477	27.69	44.8
50.5	61.04	1715	5.47	69.9	80.2	109.29	4530	13.50	56.9	80.8	110.17	5836	27.57	50.3
60.3	76.91	1761	5.62	79.1	100.4	142.17	4707	13.66	64.1	100.3	141.99	6179	27.62	55.1
70.0	92.74	1848	5.68	86.7	120.2	174.35	4666	13.89	72.4	120.8	175.19	6394	28.07	60.1
80.1	109.16	1875	5.89	96.0	140.6	207.40	4880	13.83	78.5	140.2	206.75	6377	28.14	65.9
90.3	125.72	2114	5.91	98.7	160.1	239.17	4617	14.50	89.1	160.7	240.10	6539	28.16	70.9
101.3	143.49	2413	6.33	100.5	180.5	272.28	4140	17.57	105.6	179.9	271.32	6751	28.95	74.9
110.7	158.77	2692	6.76	101.5	200.8	305.35	4550	17.36	108.6	200.5	304.86	6689	29.34	81.3
120.6	174.92	3024	6.99	101.9	220.0	336.56	4916	17.63	111.6	220.4	337.22	6540	29.83	88.0
140.5	207.29	3544	7.45	105.1	240.3	369.57	5292	18.03	114.9	240.4	369.73	5956	31.81	99.9
160.5	239.87	4110	8.14	107.8	260.3	402.09	5661	18.32	118.3	250.0	385.34	5329	33.64	111.9
180.3	271.95	4728	8.88	110.2	280.2	434.44	6027	19.11	121.8	260.9	403.06	5480	33.79	113.7
199.9	303.88	5453	10.57	113.0						270.6	418.84	5592	33.71	115.6
220.8	337.87	6278	15.51	117.5						280.1	434.28	5722	33.93	117.3
										290.8	451.68	5882	33.95	118.8
										299.8	466.31	6017	34.26	120.1
										310.8	484.20	6180	33.90	121.7
										320.1	499.32	6288	34.02	123.4
										329.7	514.93	6419	34.15	124.9
										340.9	533.14	6559	34.37	127.0
										350.6	548.91	6675	34.54	129.0
										360.2	564.52	6781	34.72	130.9
										369.9	580.29	6878	35.32	133.2
										380.5	597.52	7008	36.11	135.4

Table F23. Experimental data for a 1% emulsion on Porous Surface 1, D_h = 1000 µm, T_i = 30 °C.

D_h = 1000 µm															
G = 150 kg/m^{2}s					G = 350 kg/m^{2}s					G = 550 kg/m^{2}s				
q [W]	q"$_{net}$ [kW/m^2]	h [W/m^{2}K]	ΔP [kPa]	T_w [°C]	q [W]	q"$_{net}$ [kW/m^2]	h [W/m^{2}K]	ΔP [kPa]	T_w [°C]	q [W]	q"$_{net}$ [kW/m^2]	h [W/m^{2}K]	ΔP [kPa]	T_w [°C]
20.3	11.90	1084	3.70	36.2	20.4	12.03	1972	8.29	32.8	20.7	12.52	2219	15.12	31.6
40.0	43.82	2328	3.73	44.5	40.7	44.96	4456	8.36	36.9	40.5	44.66	5316	15.18	34.5
60.7	77.48	2833	3.80	53.4	60.3	76.87	5528	8.34	40.7	60.6	77.46	6979	15.27	37.4
80.3	109.34	3122	3.72	61.3	81.0	110.48	6183	8.33	44.7	80.5	109.72	7977	15.15	40.1
100.5	142.32	3489	3.84	67.4	100.8	142.67	6678	8.35	48.2	100.4	142.12	8672	15.28	42.9
120.3	174.48	3619	3.81	75.1	120.2	174.25	7013	8.35	51.8	121.2	175.89	9220	15.18	45.7
139.8	206.20	3755	3.85	82.2	140.6	207.53	7629	8.36	54.2	141.1	208.23	9549	15.22	48.6
161.2	240.94	3924	3.87	89.0	160.2	239.37	7840	8.19	57.7	161.0	240.70	10152	15.19	50.7
181.0	273.11	4095	3.88	94.6	180.9	272.93	8122	8.35	60.9	180.6	272.44	10467	15.18	53.0
200.8	305.35	4499	3.76	96.1	200.8	305.35	8196	8.21	64.6	200.7	305.18	10722	15.11	55.8
220.3	337.05	4817	3.75	98.5	220.2	336.89	8343	8.32	67.9	220.4	337.22	10883	15.27	58.5
240.6	370.06	5227	3.77	99.6	240.2	369.41	8454	8.23	71.4	239.9	368.92	11047	15.19	61.1
260.1	401.76	5611	3.66	100.6	260.7	402.74	8557	8.20	75.0	260.6	402.58	11166	15.13	64.2
280.3	434.61	6006	3.54	101.5	279.8	433.79	8699	8.28	78.0	280.3	434.61	11273	15.17	67.0
300.1	466.80	6416	3.47	102.1	299.9	466.48	8827	8.27	81.2	299.7	466.15	11312	15.01	70.2
321.3	501.27	6846	3.48	102.8	319.8	498.83	9046	8.27	83.7	320.4	499.81	11400	14.62	73.5
341.2	533.63	7242	3.49	103.3	340.2	532.00	9052	8.16	87.8	340.9	533.14	11468	14.73	76.9
359.8	563.87	7620	3.50	103.9	359.7	563.70	9134	8.07	91.2	360.7	565.33	11516	14.61	79.9
381.5	599.15	8072	3.62	104.3	380.4	597.36	9113	7.84	96.1	374.7	588.09	11572	14.59	82.0

Table F24. Experimental data for a 2% emulsion on Porous Surface 1, G = 350 kg/m^{2}s, T_i = 30 °C.

D_h = 200 µm					D_h = 500 µm					D_h = 1000 µm				
G = 350 kg/m^{2}s					G = 350 kg/m^{2}s					G = 350 kg/m^{2}s				
q [W]	q"$_{net}$ [kW/m^2]	h [W/m^{2}K]	ΔP [kPa]	T_w [°C]	q [W]	q"$_{net}$ [kW/m^2]	h [W/m^{2}K]	ΔP [kPa]	T_w [°C]	q [W]	q"$_{net}$ [kW/m^2]	h [W/m^{2}K]	ΔP [kPa]	T_w [°C]
20.2	11.69	1324	23.98	39.8	20.3	11.92	1902	15.02	36.1	20.4	12.05	2043	8.46	32.7
30.6	28.65	2042	24.47	46.5	40.7	45.04	3595	14.74	43.4	40.4	44.55	4643	8.37	36.4
40.5	44.63	2163	24.70	54.7	60.4	77.10	4133	14.85	50.5	60.4	77.10	5836	8.31	40.1
50.3	60.63	2217	25.55	62.8	80.6	109.88	4413	15.07	57.9	80.1	109.15	6442	8.29	43.9
					100.7	142.64	4545	15.31	65.4	100.9	142.97	6841	8.18	47.9
					120.6	174.88	4562	15.73	73.4	120.4	174.57	7159	8.16	51.5
					140.1	206.67	4652	16.39	80.6	141.4	208.70	7515	8.11	54.9
					160.4	239.61	4568	16.99	90.0	160.9	240.47	7787	8.19	58.2
					180.5	272.32	4116	19.47	106.0	180.2	271.84	7910	8.19	61.9
					200.1	304.21	4465	19.87	109.5	200.3	304.53	8177	8.12	64.9
					220.6	337.54	4844	20.52	112.5	220.1	336.73	8217	8.12	68.7
					240.5	369.90	5228	21.09	115.3	240.4	369.73	8410	8.17	71.9
					260.1	401.76	5608	21.06	118.0	260.2	401.93	8540	8.09	75.2
					280.7	435.26	5966	21.87	121.7	279.7	433.63	8571	8.05	79.0
					300.1	466.80	6323	23.00	126.6	300.5	467.45	8712	7.90	82.5
										321.1	500.94	8776	7.86	86.1
										339.9	531.51	8904	7.82	89.4
										359.8	563.87	8879	7.68	93.9
										379.8	596.39	9055	7.68	96.6

Table F25. Experimental data for water on Porous Surface 2, D_h = 200 µm, T_i = 30 °C.

D_h = 200 µm															
G = 150 kg/m^{2}s					**G = 350 kg/m^{2}s**					**G = 550 kg/m^{2}s**				
q [W]	**q"$_{net}$ [kW/m^2]**	**h [W/m^{2}K]**	**ΔP [kPa]**	**T_w [°C]**	**q [W]**	**q"$_{net}$ [kW/m^2]**	**h [W/m^{2}K]**	**ΔP [kPa]**	**T_w [°C]**	**q [W]**	**q"$_{net}$ [kW/m^2]**	**h [W/m^{2}K]**	**ΔP [kPa]**	**T_w [°C]**
20.2	11.29	796	11.45	45.7	20.4	11.62	1436	43.54	38.8	20.5	11.79	2078	88.88	35.4
30.1	26.93	1282	11.46	54.7	30.5	27.57	2072	42.73	45.5	40.7	43.75	3786	100.19	42.6
40.2	42.99	1513	11.67	64.7	40.6	43.59	2357	43.94	52.3	60.0	74.24	4033	109.17	51.2
50.4	58.97	1524	12.26	77.7	50.8	59.69	2424	45.85	60.0	80.3	106.14	4070	119.54	60.6
59.9	74.01	1295	14.11	98.5	60.4	74.83	2322	48.76	69.4	100.2	137.66	3654	133.83	74.3
70.7	91.05	1569	14.22	100.9	70.7	91.07	2243	53.14	79.4	110.0	153.13	2864	148.26	91.7
					80.3	106.27	2052	59.62	92.0	120.7	170.01	2795	152.75	100.5
					90.8	122.76	1997	67.65	103.1	130.4	185.28	2781	156.26	107.4
					101.2	139.17	2175	74.26	107.5	140.0	200.41	2572	175.40	120.9
					110.3	153.51	2368	78.23	110.0	161.1	233.78	3067	180.32	123.6
					120.7	170.00	2612	84.76	112.0					
					130.6	185.64	2858	104.22	116.2					
					141.2	202.38	3019	135.90	122.5					

Table F26. Experimental data for water on Porous Surface 2, D_h = 500 µm, T_i = 30 °C.

D_h = 500 µm															
G = 150 kg/m^{2}s					G = 350 kg/m^{2}s					G = 550 kg/m^{2}s				
q [W]	q"$_{net}$ [kW/m^2]	h [W/m^{2}K]	ΔP [kPa]	T_w [°C]	q [W]	q"$_{net}$ [kW/m^2]	h [W/m^{2}K]	ΔP [kPa]	T_w [°C]	q [W]	q"$_{net}$ [kW/m^2]	h [W/m^{2}K]	ΔP [kPa]	T_w [°C]
20.1	11.24	1330	10.89	39.3	20.2	11.43	2094	31.20	35.2	20.4	11.68	3093	62.21	33.2
40.1	42.69	2543	11.29	49.5	40.1	42.84	3867	31.66	41.9	40.9	44.05	5740	62.45	37.9
50.3	58.92	2718	11.47	55.5	60.1	74.27	4376	32.47	48.9	60.8	75.40	6508	63.07	42.5
60.3	74.57	2781	12.06	61.8	80.3	106.28	4446	33.15	56.9	80.2	106.00	6815	63.11	47.2
70.4	90.64	2792	11.70	68.6	100.0	137.36	4377	34.05	65.5	100.4	137.97	6963	63.67	52.1
80.1	105.95	2697	12.27	76.5	120.1	168.96	4204	35.07	75.7	120.4	169.43	6958	64.19	57.4
89.8	121.20	2305	13.14	91.0	140.3	200.95	3830	36.06	89.3	140.7	201.58	6797	64.94	63.6
100.0	137.33	2349	13.48	97.6	160.9	233.43	3773	36.60	100.1	160.5	232.78	6665	65.34	69.8
110.5	153.85	2566	13.80	100.5	180.9	265.01	4251	36.86	101.7	180.5	264.29	6499	66.17	76.5
121.3	170.87	2871	13.94	101.3	201.1	296.88	4738	37.09	103.6	200.1	295.30	5786	67.10	87.9
140.4	201.04	3460	14.83	102.5	220.3	327.18	5235	38.14	105.0	219.8	326.39	5540	68.04	96.9
160.2	232.29	4128	15.70	103.2	240.9	359.69	5742	38.97	107.3	240.2	358.59	5597	67.92	103.2
180.2	263.87	4924	17.62	104.6	260.7	390.94	6231	40.27	109.3	260.2	390.15	6057	68.00	104.5
200.4	295.77	5719	19.00	106.7	280.7	422.51	6758	41.36	111.5	280.1	421.56	6455	69.03	106.8
219.8	326.39	6371	22.65	115.0	300.6	453.92	7340	41.94	112.8	301.0	454.55	6746	69.20	110.5
					319.9	484.38	7784	42.43	115.6	320.4	485.17	7044	69.23	112.9
					341.0	517.68	8185	43.00	118.3	341.0	517.68	7056	69.73	118.8

Table F27. Experimental data for water on Porous Surface 2, D_h = 1000 µm, T_i = 30 °C.

D_h = 1000 µm															
G = 150 kg/m^{2}s					G = 350 kg/m^{2}s					G = 550 kg/m^{2}s				
q [W]	q"$_{net}$ [kW/m^2]	h [W/m^{2}K]	ΔP [kPa]	T_w [°C]	q [W]	q"$_{net}$ [kW/m^2]	h [W/m^{2}K]	ΔP [kPa]	T_w [°C]	q [W]	q"$_{net}$ [kW/m^2]	h [W/m^{2}K]	ΔP [kPa]	T_w [°C]
20.4	11.66	2375	2.21	34.8	20.8	12.34	3254	6.68	33.3	20.8	12.34	3730	12.65	32.6
41.1	44.33	4520	2.19	41.0	40.8	43.88	6162	6.63	37.1	40.9	43.97	7223	12.72	35.7
60.4	74.78	5235	2.11	46.7	61.1	75.87	7209	6.60	41.0	60.4	74.83	8584	12.88	38.7
80.5	106.46	5669	2.16	52.4	80.6	106.68	7743	6.59	44.8	80.9	107.12	9316	12.87	41.8
100.5	138.13	5924	2.10	58.1	100.1	137.42	8112	6.51	48.5	100.5	138.09	9733	12.84	44.9
120.8	170.14	6068	2.11	64.1	120.8	170.08	8359	6.40	52.4	120.8	170.14	10034	12.74	48.0
140.0	200.44	6151	2.11	69.9	141.1	202.10	8535	6.37	56.4	140.7	201.55	10207	12.74	51.1
160.9	233.35	6179	2.16	76.3	160.7	233.08	8662	6.33	60.1	161.1	233.81	10353	12.70	54.4
180.9	264.98	6210	2.15	82.5	180.4	264.24	8592	6.24	64.5	180.0	263.58	10467	12.67	57.3
200.2	295.46	5741	2.39	92.4	200.1	295.30	8454	6.21	69.2	200.0	295.14	10564	12.65	60.5
220.7	327.81	5819	2.45	98.6	220.0	326.71	8423	6.16	73.6	220.7	327.81	10621	12.50	64.0
240.1	358.43	6088	2.43	102.3	240.2	358.59	8481	6.13	77.7	240.4	358.90	10638	12.48	67.7
261.5	392.21	6613	2.36	104.0	260.0	389.84	8347	6.15	82.7	260.9	391.26	10382	12.28	72.6
281.4	423.61	7139	2.60	105.1	280.6	422.35	8171	6.05	88.3	280.4	422.04	10343	12.22	76.5
301.4	455.18	7764	2.71	105.6	301.2	454.86	8182	5.96	93.0	300.2	453.29	10236	12.09	81.0
321.0	486.11	8406	2.68	106.1	319.7	484.06	8103	5.95	97.9	319.9	484.38	10112	12.02	85.4
341.3	518.15	9111	2.82	106.6	340.5	516.89	8253	5.83	101.7	340.9	517.52	10129	11.85	89.3
360.0	547.67	9751	3.04	107.0	359.8	547.35	8437	5.81	104.9	360.1	547.83	10015	11.80	94.1
380.5	580.02	10521	2.91	107.3	380.1	579.39	8881	5.75	106.0	380.0	579.23	10101	11.80	97.3

Table F28. Experimental data for a 0.1% emulsion on Porous Surface 2, G = 350 kg/m^{2}s, T_i = 30 °C.

D_h = 200 µm					D_h = 500 µm					D_h = 1000 µm				
G = 350 kg/m^{2}s					G = 350 kg/m^{2}s					G = 350 kg/m^{2}s				
q [W]	q"$_{net}$ [kW/m^2]	h [W/m^{2}K]	ΔP [kPa]	T_w [°C]	q [W]	q"$_{net}$ [kW/m^2]	h [W/m^{2}K]	ΔP [kPa]	T_w [°C]	q [W]	q"$_{net}$ [kW/m^2]	h [W/m^{2}K]	ΔP [kPa]	T_w [°C]
20.5	11.87	1093	24.44	41.9	20.4	11.71	1971	18.86	35.4	20.5	11.85	3325	7.71	32.8
30.3	27.34	1698	24.39	48.4	40.5	43.36	3410	18.79	43.2	40.4	43.17	5919	7.63	37.1
40.3	43.14	1966	24.66	55.8	60.7	75.30	3924	18.80	50.6	60.1	74.40	6730	7.63	41.4
50.5	59.23	2171	24.81	62.4	80.6	106.71	4230	18.64	57.6	80.3	106.28	6981	7.56	46.1
60.3	74.72	2311	24.93	68.9	100.8	138.64	4417	18.55	64.8	100.6	138.31	7297	7.59	50.3
70.0	89.96	2408	25.05	75.4	120.3	169.34	4552	18.68	71.6	120.7	170.05	7424	7.47	54.8
80.5	106.54	2678	28.52	78.6	140.2	200.77	4596	18.87	79.0	140.2	200.73	7448	7.48	59.5
90.4	122.21	2819	29.24	83.4	160.8	233.34	4721	19.45	85.8	160.1	232.21	7555	7.49	63.8
100.1	137.47	2884	30.87	89.2	180.9	264.92	4774	19.88	92.8	181.0	265.14	7636	7.38	68.3
110.8	154.33	3013	31.94	94.8	201.1	296.88	4965	19.66	98.1	200.2	295.46	7683	7.31	72.5
120.8	170.11	3096	33.21	100.4	220.3	327.18	5349	19.48	100.3	220.4	327.34	7795	7.31	76.6
131.2	186.49	3385	33.12	101.7	241.3	360.32	5765	19.99	103.1	240.6	359.22	7896	7.28	80.6
141.3	202.50	3738	34.56	103.3	260.7	390.94	6030	20.24	106.6	260.7	390.94	7944	7.21	84.9
					281.8	424.25	6328	20.93	110.2	280.7	422.51	7990	7.18	89.2
					301.5	455.34	6733	21.29	111.8	300.6	453.92	7987	7.02	94.1
					320.6	485.48	6990	21.94	114.5	321.2	486.43	8090	6.96	98.2
					340.2	516.42	7257	22.06	117.3	340.6	517.05	8319	6.89	101.1
										360.5	548.46	8666	6.80	103.2
										380.8	580.50	9161	6.87	104.2

Table F29. Experimental data for a 0.5% emulsion on Porous Surface 2, G = 350 kg/m^{2}s, T_i = 30 °C.

D_h = 200 µm					D_h = 500 µm					D_h = 1000 µm				
G = 350 kg/m^{2}s					G = 350 kg/m^{2}s					G = 350 kg/m^{2}s				
q [W]	q"$_{net}$ [kW/m^2]	h [W/m^{2}K]	ΔP [kPa]	T_w [°C]	q [W]	q"$_{net}$ [kW/m^2]	h [W/m^{2}K]	ΔP [kPa]	T_w [°C]	q [W]	q"$_{net}$ [kW/m^2]	h [W/m^{2}K]	ΔP [kPa]	T_w [°C]
20.4	11.65	1444	35.30	38.5	20.5	11.76	1854	19.42	36.2	20.5	11.82	3300	8.63	32.8
30.5	27.68	2234	36.27	44.1	40.6	43.62	3387	19.53	43.7	40.3	43.02	6129	8.62	36.9
40.4	43.20	2571	36.62	49.9	60.1	74.31	3916	19.70	50.5	60.8	75.43	6919	8.67	41.3
50.3	58.79	2718	37.49	55.9	80.7	106.84	4229	19.79	57.9	80.2	106.08	7261	8.70	45.5
60.1	74.26	2724	38.30	62.9	100.5	138.13	4395	19.90	65.0	100.5	138.07	7471	8.61	49.9
70.4	90.66	2674	39.72	71.1	120.4	169.57	4470	20.01	72.4	121.1	170.60	7624	8.63	54.3
80.6	106.68	2664	40.61	78.6	140.7	201.53	4806	21.46	77.0	140.2	200.71	7768	8.53	58.3
90.3	122.00	2698	41.73	85.3	160.3	232.45	4904	21.53	83.3	160.8	233.27	7877	8.50	62.6
100.1	137.41	2787	42.93	90.6	181.4	265.72	4975	21.72	90.3	180.6	264.44	7956	8.48	66.6
110.7	154.14	2892	44.28	96.6	200.1	295.30	5096	21.61	95.7	200.4	295.77	8061	8.52	70.6
120.8	170.17	3011	45.61	101.6	221.1	328.44	5431	22.09	99.3	219.7	326.23	8122	8.44	74.7
131.2	186.60	3302	45.67	102.9	240.8	359.54	5829	22.68	101.5	240.6	359.22	8129	8.41	79.2
					261.2	391.73	6147	22.96	104.6	260.0	389.84	8144	8.37	83.4
					281.9	424.40	6531	23.02	106.8	280.8	422.67	8089	8.25	88.6
					300.7	454.07	6818	23.27	109.4	300.6	453.92	8136	8.22	92.8
					321.4	486.75	7149	23.63	112.0	321.2	486.43	8217	8.13	97.2
					341.0	517.68	7406	24.01	114.9	340.9	517.52	8450	8.08	100.0
										360.7	548.77	8808	7.93	101.8
										380.3	579.71	9168	7.86	103.5

Table F30. Experimental data for a 1% emulsion on Porous Surface 2, D_h = 200 µm, T_i = 30 °C.

D_h = 200 µm															
G = 150 kg/m^{2}s					G = 350 kg/m^{2}s					G = 550 kg/m^{2}s				
q [W]	q"$_{net}$ [kW/m^2]	h [W/m^{2}K]	ΔP [kPa]	T_w [°C]	q [W]	q"$_{net}$ [kW/m^2]	h [W/m^{2}K]	ΔP [kPa]	T_w [°C]	q [W]	q"$_{net}$ [kW/m^2]	h [W/m^{2}K]	ΔP [kPa]	T_w [°C]
20.4	11.73	866	15.56	45.9	20.3	11.51	1443	42.88	39.6	20.5	11.76	1964	80.69	36.2
30.4	27.40	1289	16.44	55.9	30.5	27.67	2268	43.77	44.7	30.7	27.94	3021	83.28	40.1
40.2	42.96	1478	17.56	65.8	40.4	43.31	2697	45.04	49.6	40.7	43.78	3667	88.87	43.5
50.5	59.14	1578	18.14	76.5	50.4	59.03	2957	46.47	54.7	50.5	59.20	3962	91.14	47.1
59.8	73.93	1596	19.14	87.7	60.5	74.89	3247	45.33	58.7	60.6	75.11	4059	91.83	51.5
70.2	90.23	1725	19.49	95.9	70.3	90.37	3228	47.27	64.6	70.2	90.22	4206	93.17	55.4
80.4	106.44	1957	20.03	100.2	80.6	106.72	3303	48.57	70.4	80.8	106.96	4277	94.14	59.8
					90.5	122.30	3280	50.59	76.7	90.9	123.01	4373	96.67	63.7
					100.7	138.48	3344	52.07	82.4	100.4	138.01	4332	98.63	68.3
					109.7	152.68	3296	54.77	88.9	111.0	154.69	4535	106.08	71.4
					120.7	169.94	3285	57.53	96.5	120.4	169.49	4566	108.39	75.2
					130.4	185.32	3354	59.10	102.0	130.8	185.95	4461	113.13	80.9
										140.7	201.52	4270	119.27	87.8
										150.5	216.94	4196	120.29	93.8
										160.4	232.67	4107	124.56	100.0
										170.2	248.14	4124	126.67	104.8
										181.2	265.53	4306	127.31	107.7
										189.9	279.14	4471	130.67	110.4

Table F31. Experimental data for a 1% emulsion on Porous Surface 2, D_h = 500 µm, T_i = 30 °C.

D_h = 500 µm															
G = 150 kg/m^{2}s					G = 350 kg/m^{2}s					G = 550 kg/m^{2}s				
q [W]	q"$_{net}$ [kW/m^2]	h [W/m^{2}K]	ΔP [kPa]	T_w [°C]	q [W]	q"$_{net}$ [kW/m^2]	h [W/m^{2}K]	ΔP [kPa]	T_w [°C]	q [W]	q"$_{net}$ [kW/m^2]	h [W/m^{2}K]	ΔP [kPa]	T_w [°C]
20.6	11.93	1193	8.65	40.6	20.5	11.76	1874	20.86	36.1	20.8	12.23	2596	37.93	33.9
30.4	27.53	1893	8.27	46.0	40.4	43.23	3582	21.24	42.7	40.6	43.56	4660	38.20	39.3
40.6	43.56	2223	8.40	52.0	60.3	74.61	4172	21.31	49.4	60.7	75.24	5371	40.78	44.7
50.9	59.82	2483	8.35	57.4	80.1	105.97	4531	21.50	55.8	80.4	106.33	5777	40.84	49.6
60.8	75.49	2629	8.52	63.1	99.9	137.20	4680	21.59	62.6	99.9	137.14	5944	41.31	54.9
70.7	91.07	2747	8.41	68.4	120.8	170.08	4778	21.88	69.9	120.8	170.11	6110	41.57	60.2
80.2	105.98	2831	8.48	73.5	140.2	200.76	4744	21.66	77.6	140.5	201.15	6216	42.23	65.4
90.0	121.45	2913	8.14	78.9	160.3	232.47	4841	21.76	84.2	160.0	232.07	6219	42.66	71.0
100.5	138.04	2913	8.27	85.6	179.8	263.28	4884	22.04	91.1	181.1	265.36	6523	46.30	74.8
111.2	154.99	2989	8.35	91.1	200.5	295.93	4988	22.50	97.5	200.9	296.56	6612	47.75	79.4
120.8	170.11	3037	8.37	96.3	219.6	326.08	5345	22.46	100.1	220.2	327.02	6619	48.58	84.6
130.3	185.09	3242	8.29	98.2	241.1	360.01	5857	22.47	101.6	240.7	359.38	6673	49.17	89.6
140.5	201.23	3529	8.53	99.6	260.8	391.10	6213	22.83	104.3	260.2	390.15	6710	49.68	94.5
161.3	234.09	4161	9.40	101.9	280.5	422.19	6542	23.09	107.0	281.1	423.14	6817	50.42	98.9
181.5	265.91	4822	9.35	102.8	300.8	454.23	6853	23.40	110.0	301.3	455.02	7115	50.35	101.5
201.7	297.82	5431	9.19	104.4	320.5	485.32	7142	23.88	113.0	320.9	485.96	7488	51.41	103.2
220.8	327.97	6041	9.65	107.1	340.7	517.21	7434	24.50	116.0	340.5	516.89	7782	52.28	105.8
239.9	358.11	6784	10.88	109.6						360.2	547.98	7938	51.99	109.1

Table F32. Experimental data for a 1% emulsion on Porous Surface 2, D_h = 1000 µm, T_i = 30 °C.

D_h = 1000 µm															
G = 150 kg/m^{2}s					G = 350 kg/m^{2}s					G = 550 kg/m^{2}s				
q [W]	q"$_{net}$ [kW/m^2]	h [W/m^{2}K]	ΔP [kPa]	T_w [°C]	q [W]	q"$_{net}$ [kW/m^2]	h [W/m^{2}K]	ΔP [kPa]	T_w [°C]	q [W]	q"$_{net}$ [kW/m^2]	h [W/m^{2}K]	ΔP [kPa]	T_w [°C]
20.8	12.23	2732	4.16	34.3	20.8	12.30	3371	10.61	32.9	20.5	11.89	4079	18.38	32.0
40.2	42.90	4727	4.28	40.1	40.7	43.73	6125	10.58	36.9	40.4	43.18	7392	18.35	35.3
60.5	74.94	5273	4.26	46.6	60.5	75.00	7060	10.65	41.0	61.0	75.68	8573	18.44	38.7
80.5	106.46	5644	4.21	52.3	80.3	106.25	7491	10.49	45.0	80.4	106.42	9047	18.12	42.0
100.4	138.01	5857	4.21	58.4	100.7	138.34	7757	10.51	49.3	100.9	138.73	9372	18.14	45.4
120.6	169.81	5986	4.22	64.4	120.7	170.01	8016	10.43	53.2	120.6	169.86	9611	18.41	48.6
140.4	201.07	6093	4.21	70.3	140.3	200.89	8202	10.24	57.0	141.0	202.08	9808	18.53	51.9
160.5	232.80	6069	4.27	77.0	160.8	233.27	8181	10.28	61.6	160.8	233.19	9943	18.38	55.1
180.4	264.14	6094	4.28	83.1	180.6	264.51	8255	10.25	65.6	180.9	265.01	10046	18.29	58.4
200.4	295.77	6194	4.23	88.7	200.2	295.46	8346	10.24	69.6	200.7	296.25	10147	18.18	61.6
219.7	326.23	6191	4.29	94.7	219.8	326.39	8439	10.21	73.3	220.1	326.86	10137	18.22	65.2
240.3	358.75	6394	4.21	99.5	240.6	359.22	8469	10.22	77.7	241.4	360.48	10263	18.09	68.7
260.3	390.31	6956	4.20	100.9	260.2	390.15	8505	10.14	81.7	260.7	390.94	10338	17.66	72.1
280.3	421.88	7450	4.21	102.5	279.5	420.61	8573	9.89	85.6	280.4	422.04	10381	17.82	75.7
300.9	454.39	8010	4.31	104.3	301.2	454.86	8614	9.75	90.2	300.7	454.07	10465	17.73	79.2
321.2	486.43	8617	4.24	105.3	320.0	484.54	8588	9.62	95.0	320.8	485.80	10581	17.54	82.6
341.5	518.47	9341	4.27	105.8	340.2	516.42	8644	9.50	99.4	340.1	516.26	10565	17.41	86.9
360.1	547.83	10020	4.27	106.4	360.2	547.98	8981	9.50	101.5	360.0	547.67	10541	17.48	90.8
380.9	580.65	10784	4.35	107.1	380.3	579.71	9370	9.30	103.1	380.0	579.23	10617	17.24	94.2

Table F33. Experimental data for a 2% emulsion on Porous Surface 2, G = 350 kg/m^{2}s, T_i = 30 °C.

D_h = 200 µm					D_h = 500 µm					D_h = 1000 µm				
G = 350 kg/m^{2}s					G = 350 kg/m^{2}s					G = 350 kg/m^{2}s				
q [W]	q"$_{net}$ [kW/m^2]	h [W/m^{2}K]	ΔP [kPa]	T_w [°C]	q [W]	q"$_{net}$ [kW/m^2]	h [W/m^{2}K]	ΔP [kPa]	T_w [°C]	q [W]	q"$_{net}$ [kW/m^2]	h [W/m^{2}K]	ΔP [kPa]	T_w [°C]
20.6	12.03	1514	50.67	38.9	20.7	12.15	1944	22.06	36.0	20.7	12.18	3433	11.79	32.8
30.5	27.65	2283	50.78	44.5	40.4	43.21	3538	22.06	42.8	40.3	43.04	6240	11.42	36.7
40.7	43.72	2572	50.97	50.8	60.2	74.53	4067	21.99	49.8	60.8	75.40	7221	11.16	40.8
50.2	58.78	2778	50.94	56.4	81.0	107.31	4390	22.26	56.9	80.2	106.03	7785	11.07	44.5
60.9	75.60	2886	52.68	62.8	100.9	138.72	4553	22.27	63.9	100.6	138.23	8066	11.01	48.5
70.6	90.96	2895	52.82	69.8	120.2	169.26	4560	22.34	71.5	120.7	169.92	8244	11.06	52.4
80.8	107.01	2879	55.59	77.0	140.3	200.95	4654	22.38	78.5	140.4	201.00	8463	11.10	56.2
90.8	122.73	2825	58.95	85.2	160.4	232.59	4745	22.54	85.4	161.1	233.73	8502	11.03	60.4
101.0	138.81	2899	60.90	91.4	180.7	264.63	4825	23.07	92.1	180.9	265.01	8550	10.87	64.4
120.2	169.22	3050	66.39	102.2	200.2	295.46	4940	23.27	98.0	200.7	296.25	8689	10.87	67.9
131.1	186.40	3349	67.78	104.0	220.6	327.65	5347	23.20	100.3	220.2	327.02	8789	10.66	71.6
140.1	200.54	3537	78.01	109.0	241.2	360.17	5816	23.63	102.0	241.2	360.17	8802	10.30	75.8
					260.1	390.00	6087	24.59	105.3	260.6	390.79	8853	10.38	79.7
					280.2	421.72	6244	25.41	110.0	280.0	421.40	8861	10.30	84.1
					300.4	453.60	6648	25.85	111.6	301.7	455.65	8947	10.18	88.3
					321.5	486.90	7053	26.54	113.7	321.2	486.43	8959	10.13	92.9
					340.9	517.52	7313	26.90	116.6	340.9	517.52	8985	9.50	97.2
										360.7	548.77	9156	9.59	100.8
										380.8	580.50	9540	9.59	102.5

Table F34. Experimental data for water on Porous Surface 3, D_h = 200 µm, T_i = 30 °C.

D_h = 200 µm															
G = 150 kg/m^{2}s					G = 350 kg/m^{2}s					G = 550 kg/m^{2}s				
q [W]	q"$_{net}$ [kW/m^2]	h [W/m^{2}K]	ΔP [kPa]	T_w [°C]	q [W]	q"$_{net}$ [kW/m^2]	h [W/m^{2}K]	ΔP [kPa]	T_w [°C]	q [W]	q"$_{net}$ [kW/m^2]	h [W/m^{2}K]	ΔP [kPa]	T_w [°C]
20.3	11.50	613	12.70	49.3	20.3	11.48	1073	63.08	41.8	20.6	12.05	1649	116.71	37.6
30.0	26.84	887	11.62	63.6	29.9	26.76	1499	66.02	50.1	30.2	27.25	2430	119.70	42.4
40.3	43.19	1063	11.97	76.4	40.4	43.34	1555	65.72	61.6	40.6	43.57	2818	123.44	47.6
50.3	58.99	1143	12.54	89.5	50.3	58.99	1607	67.42	72.5	50.5	59.23	2892	127.05	53.7
60.1	74.51	1227	14.05	99.9	60.6	75.35	1724	68.58	81.7	60.3	74.82	2767	131.70	61.6
71.1	91.81	1532	14.72	100.7	70.2	90.48	1837	69.96	89.1	70.8	91.37	2613	136.87	71.1
80.5	106.71	1848	21.47	104.4	80.2	106.30	1912	70.12	97.2	80.9	107.44	2638	140.05	78.6
					89.8	121.48	1973	70.68	104.6	90.5	122.63	2643	142.68	85.9
					100.7	138.67	2253	71.01	106.6	100.2	137.88	2667	143.03	92.9
										110.7	154.49	2677	143.48	100.3
										119.6	168.58	2618	144.76	108.3
										130.5	185.86	2882	145.57	109.9
										140.6	201.82	3145	147.09	111.6
										151.0	218.22	3400	147.87	113.9

Table F35. Experimental data for water on Porous Surface 3, D_h = 500 µm, T_i = 30 °C.

D_h = 500 µm															
G = 150 kg/m^{2}s					G = 350 kg/m^{2}s					G = 550 kg/m^{2}s				
q [W]	q"$_{net}$ [kW/m^2]	h [W/m^{2}K]	ΔP [kPa]	T_w [°C]	q [W]	q"$_{net}$ [kW/m^2]	h [W/m^{2}K]	ΔP [kPa]	T_w [°C]	q [W]	q"$_{net}$ [kW/m^2]	h [W/m^{2}K]	ΔP [kPa]	T_w [°C]
20.6	12.02	1302	5.15	40.2	20.2	11.37	1826	12.15	36.3	20.8	12.30	2816	23.63	33.9
30.2	27.23	2034	5.24	45.1	40.1	42.86	3570	12.35	42.9	40.4	43.27	5230	24.02	38.5
40.4	43.34	2427	5.27	50.5	60.4	74.95	4143	12.51	49.9	60.1	74.41	5996	23.42	43.2
50.4	59.10	2635	5.20	56.0	80.4	106.58	4480	12.53	56.5	80.2	106.34	6379	23.95	48.1
60.3	74.82	2766	5.29	61.6	100.3	138.13	4679	12.62	63.3	100.6	138.47	6598	24.00	53.1
70.2	90.40	2833	5.25	67.4	120.8	170.54	4688	12.60	71.3	120.5	169.97	6717	24.12	58.2
80.3	106.47	2726	5.29	75.6	140.5	201.71	4456	12.83	81.3	140.5	201.60	6610	24.26	64.0
90.8	123.05	2601	5.46	84.7	159.9	232.38	3868	13.68	97.0	161.1	234.24	6608	24.26	69.6
100.2	137.98	2320	5.80	97.8	180.0	264.06	4110	14.42	102.4	180.6	265.05	6503	24.39	75.7
110.3	153.90	2519	5.99	100.4	200.6	296.70	4522	15.63	105.2	200.3	296.23	6583	24.30	80.5
120.5	169.95	2807	6.41	101.1	220.6	328.33	5013	16.19	106.5	220.0	327.38	6500	24.88	86.6
130.4	185.63	3065	6.97	102.5	240.6	359.96	5531	16.72	107.4	240.4	359.65	5474	27.06	103.4
140.6	201.81	3349	7.22	103.5	260.7	391.75	6078	17.39	108.2	260.6	391.59	5773	27.78	107.3
151.3	218.67	3648	7.75	104.4	281.2	424.17	6705	18.05	108.9	280.5	423.07	6233	28.81	109.0
161.1	234.15	3930	8.01	105.1	300.3	454.38	7311	19.02	109.9	300.1	454.06	6718	29.26	110.0
170.4	248.94	4256	8.76	105.5	321.6	488.07	8032	20.33	111.0	321.6	488.07	7285	29.54	110.8
180.6	265.08	4623	9.58	106.1	340.1	517.33	8810	22.04	112.0	340.2	517.48	7826	30.05	111.7
191.1	281.64	4992	10.28	106.7	360.3	549.27	9798	23.58	113.0	360.2	549.12	8483	30.98	113.1
200.4	296.38	5330	10.70	107.0										
220.5	328.17	6222	12.43	108.0										
240.3	359.49	7180	14.20	109.1										

Table F36. Experimental data for water on Porous Surface 3, D_h = 1000 µm, T_i = 30 °C.

D_h = 1000 µm															
G = 150 kg/m^{2}s					G = 350 kg/m^{2}s					G = 550 kg/m^{2}s				
q [W]	q"$_{net}$ [kW/m^2]	h [W/m^{2}K]	ΔP [kPa]	T_w [°C]	q [W]	q"$_{net}$ [kW/m^2]	h [W/m^{2}K]	ΔP [kPa]	T_w [°C]	q [W]	q"$_{net}$ [kW/m^2]	h [W/m^{2}K]	ΔP [kPa]	T_w [°C]
20.5	11.78	2032	2.40	35.7	20.5	11.91	2690	5.69	33.9	20.8	12.29	3054	9.87	33.2
40.8	43.92	3793	2.33	42.4	40.3	43.21	5145	5.65	38.4	40.4	43.27	5895	9.99	36.9
60.3	74.86	4384	2.27	49.0	60.9	75.68	6064	5.79	42.9	60.2	74.57	6961	9.88	40.6
80.3	106.47	4677	2.26	55.8	80.3	106.42	6560	5.83	47.1	80.5	106.79	7528	9.94	44.4
100.2	137.93	4799	2.27	62.8	100.7	138.64	6872	5.83	51.5	101.0	139.16	7834	9.82	48.4
120.1	169.40	4884	2.26	69.8	120.7	170.37	7076	5.79	56.0	120.1	169.40	8053	9.78	52.0
140.1	200.95	4876	2.18	77.6	140.4	201.51	7223	5.77	60.3	141.1	202.60	8144	9.74	56.2
161.0	234.13	4934	2.27	84.9	160.5	233.33	7268	5.73	65.0	160.2	232.85	8283	9.86	59.7
180.3	264.56	4943	2.34	92.0	180.3	264.61	7342	5.71	69.5	180.1	264.26	8272	9.74	63.9
200.3	296.23	5039	2.49	98.4	200.1	295.91	7271	5.73	74.6	200.1	295.91	8395	9.65	67.7
219.9	327.22	5342	2.38	101.9	220.7	328.49	6782	5.68	82.8	220.2	327.70	8410	9.66	71.7
241.0	360.59	5766	2.47	104.3	240.5	359.80	6749	5.74	88.3	240.4	359.65	8387	9.79	76.2
260.5	391.43	6295	2.46	105.1	260.5	391.43	6850	5.71	92.7	260.3	391.12	8382	9.57	80.6
280.8	423.54	6867	2.52	105.8	280.4	422.91	6957	5.74	97.3	279.8	421.96	8435	9.72	84.8
300.9	455.33	7524	2.59	105.9	300.5	454.70	7096	5.74	101.3	300.2	454.22	8370	9.81	90.1
320.5	486.33	8084	2.77	106.4	321.6	488.07	7513	5.71	102.8	320.7	486.64	8398	9.40	94.8
341.1	518.91	8737	2.74	107.1	340.2	517.48	7800	5.73	104.9	340.2	517.48	8546	9.48	98.1
360.2	549.12	9367	2.70	107.6	360.7	549.91	8312	5.73	105.5	360.8	550.06	8689	9.51	101.5
380.6	581.38	9989	2.85	108.3	381.4	582.64	8750	5.57	106.6	381.2	582.33	9114	9.54	102.6
393.1	601.15	10472	2.81	108.4										

Table F37. Experimental data for a 0.1% emulsion on Porous Surface 3, G = 350 kg/m^{2}s, T_i = 30 °C.

D_h = 200 µm					D_h = 500 µm					D_h = 1000 µm				
G = 350 kg/m^{2}s					G = 350 kg/m^{2}s					G = 350 kg/m^{2}s				
q [W]	q"$_{net}$ [kW/m^2]	h [W/m^{2}K]	ΔP [kPa]	T_w [°C]	q [W]	q"$_{net}$ [kW/m^2]	h [W/m^{2}K]	ΔP [kPa]	T_w [°C]	q [W]	q"$_{net}$ [kW/m^2]	h [W/m^{2}K]	ΔP [kPa]	T_w [°C]
20.3	11.50	1038	77.03	42.0	20.6	11.99	1994	10.91	36.5	20.4	11.75	2566	5.78	33.9
30.5	27.69	1393	80.29	52.3	40.7	43.78	3878	10.90	42.6	40.2	43.00	4912	5.79	38.6
40.3	43.11	1378	81.60	65.5	60.3	74.87	4476	11.07	48.9	60.7	75.41	5642	5.82	43.7
50.3	59.02	1388	83.71	78.9	80.6	106.85	4575	10.82	56.4	80.9	107.31	6083	5.87	48.5
60.2	74.71	1491	84.31	88.2	100.8	138.81	4783	10.71	62.9	100.2	137.85	6235	5.83	53.5
69.9	89.96	1527	86.72	99.4	120.2	169.56	4843	10.67	69.8	120.0	169.24	6377	5.77	58.4
80.5	106.71	1682	86.89	105.3	140.4	201.54	4841	10.68	77.5	140.7	202.00	6562	5.79	63.2
90.7	122.90	1962	87.06	106.1	160.8	233.79	4920	10.71	84.4	160.7	233.66	6668	5.78	68.0
100.4	138.18	2230	88.14	108.1	180.7	265.21	4908	10.84	91.8	181.0	265.62	6699	5.67	73.1
					201.1	297.49	5037	11.21	98.0	201.2	297.65	6748	5.74	78.2
					219.8	327.07	5189	13.18	103.3	220.4	328.01	6651	5.67	83.9
					241.8	361.86	5683	14.27	105.3	239.7	358.54	6690	5.61	88.7
					261.1	392.38	6177	15.21	106.5	261.0	392.23	6727	5.69	94.0
					281.4	424.49	6736	15.98	107.4	281.0	423.86	6845	5.63	98.1
					300.6	454.86	7259	16.46	108.4	301.1	455.65	7115	5.55	100.8
					320.1	485.70	7766	16.87	109.5	321.7	488.23	7522	5.60	102.2
					340.2	517.48	8325	17.18	110.6	340.1	517.33	7891	5.54	103.4
					360.3	549.27	8877	17.91	111.8	360.7	549.91	8351	5.71	104.3
					381.4	582.64	9386	18.61	113.5	381.5	582.80	8786	5.42	105.6
					395.0	604.15	9723	19.46	115.0					

Table F38. Experimental data for a 0.5% emulsion on Porous Surface 3, G = 350 kg/m^{2}s, T_i = 30 °C.

D_h = 200 µm					D_h = 500 µm					D_h = 1000 µm				
G = 350 kg/m^{2}s					G = 350 kg/m^{2}s					G = 350 kg/m^{2}s				
q [W]	q"$_{net}$ [kW/m^2]	h [W/m^{2}K]	ΔP [kPa]	T_w [°C]	q [W]	q"$_{net}$ [kW/m^2]	h [W/m^{2}K]	ΔP [kPa]	T_w [°C]	q [W]	q"$_{net}$ [kW/m^2]	h [W/m^{2}K]	ΔP [kPa]	T_w [°C]
20.2	11.37	1179	90.62	40.4	20.5	11.81	1897	12.93	36.1	20.3	11.53	2863	6.15	33.6
30.5	27.66	1678	91.54	48.8	40.8	43.94	3581	13.03	43.1	40.3	43.18	5283	6.09	38.2
40.3	43.24	1639	94.72	60.5	60.4	74.89	4038	12.99	50.3	60.0	74.35	5956	6.11	42.9
50.1	58.68	1603	94.46	72.7	80.2	106.33	4297	12.84	57.5	80.0	106.01	6017	6.12	49.0
60.3	74.81	1614	95.73	84.6	101.0	139.16	4220	12.80	66.7	100.4	138.24	6418	6.21	52.9
70.6	91.05	1678	96.56	94.4	120.5	169.95	4354	12.69	73.9	120.4	169.78	6541	6.24	57.8
80.4	106.61	1734	96.88	103.8	140.8	202.15	4515	12.82	80.6	140.5	201.65	6683	6.14	62.6
90.5	122.59	1958	96.91	106.2	160.3	232.95	4525	12.85	88.3	159.8	232.19	6672	6.17	67.8
100.7	138.69	2222	97.49	108.4	179.8	263.87	4530	12.92	96.0	180.8	265.35	6800	6.16	72.5
					200.1	295.91	4738	14.22	101.8	200.6	296.70	6886	6.14	77.1
					220.4	328.01	5180	14.85	104.6	220.4	328.01	6844	6.17	82.5
					241.2	360.91	5722	15.74	106.0	240.3	359.49	6910	6.18	87.2
					260.6	391.59	6285	16.48	107.0	260.0	390.64	6921	6.05	92.0
					280.7	423.38	6825	16.87	108.2	280.0	422.28	6965	6.12	96.9
					301.2	455.80	7355	17.29	109.7	300.2	454.22	7206	6.05	99.8
					320.1	485.70	7932	17.73	110.6	320.4	486.17	7522	6.03	101.9
					340.9	518.59	8547	18.35	111.9	340.8	518.43	7979	6.07	102.9
					361.0	550.38	9278	19.60	113.8	361.3	550.86	8417	6.16	104.1
										380.4	581.06	8828	6.02	105.1

Table F39. Experimental data for a 1% emulsion on Porous Surface 3, D_h = 200 μm, T_i = 30 °C.

D_h = 200 μm										
G = 150 kg/m^{2}s						G = 350 kg/m^{2}s				
q [W]	q"$_{net}$ [kW/m^2]	h [W/m^{2}K]	ΔP [kPa]	T_w [°C]		q [W]	q"$_{net}$ [kW/m^2]	h [W/m^{2}K]	ΔP [kPa]	T_w [°C]
20.1	11.18	701	41.77	47.2		20.6	12.07	1229	95.06	40.5
30.5	27.61	867	46.44	65.4		30.4	27.58	1668	95.20	48.6
40.4	43.30	842	49.22	87.9		40.3	43.13	1640	93.87	60.7
50.7	59.61	982	49.52	99.8		51.1	60.23	1762	122.40	70.4
60.6	75.20	1182	49.65	104.0		60.7	75.39	1842	128.41	78.7
70.6	91.05	1464	50.33	105.5		70.3	90.61	1885	130.64	87.7
						80.2	106.28	1931	132.25	96.5
						90.8	123.08	2019	133.24	104.3
						100.4	138.18	2189	135.02	107.6
						110.9	154.87	2465	139.56	109.5
						121.4	171.47	2781	165.31	112.0
						130.2	185.37	2949	165.62	113.2
						141.0	202.42	3152	177.94	119.0

Note that the experimental trial on Porous Surface 3 with G = 550 kg/m^{2}s in the 200 μm gap had a pressure drop that was too large for the pressure transducers used to collect data.

Table F40. Experimental data for a 1% emulsion on Porous Surface 3, D_h = 500 µm, T_i = 30 °C.

D_h = 500 µm															
G = 150 kg/m^{2}s					G = 350 kg/m^{2}s					G = 550 kg/m^{2}s				
q [W]	q"$_{net}$ [kW/m^2]	h [W/m^{2}K]	ΔP [kPa]	T_w [°C]	q [W]	q"$_{net}$ [kW/m^2]	h [W/m^{2}K]	ΔP [kPa]	T_w [°C]	q [W]	q"$_{net}$ [kW/m^2]	h [W/m^{2}K]	ΔP [kPa]	T_w [°C]
20.4	11.62	1206	5.90	40.4	20.7	12.16	1921	14.16	36.3	20.7	12.21	2679	27.51	34.0
30.8	28.07	1899	5.79	46.5	40.7	43.79	3481	14.28	43.6	40.2	43.07	4796	27.80	38.9
40.6	43.68	2196	5.71	52.7	60.2	74.59	3919	14.04	51.0	60.7	75.39	5528	27.73	44.3
50.1	58.71	2323	5.59	59.0	80.1	106.09	4219	14.13	58.0	80.9	107.39	5845	27.72	49.6
59.9	74.24	2380	5.56	65.7	100.8	138.78	4323	14.18	65.9	100.1	137.80	6049	27.65	54.7
70.5	90.97	2474	5.49	72.6	120.7	170.27	4464	14.18	73.0	120.1	169.35	6283	27.64	59.6
80.7	107.07	2504	5.75	79.7	140.4	201.52	4665	14.23	78.9	140.7	201.96	6492	27.68	64.4
89.9	121.67	2385	5.55	89.7	160.7	233.64	4669	14.28	86.7	160.9	233.83	6622	27.65	69.3
100.3	137.99	2377	5.61	97.6	180.5	264.83	4754	14.24	93.3	180.6	265.10	6630	27.65	74.6
111.4	155.59	2652	5.93	99.8	200.6	296.70	4943	14.54	98.6	200.1	295.91	6585	27.74	80.2
120.5	169.95	2901	6.25	100.9	220.5	328.17	5105	16.98	105.0	220.1	327.54	6703	27.82	84.9
130.5	185.75	3165	6.62	102.1	241.1	360.75	5636	17.92	106.4	240.4	359.65	6834	27.93	89.2
140.8	202.08	3489	6.92	103.1	260.5	391.43	6209	18.95	107.5	259.8	390.33	6599	28.44	96.4
151.3	218.70	3829	7.39	103.8	280.6	423.22	6723	19.30	108.7	280.3	422.75	6689	29.46	101.5
161.7	235.21	4177	7.79	104.3	300.1	454.06	7150	19.21	110.5	300.6	454.86	6701	31.90	108.5
170.4	248.86	4484	8.45	104.7	321.0	487.12	7556	19.68	113.5	321.5	487.91	7174	32.59	110.3
180.6	265.01	4913	9.08	105.2	341.0	518.75	8275	20.57	114.4	341.4	519.38	7584	32.18	112.0
200.4	296.38	5718	10.00	105.8	360.0	548.80	8585	22.70	121.1	359.8	548.48	7972	32.32	113.4
220.5	328.17	6581	11.61	108.1						380.8	581.70	8287	32.24	115.4
240.0	359.01	7523	14.25	112.0										

Table F41. Experimental data for a 1% emulsion on Porous Surface 3, D_h = 1000 µm, T_i = 30 °C.

D_h = 1000 µm															
G = 150 kg/m^{2}s					G = 350 kg/m^{2}s					G = 550 kg/m^{2}s				
q [W]	q"$_{net}$ [kW/m^2]	h [W/m^{2}K]	ΔP [kPa]	T_w [°C]	q [W]	q"$_{net}$ [kW/m^2]	h [W/m^{2}K]	ΔP [kPa]	T_w [°C]	q [W]	q"$_{net}$ [kW/m^2]	h [W/m^{2}K]	ΔP [kPa]	T_w [°C]
20.3	11.61	2300	2.62	34.6	20.5	11.78	2826	6.35	34.2	20.5	11.89	3285	11.81	32.5
40.7	43.84	4086	2.53	41.5	40.2	43.07	5226	6.47	38.0	40.4	43.26	6076	11.84	36.4
60.3	74.73	4574	2.64	48.3	60.8	75.58	6075	6.55	42.5	60.4	74.89	7147	11.80	40.1
80.1	106.11	4683	2.47	55.9	80.1	106.19	6407	6.49	47.1	80.7	107.10	7696	11.85	43.9
100.8	138.81	4734	2.51	63.7	100.3	138.13	6527	6.36	52.2	100.7	138.70	7908	11.82	47.9
120.8	170.49	4924	2.47	70.1	120.3	169.69	6709	6.41	56.9	120.4	169.91	7953	11.81	52.2
139.9	200.76	4968	2.48	76.9	141.0	202.49	6867	6.32	61.7	140.7	202.00	8053	11.86	56.2
160.9	233.90	5145	2.49	83.2	161.1	234.21	6916	6.30	66.6	160.4	233.12	8201	11.85	60.0
180.4	264.72	5306	2.51	89.0	180.2	264.45	6987	6.34	71.1	180.2	264.44	8240	11.85	64.0
200.9	297.17	5453	2.53	95.0	200.6	296.70	7025	6.27	76.0	200.7	296.86	8312	11.73	68.1
220.5	328.17	5664	2.56	99.6	219.8	327.07	7062	6.33	80.7	220.3	327.86	8369	11.78	71.9
240.1	359.17	6151	2.62	101.2	240.6	359.96	7089	6.25	85.7	240.3	359.49	8488	11.73	75.5
260.9	392.07	6667	2.69	103.0	260.6	391.59	7210	6.30	89.7	260.6	391.59	8477	11.57	80.0
281.7	424.96	7251	2.71	104.2	280.4	422.91	7162	6.28	95.0	279.9	422.12	8630	11.64	83.6
301.0	455.49	7860	2.64	104.9	300.4	454.54	7314	6.32	98.8	299.8	453.59	8653	11.54	88.1
320.6	486.49	8446	2.63	105.6	320.4	486.17	7605	6.32	101.3	321.2	487.44	8769	11.54	92.0
340.3	517.64	9127	2.77	106.1	340.8	518.43	8051	6.19	102.3	339.9	517.01	8712	11.48	96.8
360.2	549.12	9823	2.77	106.7	360.6	549.75	8481	6.41	103.3	360.1	548.96	8919	11.43	99.6
380.1	580.59	10504	2.80	107.3	381.2	582.33	8939	6.26	104.4	381.3	582.49	9220	11.51	102.0

Table F42. Experimental data for a 2% emulsion on Porous Surface 3, G = 350 kg/m^{2}s, T_i = 30 °C.

D_h = 200 µm					D_h = 500 µm					D_h = 1000 µm				
G = 350 kg/m^{2}s					G = 350 kg/m^{2}s					G = 350 kg/m^{2}s				
q [W]	q"$_{net}$ [kW/m^2]	h [W/m^{2}K]	ΔP [kPa]	T_w [°C]	q [W]	q"$_{net}$ [kW/m^2]	h [W/m^{2}K]	ΔP [kPa]	T_w [°C]	q [W]	q"$_{net}$ [kW/m^2]	h [W/m^{2}K]	ΔP [kPa]	T_w [°C]
20.3	11.59	1307	209.90	39.3	20.5	11.78	1880	15.45	36.1	20.5	11.80	2739	6.82	33.8
30.7	27.96	1914	216.56	46.3	40.0	42.70	3342	15.23	43.5	40.2	43.00	5115	6.78	38.3
40.2	43.05	2183	225.38	52.5	60.2	74.57	3867	15.33	51.0	60.8	75.52	5992	6.81	43.0
50.8	59.85	2387	231.91	59.4	80.0	105.96	4106	15.31	58.4	80.1	106.11	6230	6.83	47.9
60.6	75.27	2331	237.95	67.9	100.9	138.97	4393	15.23	65.2	100.3	138.10	6503	6.75	52.7
70.1	90.37	2330	242.14	76.8	120.4	169.89	4476	15.17	72.4	120.2	169.46	6645	6.71	57.5
80.8	107.23	2658	321.49	78.8	140.5	201.57	4490	15.24	80.4	141.0	202.47	6805	6.65	62.2
90.2	122.16	2758	330.01	83.8	160.0	232.50	4579	15.29	87.3	161.0	234.09	6922	6.81	66.9
100.5	138.43	2859	348.95	89.1	180.8	265.31	4565	15.62	95.8	180.1	264.33	7057	6.61	71.0
110.7	154.55	2887	330.68	96.0	200.1	295.91	4671	17.24	102.7	200.5	296.54	7118	6.62	75.7
121.1	170.95	3003	334.64	100.9	220.4	328.01	5074	18.47	105.5	219.5	326.59	7048	6.66	80.9
130.4	185.63	3042	334.90	106.4	240.4	359.65	5586	19.52	106.8	240.9	360.44	7096	6.63	85.9
140.0	200.87	3112	336.81	111.4	260.3	391.12	6151	20.39	107.8	260.8	391.91	7149	6.61	90.6
150.4	217.32	3337	338.94	113.6	280.7	423.38	6661	20.14	108.9	280.2	422.59	7193	6.56	95.2
161.1	234.21	3567	341.33	116.4	301.6	456.44	7132	20.84	111.4	301.0	455.49	7326	6.57	99.4
					320.5	486.33	7489	21.31	114.0	320.7	486.64	7652	6.41	101.5
					340.0	517.17	8003	23.23	117.6	341.6	519.70	8117	6.55	102.5
					360.1	548.96	8507	25.01	121.7	360.8	550.06	8578	6.31	103.7
										381.5	582.80	9022	6.15	105.0

G. Other Forms of Emulsion Correlations

From the physical mechanisms discussed in Chapter 5, the following system parameters are deemed to be important for correlating the emulsion boiling data: k_d, d, D_h, μ_c, ρ_d/ρ_c, G, h_{fg}, $C_{p,c}$, ε, q", h. Based on these parameters, seven nondimensional numbers for correlating the data are,

$$\frac{hD_h}{k_d} \qquad \frac{GD_h}{\mu_c} \qquad \frac{q"}{Gh_{fg_d}} \qquad \varepsilon$$
$$\frac{\rho_d}{\rho_c} \qquad \frac{GC_p d}{k_d} \qquad \frac{d}{D_h} \tag{G1}$$

The density ratio is not considered in this analysis because only one set of fluids is used in this study. The remaining nondimensional numbers result in the correlation,

$$h = 0.0068\frac{k_d}{D_h}\varepsilon^{-0.022}\left(\frac{d}{D_h}\right)^{-2.31}\left(\frac{GD_h}{\mu_c}\right)^{-1.41}\left(\frac{q"}{Gh_{fg_d}}\right)^{0.81}\left(\frac{GC_p d}{k_d}\right)^{2.15} \tag{G2}$$

This correlation has 96.2% of the experimental data within ±10% of the predicted value. The ratio of the emulsion heat transfer coefficient and that for water at the same wall temperature and experimental condition can also be correlated with these numbers as,

$$\frac{h-h_0}{h_0} = 0.049\varepsilon^{-0.030}\left(\frac{d}{D_h}\right)^{-1.37}\left(\frac{GD_h}{\mu_c}\right)^{-1.34}\left(\frac{q"}{Gh_{fg_d}}\right)^{0.72}\left(\frac{GC_p d}{k_d}\right)^{1.60} - 1 \tag{G3}$$

This correlation has 37.0% of the experimental data within ±15% and 59.2% within ±30% of the predicted value. The experimental boiling data is compared to the predicted heat transfer coefficients in Fig. G1.

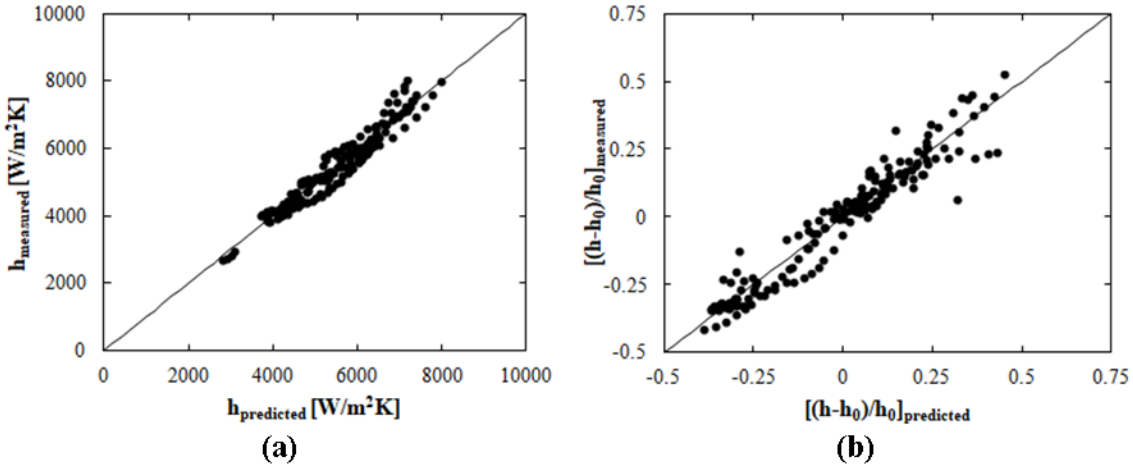

Fig. G1. (a) Comparison between the measured emulsion heat transfer coefficient and that predicted by Eqn. (G2). (b) Comparison between the measured ratio of the emulsion and water heat transfer coefficients and the ratio predicted by Eqn. (G3). The solid line represents equivalence between the measured and predicted values.

With so many parameters being used in the correlation, we may expect a good fit simply due to the number of parameters. Although the p-value- a statistical parameter that demonstrates whether a given parameter correlates with the experimental data- for every nondimensional number shows the necessity of including each, the data can be correlate without the inclusion of some numbers to view their significance. The last two numbers in Eqn. (G1) only have three values in the experimental data, aside from minor variation due to the effect of temperature on properties, so these two numbers can be neglected to view their significance. If this is done, the data is correlated as,

$$h = 1.80\frac{k_d}{D_h}\varepsilon^{-0.028}\left(\frac{GD_h}{\mu_c}\right)^{0.96}\left(\frac{q''}{Gh_{fg_d}}\right)^{0.51} \tag{G4}$$

$$\frac{h-h_0}{h_0} = 1.73\varepsilon^{-0.045}\left(\frac{GD_h}{\mu_c}\right)^{0.16}\left(\frac{q''}{Gh_{fg_d}}\right)^{0.36} - 1 \tag{G5}$$

Equation (G4) has 51.6% of the experimental data within ±15% and 87.5% within ±30% of the predicted value. Equation (G5) has 39.1% of the experimental data within

±30% of the predicted value. The experimentally measured heat transfer coefficients are plotted in comparison to the predicted values in Fig. G2. It is clear that it is necessary to include the last two nondimensional numbers in Eqn. (G1).

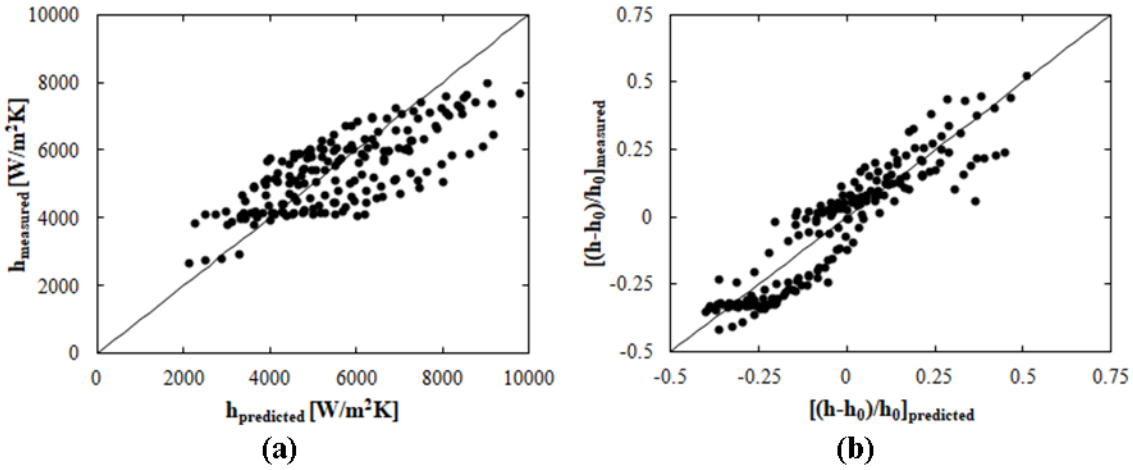

Fig. G2. (a) Comparison between the measured emulsion heat transfer coefficient and that predicted by Eqn. (G4). (b) Comparison between the measured ratio of the emulsion and water heat transfer coefficients and the ratio predicted by Eqn. (G5). The solid line represents equivalence between the measured and predicted values.

It is not clear that the boiling number is the correct parameter to account for the effect of the disperse component latent heat. It is possible that the ratio of the total sensible heat to the continuous component and the total latent heat to the disperse component would be a more appropriate nondimensional number to quantify these two effects. If this ratio is used, the resulting correlations are

$$h = 1.53\frac{k_d}{D_h}\varepsilon^{-0.13}\left(\frac{d}{D_h}\right)^{-0.28}\left(\frac{GD_h}{\mu_c}\right)^{0.97}\left(\frac{\rho_c(1-\varepsilon)C_p(T_w-T_f)}{\rho_d\varepsilon h_{fg_d}}\right)^{-0.065}\left(\frac{GC_pd}{k_d}\right)^{-0.64} \quad \text{(G6)}$$

$$\frac{h-h_0}{h_0} = 0.29\varepsilon^{0.14}\left(\frac{d}{D_h}\right)^{-0.029}\left(\frac{GD_h}{\mu_c}\right)^{0.26}\left(\frac{\rho_c(1-\varepsilon)C_p(T_w-T_f)}{\rho_d\varepsilon h_{fg_d}}\right)^{0.21}\left(\frac{GC_pd}{k_d}\right)^{-0.41} - 1 \quad \text{(G7)}$$

Equation (G6) has 81.5% of the experimental data within ±15% and 98.9% within ±30% of the predicted value. Equation (G7) has no data that falls within ±50%, with the average error being 77%. The measured heat transfer coefficient is plotted against the

predicted values in Fig. G3. It is clear that the boiling number better predicts both the heat transfer coefficient and the ratio.

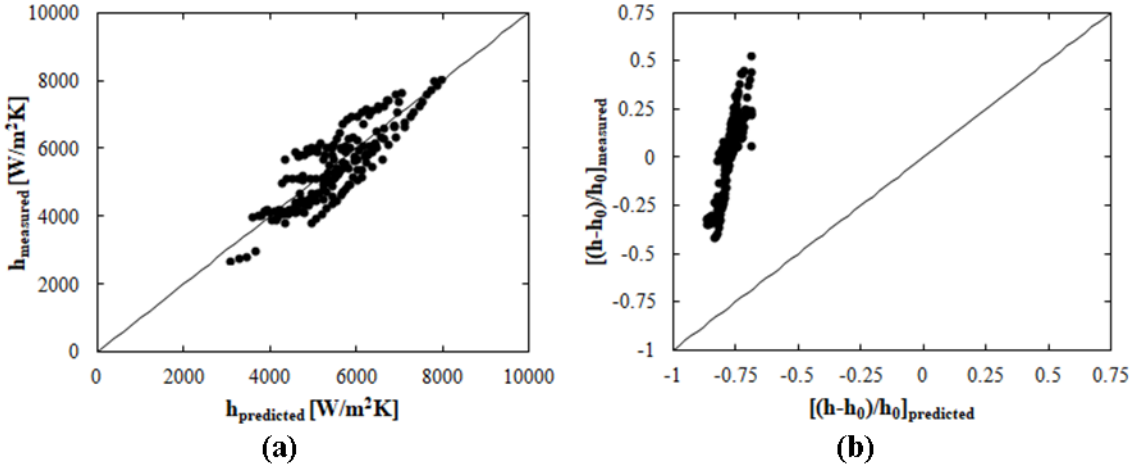

Fig. G3. (a) Comparison between the measured emulsion heat transfer coefficient and that predicted by Eqn. (G6). (b) Comparison between the measured ratio of the emulsion and water heat transfer coefficients and the ratio predicted by Eqn. (G7). The solid line represents equivalence between the measured and predicted values.

Note that the exponent on ε in Eqns. (G2) and (G3) is very close to zero. This may suggest that the use of ε in the correlation is unnecessary. However, the p-value for ε also indicates that there is a strong correlation for ε in the experimental data. Therefore, this may also indicate that the form of the number used to include ε is incorrect. The necessity of using ε will first be explored by neglecting it from the correlation procedure. The result is,

$$h = 0.0053 \frac{k_d}{D_h} \left(\frac{d}{D_h}\right)^{-2.45} \left(\frac{GD_h}{\mu_c}\right)^{-1.57} \left(\frac{q''}{Gh_{fg_d}}\right)^{0.87} \left(\frac{GC_p d}{k_d}\right)^{2.35} \tag{G8}$$

$$\frac{h - h_0}{h_0} = 0.034 \left(\frac{d}{D_h}\right)^{-1.55} \left(\frac{GD_h}{\mu_c}\right)^{-1.56} \left(\frac{q''}{Gh_{fg_d}}\right)^{0.80} \left(\frac{GC_p d}{k_d}\right)^{1.86} - 1 \tag{G9}$$

Equation (G8) has 95.1% of the experimental data within ±10% of the predicted value. Equation (G9) has 31.5% of the data within ±15% and 58.7% within ±30% of the

predicted value. The measured heat transfer coefficient is plotted against the predicted values in Fig. G4.

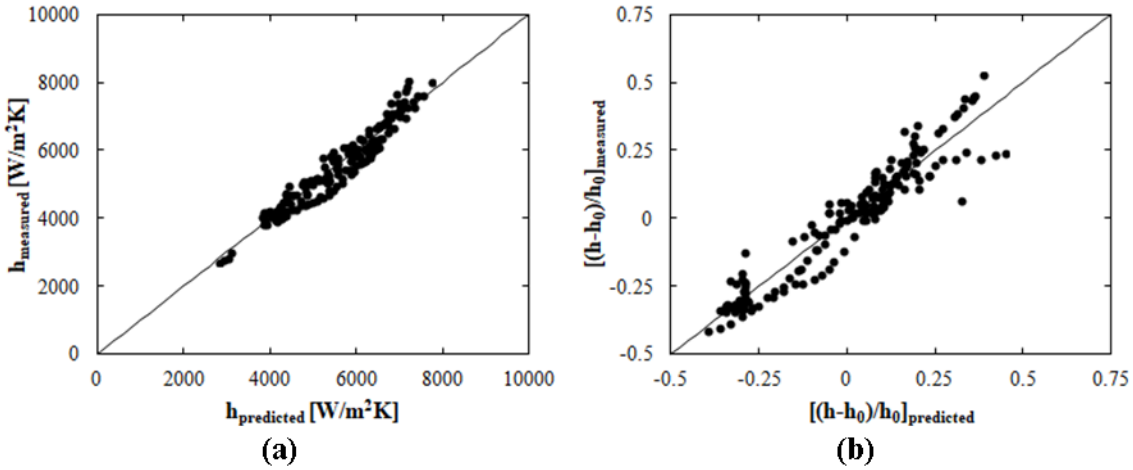

Fig. G4. (a) Comparison between the measured emulsion heat transfer coefficient and that predicted by Eqn. (G8). (b) Comparison between the measured ratio of the emulsion and water heat transfer coefficients and the ratio predicted by Eqn. (G9). The solid line represents equivalence between the measured and predicted values.

It seems the correlation is slightly worse when not including ε. The experimental results demonstrate that ε has a large effect on the heat transfer behavior at low values but the effect asymptotically decreases as ε increases. This is consistent with a form of 1/ε. Therefore, let us use 1/(1+ε) to capture this experimental trend and have the effect of ε go to 0 for ε→0. The resulting correlations are,

$$h = 0.0067 \frac{k_d}{D_h} \frac{1}{(1+\varepsilon)^{3.42}} \left(\frac{d}{D_h}\right)^{-2.37} \left(\frac{GD_h}{\mu_c}\right)^{-1.48} \left(\frac{q''}{Gh_{fg_d}}\right)^{0.84} \left(\frac{GC_p d}{k_d}\right)^{2.24} \qquad \text{(G10)}$$

$$\frac{h-h_0}{h_0} = 0.045 \frac{1}{(1+\varepsilon)^{4.15}} \left(\frac{d}{D_h}\right)^{-1.46} \left(\frac{GD_h}{\mu_c}\right)^{-1.46} \left(\frac{q''}{Gh_{fg_d}}\right)^{0.76} \left(\frac{GC_p d}{k_d}\right)^{1.73} - 1 \qquad \text{(G11)}$$

These correlations demonstrate a strong dependence on ε for small values of ε, consistent with the experimental results. Equation (G10) fits the experimental data very well, with 95.7% of the experimental data falling within ±10% of the predicted value. 36.4% of the experimental data falls within ±15% and 58.7% falls within ±30% of the

values predicted by Eqn. (G11), but this equation does a good job of capturing the trends in the data (Fig. G5). Therefore, this is the final correlation form that will be used.

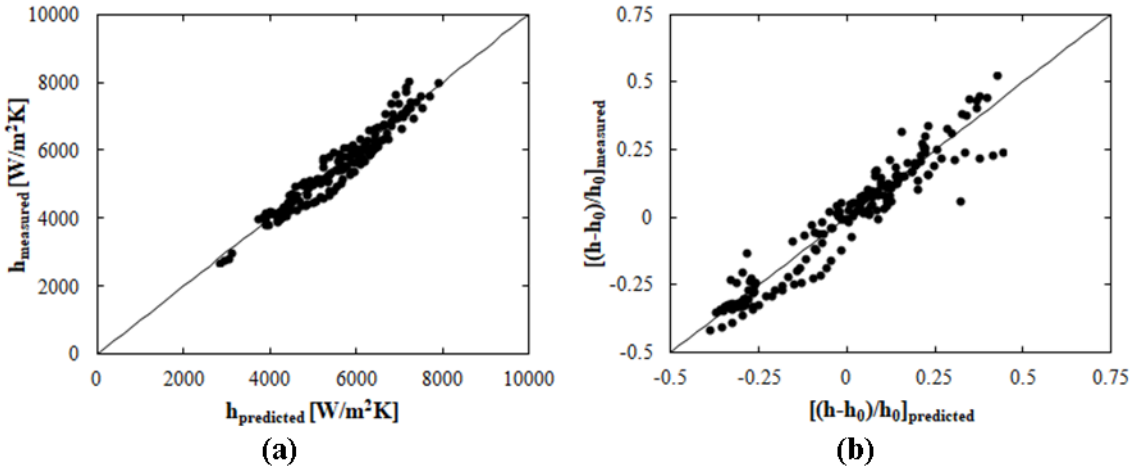

Fig. G5. (a) Comparison between the measured emulsion heat transfer coefficient and that predicted by Eqn. (G10). (b) Comparison between the measured ratio of the emulsion and water heat transfer coefficients and the ratio predicted by Eqn. (G11). The solid line represents equivalence between the measured and predicted values.